ANTI-STOKES GENERATION IN A CONTINUOUS-WAVE RAMAN LASER

by

Sytil Kathleen Murphy

A dissertation submitted in partial fulfillment
of the requirements for the degree

of

Doctorate of Philosophy

in

Physics

MONTANA STATE UNIVERSITY
Bozeman, Montana

July, 2008

APPROVAL

of a dissertation submitted by

Sytil Kathleen Murphy

This dissertation has been read by each member of the dissertation committee and has been found to be satisfactory regarding content, English usage, format, citations, bibliographic style, and consistency, and is ready for submission to the Division of Graduate Education.

Dr. John L. Carlsten

Approved for the Department of Physics

Dr. William A. Hiscock

Approved for the Division of Graduate Education

Dr. Carl A. Fox

STATEMENT OF PERMISSION TO USE

In presenting this dissertation in partial fulfillment of the requirements for a doctoral degree at Montana State University, I agree that the Library shall make it available to borrowers under rules of the Library. I further agree that copying of this dissertation is allowable only for scholarly purposes, consistent with "fair use" as prescribed in the U.S. Copyright Law. Requests for extensive copying or reproduction of this dissertation should be referred to ProQuest Information and Learning, 300 North Zeeb Road, Ann Arbor, Michigan 48106, to whom I have granted "the exclusive right to reproduce and distribute my dissertation in and from microform along with the non-exclusive right to reproduce and distribute my abstract in any format in whole or in part."

Sytil Kathleen Murphy

July, 2008

DEDICATION

To my husband,

for everything. Without you, I don't know as I would have made it through all nine years this process took. You are my biggest cheerleader.

To my family,

for your constant love, support and encouragement. And, for listening to my grumbles when things weren't going as smoothly as they could have.

To my friends,

for wonderful times together. You've made the non-Physics side of this process the best that it could be.

To my advisor,

for your guidance. I hope that my students will look up to me one day as I look up to you now.

ACKNOWLEDGMENTS

I would like to begin by thanking Dr. Christopher Fasano from Monmouth College. Without his teaching me 90% of an undergraduate Physics curriculum in a single year, I would not have made it into graduate school.

Next, I would like to thank the Montana State Physics department who took a math major and molded her into a physicist. I would especially like to thank those faculty members who I was privileged to have as instructors and the department staff for making sure all the cogs kept turning. This department goes out of its way to become the most nurturing environment possible.

THANKS to all my family and friends. There is a ton more that could (and should) be said here but there just isn't space.

Thanks to my labmates throughout these years. For the support and assistance. For wonderful conversations. For making the lab a much more lively place than it would have been with just me in it. A profound thank-you to Dr. Paul Nachman for helping shape the physics contained within this dissertation through conversation and the liberal use of a red pen. Thanks to Dr. Kevin Repasky, Dr. Jay Brasseur, Dr. Pete Roos, and Dr. Lei Meng for defining the path. Thanks to Dr. Yihan Xiong for walking the path beside me.

Finally, a big thank-you to Dr. John Carlsten for guiding my walk down the path, for letting me explore other branches, for listening, for helping, for... There are not words enough to express my gratitude. You are the best.

There are many whose names should appear here that do not. To those who I missed, I extend a profound apology.

TABLE OF CONTENTS

TABLE OF CONTENTS – CONTINUED

TABLE OF CONTENTS – CONTINUED

TABLE OF CONTENTS – CONTINUED

LIST OF TABLES

Table Page

LIST OF TABLES – CONTINUED

LIST OF FIGURES

Figure Page

LIST OF FIGURES – CONTINUED

Figure Page

LIST OF FIGURES – CONTINUED

Figure Page

LIST OF FIGURES – CONTINUED

Figure Page

LIST OF FIGURES – CONTINUED

Figure Page

LIST OF FIGURES – CONTINUED

Figure Page

LIST OF FIGURES – CONTINUED

Figure Page

LIST OF FIGURES – CONTINUED

Figure Page

LIST OF FIGURES – CONTINUED

Figure Page

LIST OF FIGURES – CONTINUED

Figure Page

LIST OF FIGURES – CONTINUED

Figure Page

LIST OF FIGURES – CONTINUED

Figure Page

LIST OF FIGURES – CONTINUED

Figure Page

ABSTRACT

The continuous-wave Raman laser system differs from other Raman systems in that it uses cavity enhancement to augment the pump laser source rather than a high-power pulsed laser source. Through interactions of the pump laser with the Raman active medium, all Raman systems can produce both red-shifted, Stokes, emission and blue-shifted, anti-Stokes, emission. Previous, continuous-wave Raman laser systems have focused on the Stokes emission. This dissertation presents theory and data on the anti-Stokes emission. Specifically, it investigates the anti-Stokes mode structure and the emitted power as a function of input pump power, detuning, pressure, and mode combination.

In order to be able to compare theory to data, the existing semi-classical CW Raman laser theory is extended to include the possibility that the spatial mode of any of the three fields (pump, Stokes, or anti-Stokes) is not the fundamental spatial mode. Numerical simulations of this theory are used to understand the behavior of the CW Raman system. All the data is compared to the theory, with varying degrees of success.

The pump laser used in this research is a frequency-doubled Nd:YAG at 532 nm and the Raman active medium is H_2. This combination results in Stokes and anti-Stokes wavelengths of 683 nm and 435 nm, respectively.

Five methods were found in this research for increasing the amount of anti-Stokes emitted: increasing the input pump power, detuning from gain line-center of the Stokes emission, increasing the reflectivity of the cavity mirrors at the anti-Stokes wavelength, switching to a higher-order spatial mode, and decreasing the H_2 pressure within the Raman cavity.

In general, it was found that the higher-order anti-Stokes modes did not agree with a single theoretical spatial mode. Superpositions were formed of multiple theoretical spatial modes giving intensity distribution across the profile similar to the measured profile. Three theoretical spatial mode symmetries were investigated: rectangular, cylindrical, and elliptical.

Also measured was the Raman gain as a function of pressure. The accepted theory for the Raman linewidth was found to be slightly off.

1

INTRODUCTION

What is a Far-Off-Resonant Continuous-Wave Raman Laser?

There are three basic necessary components to a laser oscillator: a laser medium, an optical cavity, and a method of pumping energy into the cavity. The first laser consisted of a cylindrical ruby crystal (the medium) that had its end surfaces coated in silver (forming the cavity) surrounded by a flashlamp [1]. By today's standards, this was a rather weak laser, but then, it was enough to prove the concept. Today, there are many different types of laser media ranging from solid state lasers based on sapphire and YAG crystals to gas lasers like the helium-neon (HeNe) to semiconductor diode lasers.

There are also multiple ways of creating the laser cavity. In the case of a HeNe laser, mirrors are placed at both ends of a tube filled with the laser medium while the cavity for the most basic semiconductor lasers is composed of a highly reflective dielectric coating on one of the laser's cleaved facets and the native reflectivity of the opposite facet.

And, of course, energy can be supplied in various ways. Today, lasers can still be found that use flashlamps or they can be pumped by sending another laser beam into the medium or by applying a voltage across the medium. No matter the geometry, lasers all share the same basic set of characteristics. Three of these characteristics are monochromaticity (though some more so than others), uni-directional radiation, and a pumping threshold, below which laser light is not emitted. Contrast this to the light from a standard lightbulb or a candle, which radiate broad spectrum light in all directions. If the power to the lightbulb is turned down with a dimmer switch, for example, the lightbulb will emit less light but will not turn off unless there is no

power being applied.

While all lasers share the same basic components, how lasers operate is the subject of entire books (for example, Laser Fundamentals by Silfvast [2]). Thus, only the specific example of the far-off-resonance (FOR) continuous-wave (CW) Raman laser pertinent to this dissertation will be presented here in an attempt to illustrate the roles of each of the basic laser components. Along the way, the basics of both Raman scattering and spontaneous and stimulated emission will be presented.

Scattering Basics

Scattering occurs when a photon interacts with an atom or molecule. (From here on, molecule will be used exclusively to refer to the scatterer.) There are two basic types of scattering: elastic and inelastic. During an *elastic* scattering event, such as Rayleigh or Mie scattering, the incident photon and the scattered photon have the same frequency as illustrated in Figure 1.1. In the figure, the solid lines represent real

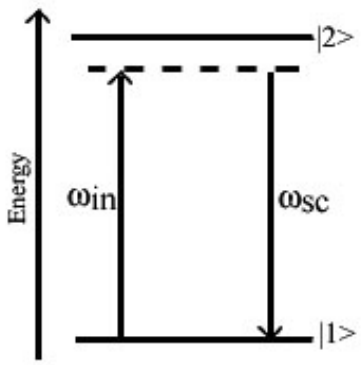

Figure 1.1: Rayleigh Scattering.

molecular energy levels, where level 1 is the molecule's ground state and level 2 is an upper excited electronic level, the dashed line is a virtual level, ω_{in} is the frequency of the incident photon, and ω_{sc} is the frequency of the scattered photon. (Levels 1 and 2 are real levels of the molecule, independent of the laser interaction. Virtual

levels are real levels that develop as a result of the interaction of the laser with the molecule.) Rayleigh scattering is probably the most familiar scattering process since it is responsible for, among other things, the sky being blue.

In an *inelastic* scattering event, unlike an elastic scattering event, the scattered photon has a frequency that differs from the incident photon. In order for energy to be conserved, the molecule must also undergo a change in energy. Two types of inelastic scattering are Raman and Brillouin. Figure 1.2 shows Raman scattering in which the scattered photon is red-shifted with respect to the incident photon. In this

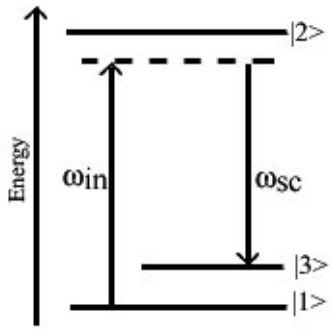

Figure 1.2: Raman Scattering.

figure, the solid lines represent real molecular energy levels: level 1 is the molecule's ground state, level 3 is the first excited vibrational state, level 2 is an upper excited electronic level, the dashed line is a virtual level, $\omega_{in}$is the frequency of the incident photon, and ω_{sc} is the frequency of the scattered photon. This red-shifted scattered photon is known as a "Stokes photon". The reverse of this is shown in Figure 1.3, where the molecule begins in an excited state and, after the scattering event, is left in its ground state. The scattered "anti-Stokes" photon therefore has more energy than the incident photon and is thus blue-shifted with respect to it.

All the photons in Figures 1.1, 1.2, and 1.3 are shown to be near resonant with electronic transitions of the medium, i.e. the separation of the virtual levels from

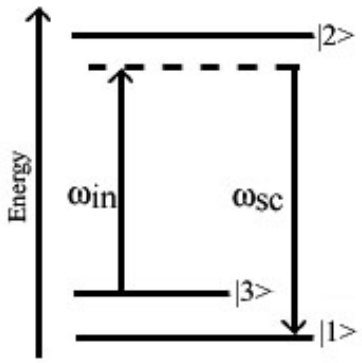

Figure 1.3: Raman Scattering.

the upper electronic level is small compared to the energy in the photons. However, this does not have to be the case. For the FOR-CW Raman laser, the laser medium is typically, as in this dissertation, H_2 [3, 4, 5, 6], though work has also been done with D_2 [7] as a medium. Figure 1.4 shows a scale energy level drawing for H_2 if the incident pump photon is from a frequency-doubled Nd:YAGlaser ($\lambda = 532$ nm), as used in this dissertation. In this figure, in contrast to Figures 1.1, 1.2, and 1.3, the photons have been relabeled to represent the three types of photons in the CW Raman laser system: ω_p is the pump photon, ω_s is the Stokes photon, and ω_a is the anti-Stokes photon. In addition, the energy of each photon (in cm^{-1}) is given along with the energy difference between the ground state, 1, and first excited vibrational level, 3, and that between the ground state, 1, and the first excited electronic level, 2. The energy contained in a photon of the input laser is roughly a factor of 10 smaller than the energy separation between levels 1 and 2. The relationship between the two energies is why the CW Raman laser is also referred to as the FOR-CW Raman laser, and it has many implications for the system. In this dissertation, unless explicitly stated otherwise, "CW Raman laser" will be used to refer to the "FOR-CW Raman laser".

Often Raman systems produce additional Stokes and anti-Stokes frequencies

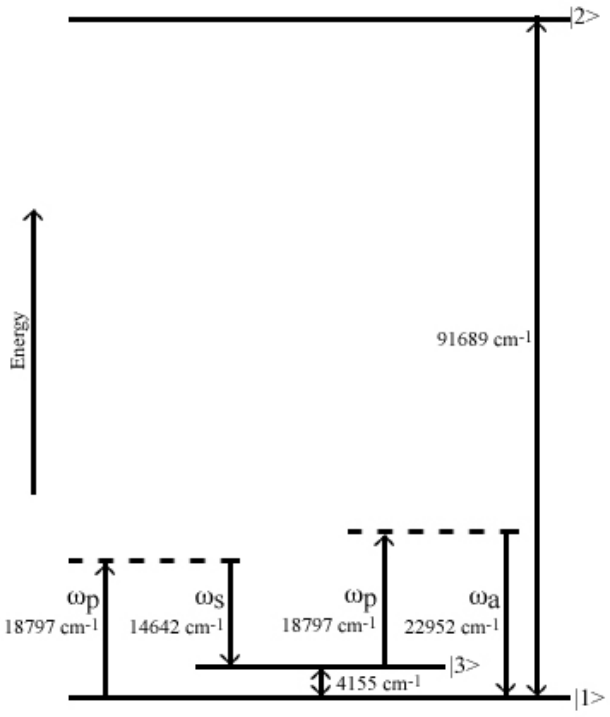

Figure 1.4: Raman Scattering. The energy separation between levels 1 and 3 was found in Herzberg [8].

beyond those shown in Figure 1.4. Stokes at the frequency shown in the figure is often referred to as the first Stokes. The second Stokes is generated when a first Stokes photon scatters off a ground-state molecule. The scattered photon has an additional red shift when compared to the original pump photon. This process can lead to a comb of emission frequencies downshifted from the original input [9]. The corresponding process involving anti-Stokes photons and excited molecules leads to an upshifted comb. These combs can be quite large. For example, in [10], 40 rotational Raman lines were generated, while in [11], the comb ranged in frequency from the near-infrared to the ultraviolet. However, as described in a later section, the CW Raman laser has a frequency selectivity that yields negligible higher order Stokes and anti-Stokes emissions.

Spontaneous and Stimulated Emission

A spontaneously emitted photon occurs when an excited molecule makes a radiative transition between energy levels, releasing a photon in the process. As shown in Figure 1.5, the molecule begins in an upper excited level. At some time later, it loses energy in the form of a photon. This photon has a very clearly defined

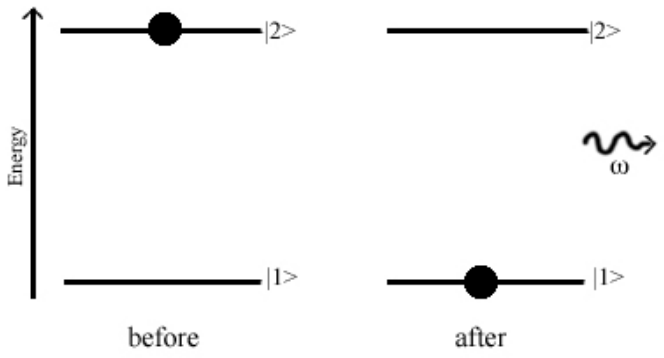

Figure 1.5: Spontaneous Emission.

energy determined by the energy levels of the molecule, if the molecule is not being influenced by an external laser.

Stimulated emission occurs when an excited molecule undergoes a radiative transition to a lower level as a result of an interaction with a photon, as shown in Figure 1.6. The emitted photon has the same energy, polarization, and direction as the incident photon. Where there once was only one photon, there are now two identical photons. Stimulated emission can lead to exponential gain if the number of photons lost (by scattering or absorption in the medium or loss due to an element of a laser cavity) is less than the number of photons generated during that same time period. When this occurs in a laser, it is said to have reached its threshold and, for any frequency that meets the threshold requirement, the stimulated emission will dominate the spontaneous emission background. In general, the laser threshold can

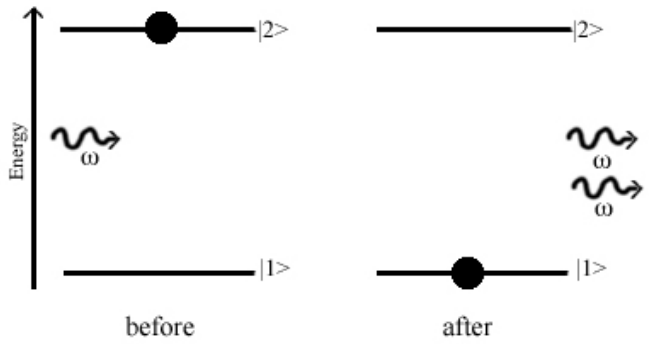

Figure 1.6: Stimulated Emission.

only be exceeded in one direction, determined by the symmetry of the system. For example, if the laser medium is a cylinder of gas, as with the CW Raman Laser, then the direction of symmetry will be along the optical axis defined by the cavity's mirrors. An important point about gain in a laser is that it can only occur, for the most part, if there is a population inversion between an upper level and a lower level. (A population inversion occurs when there is more population in the upper level than the lower.)

In the CW Raman Laser, as discussed above, the laser medium is not a simple two level system as shown in Figures 1.5 and 1.6. It is a three level system, with the 1-2 transition being FOR with the laser fields as shown in Figure 1.4. Because the upper level, 2, is FOR, it is impossible for the atom to be excited all the way up to that energy. Instead, it is excited to a virtual level. A virtual level is not a real molecular level. However it is a real level for the combined system consisting of both the laser fields and the molecules. As such, it is possible for a molecule to be excited up to the virtual level and then emit a Stokes photon by spontaneous emission to the excited vibrational level, 3, as shown in Figure 1.7. At standard temperature, the population of the H_2 molecules is almost entirely in the ground state, 1. This means that there are (fractionally) very few molecules in any of the excited levels. For the

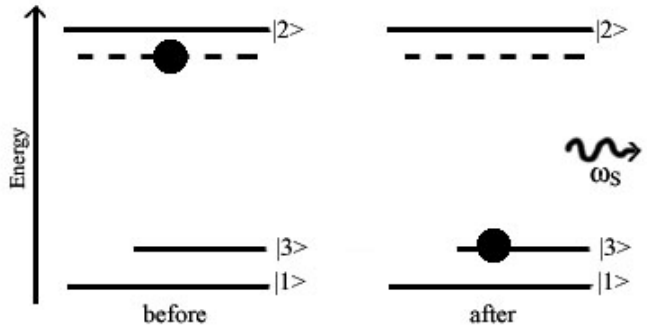

Figure 1.7: Spontaneous Raman Emission.

conversion of pump to Stokes, the population inversion for stimulated emission needs to occur between a virtual level and the excited vibrational level, 3. But, since there is negligible population in level 3, this population inversion is easily achieved, allowing stimulated Stokes emission to occur. In stimulated Raman emission, a Stokes photon

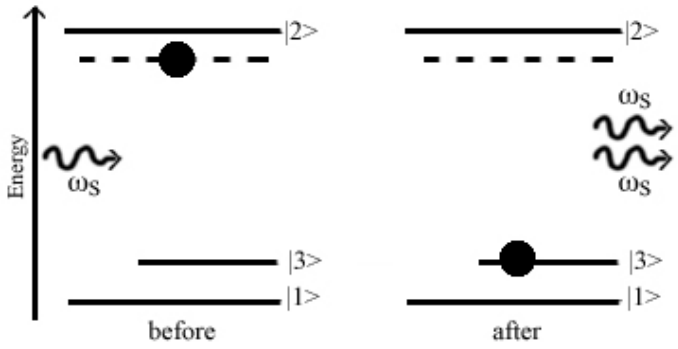

Figure 1.8: Stimulated Raman Emission.

interacts with an excited molecule causing it to make a radiative transition to the ground state, releasing a second Stokes photon in the process.

When there is an external laser field present, the energy of the scattered photon is determined by the energy difference between the virtual level and the vibrational level rather than between the upper electronic level and the vibrational level. These scattered photons can be either spontaneous or stimulated. However, in the case

of spontaneously emitted photons, as the external laser field is detuned from the electronic resonance, the emission probability decreases.

The Role of the Laser Cavity

A schematic of the CW Raman laser is shown in Figure 1.9. In the discussion so

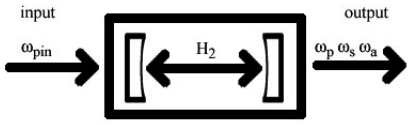

Figure 1.9: The CW Raman Laser Cavity.

far, all the pieces of the laser have been encountered except the mirrors that define the laser cavity. For perspective, in the visible, a piece of glass (like a window) is about 4% reflective, a standard silver mirror purchased from an optics company (Thorlabs PF10-03-P01) is 97% reflective, and a purchased broadband dielectric mirror is specified at ¿99% (Thorlabs BB1-E02-10). The mirrors at the ends of the CW Raman laser cavity are typically at or above 99.98% reflective and, in addition, the scattering and absorption losses of these mirrors are less than 100 parts per million [12].

Loss due to the mirrors is the primary source of loss in the CW Raman system and therefore it is very important for it to be as low as possible. These mirrors are absolutely necessary to the operation of the CW Raman laser. Traditionally, these mirrors have been coated at only the pump and first Stokes wavelength, but this dissertation will also deal with mirrors coated for the first anti-Stokes wavelength as well. A cavity composed of this type of mirrors has very narrow resonances and can

yield very high intracavity powers. For example, for a 3-in. cavity with mirrors that are 99.97% reflective, the intracavity power is ∼10,000 times the input power and the cavity linewidth is 1.8 kHz. An optical cavity made with these mirrors is often referred to as a high finesse cavity (HFC).

By being resonant at the pump wavelength, the pump power builds up within the Raman cavity, exciting some of the molecules. By being resonant at the Stokes wavelength, the stimulated emission experience regenerative feedback. This combination allows the laser threshold to be exceeded, creating a laser at the Stokes wavelength. Also, because the mirrors are coated for specific wavelengths only, typically, only the first Stokes can exceed threshold. However, in the development of the laser, it has also been found that the coating for the pump can be broad enough to also allow a rotational Stokes mode to resonate[5, 13] instead of the vibrational Stokes described in this introduction. (Rotational Stokes differs from vibrational Stokes in that the separation in energy between the ground state, a, in Figure 1.4, and state b would be smaller. For H_2, the vibrational separation is 4155 $cm^{-1}$and the rotational separation is 586.9 cm^{-1}[14])In addition, the initial anti-Stokes investigations discovered that the mirrors were also about 25% reflective at the anti-Stokes wavelength [15].

The Rest of the Story...

All the pieces are now present to make a CW Raman laser. The story begins with a pump laser. In this dissertation, that laser is a frequency doubled Nd:YAG ($\lambda = 532$ nm). There are many optics in between that are not essential to the basic operational picture being presented here, but eventually, the pump laser is incident at the front of the Raman laser cavity. The problem, now, is that the frequency of the pump laser is not necessarily resonant with the frequency of the HFC. To overcome this hurdle, an

electronic frequency stabilization scheme known as Pound-Drever-Hall locking is used [16, 17]. Pound-Drever-Hall locking uses a reference signal based on the difference between the cavity resonance frequency and the laser frequency to make adjustments to the cavity length (thereby changing the cavity resonance frequency) and the laser frequency. The initial matching of the two frequencies is accomplished manually but after that, locking electronics work to maintain the matching. This may sound easy, but in reality, it is the hardest part of running the CW Raman laser system. Once the pump is resonant with the cavity, then Stokes (and anti-Stokes) can be generated. The initial photon for starting the pump-to-Stokes conversion process is generated by spontaneous emission. After that, stimulated emission takes over, and assuming that the system is above threshold, Stokes resonates within the cavity as well. While the transmission of the cavity is small, it is not zero, and each round-trip, some of the Stokes photons are emitted, making the HFC into a Stokes laser.

Anti-Stokes, on the other hand, is not generated by a stimulated process since it is impossible to obtain a population inversion between the upper (virtual) level and the ground state. Instead, anti-Stokes is generated by a parametric process called four-wave mixing (FWM). During FWM, two pump photons, a Stokes photon and the medium interact in such a way that an anti-Stokes photon is emitted. (In fact, the interaction of the photons with the medium occurs whenever stimulated Stokes photons are generated, which is why it is often said that it is impossible to avoid generating some anti-Stokes! [18]) Luckily, as first shown theoretically by Roos in 2004 [19], anti-Stokes generation can also be cavity enhanced. Therefore, the CW Raman laser can also serve as an efficient generation technique for anti-Stokes as well as Stokes.

Historical Development of the FOR-CW Raman Laser

Rarely does an idea come along that is not based upon or an extension of a previous idea. The past 85 years have played an important role in the development of the CW Raman laser. In these years, four Nobel prizes have been awarded for work leading up to the CW Raman laser. The goal of this section is to place the work of this dissertation in an appropriate historical context. The major steps in this development are shown in Figure 1.10.

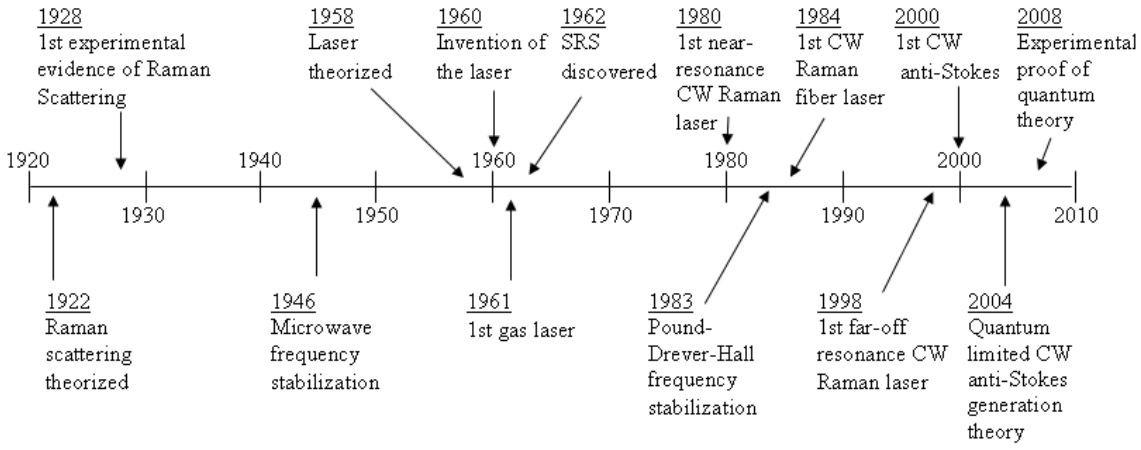

Figure 1.10: Timeline for the development of the CW Raman laser.

In 1923, A. Smekal [20] first considered a scattering system in which the scattered photon could have a frequency different from the incident photons. His theory considered conservation of energy in a system of an incident photon interacting with an atom. Five years later, several groups were making measurements of just such an effect. The Russians were making measurements in quartz, the French in gases, and a young Indian named Chandrasekhara Venkata Raman in liquids [21]. All three groups published papers on the effect in 1928 but Raman published first. Therefore his is the name that now is associated with this process and he is the one who received

all the accolades. These accolades included the Nobel Prize in Physics in 1930 "for his work on the scattering of light and for the discovery of the effect named after him. [22]" The full quantum theory for the Raman process was developed I. Tamm in 1930 and Georges Placzek in 1934 [21].

The next major step in the history leading up to the CW Raman laser is the theoretical development of the laser in 1958 by Schawlow and Townes[2]. Townes shared the 1964 Nobel Prize in Physics with Basov and Prokhorov "for fundamental work in the field of quantum electronics, which has led to the construction of oscillators and amplifiers based on the maser-laser principle. [22]" (Shawlow, on the other hand, had to wait an additional 17 years to be recognized by the Nobel committee. "For their contribution to the development of laser spectroscopy," he, along with Bloembergen, received the 1981 prize [22]. Siegbahn was also honored in 1981 but for different reasons.) Two years later, in 1960, the first laser was demonstrated by Maiman [2, 1]. This laser was a solid state laser based on a ruby crystal. Shortly thereafter, the first gas laser, a HeNe, was demonstrated by Javan, Bennett and Herriott [23]. And there have been many, many more since.

In 1962, by accident, Woodbury and Ng [24, 25] discovered stimulated Raman scattering (SRS). In the process of operating a Q-switched ruby laser, they noticed that, in addition to the standard wavelength emitted by the laser, they also had a very strong emission in the infrared. This infrared emission was the result of SRS emission of the nitrobenzene that had been placed in the laser cavity, as a Q-switching device. Arguably, this was also the first demonstration of a pulsed Raman laser since the ruby laser cavity was also resonant for the Stokes wavelength. It was another 18 years before the first *near-resonant* CW Raman laser was developed [26, 27]. The first CW fiber Raman laser was developed in 1984 [28].

The next piece of the far-off resonance CW Raman laser puzzle is the Pound-Drever-Hall electronic frequency stabilization scheme. Pound-Drever-Hall locking is a method of stabilizing a laser frequency to the frequency of a resonant system. The first paper published on what was to become known as Pound-Drever-Hall locking was in 1983 [16]. (Interestingly, Pound's name does not appear as an author on that paper. This is because the Pound-Drever-Hall locking scheme is actually an extension of work Pound did in 1946 [29] regarding the stabilization of microwave frequencies.) In 2005, Hall shared the Nobel Prize in Physics with Hansch "for their contributions to the development of laser-based precision spectroscopy, including the optical frequency comb technique. [22]" (Glauber was also honored in 2005 but for different reasons.)

And last, but not least, is the development of mirror-coating technology that allowed for mirrors to be highly reflective with very low losses. Regrettably, pinpointing when this type of mirrors were first developed is exceedingly difficult, partly because the state-of-the-art is constantly evolving. Mirrors with reflectivities of 0.9998 were reported to be in use as early as 1968 [30]. However, most of the development on high reflectivity, low loss mirrors of the type used in this dissertation seems to have taken place in the late 1970's and early 1980's as in reference [31]. In 1992, mirrors with reflectivities of 99.99984% were reported [32]. Efforts to improve the available mirror technology continue today.

Using these mirrors to create the optical cavity for the FOR-CW Raman laser is the brain-child of John Carlsten and was first demonstrated in 1998 [12, 33]. This first report only concerned the generation of the red-shifted Stokes light. Shortly thereafter, the semi-classical description of the CW Raman laser was developed and found to be in excellent agreement with the data [33, 34]. Research proceeded with an investigation of the tuning characteristics of the CW Raman laser [35], and then

the pump laser was switched from a frequency doubled Nd:YAG to a diode laser, in order to take advantage of the tuning characteristics of the diode laser [36, 37, 38]. At the same time, effort was put into understanding how to improve the efficiency of the CW Raman laser [39, 40]. Even though the system was not designed to generate them, blue-shifted anti-Stokes photons were also detected and reported in 2000 [15]. But after the initial measurements, anti-Stokes generation was not further considered until Roos developed the quantum theory [4, 41] of the CW Raman laser in 2003 and 2004 and, in the process, discovered that, if the mirrors were coated for the anti-Stokes generation in addition to the pump and Stokes, then it was theoretically possible to achieve quantum-limited anti-Stokes generation [19, 4]. Later (but not by much), Meng [5] extended the semi-classical theory to include the anti-Stokes and achieved the same result. This sparked renewed interest in anti-Stokes generation because of the possibility of generating all three colors (red, green, and blue) in one laser system. Particularly, if the medium used is D_2 instead of H_2 the three wavelengths emitted are precisely what are needed for optical imaging systems.

In February of 2008, Zaitsu et. al showed the first experimental proof of high-conversion-efficiency anti-Stokes generation [42]. Their work involved the rotational transition in H_2 and employed both chirped mirrors and a phase-matching gas to counter the dispersion of the hydrogen gas. They achieved a maximum output power of $\sim$100 μW (at an unknown input pump power). They did not fit theory to their data.

Structure of this Dissertation

The goal of this dissertation is to investigate anti-Stokes generation by the CW Raman laser. It begins by going through the semi-classical theory following the

presentation of Meng [5] but extending it to the possibility of any of the three emissions not being on the fundamental transverse mode. Chapter 3 presents numerical simulations of the CW Raman laser equations developed in Chapter 2. Chapter 4 discusses some of the experimental difficulties encountered with the CW Raman laser, with emphasis on those encountered when trying to generate anti-Stokes in addition to Stokes. The experimental result are distributed between Chapters 5 and 6. Chapter 5 focuses on the case when the pump, Stokes, and anti-Stokes are all fundamental cavity modes while Chapter 6 investigates other mode combinations. The main part of the dissertation is brought to a close in Chapter 7, which includes a summary and some thoughts for future research.

There are also 18 appendices. The first two appendices are references to help the reader. Appendix A provides a list of the acronyms used in the dissertation while Appendix B lists the variables and notation.

The next three (Appendices C, D, and E) cover the theoretical structure of the cavity spatial mode profiles for different cavity symmetries. The Hermite-Gaussian modes have rectangular symmetry, the Laguerre-Gaussian modes have cylindrical symmetry and the Ince-Gaussian modes have elliptic symmetry.

In the development of the semi-classical theory, three different types of overlap integrals are defined. Appendices F, G, and H are dedicated to the calculation of these overlap integrals.

The next appendix, I, contains the *Matlab* code used in the numerical calculations of Chapter 3, while Appendix J presents figures similar to some from Chapter 3 which are calculated in a slightly different manner.

In one of the steady-state analytic solutions to the theory found in Chapter 3, there is a choice between two possible mathematical forms. Appendix K justifies the choice of one of the two forms over the other from the stand-point of physicality.

The next two appendices, L and M, develop steady-state solutions to the light transmitted by a Fabry-Perot interferometer. The first considers the case of a source external to the interferometer while the source in the second is in between the cavity's mirrors.

Appendix N is devoted to explaining how the pictures taken of mode profiles are calibrated so that they are on the same horizontal scale. Appendix O explains how the raw data is corrected to compensate for losses due to optics between the cavity and the detectors and how the input pump is calibrated.

Appendices P and Q present additional data to what is presented in Chapters 5 and 6 from the two experiments performed as part of this dissertation work. Finally, Appendix R presents some additional thoughts on phase-matching and its relationship between the anti-Stokes data and theory.

SEMI-CLASSICAL THEORY

A semi-classical theory for a laser system treats the laser fields in a classical manner, starting from Maxwell's equations, but uses quantum mechanics to calculate the interaction of the laser fields with the molecules. Based on an extension of the theory for a continuous-wave (CW) laser, the time-dependent semi-classical theory for the CW Raman laser was first published in 1999 by Brasseur et al [34] which agreed with the previously published steady-state theory [33]. This theory was limited to two optical fields, the pump and the Stokes. In 2002, Meng extended the theory to allow the possibility of multiple fields being generated. [5] The theory presented in this dissertation will follow Meng's development, applied to three fields. (It will not completely follow his notation because of this generalization to only three fields.)

It should be mentioned that Meng developed his multiple-field theory to account for mode-hopping between rotational and vibrational Stokes shifts, not to investigate anti-Stokes generation. In his dissertation, he included some theory and numerical simulations for anti-Stokes generation, following the work done by Roos with the quantum theory [41] of anti-Stokes generation [19]. The main extension of this work beyond Meng's (and Roos's) is the inclusion of the possibility of any of the three fields not being on a fundamental cavity mode.

Figure 2.1 is a flow chart of the steps taken in the development of the CW Raman laser equations. On the left side of the chart is the classical development of the laser fields, which results in an equation for the time rate of change electric fields. This equation is proportional to the polarization of the molecules. On the right side of the chart is the quantum-mechanical development of the laser field/molecule interactions. At the top of this side is the development of the interaction potential and Hamiltonian

needed for solving the the time-dependent Schrodinger equation. The wave function amplitudes are then simplified and the density matrix elements are defined in terms of them. Finally, an equation for the polarization of the molecules due to their interactions with the laser fields is written. This is plugged into the result of the classical development, and after a few definitions, results in the CW Raman laser equations.

The first section of this chapter covers the the classical treatment of the CW laser fields within the Raman optical cavity. Section 2 develops the quantum-mechanical density-matrix to characterize the molecule/field interactions. Section 3 takes the results of the first two sections and combines them to form the time-dependent CW Raman laser equations. (To assist the reader, Appendix B contains a list of the mathematical symbols and notation used throughout the dissertation.)

Classical Treatment of the Laser Fields

Derivation of the Wave Equation

Maxwell's equations in matter are [43]:

$$\overrightarrow{\nabla} \bullet \overrightarrow{D} = \rho_f \tag{2.1}$$

$$\overrightarrow{\nabla} \bullet \overrightarrow{B} = 0 \tag{2.2}$$

$$\overrightarrow{\nabla} \times \overrightarrow{E} = -\frac{\partial \overrightarrow{B}}{\partial t} \tag{2.3}$$

$$\overrightarrow{\nabla} \times \overrightarrow{H} = \overrightarrow{J_f} + \frac{\partial \overrightarrow{D}}{\partial t}, \tag{2.4}$$

where

$$\overrightarrow{D} \equiv \varepsilon_o \overrightarrow{E} + \overrightarrow{P} \tag{2.5}$$

$$\overrightarrow{H} \equiv \frac{1}{\mu_o} \overrightarrow{B} - \overrightarrow{M}. \tag{2.6}$$

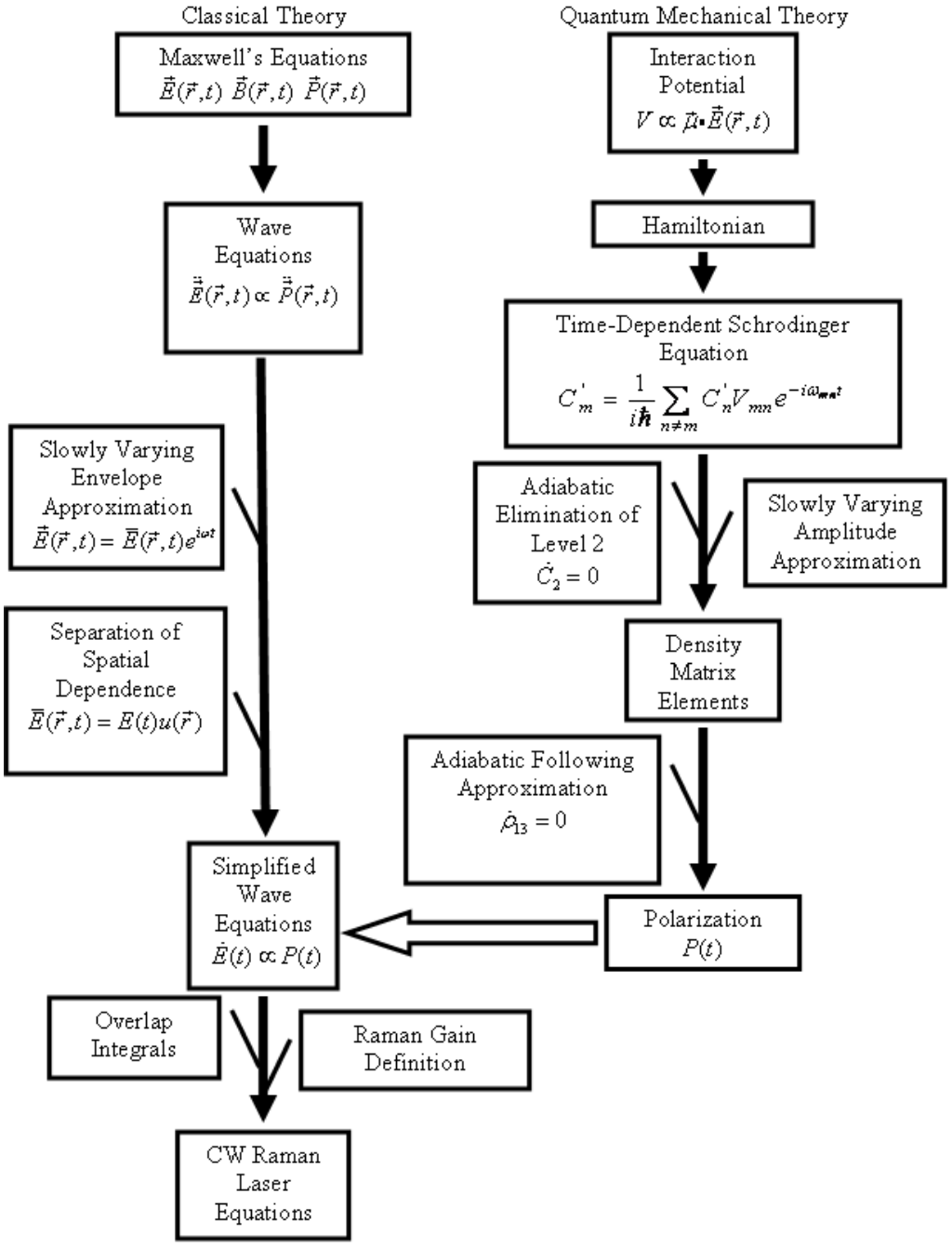

Figure 2.1: Flow chart of the semi-classical development of the CW Raman laser equations. The steps taken in the classical development of the laser fields are on the left side. The right side covers the quantum mechanical development of the laser field/molecule interactions. These two sides combine to form the CW Raman laser equations.

All the fields are functions of space and time. For example, $\overrightarrow{E} = \overrightarrow{E}(\overrightarrow{r}, t)$.

There are some simplifications that can be made based on the properties of the Raman medium, H_2. H_2 is not a magnetic material, therefore $\overrightarrow{M}$ is zero. Since $\overrightarrow{M}$ is zero, there can be no bound currents within the medium. This allows Ohm's Law to be simplified to:

$$\overrightarrow{J_f} = \sigma \overrightarrow{E} \tag{2.7}$$

where σ is the material's conductivity. Also, H_2 is a neutral gas. Therefore, there are no free charges ($\rho_f = 0$). If edge effects are ignored, then there are also no bound charges ($\rho_b = 0$). Since there are no bound charges, the following is also true:

$$-\overrightarrow{\nabla} \bullet \overrightarrow{P} = \rho_b = 0 \tag{2.8}$$

With these definitions and simplifications, the wave equation can be derived in the standard way, yielding

$$\ddot{\overrightarrow{E}} - \frac{\nabla^2 \overrightarrow{E}}{\mu_o \varepsilon_o} + \frac{\sigma}{\varepsilon_o} \dot{\overrightarrow{E}} = -\frac{1}{\varepsilon_o} \ddot{\overrightarrow{P}}. \tag{2.9}$$

The term proportional to $\dot{\overrightarrow{E}}$ is responsible for both the losses of the field circulating within the cavity and the input field entering the cavity. Since the input field adds to the field in the cavity, it is moved to the right-side of the equation and the sign is changed to indicate that it is not a loss term. The coefficient on the input term represents coupling of the input field into the cavity. Redefine this coefficient as

$$\gamma_{in} = \frac{2c}{nL} \sqrt{T_1} \tag{2.10}$$

where c is the speed of light, n is the index of refraction, L is the cavity length and T_1 is the power transmittivity of the front mirror. Similarly, the coefficient on the cavity loss term represents leakage out of the cavity. Define this as

$$\gamma_c = \frac{-c}{nL} \ln\left(\sqrt{R_1 R_2}\right), \tag{2.11}$$

where R_1 and R_2 are the power reflectivities of the front mirror and back mirrors respectively. (Because the index of refraction, reflectivities and transmittivities are dependent on wavelength, both γ_{in} and γ_c are wavelength dependent.) Separating these two effects out explicitly yields

$$\ddot{\overrightarrow{E}} - \frac{\nabla^2 \overrightarrow{E}}{\mu_o \varepsilon_o} + \gamma_c \dot{\overrightarrow{E}} = -\frac{1}{\varepsilon_o} \ddot{\overrightarrow{P}} + \gamma_{in} \dot{\overrightarrow{E}}_{in}. \tag{2.12}$$

Equation 2.12 is the wave equation for a field in the CW Raman laser system.

The Slowly-Varying Envelope Approximation

In the slowly-varying envelope approximation (SVEA), the fields (including the input field) and polarizations are each written as a slowly-varying factor or envelope multiplied by a term that oscillates at an optical laser frequency:

$$\overrightarrow{E}(\overrightarrow{r},t) = \frac{1}{2}\left(\overline{E}(\overrightarrow{r},t)e^{-i\omega t} + \overline{E}(\overrightarrow{r},t)^* e^{i\omega t}\right) \tag{2.13}$$

$$\overrightarrow{P}(\overrightarrow{r},t) = \frac{1}{2}\left(\overline{P}(\overrightarrow{r},t)e^{-i\omega t} + \overline{P}(\overrightarrow{r},t)^* e^{i\omega t}\right) \tag{2.14}$$

The slowly varying pieces are denoted by a bar over the symbol instead of an arrow. If the laser frequency is the largest frequency in the system, then any terms plugged back into the wave equation that are not proportional to either the laser frequency or its square can be discarded. Primarily, this allows time derivatives of the envelope to be ignored. After taking the derivatives of equations 2.13 and 2.14, plugging them into 2.12 and discarding all pieces that are small, the wave equation simplifies to

$$\dot{\overline{E}}(\overrightarrow{r},t) + \left[\frac{\gamma_c}{2} - \frac{i}{2\omega}(\omega^2 + c^2\nabla^2)\right]\overline{E}(\overrightarrow{r},t) = \frac{i\omega}{2\varepsilon_o}\overline{P}(\overrightarrow{r},t) + \frac{\gamma_{in}}{2}\overline{E}_{in}(\overrightarrow{r},t) \tag{2.15}$$

In the above equation, the definition of the speed of light in vacuum ($c = \frac{1}{\sqrt{\mu_o \varepsilon_o}}$) [43] has been used. Also, one term proportional to $\dot{\overline{E}}$ out of $\ddot{\overrightarrow{E}}$ was kept, even though it appears to be small, because it will be comparable to the $\nabla^2\overline{E}$ term. Equation 2.15 represents a simplified form of the wave equation in the Raman cavity.

Separation of the Spatial Dependence

The field, $\overline{E}(\overrightarrow{r},t)$, must meet the cavity boundary conditions. These boundary conditions requires the field to go to zero at the mirrors and at large distances from the cavity's axis. Thus, Laplace's equation must be satisfied if the boundary conditions are to be met. While, it has been occasionally seen that multiple cavity modes can oscillate within the Raman cavity simultaneously, it will be assumed here that only one mode per wavelength will be allowed to oscillate within the cavity at any given time. Also, assume that the field can be separated into a spatial piece multiplied by a time dependent piece:

$$\overline{E}(\overrightarrow{r},t) = E(t)\,u(\overrightarrow{r}). \tag{2.16}$$

By assuming separability, now, only $u(\overrightarrow{r})$ must satisfy Laplace's equation. Namely,

$$(\omega_c^2 + c^2\nabla^2)u(\overrightarrow{r}) = 0 \tag{2.17}$$

where ω_c is the empty (cold) cavity's resonance frequency. Equivalently,

$$c^2\nabla^2 u(\overrightarrow{r}) = -\omega_c^2 u(\overrightarrow{r}). \tag{2.18}$$

Because the u's represent the cold cavity spatial modes, they should be orthogonal. However, if, in equation 2.16, E(t) is taken to have units of electric field, making u dimensionless, then the standard normalization statement (where the integral over all space of the function multiplied by its complex conjugate equals 1) is not valid. Instead, an integral over all space results in the mode volume with units of length cubed:

$$\int_{cav} u_n(\overrightarrow{r})\,u_{n'}^*(\overrightarrow{r})\,dcav = \begin{cases} V & n = n' \\ 0 & n \neq n' \end{cases} \tag{2.19}$$

Since u represents the cavity spatial mode and there are an infinite number of possible spatial modes, a subscript, n, has been temporarily added to u in equation2.19 to

represent the different possible modes. As shown in Appendix F, this integral will be wavelength dependent but independent of the index n.

Substituting equations 2.16 and 2.18 into the simplified wave equation 2.15 yields

$$\dot{E}(t)u(\overrightarrow{r}) + \left[\frac{\gamma_c}{2} - \frac{i}{2\omega}(\omega^2 - \omega_c^2)\right] E(t)u(\overrightarrow{r}) = \frac{i\omega}{2\varepsilon_o}\overline{P}(\overrightarrow{r},t) + \frac{\gamma_{in}}{2}\overline{E}_{in}(\overrightarrow{r},t). \quad (2.20)$$

Now, multiply by $u^*$and integrate over the cavity, giving

$$\dot{E}(t) + \left[\frac{\gamma_c}{2} - \frac{i}{2\omega}(\omega^2 - \omega_c^2)\right] E(t) = \frac{i\omega}{2\varepsilon_o}P(t) + \frac{\gamma_{in}}{2}E_{in}(t), \quad (2.21)$$

where

$$P(t) = \frac{1}{V}\int_{cav} \overline{P}(\overrightarrow{r},t)\, u^*(\overrightarrow{r})\, dcav \quad (2.22)$$

$$E_{in}(t) = \frac{1}{V}\int_{cav} \overline{E}_{in}(\overrightarrow{r},t)\, u^*(\overrightarrow{r})\, dcav. \quad (2.23)$$

Because the CW Raman laser is generated in a cavity, all the fields resonate on cavity modes. Experimentally, this occurs for the pump because its frequency is actively locked to the cavity resonance frequency with external electronics. The Stokes and anti-Stokes, on the other hand, grow naturally on cavity modes. In any case, it is true that $\omega \sim \omega_c$ and

$$(\omega^2 - \omega_c^2) = (\omega + \omega_c)(\omega - \omega_c) \sim 2\omega(\omega - \omega_c) \quad (2.24)$$

It is now possible to make one additional simplification to the wave equation by plugging equation 2.24 into equation 2.21:

$$\dot{E}(t) + [\frac{\gamma_c}{2} - i(\omega - \omega_c)]E(t) = \frac{i\omega}{2\varepsilon_o}P(t) + \frac{\gamma_{in}}{2}E_{in}(t). \quad (2.25)$$

The above equation represents three equations, one for each field within the cavity. Separating these three equations out explicitly and dropping the input field terms in

the Stokes and anti-Stokes field equations yields:

$$\dot{E}_p(t) + [\frac{\gamma_{cp}}{2} - i(\omega_p - \omega_{cp})]E_p(t) = \frac{i\omega_p}{2\varepsilon_o}P_p(t) + \frac{\gamma_{in\,p}}{2}E_{in\,p}(t) \quad (2.26)$$

$$\dot{E}_s(t) + [\frac{\gamma_{cs}}{2} - i(\omega_s - \omega_{cs})]E_s(t) = \frac{i\omega_s}{2\varepsilon_o}P_s(t) \quad (2.27)$$

$$\dot{E}_a(t) + [\frac{\gamma_{ca}}{2} - i(\omega_a - \omega_{ca})]E_a(t) = \frac{i\omega_a}{2\varepsilon_o}P_a(t) \quad (2.28)$$

where the subscript p refers to the pump field, s indicates the Stokes field and a represents the anti-Stokes field.

Before it is possible to proceed with solving these equations, it is necessary to understand how the molecules of the Raman medium interact with these fields. These relationships are found via the quantum-mechanical density matrix and are the subject of the next section.

The Density Matrix

The goal of this section is a statement of how the polarization of the medium depends on the fields driving it. This is accomplished using a quantum-mechanical description for the interaction of the molecules of a medium with the fields within the medium, known as the density matrix approach. The diagonal elements of the density matrix are the populations of the energy levels and the off diagonal elements represent the coherences between the levels.

Figure 2.2 shows how the fields interact with the energy levels of the hydrogen molecule. In the figure, $\hbar\omega_q$ (q = p, s, a) is the energy contained in a field photon, level 1 is the ground state, level 2 represents all the excited electronic states, level 3 is the first excited vibrational state, $\hbar\omega_{mn}$ is the energy difference between levels m and n, and δ is the detuning of the pump-to-Stokes transition from the line center of the Raman transition. (δ can be either positive or negative.) The energy difference

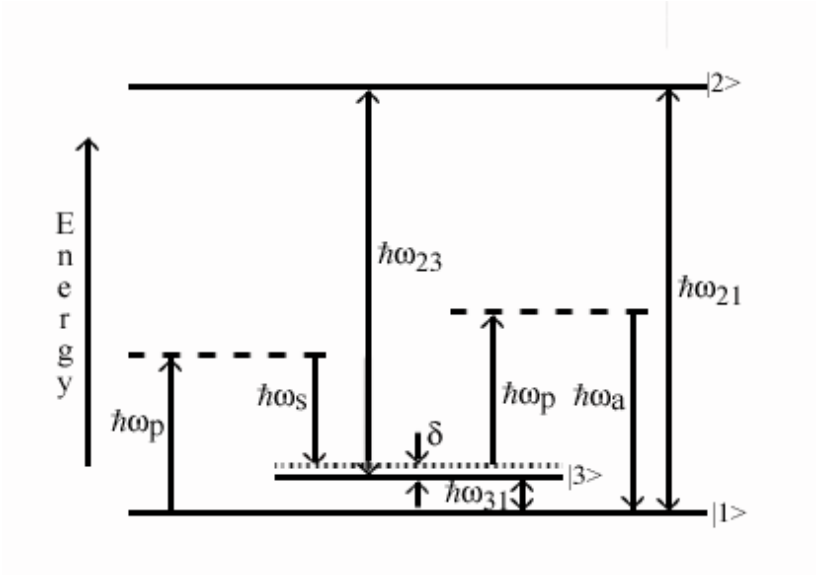

Figure 2.2: Raman scattering.

between levels 1 and 3, ω_{31}, is determined by the medium and is known as the Raman shift. For the vibrational transition in H_2, this energy difference is 4155 cm^{-1}. By looking at this figure, it is possible to derive some basic relationships between the laser frequencies and the molecular energy differences:

$$\omega_s = \omega_p - (\omega_{31} + \delta) \tag{2.29}$$

$$\omega_a = \omega_p + (\omega_{31} + \delta) \tag{2.30}$$

$$\omega_{23} + \omega_{31} = \omega_{21}. \tag{2.31}$$

The Interaction Potential and the Hamiltonian

The interaction potential is a matrix that represents, as might be expected by its name, the interaction of the molecules with the fields. Its elements are given by

$$V_{mn} = < m \,|\, V \,|\, n > \tag{2.32}$$

$$= < m \,|\, -\mu \overline{E}(\overrightarrow{r}, t) \,|\, n > \tag{2.33}$$

where $\overline{E}(\overrightarrow{r},t)$ represents a sum over the pump, Stokes and anti-Stokes fields, and μ is the electric dipole moment operator. For states of the same parity, this leads to an integral whose integrand is overall odd and, therefore, for these states, the interaction potential is zero. This is true for V_{mm} and for V_{13} and V_{31} because levels 1 and 3 are in the same electronic state. Thus,

$$V = \begin{bmatrix} 0 & V_{12} & 0 \\ V_{21} & 0 & V_{23} \\ 0 & V_{32} & 0 \end{bmatrix}, \tag{2.34}$$

where

$$V_{12} = V_{21}^* = -\mu_{12}\left(\frac{1}{2}\sum_{q=p,s,a}\left[\overline{E}_q(\overrightarrow{r},t)e^{-i\omega_q t} + \overline{E}_q^*(\overrightarrow{r},t)e^{i\omega_q t}\right]\right) \tag{2.35}$$

$$V_{23} = V_{32}^* = -\mu_{23}\left(\frac{1}{2}\sum_{q=p,s,a}\left[\overline{E}_q(\overrightarrow{r},t)e^{-i\omega_q t} + \overline{E}_q^*(\overrightarrow{r},t)e^{i\omega_q t}\right]\right) \tag{2.36}$$

The Hamiltonian for this system can now be written. The off-diagonal elements are given by the interaction potential and the diagonal elements are the energies associated with each molecular level. Thus,

$$H = \begin{bmatrix} \hbar\omega_1 & V_{12} & 0 \\ V_{21} & \hbar\omega_2 & V_{23} \\ 0 & V_{32} & \hbar\omega_3 \end{bmatrix} \tag{2.37}$$

The Time Evolution of the Wavefunction Amplitudes

With that expression for the Hamiltonian, it is now possible to find equations for the time evolution of the associated wavefunction. The general form of the wavefunction is

$$|\,\psi(t)\,> = \sum_{n=1}^{3} C_n'(t)\, e^{-i\omega_n t}|\,n\,> \tag{2.38}$$

where the amplitudes, C'_n, must obey the time-dependent Schrodinger equation (TDSE),

$$i\hbar\frac{\partial}{\partial t}|\,\psi(t)>=H\,|\,\psi(t)>\,. \tag{2.39}$$

(The primes are included here on the amplitudes for later convenience.) After plugging equation 2.38 into equation 2.39, dropping the explicit time dependence from the amplitudes and the Hamiltonian, and some algebra, the TDSE becomes

$$i\hbar\sum_{n=1}^{3}(\dot{C}'_n - i\omega_n C'_n)e^{-i\omega_n t}|\,n>=\sum_{n=1}^{3}C'_n\,e^{-i\omega_n t}H\,|\,n> \tag{2.40}$$

Now, multiply both sides by ¡m— and use $< m|n >= \delta_{mn}$. After a bit more algebra, this yields the equation that governs the time evolution of C'_m.

$$i\hbar\dot{C}'_m = \sum_{n\neq m}C'_n V_{mn}e^{-i\omega_{nm}t} \tag{2.41}$$

where $\omega_{nm}\equiv\omega_n-\omega_m$.

Now, separate equation 2.41 into three equations, one for each molecular level and plug in the expressions for the interaction potential from equations 2.35 and 2.36, yielding

$$\dot{C}'_1 = \frac{i}{2\hbar}C'_2\mu_{12}\sum_{q=p,s,a}\left[\overline{E}_q e^{-i(\omega_{21}+\omega_q)t}+\overline{E}^*_q e^{-i(\omega_{21}-\omega_q)t}\right] \tag{2.42}$$

$$\dot{C}'_2 = \frac{i}{2\hbar}C'_1\mu_{21}\sum_{q=p,s,a}\left[\overline{E}_q e^{i(\omega_{21}-\omega_q)t}+\overline{E}^*_q e^{i(\omega_{21}+\omega_q)t}\right] + \frac{i}{2\hbar}C'_3\mu_{23}\sum_{q=p,s,a}\left[\overline{E}_q e^{i(\omega_{23}-\omega_q)t}+\overline{E}^*_q e^{i(\omega_{23}+\omega_q)t}\right] \tag{2.43}$$

$$\dot{C}'_3 = \frac{i}{2\hbar}C'_2\mu_{32}\sum_{q=p,s,a}\left[\overline{E}_q e^{-i(\omega_{23}+\omega_q)t}+\overline{E}^*_q e^{-i(\omega_{23}-\omega_q)t}\right]. \tag{2.44}$$

Using equations 2.29– 2.31, it is possible to rewrite the exponents in equations 2.43 and 2.44 so that they only contain ω_{21}, the frequencies of the fields (ω_p, ω_s, and ω_a)

and δ. In this process, two terms are dropped from both equations because they would involve frequencies that correspond to higher order Stokes or anti-Stokes fields that are not pertinent to this analysis. The remaining terms are:

$$\begin{aligned}
\dot{C}_2' &= \frac{i}{2\hbar}C_1'\mu_{21}\sum_{q=p,s,a}\left[\overline{E}_q e^{i(\omega_{21}-\omega_q)t} + \overline{E}_q^* e^{i(\omega_{21}+\omega_q)t}\right] \\
&\quad + \frac{i}{2\hbar}C_3'\mu_{23}\left[\overline{E}_p e^{i(\omega_{21}-\omega_a+\delta)t} + \overline{E}_p^* e^{i(\omega_{21}+\omega_s+\delta)t}\right. \\
&\quad \left. + \overline{E}_s e^{i(\omega_{21}-\omega_p+\delta)t} + \overline{E}_a^* e^{i(\omega_{21}+\omega_p+\delta)t}\right] \qquad (2.45) \\
\dot{C}_3' &= \frac{i}{2\hbar}C_2'\mu_{32}\left[\overline{E}_p e^{-i(\omega_{21}+\omega_s+\delta)t} + \overline{E}_p^* e^{-i(\omega_{21}-\omega_a+\delta)t}\right. \\
&\quad \left. + \overline{E}_s^* e^{-i(\omega_{21}-\omega_p+\delta)t} + \overline{E}_a e^{-i(\omega_{21}+\omega_p+\delta)t}\right] \qquad (2.46)
\end{aligned}$$

The following transformation will remove the remaining dependence on δ in equations 2.42 – 2.46.

$$\begin{aligned}
C_1' &= C_1 \qquad (2.47) \\
C_2' &= C_2 \qquad (2.48) \\
C_3' &= C_3 e^{-i\delta t} \qquad (2.49)
\end{aligned}$$

After making this transformation, equations 2.42 – 2.46 become

$$\begin{aligned}
\dot{C}_1 &= \frac{i}{2\hbar}C_2\mu_{12}\sum_{q=p,s,a}\left[\overline{E}_q e^{-i(\omega_{21}+\omega_q)t} + \overline{E}_q^* e^{-i(\omega_{21}-\omega_q)t}\right] \qquad (2.50) \\
\dot{C}_2 &= \frac{i}{2\hbar}C_1\mu_{21}\sum_{q=p,s,a}\left[\overline{E}_q e^{i(\omega_{21}-\omega_q)t} + \overline{E}_q^* e^{i(\omega_{21}+\omega_q)t}\right] \\
&\quad + \frac{i}{2\hbar}C_3\mu_{23}\left[\overline{E}_p e^{i(\omega_{21}-\omega_a)t} + \overline{E}_p^* e^{i(\omega_{21}+\omega_s)t}\right. \\
&\quad \left. + \overline{E}_s e^{i(\omega_{21}-\omega_p)t} + \overline{E}_a^* e^{i(\omega_{21}+\omega_p)t}\right] \qquad (2.51) \\
\dot{C}_3 &= i\delta C_3 + \frac{i}{2\hbar}C_2\mu_{32}\left[\overline{E}_p e^{-i(\omega_{21}+\omega_s)t} + \overline{E}_p^* e^{-i(\omega_{21}-\omega_a)t}\right. \\
&\quad \left. + + \overline{E}_s^* e^{-i(\omega_{21}-\omega_p)t} + \overline{E}_a e^{-i(\omega_{21}+\omega_p)t}\right] \qquad (2.52)
\end{aligned}$$

Adiabatic Elimination of Level 2

Because this system is far-off resonance (FOR), the interaction of the laser with the molecules will not affect the electronic excited states, 2. Therefore, the population in these states will be constant. This allows for the adiabatic elimination of levels 2. The first step is to integrate equation 2.51

$$\begin{aligned}\int_{-\infty}^{t}\dot{C}_2 dt' &= \int_{-\infty}^{t}\left(\frac{i}{2\hbar}C_1\mu_{21}\sum_{q=p,s,a}\left[\overline{E}_q e^{i(\omega_{21}-\omega_q)t}+\overline{E}_q^* e^{i(\omega_{21}+\omega_q)t}\right]\right)dt' \\ &+ \int_{-\infty}^{t}\left(\frac{i}{2\hbar}C_3\mu_{23}\left[\overline{E}_p e^{i(\omega_{21}-\omega_a)t}+\overline{E}_p^* e^{i(\omega_{21}+\omega_s)t}\right]\right)dt' \\ &+ \int_{-\infty}^{t}\left(\frac{i}{2\hbar}C_3\mu_{23}\left[\overline{E}_s e^{i(\omega_{21}-\omega_p)t}+\overline{E}_a^* e^{i(\omega_{21}+\omega_p)t}\right]\right)dt' \qquad (2.53)\end{aligned}$$

There are three types of factors in this integral. There are time independent factors, like μ_{21} and μ_{23} . There are factors that are assumed to vary slowly in time, like E_q, C_1, and C_3. All of these factors can be taken outside the integrals. The remaining term in the integrand is a piece that varies rapidly in time, like $e^{i\varpi t}$, where ϖ represents any of the exponents in equation 2.53. Therefore, the only pieces of the integrals above that matter are those that take the form

$$\int_{-\infty}^{t} e^{i\varpi t}dt' = \frac{e^{i\varpi t}}{i\varpi} \qquad (2.54)$$

In the above integral, the contribution to the integral at minus infinity has been ignored. This is feasible because the population in levels 2 would have some decay rate that has been ignored thus far in the mathematical description of their behavior. After performing the integral, C_2 can be written as

$$
\begin{aligned}
C_2 &= \frac{1}{2\hbar} C_1 \mu_{21} \sum_{q=p,s,a} \left[\frac{\overline{E}_q e^{i(\omega_{21}-\omega_q)t}}{(\omega_{21}-\omega_q)} + \frac{\overline{E}_q^* e^{i(\omega_{21}+\omega_q)t}}{(\omega_{21}+\omega_q)} \right] \\
&\quad + \frac{1}{2\hbar} C_3 \mu_{23} \left[\frac{\overline{E}_p e^{i(\omega_{21}-\omega_a)t}}{(\omega_{21}-\omega_a)} + \frac{\overline{E}_p^* e^{i(\omega_{21}+\omega_s)t}}{(\omega_{21}+\omega_s)} \right. \\
&\quad \left. + \frac{\overline{E}_s e^{i(\omega_{21}-\omega_p)t}}{(\omega_{21}-\omega_p)} + \frac{\overline{E}_a^* e^{i(\omega_{21}+\omega_p)t}}{(\omega_{21}+\omega_p)} \right] \qquad (2.55)
\end{aligned}
$$

The Slowly Varying Amplitude Approximation

C_2 can now be plugged back into $\dot{C}_1$ and $\dot{C}_3$. This is, however, a very messy process because there are many cross-terms. Luckily, the slowly varying amplitude approximations (SVAA) simplifies this process. Under the SVAA, all cross terms that still oscillate at a high frequency, such as a laser frequency, are dropped.

To clarify this, a couple of steps in the simplification of $\dot{C}_1$ are shown.

$$
\begin{aligned}
\dot{C}_1 &= \frac{i}{2\hbar} \mu_{12} \left(\frac{1}{2\hbar} C_1 \mu_{21} \sum_{q'=p,s,a} \left[\frac{\overline{E}_{q'} e^{i(\omega_{21}-\omega_{q'})t}}{(\omega_{21}-\omega_{q'})} + \frac{\overline{E}_q^* e^{i(\omega_{21}+\omega_{q'})t}}{(\omega_{21}+\omega_{q'})} \right] \right) \\
&\quad \times \left(\sum_{q=p,s,a} \left[\overline{E}_q e^{-i(\omega_{21}+\omega_q)t} + \overline{E}_q^* e^{-i(\omega_{21}-\omega_q)t} \right] \right) + \ldots \qquad (2.56)
\end{aligned}
$$

With the six terms in each sum shown, there are a possibility of 36 terms for just this piece of $\dot{C}_1$. However, by looking at these terms, it is possible to see that terms that satisfy the SVAA occur only when $q = q'$. Therefore, the product of sums may be simplified to a single sum over q only.

$$
\begin{aligned}
\dot{C}_1 &= \left(\frac{i}{4\hbar^2} |\mu_{12}|^2 C_1 \sum_{q=p,s,a} \left[\frac{\overline{E}_q e^{i(\omega_{21}-\omega_q)t}}{(\omega_{21}-\omega_q)} + \frac{\overline{E}_q^* e^{i(\omega_{21}+\omega_q)t}}{(\omega_{21}+\omega_q)} \right] \right) \\
&\quad \times \left(\left[\overline{E}_q e^{-i(\omega_{21}+\omega_q)t} + \overline{E}_q^* e^{-i(\omega_{21}-\omega_q)t} \right] \right) + \ldots \qquad (2.57)
\end{aligned}
$$

There are still twelve terms remaining when equation 2.50 is fully expanded out, but only six of them involve no rapid oscillations. They are:

$$\dot{C}_1 = \left(\frac{i}{4\hbar^2} |\mu_{12}|^2 C_1 \sum_{q=p,s,a} \left[\frac{|\overline{E}_q|^2}{(\omega_{21} - \omega_q)} + \frac{|\overline{E}_q|^2}{(\omega_{21} + \omega_q)} \right] \right) + ... \tag{2.58}$$

Thus, with the SVAA, only one-sixth the initial terms for this part of $\dot{C}_1$ remain.

After this process is completed on the rest of $\dot{C}_1$ and all of $\dot{C}_3$, equations 2.50 and 2.52 become:

$$\begin{aligned} \dot{C}_1 &= \frac{i}{4\hbar^2} |\mu_{12}|^2 C_1 \sum_{q=p,s,a} \left[\frac{|\overline{E}_q|^2}{(\omega_{21} - \omega_q)} + \frac{|\overline{E}_q|^2}{(\omega_{21} + \omega_q)} \right] \\ &\quad + \frac{i}{4\hbar^2} C_3 \mu_{12} \mu_{23} \left[\frac{\overline{E}_s \overline{E}_p^*}{(\omega_{21} + \omega_s)} + \frac{\overline{E}_s \overline{E}_p^*}{(\omega_{23} - \omega_s)} \right. \\ &\quad \left. + \frac{\overline{E}_p \overline{E}_a^*}{(\omega_{21} + \omega_p)} + \frac{\overline{E}_p \overline{E}_a^*}{(\omega_{23} - \omega_p)} \right] \end{aligned} \tag{2.59}$$

$$\begin{aligned} \dot{C}_3 &= i\delta C_3 + \frac{i}{4\hbar^2} |\mu_{32}|^2 C_3 \sum_{q=p,s,a} \left[\frac{|\overline{E}_q|^2}{(\omega_{23} - \omega_q)} + \frac{|\overline{E}_q|^2}{(\omega_{23} + \omega_q)} \right] \\ &\quad + \frac{i}{4\hbar^2} C_1 \mu_{21} \mu_{32} \left[\frac{\overline{E}_p \overline{E}_s^*}{(\omega_{21} + \omega_s)} + \frac{\overline{E}_p \overline{E}_s^*}{(\omega_{23} - \omega_s)} \right. \\ &\quad \left. + \frac{\overline{E}_a \overline{E}_p^*}{(\omega_{21} + \omega_p)} + \frac{\overline{E}_a \overline{E}_p^*}{(\omega_{23} - \omega_p)} \right] \end{aligned} \tag{2.60}$$

where the denominators have again been simplified using equations 2.29 – 2.31.

The Density Matrix Elements

The expressions for $\dot{C}_1$ and $\dot{C}_3$ given in equations 2.59 and 2.60 can be written more simply in matrix form.

$$\frac{\partial}{\partial t} \begin{bmatrix} C_1 \\ C_3 \end{bmatrix} = i \begin{bmatrix} \Omega_{11} & \Omega_{13} \\ \Omega_{13}^* & \Omega_{33} + \delta \end{bmatrix} \begin{bmatrix} C_1 \\ C_3 \end{bmatrix} \tag{2.61}$$

where Ω_{11} and Ω_{33} are AC Stark shifts and Ω_{13} is a two-photon Rabi frequency. They are given by

$$\Omega_{11} = \frac{1}{2}\sum_{q=p,s,a} a_q|\overline{E}_q|^2 \tag{2.62}$$

$$\Omega_{33} = \frac{1}{2}\sum_{q=p,s,a} b_q|\overline{E}_q|^2 \tag{2.63}$$

$$\Omega_{13} = \frac{1}{2}\left[\overline{E}_s\overline{E}_p^* d_s + \overline{E}_p\overline{E}_a^* d_p\right] \tag{2.64}$$

where

$$a_p = \frac{1}{2\hbar^2}|\mu_{12}|^2\left[\frac{1}{(\omega_{21}-\omega_p)}+\frac{1}{(\omega_{21}+\omega_p)}\right] \tag{2.65}$$

$$a_s = \frac{1}{2\hbar^2}|\mu_{12}|^2\left[\frac{1}{(\omega_{21}-\omega_s)}+\frac{1}{(\omega_{21}+\omega_s)}\right] \tag{2.66}$$

$$a_a = \frac{1}{2\hbar^2}|\mu_{12}|^2\left[\frac{1}{(\omega_{21}-\omega_a)}+\frac{1}{(\omega_{21}+\omega_a)}\right] \tag{2.67}$$

$$b_p = \frac{1}{2\hbar^2}|\mu_{23}|^2\left[\frac{1}{(\omega_{23}-\omega_p)}+\frac{1}{(\omega_{23}+\omega_p)}\right] \tag{2.68}$$

$$b_s = \frac{1}{2\hbar^2}|\mu_{23}|^2\left[\frac{1}{(\omega_{23}-\omega_s)}\right] \tag{2.69}$$

$$b_a = \frac{1}{2\hbar^2}|\mu_{23}|^2\left[\frac{1}{(\omega_{23}+\omega_a)}\right] \tag{2.70}$$

$$d_p = \frac{1}{4\hbar^2}\mu_{12}\mu_{23}\left[\frac{1}{(\omega_{21}+\omega_p)}+\frac{1}{(\omega_{23}-\omega_p)}\right] \tag{2.71}$$

$$d_s = \frac{1}{4\hbar^2}\mu_{12}\mu_{23}\left[\frac{1}{(\omega_{21}+\omega_s)}+\frac{1}{(\omega_{23}-\omega_s)}\right] \tag{2.72}$$

Recalling the transformation made in equations 2.47, 2.48, and 2.49, the density matrix equations can now be written. Beginning with the coherence between levels 1 and 3, $\tilde{\rho}_{13}$.

$$\begin{aligned}\tilde{\rho}_{13} &= \left(C_1' e^{-i\omega_1 t}\right)\left(C_3' e^{i\omega_3 t}\right)\\ &= C_1 C_3^* e^{i(\omega_{31}+\delta)t}\\ \tilde{\rho}_{13} &= \rho_{13} e^{i(\omega_{31}+\delta)t}\end{aligned} \tag{2.73}$$

Similarly, the populations of levels 1 and 3 are given by

$$\tilde{\rho}_{11} = |C_1|^2 = \rho_{11} \tag{2.74}$$

$$\tilde{\rho}_{33} = |C_3|^2 = \rho_{33} \tag{2.75}$$

Using equations 2.61, 2.73, 2.74, and 2.75, it is possible to now obtain expressions for the time evolution of the populations and coherence in terms of the the Rabi frequency and Stark shifts

$$\dot{\rho}_{11} = i(\Omega_{13}\rho_{31} - \Omega_{31}\rho_{13}) + \Gamma_{31}\rho_{33} \tag{2.76}$$

$$\dot{\rho}_{33} = -i(\Omega_{13}\rho_{31} - \Omega_{31}\rho_{13}) - \Gamma_{31}\rho_{33} \tag{2.77}$$

$$\dot{\rho}_{13} = i(\Omega_{11} - \Omega_{33} - \delta)\rho_{13} + i\Omega_{13}(\rho_{33} - \rho_{11}) - \gamma_{13}\rho_{31}, \tag{2.78}$$

where phenomenological decay mechanisms have been added: Γ_{31} is the population decay rate and γ_{13} is the Raman linewidth (or coherence decay rate), both in units of (rad/s). (The Raman linewidth is a pressure-dependent quantity. Its pressure dependence was studied in [44].) It can be seen from equations 2.76 and 2.77 that a population change in level 1 has a corresponding change in level 3, as should be expected.

There are two other possible coherences, both associated with level 2. They are defined similarly to ρ_{13} and will be needed in the next section:

$$\begin{aligned} \tilde{\rho}_{12} &= \left(C_1' e^{-i\omega_1 t}\right)\left(C_2'^{*} e^{i\omega_2 t}\right) \\ &= C_1 C_2^{*} e^{i\omega_{21} t} \end{aligned} \tag{2.79}$$

$$\begin{aligned} \tilde{\rho}_{32} &= \left(C_3' e^{-i\omega_3 t}\right)\left(C_2'^{*} e^{i\omega_2 t}\right) \\ &= C_3 C_2^{*} e^{-i(\omega_{32}+\delta) t}. \end{aligned} \tag{2.80}$$

C_2 from equation 2.55 can be plugged into these two equations. After simplification, $\tilde{\rho}_{12}$ is given by

$$\begin{aligned}\tilde{\rho}_{12} &= \frac{1}{2\hbar}|C_1|^2\mu_{21}^* \sum_{q=p,s,a}\left[\frac{\overline{E}_q^* e^{i\omega_q t}}{(\omega_{21}-\omega_q)} + \frac{\overline{E}_q e^{-i\omega_q t}}{(\omega_{21}+\omega_q)}\right] \\ &\quad + \frac{1}{2\hbar}C_1 C_3^* \mu_{23}^* \left[\frac{\overline{E}_p^* e^{i\omega_a t}}{(\omega_{21}-\omega_a)} + \frac{\overline{E}_p e^{-i\omega_s t}}{(\omega_{21}+\omega_s)}\right. \\ &\quad \left. + \frac{\overline{E}_s^* e^{i\omega_p t}}{(\omega_{21}-\omega_p)} + \frac{\overline{E}_a e^{-i\omega_p t}}{(\omega_{21}+\omega_p)}\right]. \end{aligned} \tag{2.81}$$

And $\tilde{\rho}_{32}$ is given by

$$\begin{aligned}\tilde{\rho}_{32} &= \frac{1}{2\hbar}C_1^* C_3 \mu_{21}^* \left[\frac{\overline{E}_p^* e^{i\omega_s t}}{(\omega_{21}-\omega_p)} + \frac{\overline{E}_p e^{-i\omega_a t}}{(\omega_{21}+\omega_p)}\right. \\ &\quad \left. + \frac{\overline{E}_s e^{-i\omega_p t}}{(\omega_{21}+\omega_s)} + \frac{\overline{E}_a^* e^{i\omega_p t}}{(\omega_{21}-\omega_a)}\right] \\ &\quad + \frac{1}{2\hbar}|C_3|^2 \mu_{23}^* \left[\frac{\overline{E}_p^* e^{i\omega_p t}}{(\omega_{21}-\omega_a)} + \frac{\overline{E}_p e^{-i\omega_p t}}{(\omega_{21}+\omega_s)}\right. \\ &\quad \left. + \frac{\overline{E}_s^* e^{i\omega_s t}}{(\omega_{21}-\omega_p)} + \frac{\overline{E}_a e^{-i\omega_a t}}{(\omega_{21}+\omega_p)}\right], \end{aligned} \tag{2.82}$$

where the exponents have been simplified using equations 2.29 – 2.31, and two terms have been dropped because they do not oscillate at any of the three optical laser frequencies.

The Polarization

The goal of this section has been to find an explicit form for the polarization. All the pieces are now assembled to define it.

The polarization is given by (in equation 5.3.13 in reference [45])

$$\begin{aligned}\overrightarrow{P} &\equiv \overrightarrow{P}(\overrightarrow{r}, t) \\ &\equiv N\,\mathrm{Tr}(\tilde{\rho}\mu) \\ \overrightarrow{P} &= N\left(\mu_{21}\tilde{\rho}_{12} + \mu_{12}\tilde{\rho}_{21} + \mu_{23}\tilde{\rho}_{32} + \mu_{32}\tilde{\rho}_{23}\right) \end{aligned} \tag{2.83}$$

where N is the number density of molecules. Recall from equation 2.14 and restated here

$$\overrightarrow{P}(\overrightarrow{r},t) = \frac{1}{2}\left(\overline{P}(\overrightarrow{r},t)e^{-i\omega t} + \overline{P}(\overrightarrow{r},t)^* e^{i\omega t}\right) \tag{2.84}$$

that $\overrightarrow{P}$ should look like something plus its complex conjugate. This dependence can already be seen in equation 2.83 since

$$\mu^*_{mn} = \mu_{nm} \tag{2.85}$$

and

$$\rho^*_{mn} = \rho_{nm} \tag{2.86}$$

where n and m are 1, 2, or 3.

$\tilde{\rho}_{21}$ and $\tilde{\rho}_{23}$ as defined in equations 2.81 and 2.82 can now be plugged into 2.83 and the resulting terms grouped according to their oscillation frequencies.

$$\begin{aligned}
\overrightarrow{P}(\overrightarrow{r},t) &= e^{-i\omega_p t}\left(\frac{\overline{E}_p\frac{N}{2\hbar}|C_3|^2|\mu_{23}|^2}{(\omega_{21}+\omega_s)} + \frac{\overline{E}_p\frac{N}{2\hbar}|C_3|^2|\mu_{23}|^2}{(\omega_{21}-\omega_a)}\right.\\
&\qquad \left. + \frac{\overline{E}_a\frac{N}{2\hbar}C_1C_3^*\mu_{21}\mu_{23}^*}{(\omega_{21}-\omega_a)} + \frac{\overline{E}_a\frac{N}{2\hbar}C_1C_3^*\mu_{21}\mu_{23}^*}{(\omega_{21}+\omega_p)}\right)\\
&+ e^{-i\omega_p t}\left(\frac{\overline{E}_p\frac{N}{2\hbar}|C_1|^2|\mu_{21}|^2}{(\omega_{21}+\omega_p)} + \frac{\overline{E}_p\frac{N}{2\hbar}|C_1|^2|\mu_{21}|^2}{(\omega_{21}-\omega_p)}\right.\\
&\qquad \left. + \frac{\overline{E}_s\frac{N}{2\hbar}C_1^*C_3\mu_{21}^*\mu_{23}}{(\omega_{21}+\omega_s)} + \frac{\overline{E}_s\frac{N}{2\hbar}C_1^*C_3\mu_{21}^*\mu_{23}}{(\omega_{21}-\omega_p)}\right)\\
&+ e^{-i\omega_s t}\left(\frac{\overline{E}_p\frac{N}{2\hbar}C_1C_3^*\mu_{21}\mu_{23}^*}{(\omega_{21}-\omega_p)} + \frac{\overline{E}_p\frac{N}{2\hbar}C_1C_3^*\mu_{21}\mu_{23}^*}{(\omega_{21}+\omega_s)} + \frac{\overline{E}_s\frac{N}{2\hbar}|C_1|^2|\mu_{21}|^2}{(\omega_{21}+\omega_s)}\right)\\
&+ e^{-i\omega_s t}\left(\frac{\overline{E}_s\frac{N}{2\hbar}|C_1|^2|\mu_{21}|^2}{(\omega_{21}-\omega_s)} + \frac{\overline{E}_s|C_3|^2|\mu_{23}|^2}{(\omega_{21}-\omega_p)}\right)\\
&+ e^{-i\omega_a t}\left(\frac{\overline{E}_p\frac{N}{2\hbar}C_1^*C_3\mu_{21}^*\mu_{23}}{(\omega_{21}+\omega_p)} + \frac{\overline{E}_p\frac{N}{2\hbar}C_1^*C_3\mu_{21}^*\mu_{23}}{(\omega_{21}-\omega_a)} + \frac{\overline{E}_a\frac{N}{2\hbar}|C_1|^2|\mu_{21}|^2}{(\omega_{21}+\omega_a)}\right)\\
&+ e^{-i\omega_a t}\left(\frac{\overline{E}_a\frac{N}{2\hbar}|C_1|^2|\mu_{21}|^2}{(\omega_{21}-\omega_a)} + \frac{\overline{E}_a\frac{N}{2\hbar}|C_3|^2|\mu_{23}|^2}{(\omega_{21}+\omega_p)}\right) + c.c.
\end{aligned} \tag{2.87}$$

where $(+c.c.)$ indicates the addition of the complex conjugate.

The definitions (equations 2.65 – 2.72) associated with the two-photon Rabi frequency and AC Stark shifts along with equations 2.29 – 2.31, assuming δ is small (i.e. $\omega_{23} + \omega_p \sim \omega_{21} + \omega_s$), can now be used to write this equation more simply.

$$\begin{aligned}
\overrightarrow{P}(\overrightarrow{r},t) &= e^{-i\omega_p t}\left(\overline{E}_p N\hbar|C_1|^2 a_p + \overline{E}_p N\hbar|C_3|^2 b_p + \overline{E}_a N\hbar C_1 C_3^* d_p^* + \overline{E}_s N\hbar C_1^* C_3 d_s\right) \\
&+ e^{-i\omega_s t}\left(\overline{E}_s N\hbar|C_1|^2 a_s + \overline{E}_s N\hbar|C_3|^2 b_s + \overline{E}_p N\hbar C_1 C_3^* d_s^*\right) \\
&+ e^{-i\omega_a t}\left(\overline{E}_a N\hbar|C_1|^2 a_a + \overline{E}_a N\hbar|C_3|^2 b_a + \overline{E}_p N\hbar C_1^* C_3 d_p\right) + c.c. \qquad (2.88)
\end{aligned}$$

In terms of the density matrix elements, this becomes:

$$\begin{aligned}
\overrightarrow{P}(\overrightarrow{r},t) &= e^{-i\omega_p t} N\hbar\left(\overline{E}_p \rho_{11} a_p + \overline{E}_p \rho_{33} b_p + \overline{E}_a \rho_{13} d_p^* + \overline{E}_s \rho_{13}^* d_s\right) \\
&+ e^{-i\omega_s t} N\hbar\left(\overline{E}_s \rho_{11} a_s + \overline{E}_s \rho_{33} b_s + \overline{E}_p \rho_{13} d_s^*\right) \\
&+ e^{-i\omega_a t} N\hbar\left(\overline{E}_a \rho_{11} a_a + \overline{E}_a \rho_{33} b_a + \overline{E}_p \rho_{13}^* d_p\right) + c.c. \qquad (2.89)
\end{aligned}$$

And, finally, by analogy with equation 2.14, it is possible to separate the polarization into the three components, one for each field, needed to plug into the field equations 2.26 – 2.28. (Recall that the relationship between $\overline{P}$, the slowly varying envelope of the polarization, and P in the field equations is given by equation 2.22.)

$$\overline{P}_p(\overrightarrow{r},t) = 2N\hbar\left(\overline{E}_p \rho_{11} a_p + \overline{E}_p \rho_{33} b_p + \overline{E}_a \rho_{13} d_p^* + \overline{E}_s \rho_{13}^* d_s\right) \qquad (2.90)$$

$$\overline{P}_s(\overrightarrow{r},t) = 2N\hbar\left(\overline{E}_s \rho_{11} a_s + \overline{E}_s \rho_{33} b_s + \overline{E}_p \rho_{13} d_s^*\right) \qquad (2.91)$$

$$\overline{P}_a(\overrightarrow{r},t) = 2N\hbar\left(\overline{E}_a \rho_{11} a_a + \overline{E}_a \rho_{33} b_a + \overline{E}_p \rho_{13}^* d_p\right) \qquad (2.92)$$

The Time Evolution of the Population

Because the population is not in the upper excited states, 2, all the population must be in either state 1 or state 3. This is the same statement that allowed the

adiabatic elimination of the upper states earlier. Thus,

$$\rho_{11} + \rho_{33} = 1 \tag{2.93}$$

Of more importance, however, is the difference in population between these two levels and how it evolves with time. Define the population difference

$$D = \rho_{33} - \rho_{11} \tag{2.94}$$

As a result of this definition, the equilibrium condition (when everything is in the ground state) is $D_{eq} = -1$. Now, use equations 2.76 and 2.77 to find an expression for how D varies with time.

$$\begin{aligned} \dot{D} &= \dot{\rho_{33}} - \dot{\rho_{11}} \\ &= -2i(\Omega_{13}\rho_{31} - \Omega_{31}\rho_{13}) - 2\Gamma_{31}\rho_{33} \\ \dot{D} &= -2i(\Omega_{13}\rho_{31} - \Omega_{31}\rho_{13}) - 2\Gamma_{31}(D - D_{eq}) \end{aligned} \tag{2.95}$$

Also, $\dot{\rho}_{13}$, from equation 2.78, can be rewritten in terms of the population difference.

$$\dot{\rho}_{13} = i(\Omega_{11} - \Omega_{33} - \delta)\rho_{13} + i\Omega_{13}D - \gamma_{13}\rho_{13} \tag{2.96}$$

A Comment on the d's

Recall from equations 2.71 and 2.72 that

$$d_p = \frac{1}{4\hbar^2}\mu_{12}\mu_{23}\left[\frac{1}{(\omega_{21} + \omega_p)} + \frac{1}{(\omega_{23} - \omega_p)}\right] \tag{2.97}$$

$$d_s = \frac{1}{4\hbar^2}\mu_{12}\mu_{23}\left[\frac{1}{(\omega_{21} + \omega_s)} + \frac{1}{(\omega_{23} - \omega_s)}\right]. \tag{2.98}$$

These two formulas are very similar, differing only by which laser frequency appears in the two denominators. Given the molecular energy differences in cm^{-1} in Figure

1.4 and the pump and Stokes wavelengths of 532 nm and 683 nm respectively, the frequencies are

$$\omega_{21} = 2\pi c E_{21} = 1.7 * 10^{16} \frac{rad}{s} \tag{2.99}$$

$$\omega_{23} = 2\pi c E_{23} = 1.6 * 10^{16} \frac{rad}{s} \tag{2.100}$$

$$\omega_p = \frac{2\pi c}{\lambda_p} = 3.5 * 10^{15} \frac{rad}{s} \tag{2.101}$$

$$\omega_s = \frac{2\pi c}{\lambda_s} = 2.8 * 10^{15} \frac{rad}{s} \tag{2.102}$$

Because the molecular frequencies dominate the denominators, the difference between d_p and d_s is negligible. This will be used later.

A Check

At this point, it is possible to plug-in numbers and check the assumption that has been made regarding the distribution of the population in the molecular levels. Namely,

$$\rho_{22} = 0 \tag{2.103}$$

$$\rho_{11} + \rho_{33} = 1 \tag{2.104}$$

Begin by finding the steady-state value of ρ_{13} by setting equation 2.96 equal to zero and then solving for ρ_{13}.

$$\rho_{13} = \frac{-i\Omega_{13} D}{i(\Omega_{11} - \Omega_{33} - \delta) - \gamma_{13}} \tag{2.105}$$

Then, plug this value into the formula for the population difference (equation 2.94) and solve for the steady-state value of the population.

$$D = \frac{\Gamma_{31} D_{eq} (\gamma_{13}^2 + \delta^2)}{\Gamma_{31} (\gamma_{13}^2 + \delta^2) + 4|\Omega_{13}|^2 \gamma_{13}}, \tag{2.106}$$

where, to reach this final form, it was assumed that the difference between the AC Stark shifts, Ω_{11} and Ω_{33}, is zero . Using the definitions given in equations 2.62 and 2.63, this assumption can be examined more closely.

$$\begin{aligned} \Omega_{11} - \Omega_{33} &= \frac{1}{2} \sum_{q=p,s,a} a_q |\overline{E}_q|^2 - \frac{1}{2} \sum_{q=p,s,a} b_q |\overline{E}_q|^2 \\ &= \frac{1}{2} \sum_{q=p,s,a} |\overline{E}_q|^2 (a_q - b_q) \end{aligned} \tag{2.107}$$

If $a_q = b_q$, the assumption about the AC Stark shifts will be true. A comparison of the definitions of a_q and b_q given in equations 2.65 – 2.70 shows that a_q will equal b_q if $|\mu_{13}|^2 \sim |\mu_{23}|^2$ and $\omega_{21} \sim \omega_{23}$. The former is true because they are part of the same electronic level. The values of ω_{21} and ω_{23} are given in equations 2.99 and 2.100. While not identical, these values are very similar.

To perform the check of the assumption about the population distribution, numerical values need to be assumed or calculated.

1. The cavity parameters: Given a 3-in. (7.62-cm) long cavity, with 99.99%-reflective and 50-cm radius of curvature mirrors, the Rayleigh range, z_o, is 13.3-cm and the finesse, $\mathcal{F}$, is 31414. The Rayleigh range is calculated by matching the beam's wavefront curvature to the mirror's radii of curvature using [46]

$$R_c(z) = z \left(1 + \left(\frac{z_o}{z} \right)^2 \right) \tag{2.108}$$

where $R_c(z)$ is the radius of curvature at a position z. The finesse is calculated from [47]

$$\mathcal{F} = \frac{\pi \sqrt{R}}{1 - R} \tag{2.109}$$

where R is the power reflectivity of either mirror in a matched laser cavity. For a mismatched cavity, substitute $\sqrt{R_1 R_2}$ for R.

2. The beam parameters and power levels: The system is pumped by a frequency doubled Nd:YAG. Therefore, $\lambda_p = 532\,nm$. Given the vibrational transition in H_2, the Stokes and anti-Stokes wavelengths are $\lambda_s = 683\,nm$ and $\lambda_a = 435\,nm$, respectively. Thus, the three beam waists are $w_{op} = 0.015\,cm$, $w_{os} = 0.017\,cm$, and $w_{oa} = 0.013\,cm$, calculated from[47]

$$w_o = \sqrt{\frac{\lambda z_o}{\pi}} \tag{2.110}$$

If the input pump power is 1 mW, the intracavity circulating pump power (steady-state and undepleted) is $P_{cav} \sim \mathcal{F} P_{in} \sim 31\,W$. Finally, assume that the circulating intracavity Stokes power equals the circulating intracavity pump power and the circulating intracavity anti-Stokes power is 1/2 the circulating intracavity pump power.

3. Indices of refraction and intra-cavity field levels: Assume that the index of refraction at all three wavelengths is 1. Now, the intracavity fields can be calculated.

$$|E_p|^2 = \frac{4P_{pcav}}{\pi\omega_{op}^2 n_p}\sqrt{\frac{\mu_o}{\varepsilon_o}} = 6.6 * 10^{11}\,\frac{V}{m} \tag{2.111}$$

$$|E_s|^2 = \frac{4P_{scav}}{\pi\omega_{os}^2 n_s}\sqrt{\frac{\mu_o}{\varepsilon_o}} = 5.1 * 10^{11}\,\frac{V}{m} \tag{2.112}$$

$$|E_a|^2 = \frac{4P_{acav}}{\pi\omega_{oa}^2 n_a}\sqrt{\frac{\mu_o}{\varepsilon_o}} = 4.0 * 10^{11}\,\frac{V}{m} \tag{2.113}$$

4. Values of the coefficients associated with the AC Stark shifts and the two-photon Rabi frequency: These values can be found in the literature [48]. Assume that

$$a_p = a_s = a_a = 2.6 * 10^{-7}\,\frac{1}{V^2 s} \tag{2.114}$$

$$b_p = b_s = b_a = 2.8 * 10^{-7}\,\frac{1}{V^2 s} \tag{2.115}$$

$$d_p = d_s = 6.1 * 10^{-8}\,\frac{1}{V^2 s} \tag{2.116}$$

5. The values for the population decay rate and coherence dephasing rate are also available in the literature. From reference[49],

$$\Gamma_{31} = 2\pi * 10^4 \, \frac{rad}{s} \tag{2.117}$$

and from reference [44], at 10 atm

$$\gamma_{13} = 2\pi * 250 * 10^6 \, \frac{rad}{s} \tag{2.118}$$

6. The AC Stark shifts and the two-photon Rabi frequency can now be calculated from equations 2.62, 2.63 and 2.64. They are:

$$\Omega_{11} = 205 \, kHz \tag{2.119}$$

$$\Omega_{33} = 220 \, kHz \tag{2.120}$$

$$\Omega_{13} = 23 \, kHz \tag{2.121}$$

The values of Ω_{11} and Ω_{33} are indeed very close in value, confirming the assumption made in the calculation of the steady-state value of the population difference (equation 2.106).

7. The population difference in equation 2.106 can now be calculated. It is:

$$D = -0.999977 \tag{2.122}$$

It is indeed very close to -1, indicating that very little of the population is excited to level 3 in this process.

8. And, finally, the magnitude of the steady-state coherence can be calculated from equation 2.105.

$$|\rho_{13}| = 0.000015 \tag{2.123}$$

The Adiabatic Following Approximation

In the adiabatic following approximation (AFA), the coherence, ρ_{13} reaches its steady-state value much sooner than the fields. This approximation is outlined in reference [45] page 12. This allows the steady-state value of the coherence, calculated in equation 2.105 to be plugged into the polarization equation 2.89. Before this is done, though, simplify ρ_{13} by assuming that the two AC Stark shifts, Ω_{11} and Ω_{33}, are approximately equal to each other, as has been discussed and verified above. With this simplification, the steady-state value of ρ_{13} is:

$$\rho_{13} = \frac{-i\Omega_{13}D}{-i\delta - \gamma_{13}} \tag{2.124}$$

Using the two-photon Rabi frequency from equation 2.64, this becomes

$$\rho_{13} = \frac{-iD}{-i\delta - \gamma_{13}} \left(\frac{1}{2} \left[\overline{E}_s \overline{E}_p^* d_s + \overline{E}_p \overline{E}_a^* d_p \right] \right) \tag{2.125}$$

This can now be plugged into the three polarizations (equations 2.90 – 2.92), assuming that the population of level 3 is negligible (as shown in equation 2.122), and simplified to

$$\begin{aligned} \overline{P}_p(\overrightarrow{r},t) &= 2N\hbar\overline{E}_p\rho_{11}a_p + N\hbar\left(\frac{-iD}{-i\delta-\gamma_{13}}\right)\left(\overline{E}_p^*\overline{E}_s\overline{E}_a d_s d_p^* + \overline{E}_p|\overline{E}_a|^2|d_p|^2\right) \\ &+ N\hbar\left(\frac{iD}{i\delta-\gamma_{13}}\right)\left(\overline{E}_p|\overline{E}_s|^2|d_s|^2 + \overline{E}_p^*\overline{E}_s\overline{E}_a d_s d_p^*\right) \qquad (2.126) \\ \overline{P}_s(\overrightarrow{r},t) &= 2N\hbar\overline{E}_s\rho_{11}a_s + N\hbar\left(\frac{-iD}{-i\delta-\gamma_{13}}\right)\left(|\overline{E}_p|^2\overline{E}_s|d_s|^2 + \overline{E}_p^2\overline{E}_a^* d_s^* d_p\right) \qquad (2.127) \\ \overline{P}_a(\overrightarrow{r},t) &= 2N\hbar\overline{E}_a\rho_{11}a_a + N\hbar\left(\frac{iD}{i\delta-\gamma_{13}}\right)\left(\overline{E}_p^2\overline{E}_s^* d_s^* d_p + |\overline{E}_p|^2\overline{E}_a|d_p|^2\right) \qquad (2.128) \end{aligned}$$

At this point, it is possible to see a bit of where things are going. Looking at equation 2.127, the first term, proportional to $\overline{E}_s$, will lead to a term involving the index of refraction, the second term, proportional to $|\overline{E}_p|^2\overline{E}_s$, is the Raman term that will generate Stokes, and the third term, proportional to $\overline{E}_p^2\overline{E}_a^*$ is a FWM term. Similar terms can be seen in equations 2.126 and 2.128.

The Time-Dependent CW Raman Laser Equations

In this section, the results of the first section (equations 2.26 – 2.28), and the second section, (equations 2.126 – 2.128) (after a bit more manipulation), will be combined to form the time-dependent CW Raman laser equations (CWRLE). This section begins with a general discussion of the overlap integrals. The index of refraction and the Raman gain are then defined. Finally, the CWRLE will be written, followed by a discussion of the terms of these equations.

The Overlap Integrals

The electric fields in the polarization equations are functions of both space and time. This dependence can be separated out, following equation 2.16, as was done earlier during the development of the wave equations. Also, recall that the polarizations appearing in the wave equations are given by equation 2.22, which has had the spatial dependence integrated out. These integrals need to be identified before the polarizations can be plugged into the wave equations.

There are three basic types of integrals in the polarizations, with each type present in all three equations. Each type of integral has an appendix devoted to it, including sample calculations. The integrand of each integral is a combination of the spatial modes, $u_q(\overrightarrow{r})$, of the three fields.

There are three possibilities for the functional form of the spatial modes: the rectangularly-symmetric Hermite-Gaussian (HG) modes [47, 46], the cylindrically-symmetric Laguerre-Gaussian (LG) modes [47, 46], and the elliptically-symmetric Ince-Gaussian (IG) modes [50, 51, 52] which are discussed in Appendices C – E, respectively. Traditionally, the spatial modes are referred to as the $\mathrm{TEM}_{\mathrm{mn}}$ modes

[53], where m and n are the mode indices and the the lowest order or fundamental mode in all three symmetries is the TEM_{00} mode.

The first type of integral is covered in Appendix F. This type comes from terms in the polarizations that are proportional to only one field. The integral of these terms takes the form of :

$$\begin{aligned} Type1 &= \frac{1}{V_q}\int_{cav} \overline{E}_q(\overrightarrow{r},t)\, u^*_{q\,m}(\overrightarrow{r})\, dcav \\ &= \frac{1}{V_q}\int_{cav} E_q(t)\, u_{q\,n}(\overrightarrow{r})\, u^*_{q\,m}(\overrightarrow{r})\, dcav \\ &= \frac{E_q(t)}{V_q}\int_{cav} u_{q\,n}(\overrightarrow{r})\, u^*_{q\,m}(\overrightarrow{r})\, dcav \end{aligned} \tag{2.129}$$

where the second subscript (n or m) on the spatial mode function indicates which spatial mode is under consideration. This integral is already defined, in equation 2.19, as the normalization volume and requires that the two u's represent the same spatial mode. Thus, the result of this type of integral is

$$Type1 = E_q(t) \tag{2.130}$$

As discussed in Appendix F, the mode overlap volume, V_q is independent of the mode structure. (In other words, it is independent of the mode index.) It is, however, wavelength dependent, as indicated by the subscript q.

The second type of integral is covered in Appendix G and involves square of the absolute value of one field multiplied by a second field. These terms are the Raman terms. Notice that in these terms, the subscript on the non-squared field is always the same as the subscript on the polarization.

$$\begin{aligned} Type2 &= \frac{1}{V_q}\int_{cav} |\overline{E}_q|^2 \overline{E}^*_{q'}(\overrightarrow{r},t)\, u^*_{q'}(\overrightarrow{r})\, dcav \\ &= \frac{1}{V_q}\int_{cav} |E_q(t)|^2\, |u_q(\overrightarrow{r})|^2\, E_{q'}(t)\, u_{q'}(\overrightarrow{r})\, u^*_{q'}(\overrightarrow{r})\, dcav \\ &= \frac{|E_q(t)|^2 E_{q'}(t)}{V_q}\int_{cav} |u_q(\overrightarrow{r})|^2\, |u_{q'}(\overrightarrow{r})|^2\, dcav \end{aligned} \tag{2.131}$$

This integral in equation 2.131 has not yet been defined. Define it now as

$$V_{q\,q'} = \int_{cav} |u_q(\overrightarrow{r})|^2 \, |u_{q'}(\overrightarrow{r})|^2 \, dcav \tag{2.132}$$

which is a real quantity. The result of the second type of integral is thus

$$Type2 = |E_q(t)|^2 E_{q'}(t) \frac{V_{q\,q'}}{V_q} \tag{2.133}$$

As indicated by the subscripts, $V_{q\,q'}$ is dependent on both wavelengths. In addition, it will also be dependent on the mode structure of u_q and $u_{q'}$. However, to indicate the exact mode combination used in the calculation would require six subscripts, one for each wavelength and two for the mode indices at each wavelength. This becomes quite cumbersome. Thus, the only combination that will be written explicitly is the case when the two wavelengths are the pump and Stokes, and they are both assumed to be on the fundamental mode. This special case is identified as $V_{ps\,o}$.

The third type of integral is the most complicated because it involves the FWM terms and is discussed more fully in Appendix H. The third type of integral will have different functional dependency on the field envelopes but will always have the same integrand. Because of the different functional dependences on the fields, a specific example is going to be used to illustrate the third integral type. Integrating the first FWM term from the pump polarization (equation 2.126) yields

$$\begin{aligned} Type3 &= \frac{1}{V_q} \int_{cav} \overline{E}_p^*(\overrightarrow{r}, t) \, \overline{E}_s(\overrightarrow{r}, t) \, \overline{E}_a(\overrightarrow{r}, t) \, u_p^*(\overrightarrow{r}) \, dcav \\ &= \frac{1}{V_q} \int_{cav} E_p^*(t) \, u_p^*(\overrightarrow{r}) \, E_s(t) \, u_s(\overrightarrow{r}) \, E_a(t) \, u_a(\overrightarrow{r}) \, u_p^*(\overrightarrow{r}) \, dcav \\ Type3 &= \frac{E_p^*(t) \, E_s(t) \, E_a(t)}{V_q} \int_{cav} u_p^{*2}(\overrightarrow{r}) \, u_s(\overrightarrow{r}) \, u_a(\overrightarrow{r}) \, dcav \end{aligned} \tag{2.134}$$

Define this integral as

$$V_{FWM} = \int_{cav} u_p^{*2} \, u_s \, u_a \, dcav \tag{2.135}$$

V_{FWM} is a complex and, therefore, sometimes its complex conjugate will be needed instead of it. The result for this example of the third integral type is

$$Type3 \quad = \quad E_p^*(t)\, E_s(t)\, E_a(t) \frac{V_{FWM}}{V_q}. \tag{2.136}$$

V_{FWM} will be dependent on all three wavelengths and, like $V_{q\,q'}$, it will be dependent on the mode structure of the fields. Unlike the previous two integrals, the integrand of V_{FWM} is not explicitly an even function. However, because the integral is over the entire cavity, for the integral to result in a non-zero value, the integrand must be an even function. This restricts the possible mode combinations that can occur. Because the pump mode is squared in the integrand, its parity does not affect which anti-Stokes modes can occur. However, the parity of the Stokes and anti-Stokes modes must be the same (either both even or both odd). In the case of rectangular symmetric HG modes, this means that if the Stokes index for either the x or y direction (z being along the cavity axis) is odd, the anti-Stokes mode's index in that direction must also be odd. For example, if the Stokes mode is HG mode TEM_{10}, then the anti-Stokes mode could potentially be HG modes TEM_{10}, TEM_{30}, or TEM_{12} but not TEM_{01}, TEM_{00}, or TEM_{20}.

The integrated forms of the polarizations can now be written in terms of these integrals.

$$\begin{aligned} P_p(t) &= 2N\hbar E_p\rho_{11}a_p + N\hbar\left(\frac{-iD}{-i\delta-\gamma_{13}}\right)\left(E_p^*E_sE_ad_sd_p^*\frac{V_{FWM}}{V_p} + E_p|E_a|^2|d_p|^2\frac{V_{pa}}{V_p}\right) \\ &+ N\hbar\left(\frac{iD}{i\delta-\gamma_{13}}\right)\left(E_p|E_s|^2|d_s|^2\frac{V_{ps}}{V_p} + E_p^*E_sE_ad_sd_p^*\frac{V_{FWM}}{V_p}\right) \qquad (2.137) \\ P_s(t) &= 2N\hbar E_s\rho_{11}a_s + N\hbar\left(\frac{-iD}{-i\delta-\gamma_{13}}\right)\left(|E_p|^2E_s|d_s|^2\frac{V_{ps}}{V_s}\right. \\ &\left. + E_p^2E_a^*d_s^*d_p\frac{V_{FWM}^*}{V_s}\right) \qquad (2.138) \\ P_a(t) &= 2N\hbar E_a\rho_{11}a_a + N\hbar\left(\frac{iD}{i\delta-\gamma_{13}}\right)\left(E_p^2E_s^*d_s^*d_p\frac{V_{FWM}^*}{V_a}\right. \\ &\left. + |E_p|^2E_a|d_p|^2\frac{V_{pa}}{V_a}\right) \qquad (2.139) \end{aligned}$$

The Index of Refraction and Raman Gain

In order to develop the gain, compare equation 2.127 to equation 1.1.2 from reference [45] That equation is (with an ε_o added to change the cgs units used in reference[45] to the mks units used in this dissertation)

$$P(t) = \varepsilon_o\left(\chi^{(1)}E(t) + \chi^{(2)}E^2(t) + \chi^{(3)}E^3(t) + ...\right) \qquad (2.140)$$

where χ is the susceptibility. When this equation is compared to equation **??**, for example, it can be seen that,

$$\begin{aligned} \varepsilon_o\chi^{(1)} &= 2N\hbar a_s\rho_{11} \qquad (2.141) \\ \varepsilon_o\chi^{(3)} &= \begin{cases} N\hbar\left(\frac{iD}{i\delta+\gamma_{13}}\right)|d_s|^2 \\ N\hbar\left(\frac{iD}{i\delta+\gamma_{13}}\right)d_s^*d_p \end{cases} \qquad (2.142) \end{aligned}$$

There are two terms proportional to $\chi^{(3)}$. The upper term is associated with the Raman processes while the lower term is associated with the FWM processes. These

two terms are mathematically very similar, the only difference being in the d's. However, as discussed earlier, d_s and d_p are essentially identical numbers. Let $d_s = d_p = d_o$, so that the two third order susceptibility terms are identical.

Using the definition of the index of refraction in on either pg 180 or 383 in reference [43], the first order term, equation 2.141, can be related to the index of refraction.

$$n = \sqrt{1+\chi^{(1)}} \tag{2.143}$$

and, if $\chi^{(1)} \ll 1$, then

$$\begin{aligned} n &\sim 1+\frac{\chi^{(1)}}{2} \\ n &= 1+\frac{N\hbar a_s \rho_{11}}{\varepsilon_o} \end{aligned} \tag{2.144}$$

This equation gives the index of refraction at the Stokes wavelength. Similar equations can be written for the pump and anti-Stokes indices of refraction by changing a_s to a_p or a_a, respectively.

Now, concentrating only on the third order term.

$$\chi^{(3)} = \frac{N\hbar}{\varepsilon_o}\left(\frac{iD}{i\delta+\gamma_{13}}\right)|d_o|^2 \tag{2.145}$$

Separating into real and imaginary terms yields

$$\chi^{(3)} = \chi_R^{(3)} - i\chi_I^{(3)}, \tag{2.146}$$

where

$$\chi_R^{(3)} = \frac{N\hbar|d_o|^2 D\delta}{\varepsilon_o\left(\gamma_{13}^2+\delta^2\right)} \tag{2.147}$$

$$\chi_I^{(3)} = \frac{-N\hbar|d_o|^2 D\gamma_{13}}{\varepsilon_o\left(\gamma_{13}^2+\delta^2\right)} \tag{2.148}$$

Recall from equation 2.27 that

$$\dot{E}_s \propto iP_s \tag{2.149}$$

$$\propto \left(i\chi_R^{(3)}+\chi_I^{(3)}\right)\left(|E_p|^2 E_s\frac{V_{ps}}{V_s}+E_p^2 E_a^*\frac{V_{FWM}^*}{V_s}\right) \tag{2.150}$$

Therefore, the real part of the third-order susceptibility leads to a phase change (dispersion) of the Stokes field while the imaginary portion is related to the gain for the Raman process.

It is possible to relate the imaginary portion to the plane-wave gain coefficient, α_g, as given in reference[54]

$$\begin{aligned}
\alpha_g &= \frac{2\omega_s \chi_I^{(3)}}{n_s n_p c^2 \varepsilon_o} \\
&= \frac{2\omega_s}{n_s n_p c^2 \varepsilon_o} \left(\frac{-N\hbar |d_o|^2 D \gamma_{13}}{\varepsilon_o \left(\gamma_{13}^2 + \delta^2\right)} \right) \\
&= \frac{-2\omega_s N\hbar |d_o|^2 \gamma_{13}}{n_s n_p c^2 \varepsilon_o^2 \left(\gamma_{13}^2 + \delta^2\right)} \left(\frac{\Gamma_{31} D_{eq} \left(\gamma_{13}^2 + \delta^2\right)}{\Gamma_{31} \left(\gamma_{13}^2 + \delta^2\right) + 4|\Omega_{13}|^2 \gamma_{13}} \right) \\
\alpha_g &= \alpha_{go} \left[\frac{\gamma_{13}^2}{\delta^2 + \gamma_{13}^2 \left(1 + \frac{4|\Omega_{13}|^2}{\Gamma_{31}\gamma_{13}}\right)} \right] \qquad (2.151)
\end{aligned}$$

where the definition of the steady-state population difference from equation 2.106 has been used and α_{go} is the unsaturated or small-signal gain coefficient.

The piece in square brackets in equation 2.151 is a Lorentzian in δ, so the Raman gain has a Lorentzian profile. The maximum value of the Lorentzian occurs when $\delta = 0$ and is

$$\mathcal{L}(\delta = 0) = \frac{1}{\left(1 + \frac{4|\Omega_{13}|^2}{\Gamma_{31}\gamma_{13}}\right)} \qquad (2.152)$$

and the value of δ for which the Lorentzian is at half its maximum height is

$$\delta_{HM}^2 = \gamma_{13}^2 \left(1 + \frac{4|\Omega_{13}|^2}{\Gamma_{31}\gamma_{13}}\right) \qquad (2.153)$$

A comparison of these values to the typical values for the maximum height and half-width of a Lorentzian shows that these are modified by a value of $\left(1 + \frac{4|\Omega_{13}|^2}{\Gamma_{31}\gamma_{13}}\right)$. The only piece of this factor that is not a constant is the two-photon Rabi frequency, Ω_{13}, whose functional form is given in equation 2.64. As can be seen there, it depends on the field strengths and will become large when the pump field becomes large. The

maximum value of the Lorentzian, $\mathcal{L}(\delta = 0)$, will decrease when the field increases, a process known as saturation. On the other hand, δ_{HM} becomes large when the field increases, a phenomenon known as power broadening. However, using the values from equations 2.117, 2.118 and 2.121, the value of $\left(1 + \frac{4|\Omega_{13}|^2}{\Gamma_{31}\gamma_{13}}\right)$ is found to be ∼1.00001. Thus, power broadening and gain saturation are very small effects in this system.

Using the values given in equations 2.102, 2.116, and 2.118 and assuming the indices of refraction are 1 at both the pump and Stokes wavelength, the small-signal-gain coefficient can be estimated, as long at the number density, N, is known. The number density can be calculated using the data from the AIP Handbook pg 4-118 [55] (at 10 atm and 300 K).

$$\begin{aligned} N &= N_A \left[\left(\frac{\rho}{\rho_o} \right) \times \rho_o \right] \\ &= N_A \left(9.0575 \times 4.45860 \times 10^{-5} \frac{mole}{cm^3} \right) \\ N &= 2.43 \times 10^{26} \frac{1}{m^3} \end{aligned} \tag{2.154}$$

Plugging the values from equations 2.102, 2.116, 2.118, and 2.154 into the definition of α_{go} made when moving between the third and fourth lines of equation 2.151 yields

$$\alpha_{go} \sim 2.366 \times 10^{-11} \frac{m}{W}. \tag{2.155}$$

In reference [54], this value is measured using 532 nm pump light and found to be equal to $2.5 \pm 0.4 \times 10^{-9} \frac{cm}{W} = 2.5 \pm 0.4 \times 10^{-11} \frac{m}{W}$. The calculated value is within the error bars of the measured value.

The Raman gain is defined as

$$G \equiv \frac{1}{8} \alpha_g n_s n_p c^2 \varepsilon_o \left(\frac{\lambda_p}{\lambda_p + \lambda_s} \right) \left(\frac{b}{L} \right) \tan^{-1} \left(\frac{L}{b} \right) \tag{2.156}$$

In terms of the overlap integrals, the gain becomes

$$G = \frac{\alpha_g n_s n_p c^2 \varepsilon_o V_{ps\,o}}{2 V_s} \tag{2.157}$$

The Time-Dependent CW Raman Laser Equations

It is now possible to write down the time-dependent CW Raman field equations which are the goal of this chapter. Begin by plugging equations 2.137 – 2.139 into the wave equations (equations 2.144 – 2.28) developed in the first section:

$$\begin{aligned}
\dot{E}_p + [\frac{\gamma_{cp}}{2} - i(n_p\omega_p - \omega_{cp})]E_p &= \frac{\gamma_{in\,p}}{2}E_{in\,p} + \frac{\omega_p}{\omega_s}G\left(1 - i\frac{\delta}{\gamma_{13}}\right)E_p|E_a|^2\frac{V_{pa}V_s}{V_pV_{ps\,o}} \\
&\quad + \frac{\omega_p}{\omega_s}G\left(1 - i\frac{\delta}{\gamma_{13}}\right)\left(E_p^*E_sE_a\frac{V_{FWM}V_s}{V_pV_{ps\,o}}\right) \\
&\quad + \frac{\omega_p}{\omega_s}G\left(-1 - i\frac{\delta}{\gamma_{13}}\right)E_p|E_s|^2\frac{V_{ps}V_s}{V_pV_{ps\,o}} \\
&\quad + \frac{\omega_p}{\omega_s}G\left(-1 - i\frac{\delta}{\gamma_{13}}\right)E_p^*E_sE_a\frac{V_{FWM}V_s}{V_pV_{ps\,o}} \qquad (2.158) \\
\dot{E}_s + [\frac{\gamma_{cs}}{2} - i(n_s\omega_s - \omega_{cs})]E_s &= G\left(1 - i\frac{\delta}{\gamma_{13}}\right)|E_p|^2E_s\frac{V_{ps}}{V_{ps\,o}} \\
&\quad + G\left(1 - i\frac{\delta}{\gamma_{13}}\right)E_p^2E_a^*\frac{V_{FWM}^*}{V_{ps\,o}} \qquad (2.159) \\
\dot{E}_a + [\frac{\gamma_{ca}}{2} - i(n_a\omega_a - \omega_{ca})]E_a &= \frac{\omega_a}{\omega_s}G\left(-1 - i\frac{\delta}{\gamma_{13}}\right)E_p^2E_s^*\frac{V_{FWM}^*V_s}{V_aV_{ps\,o}} \\
&\quad + \frac{\omega_a}{\omega_s}G\left(-1 - i\frac{\delta}{\gamma_{13}}\right)|E_p|^2E_a\frac{V_{pa}V_s}{V_aV_{ps\,o}}, \qquad (2.160)
\end{aligned}$$

where the definition of the indices of refraction from equation 2.144 and the Raman gain from equation 2.157 have been used. These are the time-dependent CW Raman laser equations.

Discussion of Equations 2.158 – 2.160

Quite a bit can be determined by looking at equations 2.158 – 2.160. A term-by-term analysis of these equations is quite enlightening. Initially, the analysis is done in general for all three equations, so the subscript q, indicating any of the three wavelengths, is again employed.

The second term on the left side of each equation has two pieces. The first piece, proportional to γ_{cq}, is real and is the cavity loss term for that field. The second piece is imaginary and therefore will affect the phase of the field, rather than the amplitude. It induces a phase change in response to the difference in the cavity resonance frequency, ω_{cq}, and the optical frequency, ω_q, (multiplied by the index of refraction).

On the right side of the pump equation are five terms. The first is responsible for the coupling of the input pump field to the cavity. The second and fourth are Raman terms and affect both the amplitude and the phase of the pump field. The real part of the second term is positive, indicating that this is actually a source term for the pump field due to back conversion from the anti-Stokes field to the pump field. The real part of the fourth term is negative and is responsible for the loss due to the pump field being converted to Stokes. The third and fifth terms are both FWM terms and, again, are both complex. As written above, it appears that the real part of the third term is a source term while the real part of the fifth term is a loss term. However, some care needs to be taken with these because there is an additional phase that results from the complex fields that can (and will) change the effect these two terms have on the pump field.

The right-hand side of the Stokes equation has two terms. The first of the two terms is the standard Raman growth term. The second is a FWM term.

Finally, the right-hand side of the anti-Stokes equation also has two terms. The first of these is the FWM term that is responsible for anti-Stokes generation. But, as with the pump equation, on the surface this looks like a loss term. However, as will be seen in the next chapter, the phases of the fields will affect this term. The second term is a Raman term and is the corresponding term to the one in the pump equation responsible for back-conversion to the pump.

As should be expected, if anti-Stokes generation is ignored (i.e. all FWM terms in the pump and Stokes equations are dropped and the anti-Stokes equation is ignored), the standard CW Raman laser equations are regained[3, 5, 34].

Equations 2.158 – 2.160 are the final result of this chapter. In the next chapter, numerical simulations of these equations will be presented, including a steady-state solution along with its limitations.

FURTHER DEVELOPMENT OF THE RAMAN LASER EQUATIONS

The time-dependent CW Raman laser equations (CWRLE) for the pump, Stokes and anti-Stokes fields were derived in the previous chapter. The goal of this chapter is to further understand these equations and also to gain understanding of the behavior of this system by numerically integrating them. This chapter begins by separating the three CWRLE into six equations, three for the field amplitudes and three for the phases, followed by a discussion of the phase equations. The second section will look at the temporal evolution of the amplitudes and phases of the fields. The third section will look at the behavior of the amplitudes and phases as the Stokes frequency is scanned across the Raman gain profile. The fourth section presents a steady-state solution along with a discussion of its ramifications. This is followed by an *approximate* steady-state solution along with a discussion of its validity. The chapter concludes with a short discussion of the effects on the output powers when the system is resonant on higher-order modes (HOM).

Separation of the CWRLE into Amplitude and Phase Equations

The CWRLE (equations 2.158 – 2.160 at the end of Chapter 2) are complex. The discussion following these equations centered primarily on the amplitudes. However, quite a bit can be said about the phase evolution by simply looking at the phase evolution of the field apart from the amplitude evolution. This requires that each of those three equations be separated into two equations, one for the amplitude and one for the phase of each field.

To begin, express each field, including the input pump field, as the product of a real amplitude and a phase factor:

$$E_q(t) \;=\; A_q(t)e^{i\phi_q(t)}, \tag{3.1}$$

where the subscript q is indicates the field in question, A_q is the amplitude of the field and ϕ_q is its phase. The time derivative of the field then yields to two terms, one proportional to the time derivative of the amplitude, $\dot{A}_q$, and the other proportional to the time derivative of the phase, $\dot{\phi}_q$. After Substituting this into the CWRLE results in two equations, one for the real part and one for the imaginary. Assuming that the phase of the input field is the same as the intracavity pump field, this process yields for the derivatives of the amplitudes

$$\begin{aligned}
\dot{A}_p + \frac{\gamma_{cp}}{2}A_p \;=\;& \frac{\gamma_{in\,p}}{2}A_{in\,p} + \frac{\omega_p}{\omega_s}G\,A_pA_a^2\frac{V_{pa}V_s}{V_pV_{ps\,o}} - \frac{\omega_p}{\omega_s}G\,A_pA_s^2\frac{V_{ps}V_s}{V_pV_{ps\,o}} \\
&+2\frac{\omega_p}{\omega_s}G\frac{\delta}{\gamma_{13}}A_pA_sA_a\frac{V_s}{V_pV_{ps\,o}} \\
&\times\left(V^I_{FWM}\cos(\Delta\phi) - V^R_{FWM}\sin(\Delta\phi)\right) \qquad (3.2)\\
\dot{A}_s + \frac{\gamma_{cs}}{2}A_s \;=\;& G\,A_p^2A_s\frac{V_{ps}}{V_{ps\,o}} \\
&+G\,A_p^2A_a\frac{1}{V_{ps\,o}}\left(V^R_{FWM}\cos(\Delta\phi) + \frac{\delta}{\gamma_{13}}V^R_{FWM}\sin(\Delta\phi)\right. \\
&\left.-V^I_{FWM}\sin(\Delta\phi) + \frac{\delta}{\gamma_{13}}V^I_{FWM}\cos(\Delta\phi)\right) \qquad (3.3)\\
\dot{A}_a + \frac{\gamma_{ca}}{2}A_a \;=\;& -\frac{\omega_a}{\omega_s}G\,A_p^2A_a\frac{V_{pa}V_s}{V_aV_{ps\,o}} \\
&-\frac{\omega_a}{\omega_s}G\,A_p^2A_s\frac{V_s}{V_aV_{ps\,o}}\left(V^R_{FWM}\cos\left(\Delta\phi\right) - \frac{\delta}{\gamma_{13}}V^R_{FWM}\sin(\Delta\phi)\right. \\
&\left.+V^I_{FWM}\sin(\Delta\phi) + \frac{\delta}{\gamma_{13}}V^I_{FWM}\cos\left(\Delta\phi\right)\right) \qquad (3.4)
\end{aligned}$$

where the superscripts R and I have been used to indicate the real and imaginary parts of V_{FWM}. And the derivatives of the phases are

$$\begin{aligned}
\dot{\phi}_p - (n_p\omega_p - \omega_{cp}) &= -\frac{\omega_p}{\omega_s} G \frac{\delta}{\gamma_{13}} A_a^2 \frac{V_{pa} V_s}{V_p V_{ps\,o}} - \frac{\omega_p}{\omega_s} G \frac{\delta}{\gamma_{13}} A_s^2 \frac{V_{ps} V_s}{V_p V_{ps\,o}} \\
&\quad -2\frac{\omega_p}{\omega_s} G \frac{\delta}{\gamma_{13}} A_s A_a \frac{V_s}{V_p V_{ps\,o}} \left(V_{FWM}^R \cos(\Delta\phi) \right. \\
&\quad \left. + V_{FWM}^I \sin(\Delta\phi) \right) \qquad (3.5) \\
\dot{\phi}_s - (n_s\omega_s - \omega_{cs}) &= G \frac{\delta}{\gamma_{13}} A_p^2 \frac{V_{ps}}{V_{ps\,o}} \\
&\quad + G \frac{A_p^2 A_a}{A_s} \frac{1}{V_{ps\,o}} \left(V_{FWM}^R \sin(\Delta\phi) - \frac{\delta}{\gamma_{13}} V_{FWM}^R \cos(\Delta\phi) \right. \\
&\quad \left. + V_{FWM}^I \cos(\Delta\phi) + \frac{\delta}{\gamma_{13}} V_{FWM}^I \sin(\Delta\phi) \right) \qquad (3.6) \\
\dot{\phi}_a - (n_a\omega_a - \omega_{ca}) &= -\frac{\omega_a}{\omega_s} G \frac{\delta}{\gamma_{13}} A_p^2 \frac{V_{pa} V_s}{V_a V_{ps\,o}} \\
&\quad - \frac{\omega_a}{\omega_s} G \frac{A_p^2 A_s}{A_a} \frac{V_s}{V_a V_{ps\,o}} \left(V_{FWM}^R \sin(\Delta\phi) + \frac{\delta}{\gamma_{13}} V_{FWM}^R \cos(\Delta\phi) \right. \\
&\quad \left. - V_{FWM}^I \cos(\Delta\phi) + \frac{\delta}{\gamma_{13}} V_{FWM}^I \sin(\Delta\phi) \right) \qquad (3.7)
\end{aligned}$$

where $\Delta\phi \equiv 2\phi_p - \phi_s - \phi_a$ is the phase mismatch of the three fields. It can be seen that equations 3.2 – 3.7 are coupled differential equations. No analytic steady-state solution to these equations is known.

$\triangle\phi$ is referred to as the "phase mismatch". It is looking at the temporal phase relationships between the pump, Stokes and anti-Stokes fields. On the other hand, "phase matching," as it is traditionally referred to in the optics community, looks at the spatial relationships between the fields and is calculated from their wave vectors. (The wave vectors are dependent on the optical frequencies and their corresponding indices of refraction.) Phase matching *is* a concern for this system and is discussed in Chapter 4.

Comments on the Phase Equations

In his dissertation, Meng [5] went into a fair bit of detail regarding frequency pulling effects in the CW Raman laser. Recall that, in the previous chapter, it was assumed the complex field could be written as a slowly varying envelope multiplied by a rapid oscillation at an optical frequency, as shown in equation 2.13. If this assumption is combined with equation 3.1, then the complex field can be written as (ignoring the spatial dependence)

$$\overrightarrow{E}(t) \quad = \quad A(t)e^{-i\omega t - i\phi(t)}. \tag{3.8}$$

From this perspective, the phase evolution looks like a modification to the laser frequency – such evolution of the phase would pull a field's frequency away from the expected value.

The development by Meng is not incorrect, but there is an easier way to understand what is happening to the phases. This analysis can be done with any of the three phase equations. Rearranging the pump phase equation 3.5 gives

$$\begin{aligned}\dot{\phi}_p \quad = \quad \omega_{cp} - \omega_p \Bigg[n_p - \frac{1}{\omega_s} G \frac{\delta}{\gamma_{13}} A_a^2 \frac{V_{pa} V_s}{V_p V_{ps\,o}} - \frac{1}{\omega_s} G \frac{\delta}{\gamma_{13}} A_s^2 \frac{V_{ps} V_s}{V_p V_{ps\,o}} \\ -2 \frac{1}{\omega_s} G \frac{\delta}{\gamma_{13}} A_s A_a \frac{V_s}{V_p V_{ps\,o}} \left(V_{FWM}^R \cos(\Delta\phi) + V_{FWM}^I \sin(\Delta\phi) \right) \Bigg]. \end{aligned} \tag{3.9}$$

On the right side of this equation is a piece in square brackets, the first term of which is the linear index, n_p.

The remaining terms in the square brackets are also index effects. However, they are higher-order effects, due to the nonlinear susceptibility. Recall that the Raman gain, G, has a Lorentzian profile (in δ) as shown in equation 2.151. Then, if the power-broadening and gain-saturation effects are ignored, the non-linear index is proportional to

$$n_{nl} \quad \propto \quad \frac{\delta}{\delta^2 + \gamma_{13}^2}. \tag{3.10}$$

Equation 3.10 is plotted in Figure 3.1, given that $\gamma_{13} = 2\pi * 250 * 10^6$ rad/s at 10 atm [44]. A comparison of this plot to the plot on page 403 of reference [43] of the

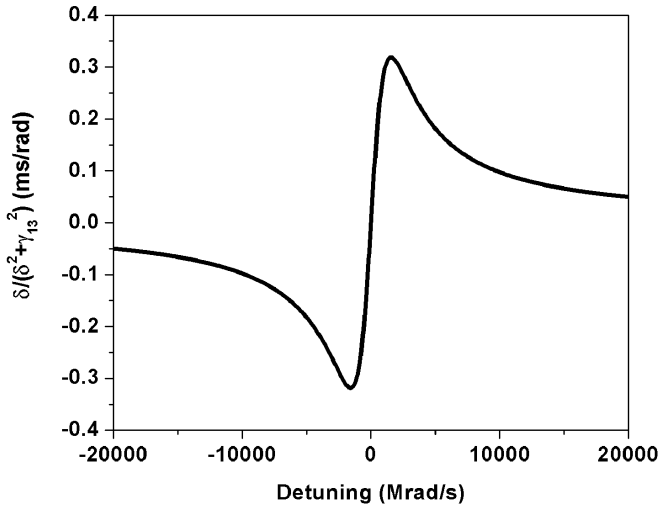

Figure 3.1: Plot of the functional dependence of the non-linear index on the detuning as given in Equation 3.10 .

behavior of the index of refraction near a resonance reveals the same basic shape but reversed left to right. The only difference is that here the index effect is relative to a two-photon resonance rather than a single-photon resonance. Note, however, that when the system is below threshold such that A_s and A_a are zero, the nonlinear index terms go to zero as should be expected. Also, for the pump, all the non-linear index terms go to zero when the detuning from Raman gain line center, δ, goes to zero. However, this is not true for the Stokes and anti-Stokes because the overlap integral V_{FWM} is complex (see equations 3.3 – 3.4).

It is unusual to find an index multiplying a frequency; traditionally frequencies are viewed to be constant regardless of the medium. However, if equation 3.9 is rearranged such that

$$\omega_p = \frac{\omega_{cp} - \dot{\phi}_p}{n_p - n_{pnl}} \tag{3.11}$$

where n_{pnl} represents all the nonlinear index terms, it can be seen that the optical frequency is really the cold cavity resonance frequency modified by all the index effects associated with the system. (Similar equations can be written for the Stokes and anti-Stokes frequencies.) For the pump frequency, what really happens experimentally is that the cavity length adjusts, adjusting ω_{cp} in the process, to account for these index effects because the cavity is frequency locked to the input pump laser frequency. Because the Stokes and anti-Stokes fields grow on cavity resonances, the optical frequency changes as the index changes (ignoring changes in the cavity resonance frequencies associated with the cavity length changing to maintain the pump frequency lock). If it were possible to know both the linear and non-linear indices before-hand, then $\dot{\phi}_p$ would equal zero. However, because the non-linear index depends on the field amplitudes, it is very hard to know this *a priori*. Therefore, when calculating the phase evolution, it is assumed that $\omega_{cp} = n_p\omega_p$, which is easily calculated before-hand. The temporal evolution of the phase then handles the non-linear index effects.

Phase Mismatch and Anti-Stokes Growth.

From equation 3.4, it would appear that the most logical scenario for anti-Stokes growth is when the phase mismatch, $\Delta\phi$, equaled $n\pi$, where n is an odd integer. When this occurs, $\cos(\Delta\phi) \rightarrow -1$ and $\sin(\Delta\phi) \rightarrow 0$. In this case, equation 3.4 becomes

$$\begin{aligned} \dot{A}_a + \frac{\gamma_{ca}}{2}A_a &= -\frac{\omega_a}{\omega_s}G\,A_p^2 A_a \frac{V_{pa}V_s}{V_a V_{ps\,o}} \\ &\quad + \frac{\omega_a}{\omega_s}G\,A_p^2 A_s \frac{V_s}{V_a V_{ps\,o}}\left(V_{FWM}^R + \frac{\delta}{\gamma_{13}}V_{FWM}^I\right). \end{aligned} \tag{3.12}$$

In this case, the FWM term looks like a gain term in that its sign is opposite that of either the Raman term or the cavity loss term. In this case, the growth of the field magnitude as a function of time will be positive.

However, an equivalent scenario is the case when $\Delta\phi$ is $n\pi$, where n is an even integer. When this occurs, $\cos(\Delta\phi) \rightarrow 1$ and $\sin(\Delta\phi) \rightarrow 0$. In this case, equation 3.4 becomes

$$\begin{aligned} \dot{A}_a + \frac{\gamma_{ca}}{2} A_a &= -\frac{\omega_a}{\omega_s} G\, A_p^2 A_a \frac{V_{pa} V_s}{V_a V_{ps\,o}} \\ &\quad -\frac{\omega_a}{\omega_s} G\, A_p^2 A_s \frac{V_s}{V_a V_{ps\,o}} \left(V_{FWM}^R + \frac{\delta}{\gamma_{13}} V_{FWM}^I \right). \end{aligned} \tag{3.13}$$

On the surface, this case looks bad because there is no obvious gain term. However, if the anti-Stokes field magnitude were to grow negative, then the sign of both the cavity loss term and the Raman term would flip because they are proportional to A_a while the sign of the FWM term would remain unchanged. Now, the FWM term looks like a gain term for "negative growth," but the field's magnitude would still be growing. The cavity loss and Raman terms are positive and are, thus, loss terms for the negative anti-Stokes field magnitude.

In both cases, the output power would be the same because it is proportional to the square of the field magnitude.

Converting Intracavity Fields to Output Powers

Experimentally, the measured quantities are powers outside the cavity. Therefore, in order to compare theory to data, it is necessary to convert intracavity fields to output powers. Before proceeding with theoretical results, the procedure for converting fields to powers will be outlined.

This process is begun by defining the irradiance (power/area). As defined on page 383 of reference [43], it is

$$I = \frac{1}{2} v \varepsilon |\overline{E}(\overrightarrow{r}, t)|^2 \tag{3.14}$$

where v is the speed of light in the material and ε is the permittivity in the medium. By definition, $v \equiv c/n$ and $\varepsilon \equiv n^2\varepsilon_o$ (from page 180 or 383 of reference [43]). Power is obtained by integrating the irradiance over the transverse dimensions.

$$\Pi(t) \;=\; \int \frac{1}{2} v\varepsilon |E(t)|^2 |u(\overrightarrow{r})|^2 dA_T \tag{3.15}$$

where equation 2.16 has been used. This integral is the same (omitting the integral in the z-direction) as that used to calculate the mode volume, V_q. The functional form of $u(\overrightarrow{r})$ is the same as given in Appendices C – E with the exception that the field outside the cavity is not a standing wave but a traveling wave. Therefore, the quantity $\sin(kz)$ needs to be changed to e^{ikz}. As shown in Appendix F, this integral results in the same value, regardless of the spatial mode of the field. Therefore,

$$\Pi(t) \;=\; \left(\frac{\pi w_o^2 n}{4}\sqrt{\frac{\varepsilon_o}{\mu_o}}\right)|E(t)|^2. \tag{3.16}$$

Powers external to the cavity can now be calculated. (The subscript 1 will be used to indicate quantities associated with the input end [front end] of the cavity while the subscript 2 will indicate the back end of the cavity. For example, the front mirror's power reflectivity at the pump wavelength is R_{p1} while the back mirror's pump power reflectivity is R_{p2}.) The most complex to calculate is the pump power on the input side of the cavity because, in addition to the cavity's leakage field, there is also the reflected input pump field. On resonance, the total field is:

$$E_{p1} \;=\; -\sqrt{R_{p1}}E_{in\,p} + \frac{1}{2}\sqrt{T_{p1}}E_p \tag{3.17}$$

where, as a reminder, E_{p1} is the field external to the cavity and E_p is the intracavity field. Because the intracavity field is a standing wave, only half of it, at any given time, is incident upon either mirror, as indicated by the factor of $\frac{1}{2}$ multiplying the second term of equation 3.17. The power on this side of the cavity is found by

multiplying E_{p1} by its complex conjugate and applying equation 3.16.

$$\mathcal{P}_{p_1} = R_{p1}\mathcal{P}_{in\,p} - \sqrt{T_{p_1}R_{p_1}}\sqrt{\mathcal{P}_{in\,p}\Pi_p} + \frac{1}{4}T_{p_1}\Pi_p \tag{3.18}$$

where, $\mathcal{P}_{p_1}$ is the pump power at the front of cavity and $\mathcal{P}_{in\,p}$ is the input pump power. $\mathcal{P}_{in\,p}$ is determined in a manner similar to the intracavity pump power and, in terms of the input pump field is

$$\mathcal{P}_{in\,p} = \left(\frac{\pi w_o^2 n}{4}\sqrt{\frac{\varepsilon_o}{\mu_o}}\right)|E_{in\,p}(t)|^2. \tag{3.19}$$

The interference between the reflected field and the leakage field (for this on-resonance case) can clearly be seen in equation 3.18.

The powers for the Stokes and anti-Stokes transmitted through both ends of the cavity and the pump transmitted through the back end of the cavity all take a common form. In terms of the fields, they can be written generally as

$$E_{qn} = \frac{1}{2}\sqrt{T_{qn}}E_q. \tag{3.20}$$

where the subscript q indicates the wavelength and the subscript n determines which end of the cavity is under consideration. (When q indicates the pump wavelength, n can only refer to the back of the cavity.) Thus, the powers external to the cavity can be written as

$$\mathcal{P}_{qn} = \frac{1}{4}T_{qn}\Pi_q. \tag{3.21}$$

Numerical Integration of the CWRLE

Comments on Numerical Integration

In order to study the temporal evolution of the fields and phases, it is necessary to numerically integrate equations 3.2 – 3.7. There are two possible methods for

numerically integrating the CWRLE. The first is to start with the CWRLE as written in equations 2.158 – 2.160. After integrating these three equations, it is then possible to take the complex result and separate it into its amplitude and phase pieces. If the numerical integration is going to be done in this manner, it is necessary to force the input pump field phase in the pump equation to agree with the phase of the intracavity field. This is easily accomplished by multiplying by the pump field and dividing by the pump field magnitude. Because of this division, it is impossible to start with a non-zero initial value for the pump field. The advantage of this method is that the initial conditions for the intracavity Stokes and anti-Stokes fields are what would be physically expected. Namely, the Stokes field has to have some initial non-zero seed representing the vacuum field while the anti-Stokes field does not.

The second method is to begin by separating the three CWRLE into three amplitude equations and three phase equations, yielding equations 3.2 – 3.7. The main advantage of this method is that the initial phases can be arbitrarily set, and thus, the dependence of the phase evolution on the initial phases can be investigated. The disadvantages are that a good bit of initial algebra must be done in order to separate the equations, and there are compromises that need to be made regarding the initial conditions. Unlike method 1, there is nothing to prohibit a zero initial pump magnitude. However, in both the Stokes and anti-Stokes phase equations there are terms divided by the field amplitudes. This requires non-zero initial values for both fields. For the Stokes, this represents the vacuum field and, thus, is expected. But, this is a compromise for the anti-Stokes.

Appendix I contains the Matlab code used to do the numerical integration of the CWRLE, along with a discussion of how the calculations were made. The code is designed to do the integration using either method outlined above by simply commenting or uncommenting the indicated portions. The calculations in this chapter

Parameter	Value	Parameter	Value
Raman Dependent Parameters		Experimental Parameters	
γ_{13}	$2\pi * 250 * 10^6$rad/s [44]	$R_{1p} = R_{2p}$	0.9999
Γ_{31}	$2\pi * 10^4$rad/s [49]	$T_{1p} = T_{2p}$	$50{*}10^{-6}$
Ω_{13}	$2\pi * 1.5 * 10^5$ rad/s	$R_{1s} = R_{2s}$	0.9998
α_{go}	$2.5{*}10^{-11}$ (m/W) [54]	$T_{1s} = T_{2s}$	$100{*}10^{-6}$
Initial Conditions		$R_{1a} = R_{2a}$	0.999
E_{po}	0 V/m	$T_{1a} = T_{2a}$	$900{*}10^{-6}$
E_{so}	10^{-10} V/m	R_c	50 cm
E_{ao}	10^{-10} V/m	L	$\sim$3*2.54 cm
ϕ_{po}	$\pi/4$ rad	P	10.2 atm
ϕ_{so}	$\pi/6$ rad	T	293 K
ϕ_{ao}	$\pi/7$ rad	f_{plc}	563158.295586529 GHz
$E_{in\,p}$	3.6 mW	q_p	286408

Table 3.1: Parameters used in the numerical integration of the CWRLE, unless stated explicitly in the text.

were all done using method 2 because of the ability to arbitrarily set the initial phases. The notation used in the text of the dissertation may not agree perfectly with the notation in the Matlab code – primarily, this is due to a lack of Greek characters on a standard keyboard, but, it is also due to a change in notation between when the code and the dissertation were written.

The parameters used in the numerical results of this chapter, unless explicitly mentioned in the text, are presented in Table 3.1. It was assumed that all three fields had a TEM_{00} spatial mode profile. (Some of the parameters, such as q_p, will only make sense after reading the discussion on how the code works contained in Appendix I, but for completeness they need to be included here.) The left-most columns in Table 3.1 are constants associated with the Raman processes and the initial conditions, with the subscript "o" indicating that the quantity is an initial condition. The initial phases were chosen randomly. The right-most columns are primarily cavity parameters.

Line-Center Temporal Evolution.

Figure 3.2 shows the calculated powers in the forward direction (i.e. continuing in the same direction of propagation as the input pump) and phases as a function of time when the system is on Raman gain line center ($\delta = 0$) (given the initial conditions in Table 3.1). (For comparison, Appendix J contains equivalent plots to Figure 3.2 but calculated by method 1.) Figure 3.2a shows the forward pump power, while subplots c and e show the Stokes and anti-Stokes powers respectively. From $t = 0$ to $t \sim 40$ μs, the forward pump power increases as a result of the build-up of the intracavity pump power. At $t \sim 40$ μs, the intracavity pump field has increased enough for the lasing threshold to be exceeded at which point, the Stokes and anti-Stokes begin to grow. All three then undergo a series of relaxation oscillations before settling down to their steady-state values by $t \sim 80$ μs. Subplots b, d, and f of Figure 3.2 show the temporal development of the pump, Stokes and anti-Stokes phases, respectively. The pump phase is constant in time at its initial value $\pi/4$, while the Stokes and anti-Stokes phases adjust quickly (within ~ 5 μs) to their steady-state values. This quick evolution is caused by the initial Stokes and anti-Stokes seeds leaking out of the cavity. The steady-state Stokes phase is very similar to its initial phase, $\pi/6$. The anti-Stokes evolves from its initial phase of $\pi/7$ to 1.05 rad. This change in the anti-Stokes phase is necessary in order to optimize the growth of the anti-Stokes field.

Figure 3.3 shows the temporal development of the phase mismatch, corresponding to the phases in Figure 3.2. The phase mismatch quickly evolves to zero and then is constant. Table 3.2 shows the steady-state value of $\Delta\phi$ for various initial phase values. For this zero detuning case, the phase mismatch evolves to either 0 or $\pm 2\pi$, which are mathematically equivalent. As discussed above on page 61, this is the second scenario for anti-Stokes growth within the cavity.

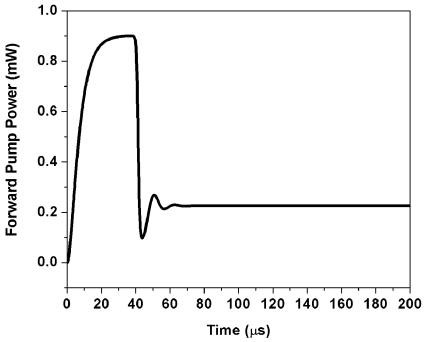

(a) Pump power.

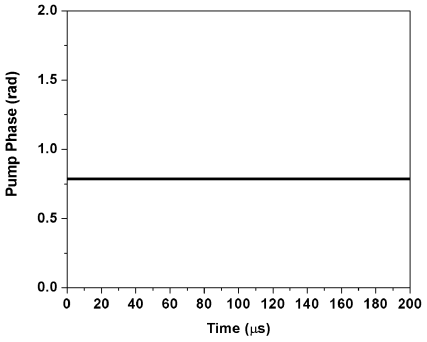

(b) Pump phase.

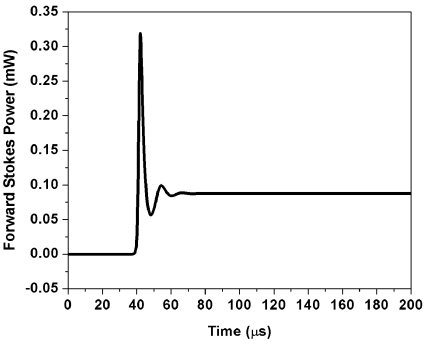

(c) Stokes power.

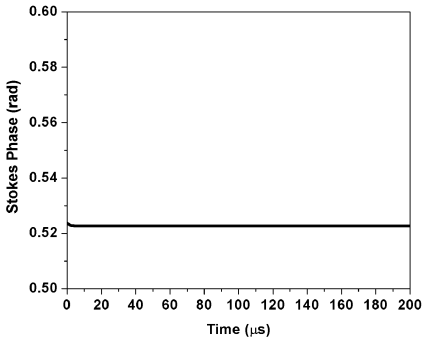

(d) Stokes phase.

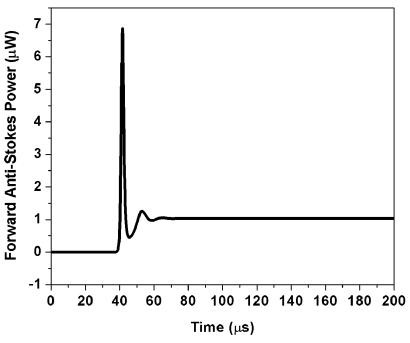

(e) Anti-Stokes power.

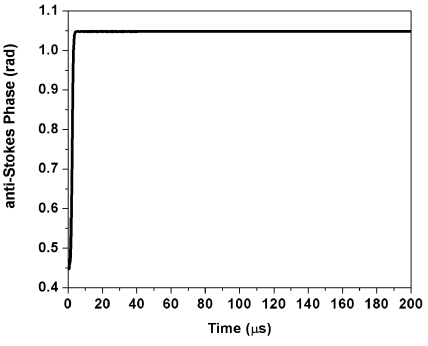

(f) Anti-Stokes phase.

Figure 3.2: Forward powers and phases as a function of time when $\delta = 0$, with conditions specified in Table 3.1 .

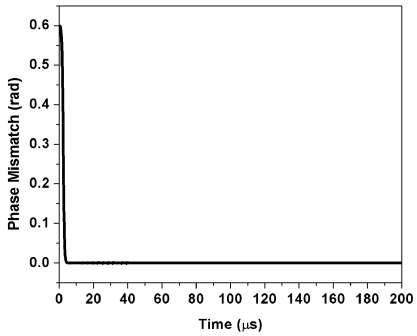

Figure 3.3: Phase mismatch evolution as a function of time when $\delta = 0$.

ϕ_{po}	ϕ_{so}	ϕ_{ao}	$\Delta\phi_{ss}$
$\pi/4$	$\pi/6$	$\pi/7$	0
$\pi/2$	$-\pi/5$	0	2π
$-\pi/2$	$\pi/5$	$\pi/3$	-2π
-π	$\pi/4$	$-\pi/8$	-2π
$\pi/9$	0	$\pi/7$	0
$\pi/3$	$\pi/5$	$\pi/7$	0
$\pi/3$	$\pi/5$	$-\pi/7$	0
$\pi/3$	$-\pi/5$	$\pi/7$	0
$\pi/3$	$-\pi/5$	$-\pi/7$	2π
$-\pi/3$	$-\pi/5$	$-\pi/7$	0
$-\pi/3$	$\pi/5$	$-\pi/7$	0
$-\pi/3$	$\pi/5$	$\pi/7$	-2π
$-\pi/3$	$-\pi/5$	$\pi/7$	0
0.95π	0.23π	0.61π	2π
0.49π	0.89π	0.76π	0
0.45π	0.02π	0.82π	0

Table 3.2: Steady-state value of $\Delta\phi$ for various input phases when $\delta = 0$. The steady-state value is independent of the initial phases.

Physically, the anti-Stokes phase wants to be in-phase with the dipole oscillations of the medium. These oscillations are generated by the pump and Stokes fields and will have a phase equal to $2\phi_p - \phi_s$ because it takes two pump photons and one Stokes photon to generate one anti-Stokes photon, as discussed in the introduction. The statement $\Delta\phi = 0$ is equivalent to stating $\phi_a = 2\phi_p - \phi_s$.

Line-Center Steady-State Behavior

Figure 3.4 shows the steady-state values of the forward powers as a function of input power (given the initial conditions in Table 3.1). These plots were made by repeatedly integrating equations 3.2 – 3.7 to steady-state for different input pump powers. The steady-state values from each integration were then plotted. Below threshold, as should be expected, the pump grows linearly with increased input pump power while the Stokes and anti-Stokes are zero. Characteristic of the CW Raman laser system, above threshold the pump power clamps (becomes constant) while the Stokes and anti-Stokes power levels both grow with a square-root dependence on the input pump power. (As will be seen in equation 3.38, technically, the Stokes field amplitude is proportional to $\sqrt{\left(\frac{A_{in\,p}}{A^{th}_{in\,p}} - 1\right)}$. However for simplicity when writing, usually this will be referred to as a square-root dependence on the input pump when above threshold.)

Figure 3.5 shows the forward Stokes and anti-Stokes conversion efficiencies (output power divided by input power) plotted as a function of pump rate (input pump divided by the threshold value). (Since the front and back mirrors used in these simulations are identical, the total conversion efficiencies can be found by multiplying the forward conversion efficiencies by two.) The conversion efficiency for both fields is maximum at a pump rate of four and for the Stokes is 2.43 % while for the anti-Stokes it is 0.029%. Because the mirror reflectivities and transmittivities are matched

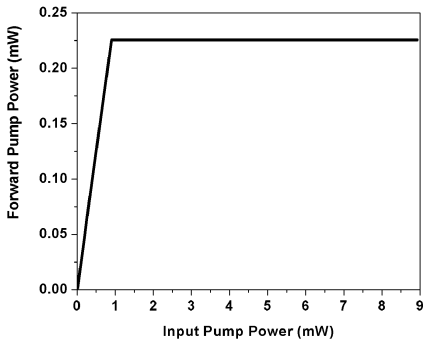

(a) Pump power.

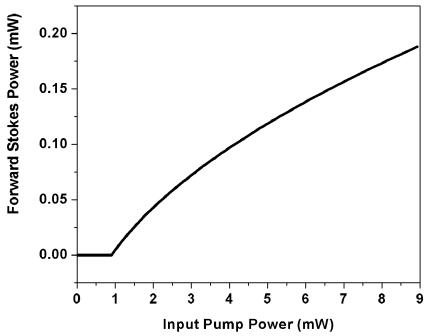

(b) Stokes power.

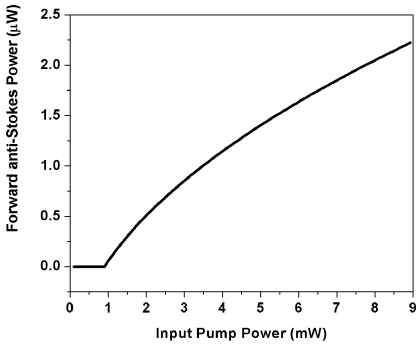

(c) Anti-Stokes power.

Figure 3.4: Forward steady-state powers as a function of input pump power when $\delta = 0$.

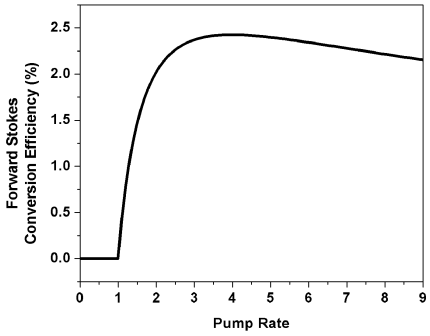

(a) Stokes conversion efficiency.

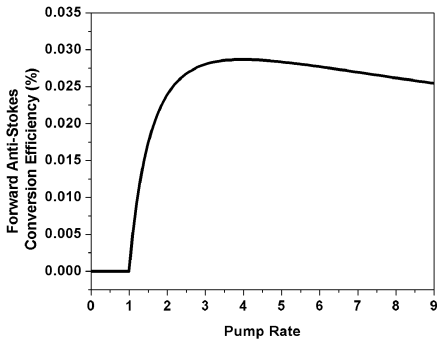

(b) Anti-Stokes conversion efficiencies.

Figure 3.5: Forward Stokes and anti-Stokes conversion efficiencies (forward output power divided by input power) as a function of pump rate (input pump divided by the threshold value) when $\delta = 0$. (The total conversion efficiencies can be found by multiplying the forward conversion efficiency by two since the simulations involve a matched cavity.)

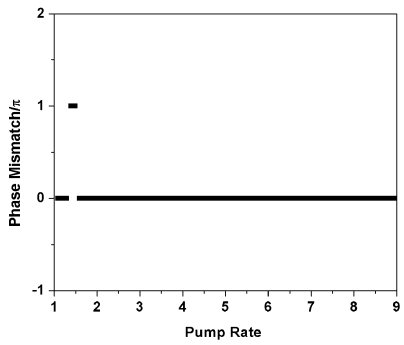

Figure 3.6: Steady-state value of the phase mismatch, $\Delta\phi$, divided by π as a function of input pump rate when $\delta = 0$. For all input pump rates, the steady-state phase mismatch is either 0 or π.

in this calculation, the theoretical maximum conversion efficiency from the pump to Stokes (ignoring anti-Stokes) is 50 % [19].To improve the conversion efficiencies to the maximum possible of 100 % conversion into the Stokes only (or 50 % Stokes and 50 % anti-Stokes), the Raman cavity needs to be impedance matched by lowering the reflectivity (and increasing the transmission) of the input pump mirror as outlined in [40].

Figure 3.6 shows the steady-state value of the phase mismatch divided by π for input pump rates greater than 1. The steady-state value of the phase is either zero or π. But, as discussed on page 60, the output power from either of these two values will be equivalent at any particular input pump rate. Therefore, on line center, it is safe to assume that the steady-state value of $\Delta\phi$ is zero.

Growth Away From Line Center

Figure 3.7 shows the temporal development of the forward powers and phases as a function of time when δ ~248 MHz. (This value was arbitrarily chosen to be within an interesting range.) Subplots a, c, and e show the temporal development of the forward pump, Stokes and anti-Stokes powers respectively while subplots b, d,

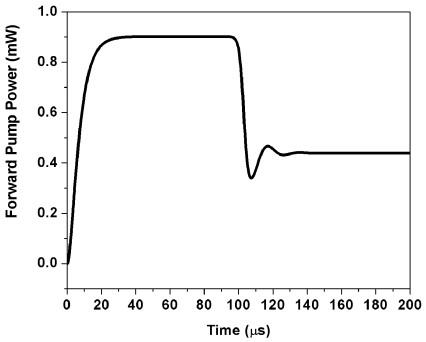

(a) Pump Power.

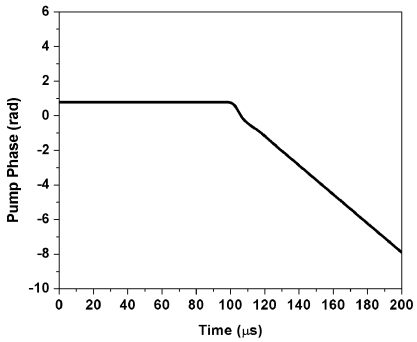

(b) Pump phase.

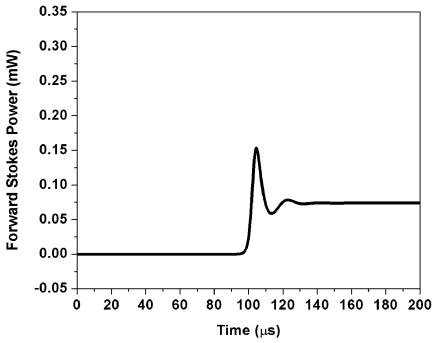

(c) Stokes power.

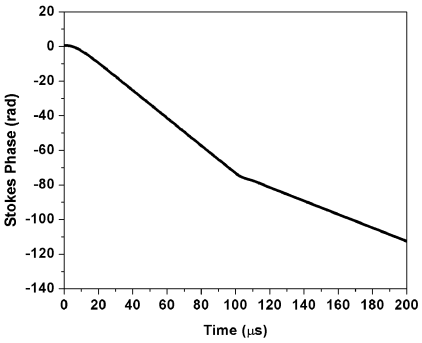

(d) Stokes phase.

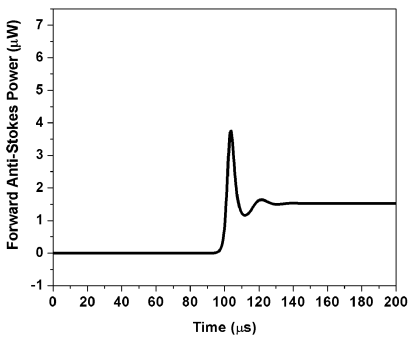

(e) Anti-Stokes power.

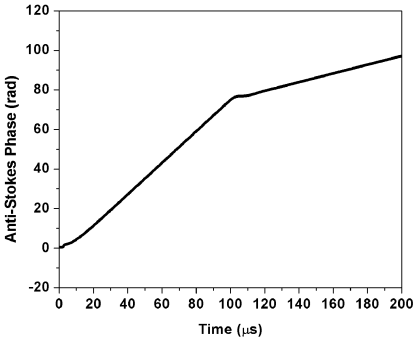

(f) Anti-Stokes phase.

Figure 3.7: Forward powers and phases as a function of time when $\delta = 248$ MHz.

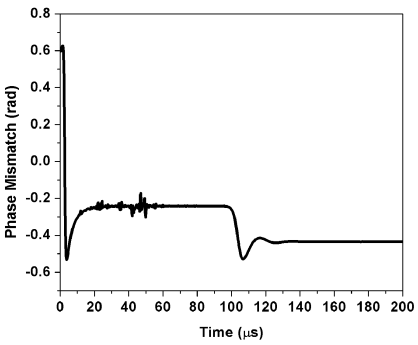

Figure 3.8: Phase mismatch evolution as a function of time when $\delta = 0$.

and f show the development of the pump, Stokes and anti-Stokes phases respectively. There are significant differences between these plots and those in Figure 3.2. First of all, the system takes longer to reach threshold, even though the input pump power is the same in both cases. Secondly, the steady-state values of the forward powers are different, in all three cases. The detuned steady-state pump and anti-Stokes powers are both higher than their line-center values while the steady-state Stokes power is lower. (This behavior will be explained shortly.) Thirdly, in Figure 3.2, the phases quickly evolve to a steady-state value and then quit evolving, whereas in Figure 3.7, the individual phases never reach a steady-state value. Their continued evolution is linear with time. As discussed in reference [47] on page 948 , there are two possibilities for the steady-state condition for phases. The first is that the $\dot{\phi} = 0$ and ϕ is therefore constant in time, as was seen in the line-center calculations. The second condition is that $\dot{\phi} = constant$, which means that ϕ is linear with time, as is being seen in the detuned calculations. (The first case is a special case of the second.) However, as shown in Figure 3.8, even though the individual phases never reach a constant steady-state value when the system is detuned, the phase mismatch does. But, unlike the line-center case, the phase mismatch does not evolve to either zero or a integral multiple of π. Instead, in this case, it stabilizes to a value of ~ -0.43 rad.

Given $\Delta\phi = 2\phi_p - \phi_s - \phi_a$,

$$\dot{\Delta\phi} = 2\dot{\phi_p} - \dot{\phi_s} - \dot{\phi_a}. \tag{3.22}$$

The time derivatives of the individual phases are given equations 3.5 – 3.7. Plugging them into 3.22, dropping the terms proportional to $(n_q\omega_q - \omega_{cq})$ as done in the numeric simulations and terms proportional to V^I_{FWM} because, in general, it is much smaller than V^R_{FWM} (as can be seen in Appendix H) and organizing the terms yields

$$\begin{aligned}
\dot{\Delta\phi} = & \frac{\delta}{\gamma_{13}}\left(-\frac{\omega_p}{\omega_s}GA_a^2\frac{V_{pa}V_s}{V_pV_{ps\,o}} - \frac{\omega_p}{\omega_s}GA_s^2\frac{V_{ps}V_s}{V_pV_{ps\,o}}\right. \\
& \left. + GA_p^2\frac{V_{ps}}{V_{ps\,o}} - \frac{\omega_a}{\omega_s}GA_p^2\frac{V_{pa}V_s}{V_aV_{ps\,o}}\right) \\
& -\frac{\delta}{\gamma_{13}}\left(+2\frac{\omega_p}{\omega_s}GA_sA_a\frac{V_s}{V_pV_{ps\,o}}V^R_{FWM}\cos(\Delta\phi)\right. \\
& \left. + G\,\frac{A_p^2A_a}{A_s}\frac{1}{V_{ps\,o}}V^R_{FWM}\cos(\Delta\phi) + \frac{\omega_a}{\omega_s}G\,\frac{A_p^2A_s}{A_a}\frac{V_s}{V_aV_{ps\,o}}V^R_{FWM}\cos(\Delta\phi)\right) \\
& + \left(G\,\frac{A_p^2A_a}{A_s}\frac{1}{V_{ps\,o}}V^R_{FWM}\sin(\Delta\phi) - \frac{\omega_a}{\omega_s}G\,\frac{A_p^2A_s}{A_a}\frac{V_s}{V_aV_{ps\,o}}V^R_{FWM}\sin(\Delta\phi)\right)
\end{aligned} \tag{3.23}$$

There are three separate sets of terms in this equation. The first set (top two lines of equation 3.23) result from Raman interactions and are proportional to $\frac{\delta}{\gamma_{13}}$. The second set (3rd and 4th lines of equation 3.23) are FWM terms and are also proportional to $\frac{\delta}{\gamma_{13}}$. When on line-center ($\delta = 0$), neither of these first two sets of terms will influence $\dot{\Delta\phi}$. The last set of terms (bottom line of equation 3.23) are also due to FWM interactions. These terms are not proportional to $\frac{\delta}{\gamma_{13}}$ and, therefore, will influence $\dot{\Delta\phi}$ when on line-center. Considering only this third set of terms, it can be seen that the only way for $\dot{\Delta\phi} = 0$, the line-center steady-state condition, is for $\sin(\Delta\phi) = 0$ or, equivalently, for $\Delta\phi = 0,\ n\pi$, where n is an integer. When detuned, the first two sets of terms come into play and no easy analysis like the line-center analysis can be used to determine the steady-state value of $\Delta\phi$.

Experimentally, the pump frequency inside the cavity is always equal to the input pump frequency, which can be measured. However, numerically, the situation is slightly different. Numerically, the pump frequency is assumed to be on a cavity resonance which, ignoring the Gouy phase shift, is calculated from knowing that the cavity length must equal an integer number of half wavelengths in the medium (as shown in Appendix L). Mathematically, this is

$$L = \frac{q_p \lambda_p}{2 n_p} \tag{3.24}$$

where q_p is the longitudinal cavity mode index at the pump wavelength, λ_p is the pump wavelength in vacuum and n_p is the linear index of refraction at the pump wavelength. (Recall that wavelength can be converted to frequency by dividing the speed of light by the wavelength.) As can be seen, the linear index is included, but, not the non-linear index. This is because, as discussed below equation 3.11, the non-linear index cannot be known *a priori*, since it depends on the intracavity field strengths. Therefore, once the system starts lasing, the guess at the pump frequency is necessarily wrong and the phase starts evolving to account for this error.

Figure 3.9 shows the steady-state behavior of the forward pump, Stokes, and anti-Stokes powers as a function of input pump power for two different detunings, $\delta = 0$ and $\delta = 248$ MHz. Subplots a, b, and c show the forward pump, Stokes and anti-Stokes powers respectively. The small "glitch" near threshold on the steady-state detuned pump curve is due to numerics and is not physical. (However, as will be seen in Chapters 5 and 6, something similar does occasionally appear on the data.) The curves for the $\delta = 0$ case are identical to those in Figure 3.4.

As can be seen in Figure 3.9a, the pump power grows linearly with respect to the input power until the lasing threshold is reached. In both the line-center and the detuned cases, the forward pump power clamps above threshold. Due to the

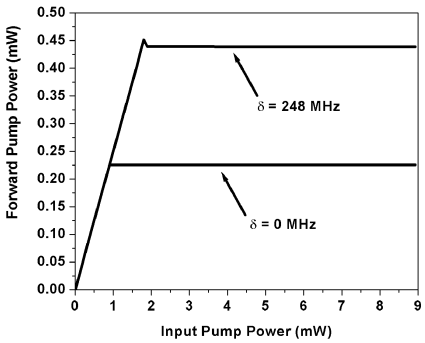

(a) Pump power.

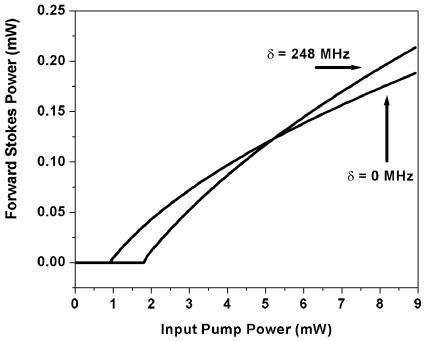

(b) Stokes power.

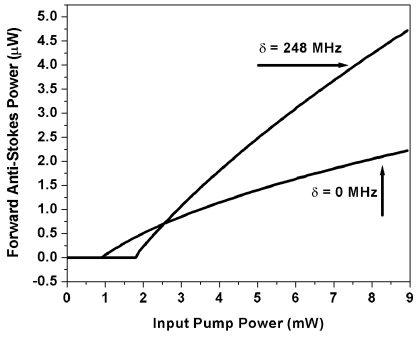

(c) Anti-Stokes power.

Figure 3.9: Forward steady-state powers as a function of input pump power when $\delta = 0$ and 248 MHz.

Lorentzian profile of the Raman gain as a function of detuning, the Raman gain is smaller when the system is detuned. Therefore, the threshold for the detuned case is higher than the line-center case and the pump clamps at a higher level.

Some general trends can be seen in both the Stokes and anti-Stokes subplots, Figures 3.9b and c. As was seen in 3.9a, the threshold is higher when detuned than when on line-center. Whether detuned or line-center, both the Stokes and anti-Stokes powers increase as the square-root of the input power above threshold. Perhaps surprisingly, the detuned and line-center Stokes curves cross at an input pump power of 5.2 mW and the anti-Stokes curves cross at 2.6 mW.

The reason why the curves cross is difficult to understand and is related to impedance matching and conversion efficiencies, as discussed in reference [40, 39]. However, those arguments are complex in their own right, so here an attempt will be made to describe the behavior based on conservation of energy in the pump field. To simplify the discussion, the absorption and scattering in the mirrors is going to be set equal to zero. In addition, it is going to be assumed that the pump energy can only go into Stokes (instead of Stokes and anti-Stokes). The parameters used in the plots during this discussion are identical to those in Table 3.1 except that the transmission for the pump and Stokes equal $1-R_p$ and $1-R_s$ respectively (because the absorptions are 0) and the anti-Stokes reflectivity is 0.1 so that very little anti-Stokes is generated.

Figure 3.10a shows the forward pump power as a function of input pump power, the solid line is for line-center and the dotted line is detuned 248 MHz. Below threshold, the transmitted pump increases as the input pump is increased. Since there is no absorption, the slope of this growth is one. This means that the input is completely transmitted through the cavity. Above threshold, the pump clamps. The threshold and clamp level are larger when detuned because of the decrease in the Raman gain, G. This is the exact same behavior seen in Figure 3.9a.

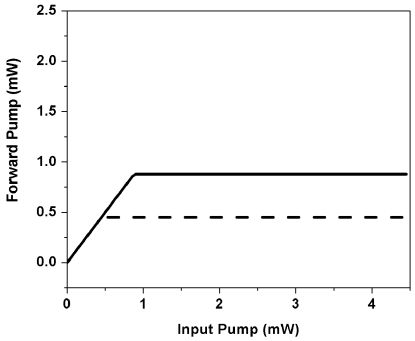

(a) Forward pump power.

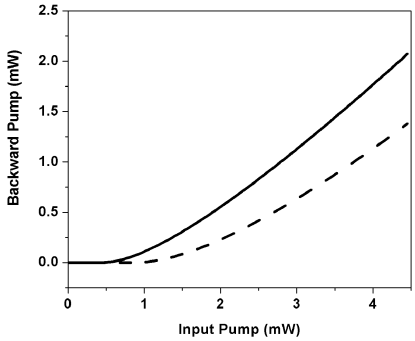

(b) Backward pump power.

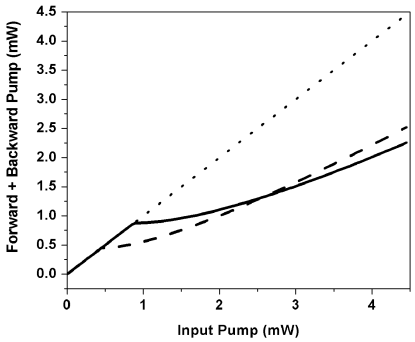

(c) Sum of forward and backward pump powers.

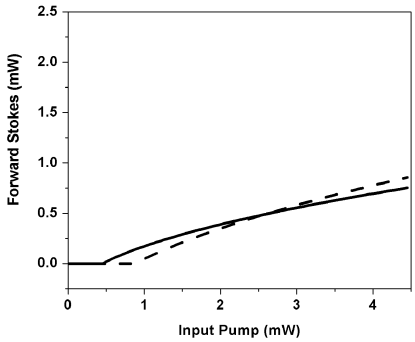

(d) Forward Stokes power.

Figure 3.10: Steady-state powers as a function of input pump power when $\delta = 0$ (solid line) and 248 MHz (dashed line), assuming no absorption or scattering in the mirrors.

Figure 3.10b shows the backward pump power as a function of the input pump power, the solid line is for line-center and the dashed line is detuned 248 MHz. As a reminder, the backward pump power is calculated using equation 3.18. Below threshold, the initial reflection is perfectly canceled by the leakage field. Therefore, the backward pump power is zero. Thus, energy is conserved below threshold – none is reflected and all is transmitted. Above threshold, the leakage field clamps. Therefore, the leakage field is not large enough to cancel the initial reflection and the backward pump power begins to grow. This means that there is not as much energy entering the cavity to be converted to Stokes. As can be seen from equation 3.18, the amount of backward pump power will always be less when the system is detuned because the pump clamp level is higher.

Figure 3.10c shows the sum of the forward and backward pump powers, the solid line is for line-center and the dotted line is detuned 248 MHz. Also plotted on Figure 3.10c is the line $y = x$ (dotted), which in this case of no absorption, represents the total energy available to the system. These line-center and detuned lines cross at an input pump power of approximately 2.6 mW. The pump clamp level is lower on line-center, but, since the system reaches threshold at a smaller input pump power, the pump power reflected from the front of the cavity starts growing earlier. When detuned, the pump clamp level is larger, but the reflected power is smaller. At 2.6 mW, the amount of power reflected on line-center has grown enough so that even though the pump clamp level is smaller, the sum of the forward and backward pump powers has grown enough to exceed the detuned sum of forward and backward powers.

The difference between the sum of the transmitted and reflected powers and the line $y = x$, the total energy available to the system, is the amount of energy available for conversion to Stokes. Below 2.6 mW, there is more energy available for conversion to Stokes on line-center than detuned. At 2.6 mW, the energy for conversion is equal

for the line-center and detuned cases. And, above 2.6 mW, there is more energy available in the detuned case. Therefore, it would be expected, from conservation of energy, that the Stokes produced on line-center will be exceeded by the Stokes generated when detuned at an input pump value of 2.6 mW. This is exactly what is seen in Figure 3.10d, which shows the forward Stokes power as a function input pump power for line center (solid line) and detuned 248 MHz (dashed line).

Through conservation of energy, it is now possible to understand why the two curves in Figures 3.9b and c cross. However, it is still a mystery as to why the anti-Stokes curves cross at a lower input pump power than the Stokes. The answer to this question lies in phase effects. To see this, begin by ignoring such effects so that the FWM term in equation 3.4 is proportional to $GA_p^2A_s$. The other factors (such as the overlap integrals) do not depend on the detuning, whereas $\Delta\phi$ will. The quantity, GA_p^2, is the gain for the Stokes laser transition, which, above threshold, must equal the losses at the Stokes wavelength, and thus, is constant for all detunings and all input powers even though, as the system is detuned from resonance, A_p^2 is increasing (as seen in Figure 3.9a) and the Raman gain, G, is decreasing. If the discussion is confined to the value of input power for which the two Stokes curves in Figure 3.9b cross ($\mathcal{P}_{in\,p} \sim 5.2$ mW), then A_s is also constant. This analysis leads to the result that, as with the Stokes, the detuned and line-center anti-Stokes curves in Figure 3.9c should be equal when $\mathcal{P}_{in\,p} \sim 5.2$ mW. But, as can be seen in Figure 3.9c, they are not equal, confirming the statement that the phase effects cannot be disregarded.

Figure 3.11 shows the forward powers as a function of detuning for three different input pump powers. In each subplot, there are three curves plotted. The curve labeled I is for an input pump power of 7.27 mW (8 times the line-center threshold) while the curves labeled II and III are for 3.63 mW (4 times the line-center threshold) and 1.82 mW (2 times the line-center threshold).

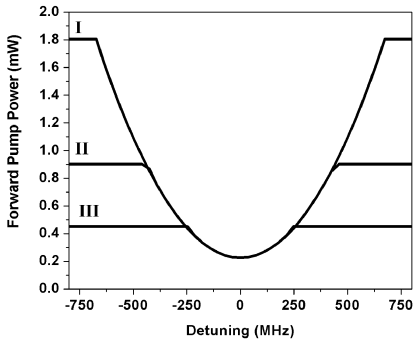

(a) Pump power.

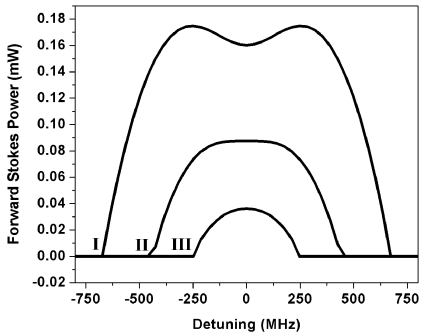

(b) Stokes power.

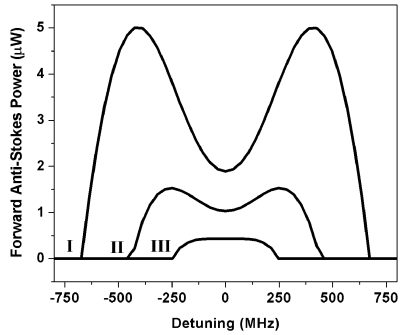

(c) Anti-Stokes power.

Figure 3.11: Forward steady-state powers as a function of detuning for three different input pump powers. In each subplot, there are three curves labeled I, II and III. The curve labeled I is for an input pump power of 7.27 mW, while the curves labeled II and III are for input pump powers of 3.63 mW and 1.82 mW respectively, which are 8, 4, and 2 times the line center threshold.

All three forward pump curves in Figure 3.11a follow the same basic profile. At detunings for which the Stokes is not lasing the pump power is constant because it is not being converted to Stokes and, as expected, is higher when the input pump is higher. Because the Raman gain is less for larger detunings, the input pump power needed to reach threshold is larger for larger detunings. Therefore, the detuning at which the pump power starts to be depleted by conversion into Stokes and anti-Stokes is smaller when the input pump power is less. However, since the pump clamps above threshold, the value of the pump power when the system is lasing is the same for all three input pump powers at a given detuning. The forward pump power is least when the system is not detuned.

In subplot b, the detuning at which forward Stokes can start to be generated depends on the input pump power because the Raman gain is less for larger detunings. The behavior of the forward Stokes power for each of the three input powers can be understood with the help of Figure 3.9a. An input pump power of 1.82 mW (curve III) is twice the line-center threshold but it just equals threshold when the system is detuned by 248 MHz, so at this power and detuning the forward Stokes is just barely lasing. Therefore, for curve III of Figure 3.11b, the forward Stokes power is much larger at line-center than it is at a detuning of 248 MHz. However, when the input pump power is increased to 3.63 mW, as seen in Figure 3.9a, the line-center and detuned forward Stokes powers are not equal, but much closer in value. On curve II of Figure 3.11b, the value of the forward Stokes power is slightly less when detuned by about 250 MHz compared with the line-center value. However, when the input pump power is again increased to 7.27 mW, the input pump power has increased past the point where the detuned curve and line-center curves of Figure 3.9a have crossed and the detuned forward Stokes power is greater than the line-center power. In Figure 3.11b, the value of the forward Stokes for curve I at a detuning of roughly 250 MHz

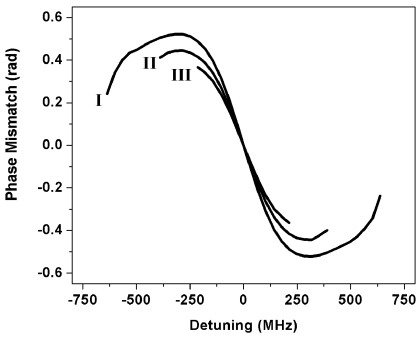

(a) Forward steady-state pump power.

Figure 3.12: Phase mismatch as a function of detuning for three different input pump powers. In each subplot, there are three curves labeled I, II and III. The curve labeled I is for an input pump power of 7.27 mW, while the curves labeled II and III are for input pump powers of 3.63 mW and 1.82 mW respectively, which are 8, 4, and 2 times the line center threshold. For each input pump power, the phase mismatch is only plotted for detunings for which the Stokes is above threshold.

is larger than the line-center value.

An analysis similar to that for the Stokes can be done to understand the anti-Stokes behavior in Figure 3.11c. By looking at Figure 3.9c, it can be seen that at 1.81 mW, the line-center anti-Stokes power is above threshold while the detuned power is barely above threshold. But, for an input pump power of 3.63 mW, the two curves have already crossed and the detuned power is now bigger than the line-center power, though not by nearly as much as at 7.27 mW. Therefore in Figure 3.11c, the forward anti-Stokes power for curve III is smaller when detuned 250 MHz than it is when on line-center. But, for curves I and II, the detuned power is larger, and in the case of curve III, it is much larger. For curve I, the forward anti-Stokes power when detuned by 500 MHz for an input pump power of 7.27 mW is over twice the line-center power.

Figure 3.12 shows the phase mismatch as a function of detuning for the same three input pump power levels. Curve I is for an input pump power of 7.27 mW,

curve II is for 3.63 mW and curve III is for 1.81 mW. Each curve is plotted only for detunings that correspond to Stokes being generated at that input pump power. The small "glitch" in curve I at a detuning of ∼-500 MHz is a result of the numerics. The phase mismatch evolves to different steady-state values depending on both the detuning and the input pump level, except for the case when $\delta = 0$.

Analytic Steady-State Solution

As can be seen of Figure 3.12, the only detuning for which the steady-state value of the phase is constant for all input pump powers is $\delta = 0$. Thus, the only detuning that an analytic steady-state solution can be found that is valid for all input pump powers is when $\delta = 0$. Along with making them independent of the phase mismatch, this condition significantly simplifies equations 3.2– 3.4. The steady-state behavior for all other detunings can only be found by numerically integrating the CWRLE.

The simplified forms of equations 3.2– 3.4 are

$$\dot{A}_p + \frac{\gamma_{cp}}{2} A_p = \frac{\gamma_{in\,p}}{2} A_{in\,p} + \frac{\omega_p}{\omega_s} G\, A_p A_a^2 \frac{V_{pa} V_s}{V_p V_{ps\,o}} - \frac{\omega_p}{\omega_s} G\, A_p A_s^2 \frac{V_{ps} V_s}{V_p V_{ps\,o}} \tag{3.25}$$

$$\dot{A}_s + \frac{\gamma_{cs}}{2} A_s = G\, A_p^2 A_s \frac{V_{ps}}{V_{ps\,o}} + G\, A_p^2 A_a \frac{V_{FWM}^R}{V_{ps\,o}} \tag{3.26}$$

$$\dot{A}_a + \frac{\gamma_{ca}}{2} A_a = -\frac{\omega_a}{\omega_s} G\, A_p^2 A_a \frac{V_{pa} V_s}{V_a V_{ps\,o}} - \frac{\omega_a}{\omega_s} G\, A_p^2 A_s \frac{V_s V_{FWM}^R}{V_a V_{ps\,o}}. \tag{3.27}$$

These equations now look very similar to the equations derived by Roos using the quantum theory [41]. There are some changes in notation: for example, in his paper, Roos uses κ_p for the cavity loss coefficient as opposed to $\frac{\gamma_{cp}}{2}$ used here. Just as the gain coefficients in reference [41] depended on the overlap volumes, here they do, too, but they have been separated out from the Raman gain, G, and written explicitly as factors multiplying the various terms.

To find the steady-state solutions, set the time derivatives to zero. A ratio of the steady-state anti-Stokes power to the steady-state Stokes power can be found by dividing 3.26 by 3.27. After a bit of algebra, this yields

$$\frac{A_{a\,ss}^2}{A_{s\,ss}^2} + \frac{A_{a\,ss}}{A_{s\,ss}} \frac{(\zeta V_{pa} + V_{ps})}{V_{FWM}^R} + \zeta \;=\; 0 \tag{3.28}$$

where

$$\zeta \;=\; \frac{\omega_a V_s \gamma_{cs}}{\omega_s V_a \gamma_{ca}}. \tag{3.29}$$

The solutions of equation 3.28 are

$$\frac{A_{a\,ss}}{A_{s\,ss}} \;=\; \frac{-(\zeta V_{pa} + V_{ps})}{2V_{FWM}^R} \pm \frac{1}{2}\sqrt{\frac{(\zeta V_{pa} + V_{ps})^2}{V_{FWM}^{R\,2}} - 4\zeta}. \tag{3.30}$$

Physically, the ratio of the anti-Stokes field magnitude to the Stokes field magnitude must be less than one because the amount of anti-Stokes generated cannot exceed the amount of Stokes generated. However, as shown in Appendix K, the root that results in a physical value depends on the pressure at which the calculation is being made because V_{FWM}^R is not always a positive number (as shown in Figure H.1). When V_{FWM}^R is positive (negative), then the positive (negative) root is physical. Define the constant of proportionality between the anti-Stokes and Stokes field magnitudes as β, with the sign in front of the square root chosen based on the value of V_{FWM}^R.

$$\beta \;\equiv\; \frac{-(\zeta V_{pa} + V_{ps})}{2V_{FWM}^R} \pm \frac{1}{2}\sqrt{\frac{(\zeta V_{pa} + V_{ps})^2}{V_{FWM}^{R\,2}} - 4\zeta}. \tag{3.31}$$

Thus,

$$A_{a\,ss} \;=\; \beta A_{s\,ss}. \tag{3.32}$$

Equation 3.32 can be plugged back into equations 3.25 and 3.26 yielding (in steady-state)

$$\begin{aligned}\frac{\gamma_{cp}}{2}A_{p\,ss} &= \frac{\gamma_{in\,p}}{2}A_{in\,p} + \frac{\omega_p}{\omega_s}G\,A_{p\,ss}\,(\beta A_{s\,ss})^2\,\frac{V_{pa}V_s}{V_pV_{ps\,o}} \\ &\quad -\frac{\omega_p}{\omega_s}G\,A_{p\,ss}A_{s\,ss}^2\frac{V_{ps}V_s}{V_pV_{ps\,o}} \qquad (3.33)\\ \frac{\gamma_{cs}}{2}A_{s\,ss} &= G\,A_{p\,ss}^2A_{s\,ss}\frac{V_{ps}}{V_{ps\,o}} + G\,A_{p\,ss}^2\beta A_{s\,ss}\frac{V_{FWM}^R}{V_{ps\,o}}. \qquad (3.34)\end{aligned}$$

These two equations are now functions of only the steady-state pump and Stokes field magnitudes and can be solved for them. Equation 3.34 can be solved for the above threshold steady-state pump field amplitude, yielding

$$A_{p\,ss} = \sqrt{\frac{V_{ps\,o}\gamma_{cs}}{2G(V_{ps}+\beta V_{FWM}^R)}} \qquad (3.35)$$

As expected from the previous numeric simulations (Figure 3.4), above threshold, the steady-state pump is constant. Now, equation **??** can be solved for the steady-state Stokes magnitude. After a bit of algebra,

$$A_{s\,ss} = \sqrt{\frac{\omega_s}{\omega_p}\frac{V_pV_{ps\,o}}{V_s}\frac{\gamma_{cp}}{2G(V_{ps}+\beta^2V_{pa})}\left(\frac{\gamma_{in\,p}}{\gamma_{cp}}\frac{A_{in\,p}}{A_{p\,ss}}-1\right)}. \qquad (3.36)$$

As expected from Figure 3.4, the steady-state Stokes amplitude depends on the square root of the input pump field amplitude. And, since the anti-Stokes is proportional to the Stokes (equation 3.32), the square-root dependence of the anti-Stokes is also explained.

The threshold value is found by setting $A_{s\,ss}=0$. It is

$$A_{in\,p}^{th} = \frac{\gamma_{cp}}{\gamma_{in\,p}}A_{p\,ss}. \qquad (3.37)$$

The steady-state Stokes field amplitude can be written in terms of the threshold field amplitude. It is:

$$A_{s\,ss} = \sqrt{\frac{\omega_s}{\omega_p}\frac{V_pV_{ps\,o}}{V_s}\frac{\gamma_{cp}}{2G(V_{ps}+\beta^2V_{pa})}\left(\frac{A_{in\,p}}{A_{in\,p}^{th}}-1\right)}. \qquad (3.38)$$

Finally, the Stokes and anti-Stokes conversion efficiencies can be calculated. Conversion efficiency, by definition, is the ratio of the output power to the input power.

$$\begin{aligned} \eta_s &\equiv \frac{|A_{s\,ss}|^2}{|A_{in\,p}|^2} \\ &= \frac{\omega_s}{\omega_p}\frac{V_p V_{ps\,o}}{V_s}\frac{\gamma_{cp}}{2G(V_{ps}+\beta^2 V_{pa})}\left(\frac{1}{A_{in\,p}A_{in\,p}^{th}}-\frac{1}{A_{in\,p}^2}\right) \end{aligned} \tag{3.39}$$

where the threshold value from equation 3.37 has been substituted in. And,

$$\begin{aligned} \eta_a &\equiv \frac{|A_{a\,ss}|^2}{|A_{in\,p}|^2} \\ &= \beta^2\eta_s. \end{aligned} \tag{3.40}$$

Since both the Stokes and anti-Stokes conversion efficiencies have the same dependence on the input pump, they will both achieve their maximum conversion efficiencies at the same input pump power. This power is found by taking the derivative of η_s with respect to the input pump field amplitude, setting it equal to zero, and then solving for the input pump field amplitude in terms of the threshold value. This yields

$$A_{in\,p} = 2A_{in\,p}^{th}. \tag{3.41}$$

While the maximum conversion efficiency occurs at a value of two times the threshold value in field amplitude, in power, the maximum conversion efficiency occurs at four times the threshold power, as seen in Figure 3.5.

The results of this steady-state analysis explain the effects that were seen in behavior of the steady-state field amplitudes and conversion efficiencies, such as the growth of the Stokes power being proportional to the square root of the input power and the maximum conversion efficiency occurring at an input pump power of four times the threshold power. To show the validity of this solution, Figure 3.13 plots the results shown in Figure 3.4 for the steady-state values of the forward powers as

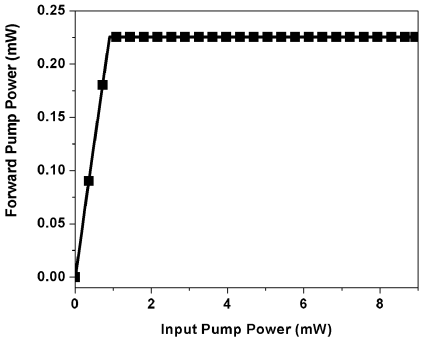

(a) Pump power.

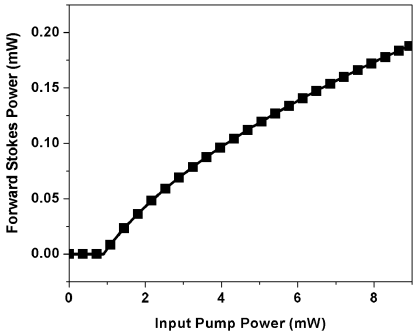

(b) Stokes power.

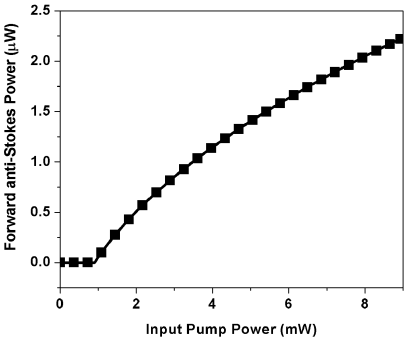

(c) Anti-Stokes power.

Figure 3.13: Forward steady-state powers as a function of input pump power when $\delta = 0$. The lines are the result of numerically integrating equations 3.2 – 3.7 using the parameters given in Table 3.1. The squares are the steady-state solution from equations 3.32, 3.35, and 3.36.

a function of the input pump power when the system is not detuned. The line is the result of numerically integrating equations 3.2 – 3.7 while the squares are the steady-state solutions from equations 3.32, 3.35, and 3.36. As hoped, they overlap perfectly.

Undepleted Pump Limit

In the undepleted pump limit, it is assumed that the anti-Stokes is not strong enough to significantly affect the pump and Stokes levels. In this limit, a different, simpler steady-state solution can be found. This solution is again restricted to line-center because, even in this regime, the phase mismatch, $\Delta\phi$ affects the anti-Stokes tuning even though it doesn't affect the tuning of the pump and Stokes. This solution is found by first dropping all the terms in the pump and Stokes field amplitude equations (3.3 and 3.3) that involve the anti-Stokes field, leaving.

$$\dot{A}_p + \frac{\gamma_{cp}}{2} A_p = \frac{\gamma_{in\,p}}{2} A_{in\,p} - \frac{\omega_p}{\omega_s} G\, A_p A_s^2 \frac{V_{ps} V_s}{V_p V_{ps\,o}} \tag{3.42}$$

$$\dot{A}_s + \frac{\gamma_{cs}}{2} A_s = G\, A_p^2 A_s \frac{V_{ps}}{V_{ps\,o}} \tag{3.43}$$

These are the standard CWRLE for the case of pump to Stokes conversion only [3, 5, 34]. The steady-state solution for the pump amplitude is found by setting the time derivative in equation 3.43 equal to zero and then solving for $A_{p\,ss}$.

$$A_{p\,ss} = \sqrt{\frac{\gamma_{cs} V_{ps\,o}}{2 G V_{ps}}} \tag{3.44}$$

In this limit, the above threshold pump field amplitude (and thus power) is still clamped, as found in previous work with the CW Raman laser [3, 5, 34]. The steady-state value of the Stokes field amplitude is found by setting the $\dot{A}_p = 0$ in equation

3.42 and then solving for $A_{s\,ss}$.

$$A_{s\,ss} = \sqrt{\frac{2V_pV_{ps\,o}\omega_s}{V_{ps}V_s\omega_pG\gamma_{cp}}\left(\frac{\gamma_{in\,p}A_{in\,p}}{\gamma_{cp}A_{p\,ss}}-1\right)}. \tag{3.45}$$

As expected, $A_{s\,ss}$ shows the standard (for the CW Raman laser) square-root dependence of the Stokes field amplitude on the input pump field amplitude. The threshold value for this system is found by setting $A_{s\,ss}$ equal to zero, yielding

$$A^{th}_{in\,p} = \frac{\gamma_{cp}}{\gamma_{in\,p}}A_{p\,ss} \tag{3.46}$$

which looks exactly equivalent to equation 3.37. However, since the form of $A_{p\,ss}$ is different in the complete steady-state solution versus the undepleted pump limit, the threshold will be depend on how much anti-Stokes is being generated. As was found in the complete steady-state theory, the maximum conversion efficiency for Stokes generation in this limit will occur at four times the threshold pump power.

The steady-state value of the anti-Stokes is found by dropping the term in equation 3.4 that is responsible for loss by back conversion to the pump field. This leaves

$$\dot{A}_a + \frac{\gamma_{ca}}{2}A_a = -\frac{\omega_a}{\omega_s}G\,A_p^2A_s\frac{V_sV^R_{FWM}}{V_aV_{ps\,o}}. \tag{3.47}$$

Solving this equation for the steady-state case yields

$$A_{a\,ss} = -\frac{2}{\gamma_{ca}}\frac{\omega_a}{\omega_s}G\,A^2_{p\,ss}A_{s\,ss}\frac{V_sV^R_{FWM}}{V_aV_{ps\,o}} \tag{3.48}$$

In equation 3.48, the only quantity dependent on the input pump level is $A_{s\,ss}$. Therefore, the anti-Stokes will exhibit the same square root dependence on input pump field magnitude as the Stokes and the maximum anti-Stokes conversion efficiency will occur at an input pump equal to four times the threshold value.

The validity of the undepleted pump approximation will depend on the size of γ_{ca}, which in turn, depends on the reflectivities at the anti-Stokes wavelength, as given by

R_a	$\frac{P_{th}}{P_{th\,approx}}$	$\frac{P_{p\,ss}}{P_{p\,ss\,approx}}$	$\frac{P_{s\,ss}}{P_{s\,ss\,approx}}$	$\frac{P_{a\,ss}}{P_{a\,ss\,approx}}$
0.999	1.003	1.003	0.996	0.515
0.99	1.004	1.004	0.999	0.926
0.9	1.000	1.000	0.999	0.993
0.8	1.000	1.000	0.999	0.996
0.7	1.000	1.000	0.999	0.998
0.6	1.000	1.000	0.999	0.998
0.5	1.000	1.000	0.999	0.999

Table 3.3: Ratios of the threshold and forward steady-state powers calculated using the full theory to the corresponding quantities calculated in the undepleted-pump limit, as functions of the anti-Stokes reflectivity.

equation 2.11. Table 3.3 gives the steady-state pump, Stokes and anti-Stokes powers for both the full steady-state solution and the approximate solution for an input pump power of 3.63 mW, assuming that all three fields have a TEM_{00} mode profile. If not otherwise stated, all the other parameters are as given in Table 3.1. The cavity is assumed to be matched, therefore, $R_a = R_{1a} = R_{2a}$. As can be seen, even at high anti-Stokes reflectivities for this cavity, the thresholds, clamped power, and Stokes powers agree fairly well in both the steady-state calculations. This would not be the case if the anti-Stokes conversion efficiency were higher. Even so, the anti-Stokes power calculated in the undepleted pump limit, thus $P_{a\,ss}/P_{a\,ss\,approx}$ is significantly less than 1 as in the upper right corner of Table 3.3, is much larger for higher reflectivities than it is in the full steady-state treatment because back-conversion into the pump has been ignored. This is also why the pump clamp level and the threshold are slightly low in the undepleted pump approximation. For anti-Stokes reflectivities less than or equal to 70%, the two theories agree quite well.

The Higher-Order Modes

So far, the discussion has been confined to the case where the pump, Stokes, and anti-Stokes all have a TEM_{00} mode profile. However, since the optical cavity is neither flat/flat nor confocal, ($R_c = 50$ cm and $L = 7.62$ cm), the cavity resonance frequencies for the HOM's are different than for the fundamental mode because of the Gouy phase shift, as outlined in the next chapter. As such, it is possible for any of the three fields to be on a higher-order mode (HOM).

For the pump, this requires that the cavity be frequency locked to the HOM. In general, the system is mode-matched such that the majority of the input pump light is coupled into the fundamental cavity mode. But, this does not need to be the case. If the mode-matching is such that, for a given input pump power, there is sufficient light coupled into a HOM that the lasing threshold can be exceeded, then that mode will lase.

The Stokes will lase on whatever cavity mode, fundamental or HOM, has the most gain. In general, this will be the fundamental mode since the overlap integral, V_{ps}, is largest for the fundamental mode, as shown in Appendix G. But, if the fundamental mode is further away from Raman gain line-center than a given HOM, then it is possible for the HOM to have more gain and, therefore, be the lasing mode.

The anti-Stokes growth will occur on any allowable cavity spatial mode that is resonant in the cavity. There are two things which determine if a given anti-Stokes mode will be allowed. The first is the overlap integral, V_{FWM}, as discussed in Appendix H and briefly outlined in the main body of Chapter 2 on page 47. The other is the cavity resonances, which will be discussed in the next chapter. For the moment, the assumption is going to be made that the anti-Stokes is resonant within the cavity.

Looking at equations 3.32, 3.35, 3.36, and 3.37, some of the effects of not being on fundamental modes can be seen. Basic trends like the square root dependence of the Stokes (and therefore anti-Stokes) on the input pump power and clamping of the pump power above threshold will remain. However, the pump clamp level will increase because both V_{ps} and V_{FWM} are smaller for HOM combinations than for the fundamental mode combination, as seen in Appendices G and H, respectively. Corresponding to this increase in pump clamp level will be an increase in threshold. The steady-state Stokes value is going to be a trade-off between V_{ps} being smaller and the pump clamp level being larger and is not easily determined by just looking at the equations. It is also unclear whether the value of β from equation 3.30 will increase or decrease and therefore it is impossible to determine if more or less anti-Stokes will be produced by simply looking at the equations.

Table 3.4 shows the steady-state forward powers in the three fields and the threshold value as a function of input pump power and cavity mode combination. For this analysis, it is assumed that all three modes are HG modes with rectangular symmetry. The reflectivities and transmittivities are as given in Table 3.1, along with medium dependent parameters like γ_{13}. The pressure is assumed to be 10 atm, the temperature 293 K and the cavity length approximately 7.62 cm. Given these parameters, pump frequencies and longitudinal mode indexes were chosen for each mode combination such that $\delta = 0$ for that combination.

Table 3.4 shows that for the HOM combinations given, the amount of Stokes and anti-Stokes produced can either be higher or lower than for the fundamental mode combination.

Pump Mode	Stokes Mode	anti-Stokes Mode	P_{th} (mW)	P_{inp} (mW)	P_{pss} (mW)	P_{sss} (mW)	P_{ass} (μW)
TEM_{00}	TEM_{00}	TEM_{00}	0.90	5	0.23	0.12	1.43
				10	0.23	0.20	2.45
TEM_{10}	TEM_{10}	TEM_{10}	1.22	5	0.31	0.12	1.43
				10	0.31	0.22	2.60
TEM_{10}	TEM_{00}	TEM_{00}	1.60	5	0.40	0.12	0.91
				10	0.40	0.23	1.78
TEM_{00}	TEM_{10}	TEM_{10}	2.06	5	0.51	0.11	1.03
				10	0.51	0.24	2.23
TEM_{00}	TEM_{20}	TEM_{20}	2.57	5	0.64	0.10	0.19
				10	0.64	0.24	0.47

Table 3.4: Threshold value and forward power levels as a function of both input pump power and cavity mode combinations. All modes are assumed to be HG.

Concluding Thoughts

This chapter began where the previous chapter left off by taking the CWRLEs and developing them further. It began by separating the CWRLEs into separate equations for the amplitude and phase development and proceeded by looking at the phase development.

Through numerical integration, the behavior of the pump, Stokes and anti-Stokes emitted from the Raman cavity was investigated. When the input pump power is increased, keeping the detuning constant, the pump increases until the threshold value is reached, after which it clamps. Above threshold, the Stokes and anti-Stokes grow proportional to the square root of the input pump power.

As a function of detuning, for a constant input pump power, the pump power increases to either side of gain line-center. The behavior of the Stokes and anti-Stokes as a function of detuning depends on the input pump level.

While the individual phases did not always reach a constant steady-state value,

the phase mismatch did. However, when detuned, the steady-state value of the phase mismatch was found to depend on the input pump level. Therefore, an analytic steady-state solution valid for all input pump powers could only be found when $\delta = 0$. This analytic solution showed all the same behaviors that were found by numerically integrating the CWRLEs to steady-state.

An additional steady-state solution was found that is valid only when the reflectivity of the mirrors forming the Raman cavity at the anti-Stokes wavelength is less than $\sim$0.7 and $\delta = 0$.

The chapter concluded with a quick discussion of how the output would change depending on the spatial modes of the pump, Stokes, and anti-Stokes. It was found that the threshold power and the pump clamp level increased. The Stokes and anti-Stokes output powers depended on which mode combination was being investigated.

In Chapters 5 and 6, these results will be used for comparison with experimental data. The next chapter, 4, is devoted to understanding some of the experimental hurdles associated with anti-Stokes generation in the CW Raman cavity and how to overcome them.

EXPERIMENTAL CHALLENGES

This chapter discusses some of the experimental challenges facing anti-Stokes generation in a CW Raman laser, all of which depend in some way on the H_2 pressure within the cavity. It begins with a discussion of dispersion, the problems it causes, and ways to compensate for it. The third section discusses phase-matching in the CW Raman laser. The fourth section looks at the pressure dependence of the Raman linewidth and its repercussions. Finally, the chapter concludes by outlining the experiments performed, along with a discussion of why they were chosen.

Dispersion Effects on Cavity Resonances

As found in Appendix L (equation L.4), the steady-state power transmitted through an optical cavity is given by

$$\mathcal{P}_f = \frac{T^2 \mathcal{P}_{in}}{1 + R^2 - 2R\cos(2kx)} \tag{4.1}$$

where the subscript, f, indicates the forward direction, $\mathcal{P}_{in}$ is the input power at an arbitrary wavelength, R (T) is the power reflectivity (transmittivity), k is the wavenumber, and x is an arbitrary cavity length. $\mathcal{P}_f$, known as an Airy function, is a function of many variables, the most obvious of which are reflectivity (transmittivity) of each (identical) mirror, cavity length, and wavenumber. Less obvious is its dependence on pressure because this dependence is buried inside the index of refraction which is in turn hidden within k. Since, by definition, $k \equiv {}^{2\pi n}/_{\lambda}$ (where λ is the wavelength of the light in vacuum and n is the index of refraction), it can be seen that $\mathcal{P}_f$ will reach a maximum value whenever

$$x = \frac{q\lambda}{2n} \tag{4.2}$$

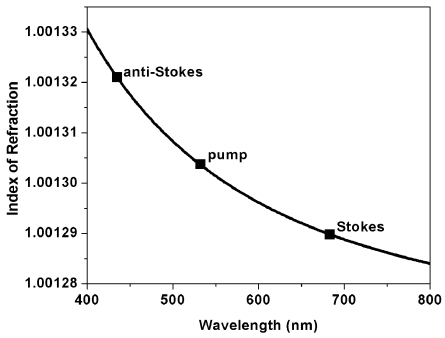

Figure 4.1: Variation of the index of refraction with wavelength. The pump, Stokes, and anti-Stokes wavelengths are marked.

where q is a positive integer. These values of x determine which cavity lengths will resonate a given wavelength of light. The change in cavity length needed to move from one resonance to the next (q to $q+1$) is

$$\Delta x = \frac{\lambda}{2n}. \tag{4.3}$$

When the index is constant, then the change in cavity length needed to move from one resonance to the next is always the same. However, with the exception of in a vacuum, the index of refraction is not constant. Therefore, the amount the cavity length needs to change to move from one resonance to another is different at the pump, Stokes, and anti-Stokes wavelengths.

Figure 4.1 shows the index of refraction of H_2 as a function of wavelength at 293 K and 10 atm. This plot was made by fitting a polynomial fit to the index of refraction data in the AIP handbook [55]. (The resulting formula is in Appendix H.) Labeled specifically in Figure 4.1 are the wavelengths for the pump (532 nm), Stokes (683 nm), and anti-Stokes (435 nm) pertinent to the experiments presented in this dissertation. As can be seen, the index at the anti-Stokes wavelength is higher than at the pump and Stokes wavelengths. Table 4.1 shows both the index of refraction and how much the cavity length has to change at the pump, Stokes and anti-Stokes wavelengths

λ (nm)	n-1	$\triangle x$ (nm)
435	0.001321	217.2
532	0.001303	265.7
683	0.001289	341.1

Table 4.1: Index of refraction and change in cavity length needed to move between successive resonances at the pump, Stokes, and anti-Stokes wavelengths.

to move between successive resonances. Even though the index of refraction change between the Stokes and anti-Stokes may not seem large, this effect is significant when trying to simultaneously resonate all three wavelengths within the cavity.

Another way to look at this situation is by considering the cavity resonant frequencies for a fixed cavity length. Ignoring the Gouy phase shift for the moment (it will be considered later), these are given by

$$f_c = \frac{qc}{2nL} \tag{4.4}$$

where c is the speed of light in vacuum, and L is the cavity length. As with the change in cavity length, the change in frequency between successive resonances will be smaller for the anti-Stokes than for the pump or the Stokes. Figure 4.2 shows a schematic drawing of the implications of the resonance frequencies being unequally spaced. Even though in reality, the cavity resonances have some width (in frequency), for the purpose here, the resonances in Figure 4.2 are represented by lines at the center of each resonance. In Figure 4.2, f_p is the pump frequency, f_s is the Stokes frequency, f_a is the anti-Stokes frequency, f_R is the Raman shift, and δ is the detuning of the Stokes frequency from gain line-center. In Figure 4.2a, the index has been assumed to be independent of frequency, and so, in this case, the cavity resonances are all equally spaced. The pump is assumed to be locked on the indicated mode. The Stokes is lasing on a mode underneath the Raman gain profile. Since the anti-Stokes optical frequency is determined by $f_a = 2f_p - f_s = f_R + \delta$ and the index effects have

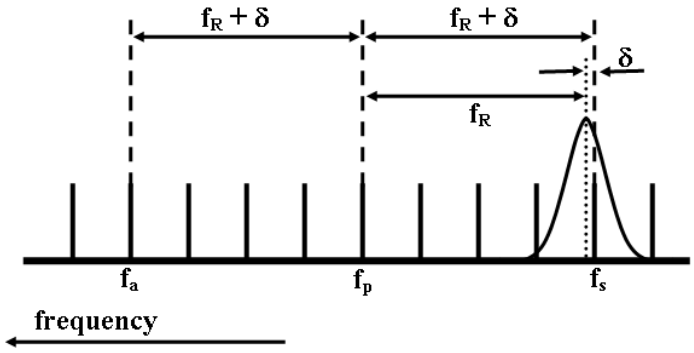

(a) Without dispersion.

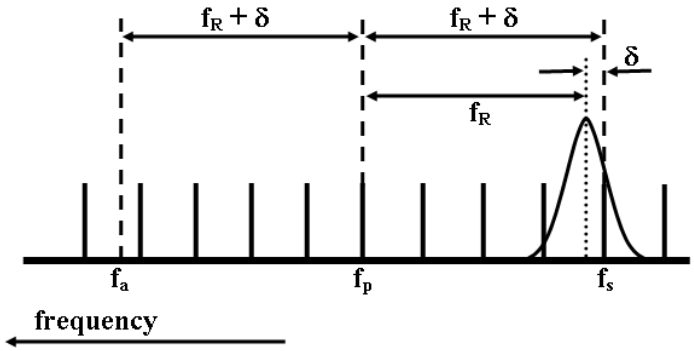

(b) With Dispersion

Figure 4.2: Schematic drawings of the effects of dispersion on cavity resonance frequencies.

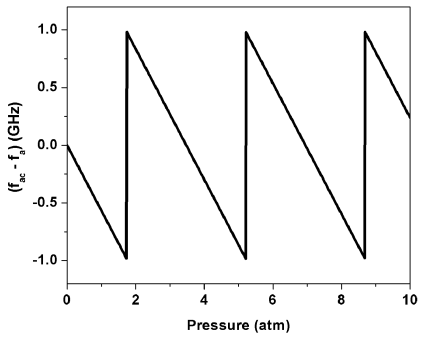

Figure 4.3: Difference between the anti-Stokes optical frequency and nearest cavity resonance as a function of pressure.

been ignored, the anti-Stokes grows on a mode that is the same distance in frequency from the pump mode as the Stokes. On the other hand, Figure 4.2b shows the same situation but with the effect of the index of refraction included. In this case, the pump is still locked to the indicated mode. The Stokes grows on the mode with the most gain. Since the anti-Stokes optical frequency is still determined in the same manner, but the cavity modes are no longer evenly spaced, the anti-Stokes optical frequency does not fall on the center of a cavity resonance. Since there is no gain for the anti-Stokes transition, the anti-Stokes will not be able to resonate on the nearest cavity mode as the Stokes does. Depending on the width of the resonance, the anti-Stokes either will not resonate or will not resonate as efficiently.

Figure 4.3 shows the frequency difference between the anti-Stokes optical frequency and the nearest cavity resonance as a function of pressure. In making Figure 4.3, the pump wavelength was assumed to be constant at 532 nm, the indices of refraction were calculated using equation 2.144 from Appendix H with the temperature fixed at 298 K, the cavity length was assumed to be near 7.62 cm, and the Stokes frequency was restricted to the cavity mode nearest to the line-center frequency. In these calculations, equation 4.4 was used repeatedly. The frequency

difference is zero at a pressure of 0 atm because the index of refraction is constant at that pressure. The difference then decreases to a minimum value of about -1 GHz before the anti-Stokes mode-hops to the next cavity resonance. At the mode-hop, the difference goes from about - 1 GHz to + 1 GHz. After the hop, the difference begins to decrease again until it again reaches -1GHz where upon it hops again and the process repeats.

The frequency difference between successive resonances is known as the free spectral range (FSR). It is calculated by

$$\text{FSR} = \frac{c}{2nL} \tag{4.5}$$

For a cavity that is 7.62 cm long, the FSR is 2 GHz. Thus, the anti-Stokes frequency can miss the cavity resonance frequency by, at most, ½ the FSR.

Ideally, the system is run at a pressure where the frequency difference is zero. However, in reality, things are not as simple as discussed above, and extra effort has to be used to achieve the desired result.

Forcing Resonance

The discrepancy between the cavity resonance frequency and anti-Stokes optical frequency is a problem – in fact, it is the main experimental hurdle for generating anti-Stokes with the CW Raman laser. Luckily, there are some ways to overcome it.

Broad Cavity Resonances

The easiest way to achieve resonance for the anti-Stokes is decrease the reflectivity at the anti-Stokes wavelength, causing the cavity resonances to become broader. Plotted in Figure 4.4 is the transmitted power relative to maximum, (from equation

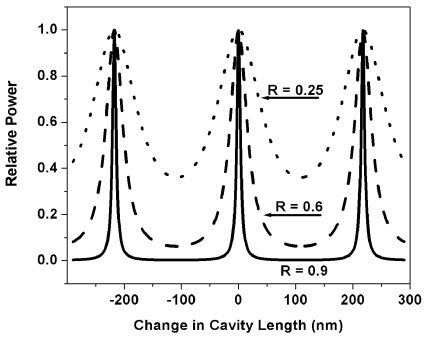

Figure 4.4: Graph of the relative power transmitted by an optical cavity as a function of the change in cavity length for $R = 0.9$, 0.6, and 0.25, assuming $A = 100 * 10^{-6}$.

L.9 or M.17), as a function of cavity length at the anti-Stokes wavelength for three different reflectivities, $R = 0.9$, 0.6, and 0.25 and $A = 100 * 10^{-6}$. As the reflectivity is decreased, the resonances become wider and the dips between the resonances become shallower. If the resonance is broad enough, then even if the anti-Stokes optical frequency misses the center frequency of the cavity resonance, it will still resonate, though with decreased efficiency compared to if it were at the center of the cavity resonance.

Since the CWRLE's of the previous chapters assume that the anti-Stokes is on the center of a cavity resonance, this decreased efficiency needs to be included. It seems to be sufficient to place the result of the CWRLE (either integrated or in steady-state) into equation 4.1 in place of $\mathcal{P}_{in}$, even though there is no external input field for the anti-Stokes. It should be noted that a fair bit of concern was placed on understanding anti-Stokes resonances since, unlike the pump which has an input field and the Stokes which requires a seed from the vacuum field, the anti-Stokes does not require any field external to the cavity in order to grow. Thus, the analysis done in Appendix L, does not, at least on the surface, seem to apply to anti-Stokes generation and therefore the use of the result is questionable. Appendix M goes through a similar calculation

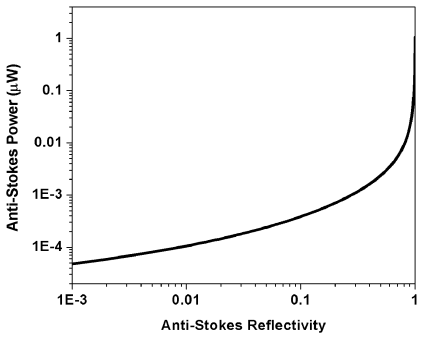

Figure 4.5: Graph of the anti-Stokes power as a function of the reflectivity.

to Appendix L for a source *within* a cavity. There are still questions associated with that analysis, as outlined in Appendix M, but, it seems to be sufficient to allow the use of the result from Appendix L since the relative power calculated in Appendix M shows the same variation from maximum to minimum.

On the other hand, the amount of anti-Stokes produced increases as the reflectivity is increased as shown in Figure 4.5. This graph in Figure 4.5 was made using the parameters in Table 3.1 and the full steady-state solution presented in Chapter 3 on page 85, assuming the anti-Stokes is on the center of a cavity resonance. At a reflectivity of about 0.9, the amount of anti-Stokes produced increases dramatically. Therefore, a higher reflectivity is desirable for increased anti-Stokes generation.

Higher-Order Modes

This is also an extremely easy method for achieving anti-Stokes resonance, especially for lower reflective cavities. To see the advantage of HOM combinations the Gouy phase shift, which has so far been ignored, needs to be included. As discussed in Siegman [47] on pages 683 - 686, the Gouy phase shift (or as Siegman calls it, the "Gouy effect") is an extra phase shift obtained by a field as it passes through a focus. Because of their more complex transverse structure, HOM's will obtain a larger shift

when passing through the focus than a fundamental mode. Because of this, the cavity resonance frequency is dependent on the spatial mode indices of the field. Specifically, for the rectangularly symmetric Hermite-Gaussian modes, as shown on page 336 of reference [46], it is

$$f_c = \frac{qc}{2nL} + (l+m+1)\frac{c}{\pi nL}\tan^{-1}\left(\frac{L}{2z_o}\right) \tag{4.6}$$

where q is the longitudinal mode index, l and m are the spatial mode indices, c is the speed of light, L is the cavity length, z_o is the cavity's Rayleigh range, and n is the index of refraction. As can be seen from equation 4.6, modes for which the quantity $(l+m+1)$ is equal will resonate at the same frequency, i.e. the TEM_{20}, TEM_{02}, and TEM_{11} modes will all resonate at the same frequency. For $L = 7.62$ cm, $R_c = 50$ cm (coinciding with the experimental parameters used in this dissertation) and $\lambda = 435$ nm, then the cavity resonance frequency changes by ~ 350 MHz when the quantity $(l+m+1)$ is increased by one. However, as discussed in Appendix H, only certain anti-Stokes modes will, in theory, be allowed to grow.

Figure 4.6 shows a plot of the power transmitted by a cavity relative to maximum, $\mathcal{P}_{rel}$ (from equationM.17), at the anti-Stokes wavelength as a function of cavity length for several HOM's when the reflectivity at the anti-Stokes wavelength is $R = 0.9$ (solid lines) and 0.25 (dashed lines). In this discussion, all modes are assumed to be the rectangular symmetric HG modes. Figure 4.6a shows only HOM anti-Stokes resonances allowed when the Stokes mode is assumed to be TEM_{00}. The curve labeled A gives the transmission of anti-Stokes modes whose mode indices add to zero, i.e. $(l+m) = 0$. The only mode for which this is possible is if the anti-Stokes is also TEM_{00}. The curve labeled B gives the transmission of anti-Stokes modes where $(l+m) = 2$. In this case, there are three possibilities that meet this condition, TEM_{20}, TEM_{02}, and TEM_{11}. However, even though the TEM_{11} mode resonates at

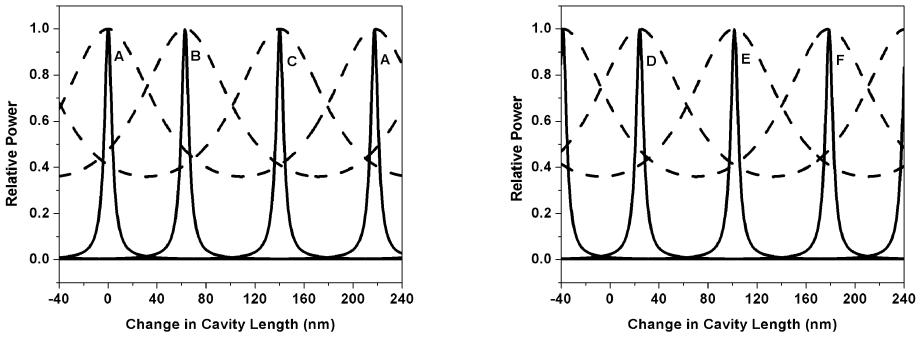

(a) (b)

Figure 4.6: Graph of the power relative to maximum transmitted by an optical cavity as a function of the change in cavity length for $R = 0.9$ (solid lines) and 0.25 (dashed lines), assuming $A = 100 * 10^{-6}$. In subplot a, the Stokes is assumed to be TEM_{00} and the peak labeled a is for anti-Stokes modes whose indices, l and m, add to zero, b is for $(l + m) = 2$, and c is for $(l + m) = 4$. In subplot b, the Stokes is assumed to be TEM_{10} and the peak labeled d is for anti-Stokes modes whose indices add to 1, e is for $(l + m) = 3$, and f is for $(l + m) = 5$.

that cavity length, it is not allowed because the overlap integral V_{FWM} is zero for the mode combination of TEM_{00} Stokes and TEM_{11} anti-Stokes, as outlined in Appendix H. The curve labeled C is for resonances where $(l + m) = 4$. There are three possible anti-Stokes modes that can resonate at this cavity length for which V_{FWM} is non-zero. They are TEM_{40}, TEM_{22}, and TEM_{04}. When there are multiple allowed resonances, in theory, the mode with the largest overlap integral, V_{FWM}, should dominate.

Figure 4.6b shows the resonances of allowed anti-Stokes HOM's assuming that the Stokes mode is TEM_{10}. From Appendix H, modes that will have a non-zero V_{FWM} given this Stokes mode are only those that have their first index, l, odd and the second, m, even. The curve labeled D gives the transmission of anti-Stokes modes for which $(l + m) = 1$, the TEM_{10} mode is the only allowed possibility. The curve labeled E gives the transmission of modes where $(l + m) = 3$. The allowed resonances in this case are TEM_{30} and TEM_{12}. And the curve labeled F gives the transmission

of anti-Stokes modes for which the $(l + m) = 5$, or the TEM_{14}, TEM_{32} and TEM_{50}.

When the reflectivity is high, as seen in both Figure 4.4 and Figure 4.6, the resonances are deep and narrow. In this case, only the modes that are allowed (as outlined in the previous two paragraphs) at a particular cavity length will be able to resonate since the transmitted power is zero when not near a resonance. However, as shown by the dashed lines in Figure 4.6, when the reflectivity is low, it is possible for all the allowed modes to be (at least partially) resonant within the cavity. Experimentally, this sometimes leads to the anti-Stokes mode profiles being unrecognizable as a given well-defined mode because it is a superposition of two or more modes.

Chirped Mirrors

Chirped mirrors are a relatively new technology that are designed to reflect different wavelengths at different points within the coating layers [56, 57, 58]. Often times, these are used to counter other dispersion effects in pulsed femtosecond laser systems, thus maintaining the temporal pulse shape [59, 60, 61]. However, they can also be utilized in this system to partially compensate the H_2 dispersion, as shown in reference [42].

Since all the mirrors purchased for the CW Raman system in the Carlsten group have been designed for the vibrational transition in H_2, it was necessary to apply two distinct sets of coating layers for the pump and Stokes since the wavelengths are too disparate to be covered by a single coating layer. Thus, these mirrors are inherently chirped for the pump to Stokes transition, in that one wavelength had to traverse the coating stack for the other wavelength before being reflected. This chirp, while present, was not a necessary component to the original, pump→Stokes only, CW Raman laser since the Stokes mode grows on the cavity mode with the most gain.

Mirrors designed to be highly reflective at all three wavelengths associated with the vibrational transition require three distinct sets of coating layers. This makes these mirrors harder to coat if it is desired to also design them with a specified chirp.

Dispersion Compensating Gas

The CW Raman system in reference [42] was defined for the rotational transition. Since the rotational Raman shift is smaller than the vibrational (586.9 cm^{-1} as opposed to 4155 cm^{-1}), in theory, the mirrors used in that system could have been coated in a single coating layer for all three wavelengths. Even so, the chirped mirrors they obtained had too much chirp given the dispersion of the hydrogen. Thus, xenon was used to add additional dispersion to the gas within the Raman cell in order to bring the anti-Stokes into resonance.

Another possibility is to find a gas whose index has the opposite slope when compared with the active medium at the desired wavelength. For example, at 435 nm, the index of H_2 is negatively sloped (Figure 4.1), therefore, the compensating gas would have to be positively sloped. Such a gas is going to be difficult to find because most gases have electronic resonances further into the UV than 435 nm. Therefore, at 435 nm, most gases are going to be negatively sloped like H_2.

This method was not employed in the work of this dissertation.

Phase-matching

Phase-matching is used to describe the phasing between the field-induced oscillations of the dipoles at a given frequency and fields at the same frequency. Under ideal circumstances, the dipole oscillation is such that the fields radiated from them constructively add to the fields already present in the cavity. However, it is also

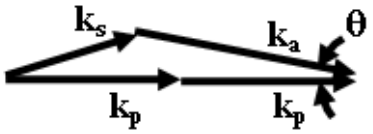

Figure 4.7: Typical arrangement of the wave vectors for anti-Stokes phase-matching.

possible that the fields radiated by the dipoles destructively interfere, diminishing the fields within the cavity.

Phase-matching is only necessary in parametric optical systems, such as second-harmonic generation and FWM. Thus, in Raman systems, only anti-Stokes generation is dependent on phase-matching. Perfect phase-matching occurs when [45]

$$\triangle \overrightarrow{k} \bullet \hat{z} \;\; = \;\; 0 \tag{4.7}$$

where, for the case of anti-Stokes generation, $\triangle \overrightarrow{k} = 2\overrightarrow{k_p} - \overrightarrow{k_s} - \overrightarrow{k_a}$ and $\overrightarrow{k_p}$, $\overrightarrow{k_s}$, and $\overrightarrow{k_a}$ are the pump, Stokes and anti-Stokes wave vectors, respectively. (The magnitude of the wave vectors are $k_q = {}^{2\pi n_q}/_{\lambda_q}$.) Because of the index of refraction, in general, the only way for this condition to be met is if the Stokes and anti-Stokes wave vectors are off-axis as shown in Figure 4.7. In Figure 4.7, θ is known as the cone angle. Because the anti-Stokes wave vector is off-axis, typically, emitted anti-Stokes is in the shape of a ring at the cone angle. Using the law of cosines, the cone angle is found to be

$$\theta_{cone} \;\; = \;\; \arccos\left[\frac{k_s^2 - k_a^2 - 4k_p^2}{-4k_p k_s}\right]. \tag{4.8}$$

Figure 4.8 shows the anti-Stokes cone angle as a function of pressure. As pressure increases, the cone angle increases.

The CW Raman laser system is different from most traditional Raman systems because the FWM is done intracavity. Thus, instead of simply traveling down the medium, the anti-Stokes traverses the same path through the medium multiple times

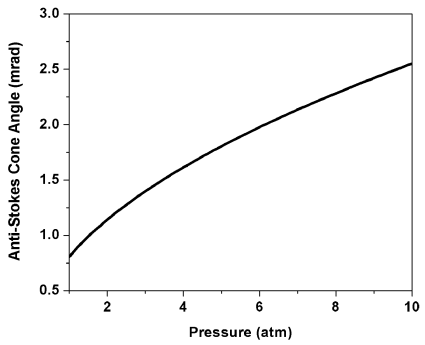

Figure 4.8: Anti-Stokes cone angle as a function of pressure.

(determined by the anti-Stokes reflectivity). And, at either mirror, the anti-Stokes is reflected back upon itself. Therefore, the anti-Stokes field can only get so far out of phase with respect to the dipole oscillations generated by the pump and Stokes fields before it is reflected. This allows for a net transfer of power to the electric field of the anti-Stokes cavity mode. Thus, anti-Stokes mode profiles from the CW Raman laser system are cavity modes and not rings.

Quasi-phase-matching was first considered by Armstrong and Bloembergen [62] in 1962, though not by that name. In their paper, they proposed three methods of quasi-phase-matching harmonic generation. The first method involves flipping the sign of the nonlinearity of a medium every coherence length. Generally, this required a stack of crystals, alternating the nonlinearity's sign every other layer. (Further discussion of this method can be found in references [63, 64, 65].) Some of the first experiments demonstrating this method of phase-matching used ferroelectric crystal domains [66], crystal lattice properties [67] and rotational twins [68, 69]. It was extended to quasi-phase-matching anti-Stokes generation in 2002 by Bespalov and Makarov [70]. The second method (from reference [62]) uses total internal reflection within the crystal to correct the phase. This method was first used in 1966 by Boyd and Patel [71] to phase-match second-harmonic generation. It was again used in 1997

[72]. These first two methods are really only applicable to systems involving crystals or crystalline structures. In the last method (from reference [62]), a traveling wave at the fundamental frequency passes through a cavity containing a dielectric material resonant for the second harmonic. After the harmonic has reflected again off the first surface of the cavity, it is back in-phase with both itself and the fundamental traveling wave. The first experimental use of this method was in 1966 by Ashkin, Boyd and Dziedzic [73]. This method could be extended to third harmonic, anti-Stokes generation and other FWM processes in a gas. Since 1962, other methods have been developed for quasi-phase-matching such as photonic band gap structures [74] and periodic poling [75].

No matter what technique is being used to accomplish the quasi-phase-matching, the goal is to somehow bring the field needing to be phase-matched, whether it is a harmonic of the fundamental or a field generated through FWM, back into phase with the generating field or fields. This is exactly the effect that the anti-Stokes generated in the CW Raman laser experiences by being reflected by the Raman mirrors. This is most easily put in words by considering the phase-mismatch between the dipole oscillations and one of the two traveling waves composing the anti-Stokes standing wave. The mismatch is zero at the center of the cavity. As the traveling wave propagates away from the center of the cavity, the phase-mismatch grows. (As discussed below, it is possible that the phase-mismatch is 180^o.) After reflection by a mirror, the phase-mismatch shrinks until it is again zero when the wave has returned to the center of the cavity. After passing through the center, the mismatch begins to grow again and the entire process repeats. Therefore, anti-Stokes generation in a CW Raman laser is considered to be an example of quasi-phase-matching.

Even in quasi-phase-matching, the value of Δk still influences this system. It comes into play in the overlap integral V_{FWM}. Because of the complexity of the

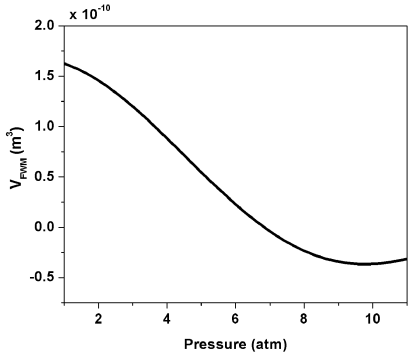

Figure 4.9: V_{FWM} as a function of pressure, as calculated by the collimated beam approximation.

V_{FWM} overlap integral, an analytic result is only possible in the collimated beam approximation, as discussed in Appendix H:

$$V_{FWM} = \frac{\pi \varpi_o^2}{4\Delta k} \sin\left[\frac{\Delta k\, L}{2}\right] \tag{4.9}$$

where

$$\frac{1}{\varpi_o^2} \equiv \left(\frac{2}{w_{op}^2} + \frac{1}{w_{os}^2} + \frac{1}{w_{oa}^2}\right) \tag{4.10}$$

and

$$\Delta k \equiv 2k_p - k_s - k_a. \tag{4.11}$$

The functional form of V_{FWM} is similar to a sinc function and, as shown in Figure 4.9, as a function of pressure, V_{FWM} shows behavior similar to a sinc function. Mathematically, it goes through zero at $\sim$7 atm because $\sin\left[\frac{\Delta k\, L}{2}\right]$ is zero at that pressure. Since the indices of refraction at the pump, Stokes, and anti-Stokes wavelengths are closer together at lower pressures, Δk is smaller at lower pressures and V_{FWM} is therefore larger.

As discussed in Boyd [45] on page 66, physically what is occurring here is that at a pressure of 7 atm, the anti-Stokes field is out-of-phase with the dipole oscillations.

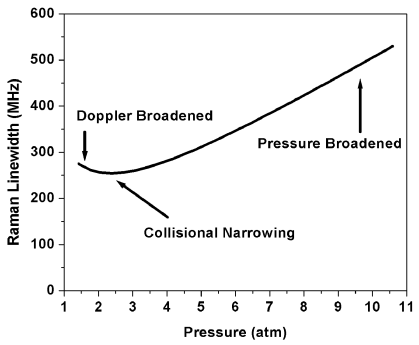

Figure 4.10: Raman linewdith, γ_{13}, as a function of pressure, as found by Bischel [44].

Any anti-Stokes generated at the center of the cavity is back converted to the pump and Stokes fields by the time the field "reaches" the mirrors and therefore none is emitted. At pressures lower than 7 atm, this back-conversion process is not completed. Therefore, some net anti-Stokes will be produced. At pressures higher than 7 atm, the anti-Stokes field and the dipole oscillations go from being perfectly aligned at the center of the cavity to being completely out-of-phase somewhere between the center and the mirror and then start coming back into phase. Because the two start coming back into phase, net anti-Stokes is again produced. V_{FWM} for HOM combinations will go through zero at higher pressures if there is a net Gouy phase shift for the combination, as shown in Appendix H.

Pressure Dependence of the Raman Linewidth

In addition to the index of refraction being dependent on the pressure, the Raman linewidth is also pressure dependent. This behavior was investigated by Bischel et. al [44]. Figure 4.10 shows the dependence of the Raman linewidth on pressure as found by Bischel. At high pressures, the Raman linewidth is pressure broadened. At low pressures, Doppler broadening, which does not depend on pressure, is dominant. At

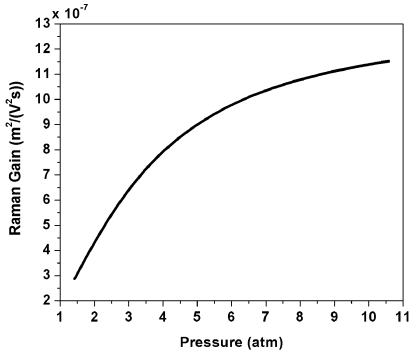

Figure 4.11: Raman gain, G, as a function of pressure.

intermediate pressures, $\sim$ 2– 3 atm, because an effect known as collisional narrowing reduces the Doppler broadening.

From equations 2.151 and 2.156, the Raman gain, G, is dependent on the Raman linewidth, γ_{13}. On its own, the decrease in the linewidth would lead to an increase in G. However, G is also dependent on the number density, N, of the molecules within the Raman cavity. As pressure decreases, the N decreases. Figure 4.11 shows that the Raman gain decreases as the pressure decreases. Thus, the decrease in the number density dominates the decrease in the Raman linewidth. This decrease in gain leads to an increase in threshold for the CW Raman laser system and a corresponding increase in the pump clamp level. As with the tuning discussion in Chapter 3 (on page 76), the amount of Stokes and anti-Stokes produced as the Raman gain decreases is not as easy to predict, especially since the anti-Stokes behavior is also dependent on the increase in V_{FWM} due to improved phase-matching.

Figure 4.12 plots the calculated threshold power (4.12a), the forward pump power (4.12b), the forward Stokes power (4.12c), the forward anti-Stokes power (4.12d) as functions of pressure. The reflectivities and transmittivities for each wavelength are given in Table 3.1. The input pump power was 10 mW. The Stokes frequency was assumed to be on gain line-center and the anti-Stokes was assumed to be perfectly

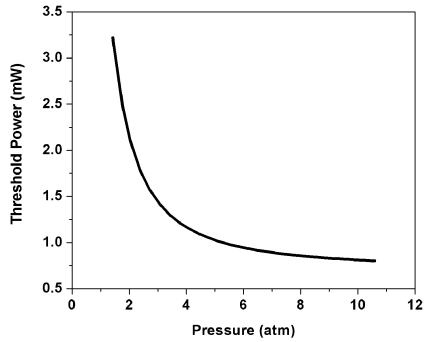

(a) Threshold power.

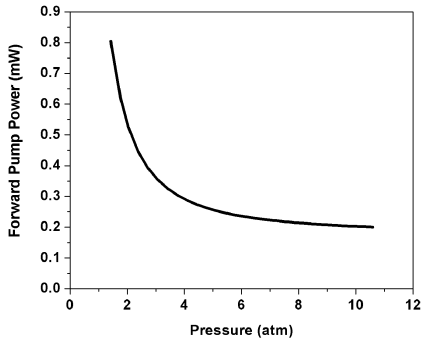

(b) Pump power.

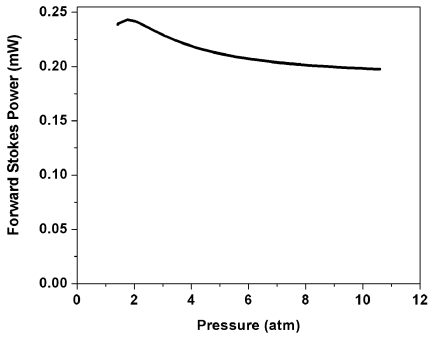

(c) Stokes power.

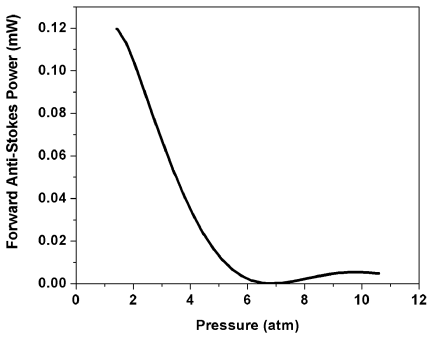

(d) Anti-Stokes power.

Figure 4.12: Forward pump, Stokes, and anti-Stokes powers and the threshold as a function of pressure. All fields were assumed to be resonant with the cavity at all pressures.

resonant with the cavity at all pressures. The calculation was made using the full steady-state solution from Chapter 3, and assumes that all three fields are on TEM_{00} spatial modes. This calculation includes the pressure dependence of both the Raman linewidth and the phase-matching.

There are several interesting features in Figure 4.12. In Figures 4.12a and 4.12b, the decrease in the power needed to reach threshold and the corresponding decrease of the pump clamp level can clearly be seen. In 4.12c, the Stokes level increases slightly until a pressure of about 2 atm and then decreases again. This is due to effects similar to those discussed in the tuning section of Chapter 3. The anti-Stokes (Figure 4.12d) increases dramatically as pressure decreases due to the improved phase-matching. The anti-Stokes power, as anticipated from V_{fWM}, is zero around 7 atm and then increases again as the pressure increases.

Experimental Design

Thus far in this chapter, the effects of the index of refraction on the CW Raman laser system and the pressure dependence of the Raman linewidth have been considered. In this section, the previous results of this chapter will be combined. To begin with, the results from this chapter are going to be summarized.

1. Because of dispersion in the H_2, the anti-Stokes will not be resonant within the Raman cavity unless somehow the dispersion is at least partially compensated.

2. There are four possible methods for forcing the anti-Stokes into resonance: lower reflectivity cavity mirrors at the anti-Stokes wavelength, use of HOM combinations, chirped mirrors and buffer gases. Only the first two methods were actively used in this dissertation.

3. The amount of anti-Stokes generated increases dramatically for reflectivities higher than ~ 0.9.

4. Phase matching is better at lower pressures. Therefore, more anti-Stokes can be generated at lower pressures.

5. The Raman gain decreases as the pressure decreases.

There are obviously trade-offs here. The lower the reflectivity of the mirrors at the anti-Stokes wavelength, the easier it is to find the anti-Stokes resonances, but less anti-Stokes can be produced. Phase-matching improves at lower pressures, increasing the amount of anti-Stokes that can be produced. But the Raman gain decreases at these lower pressures so that more input pump light is required to reach threshold.

For the first set of experiments of this dissertation, it was decided to use low reflectivity mirrors. That way, if the anti-Stokes could be generated, it would be and on any mode combination that was possible. The mirrors used were the original Raman mirrors purchased, which were coated to be high reflectors only at the pump and Stokes wavelengths. At the anti-Stokes wavelength, the mirrors were found to be about 25% reflective by Brasseur [15]. The anti-Stokes production was measured as a function of pressure while visually monitoring the mode combinations.

It was also decided to purchase a set of mirrors coated for the anti-Stokes as well. However, some of the above analysis had not been completed at the time that the mirrors were ordered, and there are two problems with these mirrors. First, their absorption was large for all wavelengths. This was especially problematic at the pump wavelength since the reflectivity was 0.99991 and the absorption was 82 ppm (parts per million), leaving only 8 ppm in transmission. This made it virtually impossible to reach the Raman threshold, even at 10 atm (where the Raman gain is highest) with the current pump laser, because it was exceedingly difficult to couple light into the

Raman cavity. The second problem with the mirrors is that their reflectivity of the mirrors at the anti-Stokes wavelength is 0.999, making the resonances very narrow. The random drifts of the pressure within the Raman cavity associated with ambient temperature fluctuations were too large to be able to control the pressure within the cavity accurately enough to stay on a resonance, assuming it could be found in the first place. In retrospect, it would have been better to purchase mirrors with lower reflectivities (and higher transmittivities) at all three wavelengths, but especially at the anti-Stokes wavelength.

However, all was not lost. As an intermediate step, a second experiment was performed using one of the new mirrors and one of the old mirrors. This decreased the effective anti-Stokes cavity reflectivity to $\sim$50%. It also decreased the absorption at the pump wavelength. Since the old mirror was used as the input coupler, more of the input pump actually was able to make it into the cavity. Even with this modest increase in the anti-Stokes reflectivity compared to the old mirrors, quite a bit more anti-Stokes was generated.

The next chapter gives the results of both sets of experiments with all three fields on TEM_{00} modes. The following chapter, Chapter 6, gives the results of both experiments for HOM combinations.

FUNDAMENTAL MODE EXPERIMENTS

This chapter will present experiments performed with the pump, Stokes and anti-Stokes confined to the TEM_{00} mode. There are two experiments presented in this chapter. The Raman cavity in the first experiment has matched mirrors with anti-Stokes reflectivities of 0.25%. The mirrors in the second experiment are mis-matched (with reflectivities of 25% and ∼99.9%). The chapter begins with descriptions of portions of the experiment that are common to both experiments. It then presents an overview of the experimental layout for the first experiment, followed by the results of this first experiment as functions of input power, detuning, and pressure. After that is the experimental layout for the second experiment and its results as a function of input power. The chapter concludes with a comparison of the two experiments.

Common Experimental Elements

This section contains descriptions of elements that are common to both experiments. The first piece discussed is the design of the Raman cavity. Second is a description of the system used to monitor and adjust the pressure within the Raman system. Last is a brief discussion of the frequency-locking system.

The Raman Cavity

Figure 5.1 shows a simplified cross-sectional schematic of the CW Raman laser cavity and its housing. (Actual machine drawings are located in reference [3].) The Raman cavity was designed by Pete Roos. It consists of two nested cylinders, separated by a rubber isolation material, to help prevent vibrations from affecting the Raman cavity. By using nested cylinders, the pressure gradient across the mirrors is

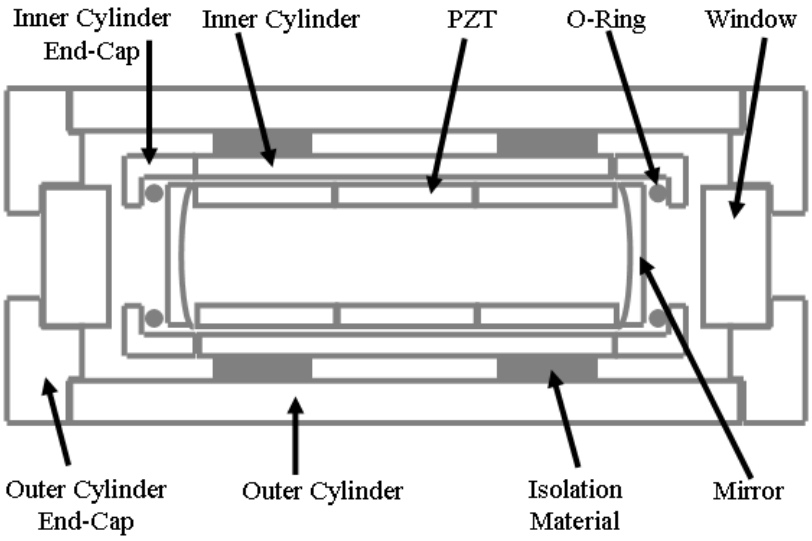

Figure 5.1: Simplified cross-sectional view of the CW Raman laser cavity and its housing.

eliminated so that the mirrors are not distorted. The outer cylinder is designed to hold ~ 10 atm. In each end cap of the outer cylinder is a window that allows light into the cavity. At either end of the inner cylinder are the highly-reflective mirrors which form the CW Raman laser cavity. The mirrors are separated by three 1-inch-long cylindrical piezo electric transducers (which define the cavity length of 7.62 cm).

Pressure System

Previous CW Raman lasers operated at a single, fixed pressure. To change the pressure in previous systems, the Raman cavity had to be physically removed from the optical set-up. Early in this dissertation work, it became apparent that the pressure would have to be easily adjusted. Figure 5.2 shows the system that was devised for this purpose. At the far left in Figure 5.2 is a cylinder of H_2. Attached to the cylinder is a regulator which brings the pressure from the cylinder down to approximately 200 psi (13 atm). After the regulator is a valve which isolates the H_2 cylinder and regulator

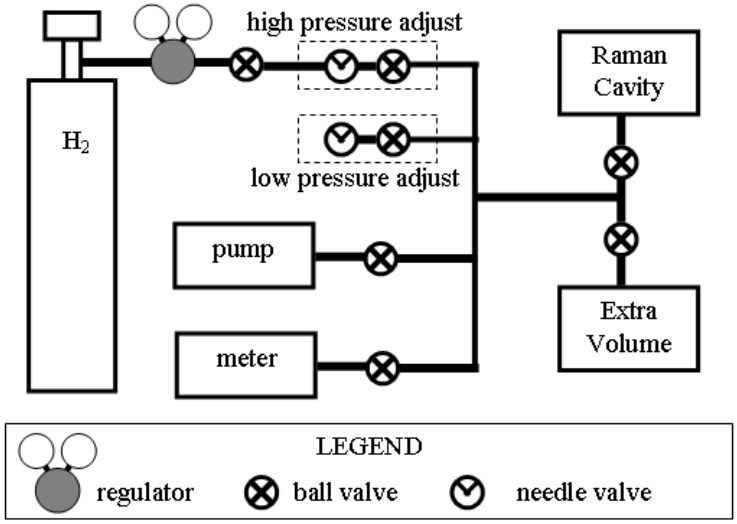

Figure 5.2: Schematic of the pressure adjustment system.

from the rest of the system, which, if necessary, allows the piping downstream from the valve to be evacuated with the pump. Following the single valve is a set of two valves, one needle and one ball, which are the high-pressure adjustment valves. The needle valve is for fine control of the flow of H_2 into the rest of the system and the ball valve is for coarse control. After the high-pressure adjustment valves, many items branch off a main trunk of piping. Moving from left to right and top to bottom in Figure 5.2, there are the fine adjustment valves, the pump, a pressure meter (Wallace and Tiernan DMP200-A-0200), the Raman cavity, and an extra volume. The pump, meter, Raman cavity, and extra volume are each isolated from the main trunk line by separate ball valves. For the same reasons as the high-pressure adjustment valves, the low-pressure adjustment valves are a needle valve and ball valve in series. The low-pressure adjustment valves vent to the room. Because it does not require any vacuum grease that could coat the mirrors, the pump is a sorption pump. (A sorption pump both absorbs and adsorbs.) The meter reads absolute pressure from 0 - 20 bar (0 - $\sim$20 atm). The extra volume has the exact same dimensions as the external

housing of the Raman cavity and was added to the system in order to allow finer adjustments to the pressure.

Ignoring the extra volume, the bulk of the H_2 in the system is within the Raman cavity. By adding the extra volume, the volume of the entire system was effectively doubled. Therefore, given a particular opening of the (either high or low adjustment) needle valve, the pressure changes about half as quickly when the extra volume is included then when it isn't when the (either high or low adjustment) ball valve is opened. This was particularly important at high pressures.

Frequency Locking

The pump laser frequency is matched to the Raman laser cavity by Pound-Drever-Hall frequency locking [16, 17]. This is an active frequency-stabilization method that uses electronic feedback to the system. The servos were based on a circuit diagram provided by Jan Hall and modified by Jay Brasseur and Kevin Repasky. They have remained relatively unchanged since that time. These designs are included in reference [3]. For more information regarding frequency locking, please refer to references [3, 5, 4, 16, 17].

Experiment 1

The original Raman mirrors purchased around 1998 were specified only to be highly reflective at the pump and Stokes wavelengths. Fortuitously, they are also 25% reflective at the anti-Stokes wavelength. At the start of this dissertation work, anti-Stokes had already been seen from a CW Raman laser incorporating these mirrors [15], Thus, it was natural to start the experiments for this dissertation using them.

This section begins with a description of the experimental layout of this first experiment. It is followed by a discussion of how the data was taken, and the parameters used to fit the theory to the data. Then, the steady-state powers as functions of input pump power and detuning are shown at a couple of pressures. This section concludes by combining those specific examples with more experimental data and plotting them all as functions of pressure.

Experimental Layout

Figure 5.3 shows the experimental layout of the CW Raman laser system. The pump laser is a 200 mW continuous-wave frequency-doubled Nd:YAG at 532 nm (JDSU M142H-532-200). It passes through a two stage isolator (OFR IOT-3-532-HP) and then an electro-optic modulator (EOM) (New Focus 12 MHz). The EOM adds phase side-bands at 12 MHz, which are necessary for the electronic frequency stabilization of the pump laser to the Raman cavity through Pound-Drever-Hall frequency locking [17, 16]. The light then enters a polarizing beam splitter (PBS). A small amount of light that leaks through the PBS and is fiber-coupled into a wavemeter (EXFO WA-1500) to monitor the pump laser frequency during tuning experiments.

The majority of the light is reflected by the PBS and double passes an acousto-optic modulator (AOM) (Isomet 1205C-2), which makes fast frequency corrections during frequency locking. After the AOM, but before the retro-reflecting mirror, the light passes through a lens and a quarter-wave plate (QWP). The lens, which is placed a focal length away from the retroreflector, prevents steering of the pump beam by the AOM (at the cost of a slight displacement of the beam) as it tunes the laser frequency. Double-passing the QWP rotates the polarization by 90^o so that when the

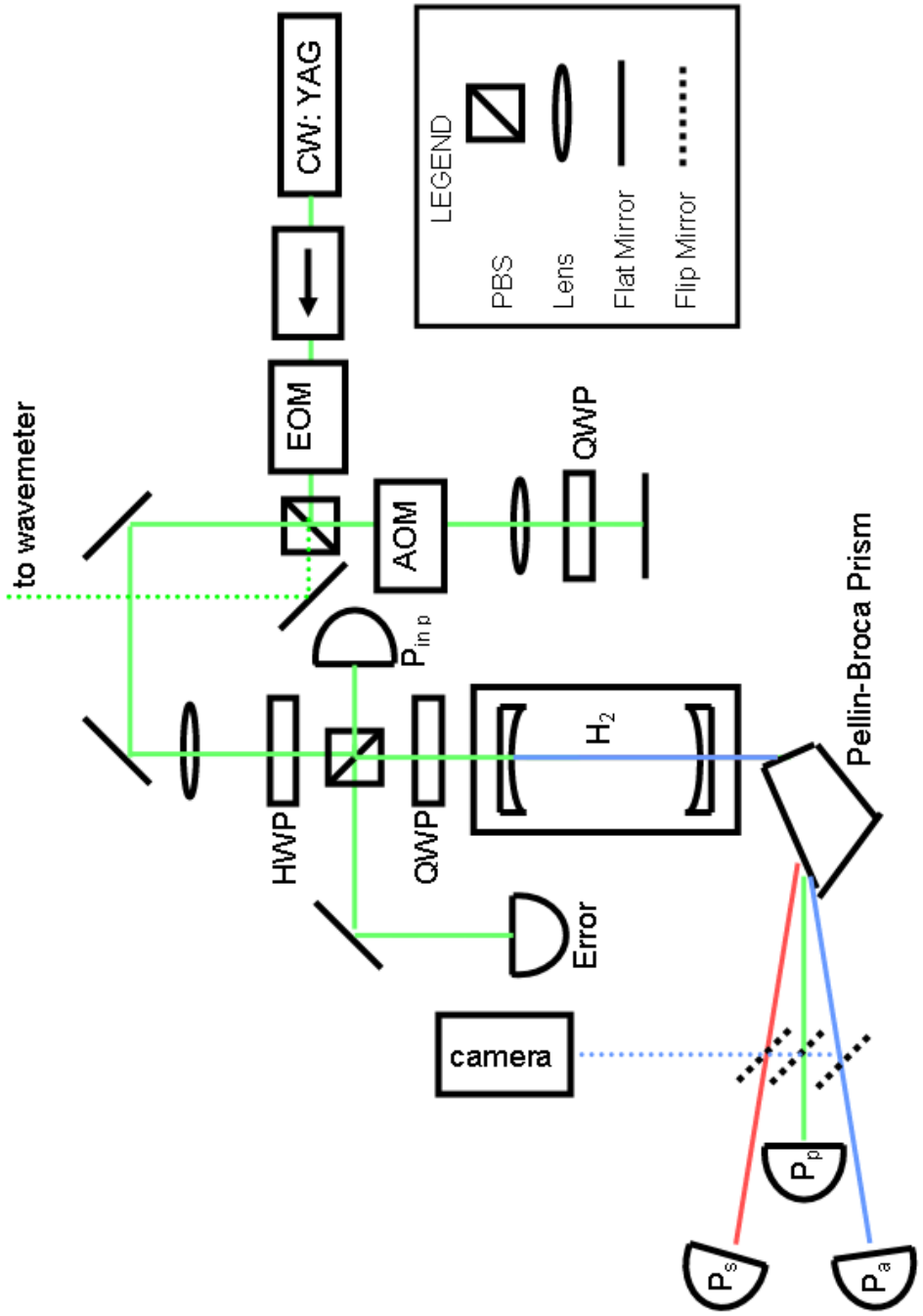

Figure 5.3: Experimental layout for the first set of experiments.

light returns to the PBS, it is now transmitted instead of being reflected back toward the pump laser.

After being transmitted by the PBS, the light is incident upon two turning mirrors used for mode-matching the laser to the cavity. (Mode-matching is the process of aligning the input beam to the cavity axis in order to maximize the amount of light coupled into a given cavity mode. Usually, the goal is to optimize the coupling into the TEM_{00} cavity mode.) After the second turning mirror, the light passes through a mode-matching lens and a half-wave plate (HWP) before being incident on a second PBS. The half-wave plate adjusts the ratio of light in each linear polarization, which, when combined with the second PBS, allows the input beam to be throttled. The light reflected by the PBS is used to monitor the input pump power. The light transmitted by the PBS passes through a QWP and then is incident on the front of the Raman cavity.

One of two things happens to the light incident on the front of the cavity: it can be reflected or it can be coupled into the Raman cavity. If it is reflected, it passes back through the QWP giving a net 90^o rotation to the polarization. This causes the reflected light to be reflected by the PBS. It is then focused onto a detector (New Focus 1801) and is used to generate the Pound-Drever-Hall error signal. If the light is coupled into the Raman cavity, then it can interact with the Raman medium and can be converted to Stokes and anti-Stokes.

After the Raman cavity, a Pellin-Broca prism is used to spatially separate the three fields. After the Pellin-Broca, the three fields continue to propagate until they are incident on either a power meter (ILX OMM 6810B and OMH 6703B) or a camera (Pulnix TM-745), depending on the orientation of a flip mirror (shown as a dashed diagonal line in Figure 5.3). The camera is used along with *Beamview* analysis software to take pictures (in the form of intensity maps) of the spatial patterns of the

three beams. Because the camera was at a different distance from the cavity for each of the three beams, the pictures taken had to be calibrated so that they were on the same angular scale. This calibration is outlined in Appendix N.

Comments on Experimental Methods

It is impossible to measure the input pump power directly while locked, since a direct measurement would require blocking the front of the Raman cavity. Therefore, the raw pump, Stokes, and anti-Stokes data were taken as functions of the input pump monitor described above. Since solid-state lasers are polarization (and power) stable, for this system it was possible to monitor the input power reflected by the PBS in front of the Raman cavity, as shown in Figure 5.3. Therefore, two data files were always taken for every data set. The first file contained the input-pump monitor, pump, Stokes, and anti-Stokes. Between the two data files, the power meter that measured the forward pump (after the Pellin-Broca prism) was placed in front of the cavity to measure the input pump directly. The second file contained input pump and input pump monitor. (If tuning data was taken, as well, then, usually, it was measured before the output vs. input data.) The second file was then used to calibrate the input-pump-monitor data contained in the first data file.

Also, there are many optics between the cavity and the power meters that measure the pump, Stokes, and anti-Stokes. (Not all the optics are shown in Figure 5.3.) Each of these optics has a loss associated with it. To compare with the theory at the exit of the cavity, the measured powers need to be adjusted to account for these losses.

The input power also needed to be corrected for losses due to the Raman mirrors (absorption and scattering) and losses due to light being reflected off the front of the cavity due to poor mode-matching. These losses determine the coupling efficiency of the input light. The coupling efficiency can be determined by the slope of the forward

pump power as a function of input power below threshold. After the input power has been adjusted to account for the coupling efficiency, it is referred to as the "coupled input power." The coupled input power is the amount of the total input power that is coupled into a particular pump cavity mode.

Appendix O shows a sample of how the raw data were adjusted to account for these issues.

The frequency-doubled CW Nd:YAG pump source (JDSU M142H-532-200) is tunable by changing the temperatures of the YAG crystal and the doubling crystal. The temperature tuning is accomplished by applying a voltage to an external port on the laser driver. When tuning, the voltage was adjusted. After a short time (~ 1 min), the data at the new frequency was taken. This wait allowed the system to reach equilibrium. For each data set, the system was first tuned to gain line-center by monitoring the forward pump power. As shown in Figure 3.11, the forward pump power is always at a minimum when the system is on gain line-center, whereas the Stokes and anti-Stokes could be at either a minimum or maximum depending on how far the input pump power is above the line-center threshold.

Experimental Parameters

Table 5.1 lists the reflectivities and transmittivities used to fit all the data for this experiment. Since the mirrors in the cavity are matched, only one reflectivity and transmittivity are given for each wavelength. Because reflectivity of the anti-Stokes is so low, the absorption at the anti-Stokes wavelength is ignored. The values of the Raman-dependent parameters (like the population decay rate and plane-wave gain coefficient) are the same as in Table 3.1, with the exception of the Raman linewidth because it is pressure dependent. The Raman linewidth as a function of pressure is given in equation 5.6.

Parameter	Value
R_p	0.9998
T_p	1.06×10^{-4}
R_s	0.99983
T_s	1.05×10^{-4}
R_a	0.25
T_a	0.75

Table 5.1: Parameters used to fit theory to data for the first experiment.

The manufacturer's (Research Electro-Optics) specified values for these mirrors at the pump and Stokes wavelengths are $R_p = 0.99979 \pm 0.00001$, $R_s = 0.99977 \pm 0.00001$, $T_p = 153 \pm 8$ ppm and $T_s = 150 \pm 20$ ppm. The values in Table 5.1 are outside the manufacturer's values, particularly the transmittivities. The change in the transmittivities could be due to the mirrors being approximately 11 years old at the writing of this dissertation. The parameters in Table 5.1 were determined by fitting the theory to the data.

As Functions of Input Power and Detuning

This subsection presents data for three different pressures: 141.23 psi (9.61 atm), 50.75 psi (3.45 atm), and 21.18 psi (1.44 atm). For each pressure, there are three figures. The first figure contains pictures of the intensity profiles of the pump, Stokes, and anti-Stokes modes. The second figure contains plots of the forward pump, Stokes and anti-Stokes powers as functions of the Stokes detuning from gain line-center. The third figure contains the plots of the forward pump, Stokes, and anti-Stokes powers as functions of input power at gain line-center. In the second and third figures, both theory (lines) and data (squares) are shown. After the three data sets, there is a discussion that compares and contrasts them. (There is additional data in Appendix P.)

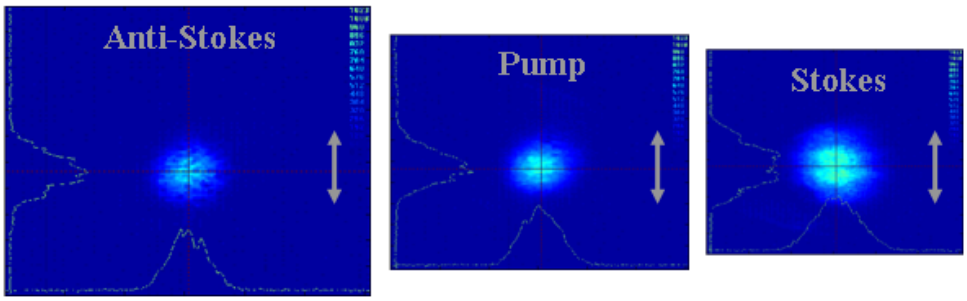

Figure 5.4: Spatial profiles of the pump, Stokes, and anti-Stokes at 141.23 psi (9.61 atm). The profiles have been rescaled to account for the different path lengths from the cavity to the camera, as outlined in Appendix N. The arrow is 2.3-mrad long.

The digital pressure meter reads in psi. Therefore, the actual pressure reading that corresponds to each data set is in psi. However, typical CW Raman data is recorded at a pressure in atm. Therefore, all pressures are given in both psi and atm.

Data at 141.23 psi (9.61 atm): Here are the mode profiles for this set of data. The pump, Stokes, and anti-Stokes are all TEM_{00} modes.

Figures 5.5a, b, and c show the forward pump, Stokes, and anti-Stokes powers, respectively, as a function of detuning at a coupled input pump power of 20.83 mW.

As shown in Figure 5.6, the line-center threshold at this pressure is about 1.6 mW. An input power of 20.83 mW, therefore, corresponds to 13 times threshold. The squares are the data and the line is the theory.

The frequency of the pump laser is measured by a wavemeter (EXFO WA-1500). This was then converted to detuning from line center by [35]

$$\delta \;=\; \delta f_p \left(1 - \frac{\lambda_p}{\lambda_s}\right), \tag{5.1}$$

where δf_p is the difference of the pump frequency from the line-center pump frequency. (The line-center pump frequency is the pump frequency that shifts to a Stokes frequency on gain line-center.) The two frequencies (pump and Stokes) do

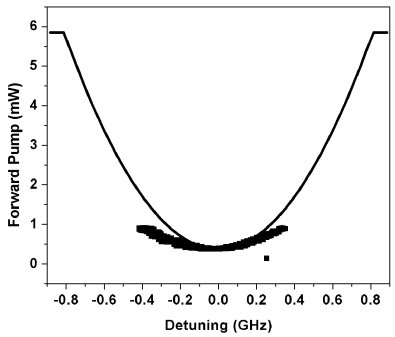

(a) Pump power.

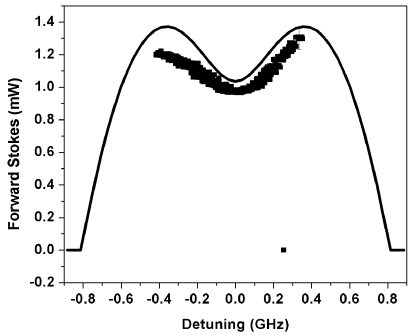

(b) Stokes power.

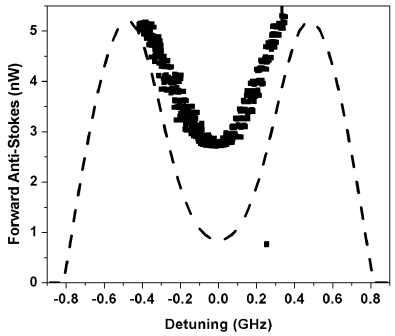

(c) Anti-Stokes power.

Figure 5.5: Output powers as a function of detuning at 141.23 psi (9.61 atm). This data was taken at a coupled input power of 20.83 mW. Data is shown as squares and theory as lines.

not tune at the same frequency because the Stokes frequency is determined by the cavity mode closest to gain line-center. Therefore, the Stokes frequency does not always differ from the pump frequency by the Raman shift. (In fact, the difference between the pump and Stokes frequencies will only equal the Raman shift when on gain line-center.) Because tuning the pump causes the cavity length to change (in order to maintain resonance with the pump), the cavity resonance frequency for the Stokes changes.

The wavemeter has a resolution of ± 0.0001 nm at 1000 nm. In frequency, it gives two decimal places in GHz. When the tuning data was taken, ~ 10 points were

recorded at each step. Therefore, on Figure 5.5, the scatter of the horizontal reading is due to fluctuations in the wavemeter reading over those 10 points.

On Figures 5.5a and b, the solid line represents the theoretical profile of the pump and Stokes powers, as calculated by equations 3.44 and 3.45. For detunings between -0.2 GHz and 0.2 GHz, the forward pump agrees well with the theoretical value. Possible reasons for the discrepancy between data and theory at detunings greater than $|0.2|$ GHz are a poor frequency lock and multiple Stokes modes trying to simultaneously lase. The forward Stokes profile (Figure 5.5b) has the correct shape but is slightly wrong in amplitude.

As the anti-Stokes reflectivity is decreased, the *Matlab* code that numerically solves the time-dependent CWRLE becomes increasingly slow. Therefore, it was impossible to theoretically fit the anti-Stokes data in Figure 5.5c. The dashed line on Figure 5.5c is the theoretical shape that the anti-Stokes would take as calculated for an anti-Stokes reflectivity of 0.999 (for the same input pump power). (Smaller values of R_a were tried and found to give the same shape but, due to the amount of time needed for the program to run, were not used here.) When detuned, the anti-Stokes data shows the same basic behavior as predicted theoretically using a higher reflectivity at

the same input pump power. Also, the amount of anti-Stokes measured when detuned by 0.33 GHz is about twice the amount produced at line-center.

Figures 5.6a, b, and c show the forward pump, Stokes and anti-Stokes powers, respectively, as functions of the input power when the system is at gain line-center. As indicated above, the threshold is about 1.6 mW. In Figures 5.6a and b, the solid lines represent the theory and the squares are data. Since this data set is on line-center and the anti-Stokes reflectivity is small, equation 3.48 can be used to fit the data. Because on line-center there is an analytic theory, it was possible to fit data and theory shape and magnitude) in Figure 5.6, even though it was not possible in Figure 5.5.

The forward pump (Figure 5.6a) increases until it reaches threshold and then clamps at 0.37 mW. Data and theory agree well.

The forward Stokes (Figure 5.6b) is zero until threshold. Above threshold, it grows with a square root dependence on the input pump power. Data and theory agree well over the entire range of coupled input power.

Since the anti-Stokes reflectivity is low, the cavity resonances at the anti-Stokes are going to be broad and shallow, as shown in Figure 4.4. Thus, the anti-Stokes can be produced even if the optical frequency does not equal the cavity resonance frequency. Thus, for the anti-Stokes data, there are two theoretical lines. The solid line assumes that the anti-Stokes optical frequency equal the cavity resonance frequency. The dashed line assumes that the optical frequency and cavity resonance frequency are as mismatched as possible. For $R_a = 0.25$, as can be seen from Figure 4.4, this corresponds to decreasing the theory to 36% of its maximum value (the solid line). The anti-Stokes data falls between these two theoretical lines.

The accuracy of the power meters used to measure the pump, Stokes, and anti-Stokes data is $\pm 5\%$ over the entire wavelength range. This value was used to add

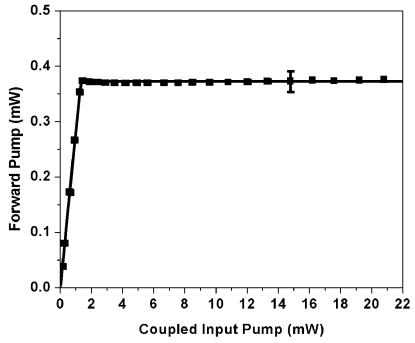

(a) Pump power.

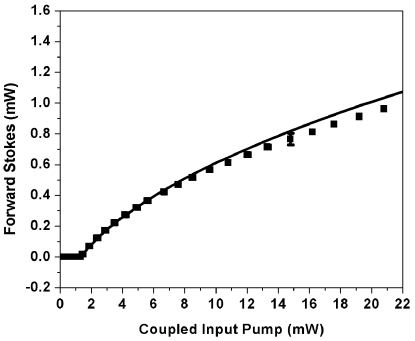

(b) Stokes power.

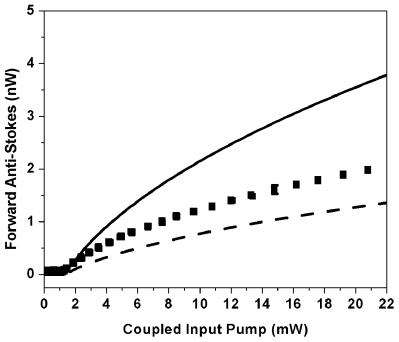

(c) Anti-Stokes power.

Figure 5.6: Output powers as functions of input power at 141.23 psi (9.61 atm) on gain line-center. Data are shown as squares and theory as lines.

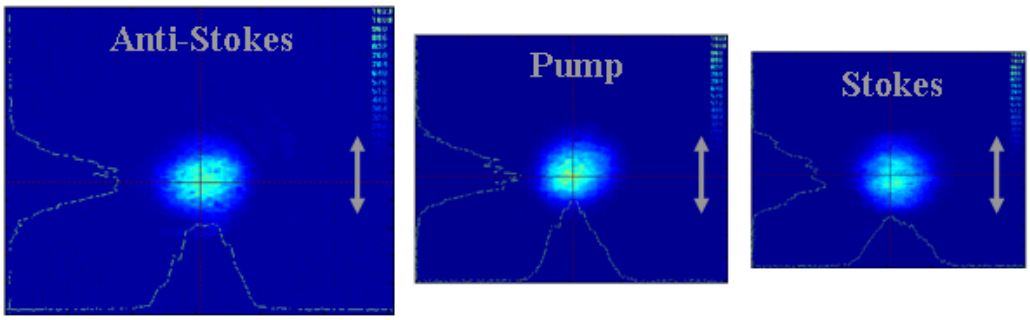

Figure 5.7: Spatial profiles of the pump, Stokes, and anti-Stokes at 50.75 psi (3.45 atm). The profiles have been rescaled to account for the different path lengths from the cavity to the camera, as outlined in Appendix N. The arrow is 2.3-mrad long.

error bars to the data. In some cases, the error bar is too small to be seen. These error bars do not include any additional errors in the data arising from uncertainties in the correction factors (found in Appendix O).

Data at 50.75 psi (3.45 atm): Figure 5.7 shows the pump, Stokes, and anti-Stokes spatial profiles at 50.75 psi (3.45 atm). They are again TEM_{00} modes.

Figures 5.8a, b, and c show the forward pump, Stokes, and anti-Stokes powers as functions of detuning from gain line center. The lines are theory and the squares are data. The theory and data in Figures 5.8a and b agree quite well. As with the data at 141.23 psi (9.61 atm), it was impossible to fit the anti-Stokes data, due to numerical problems. Therefore, a (dashed) curve showing the basic behavior of the anti-Stokes is included. This curve was theoretically calculated at the same input pump power but with the anit-Stokes reflectivity increased to 0.999. The data was taken at a coupled input power of 21.43 mW, which, given the line-center threshold of 2.26 mW from Figure 5.9, is $\sim$9.5 times the line-center threshold. There is about twice as much anti-Stokes measured when detuned 0.14 GHz than when on line-center.

Figures 5.9a, b, and c show the forward pump, Stokes, and anti-Stokes powers, respectively, as functions of input power when on gain line-center. The data is shown

as squares and theory as lines. The threshold is 2.26 mW. The pump clamp level is 0.63 mW. Agreement between data and theory for the pump and Stokes is very good. The anti-Stokes data again falls between the maximum (solid line) and minimum (dashed line) values expected from the Airy function.

Data at 21.18 psi (1.44 atm): Figure 5.10 show the spatial profiles of the pump, Stokes and anti-Stokes. They are TEM_{00} modes.

Figures 5.11a, b, and c show the forward pump, Stokes, and anti-Stokes powers as a function of detuning from gain line center. The lines are theory and the squares are data. The theory and data in Figure 5.11a agree quite well. In Figure 5.8b, there is again a slight mismatch between the data and theory. As with the data at 141.23 psi (9.61 atm), it was impossible to fit the anti-Stokes data due to numerical problems. Therefore, a (dashed) curve showing the basic behavior of the anti-Stokes is shown. The data was taken at a coupled input power of 17.79 mW, which, given the line-center threshold of 6.3 mW from Figure 5.12, is $\sim$2.8 times the line-center threshold. (Note, this corresponds quite well to the set of curves at 3 times threshold from Figure 3.11. The Stokes does not show a dip at line-center and the anti-Stokes does.) The difference in the amount of anti-Stokes generated on line-center and when detuned at this pressure is not as dramatic because the coupled input pump power was not as far above threshold.

Figures 5.11a, b, and c show the forward pump, Stokes, and anti-Stokes powers, respectively, as a function of input power when on gain line-center. The data is shown as squares and theory as lines. The threshold is 6.3 mW. The pump clamp level is 1.6 mW. Agreement between data and theory for the pump and Stokes is very good. The anti-Stokes data falls on the minimum (dashed line) value expected from the Airy function.

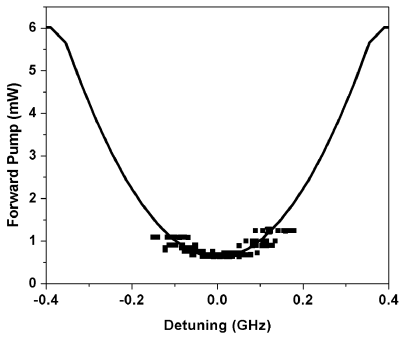

(a) Pump power.

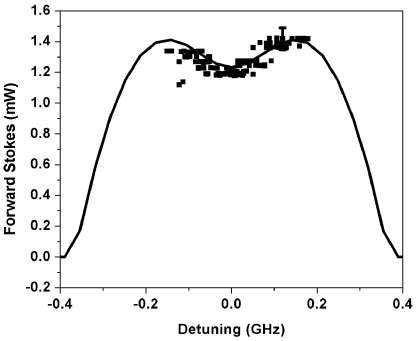

(b) Stokes power.

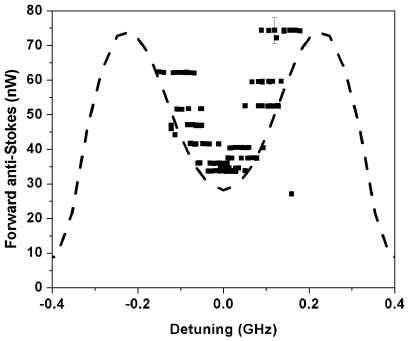

(c) Anti-Stokes power.

Figure 5.8: Output powers as functions of detuning at 50.75 psi (3.45 atm). This data was taken at a coupled input pump power of 21.43 mW. Data is shown as squares and theory as lines.

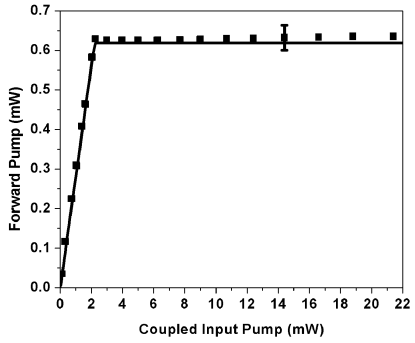

(a) Pump power.

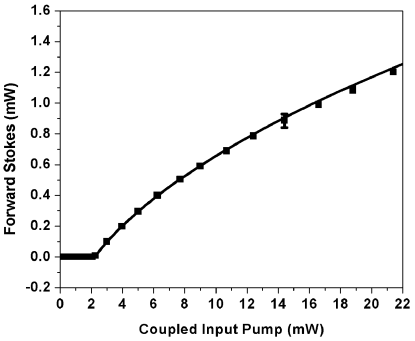

(b) Stokes power.

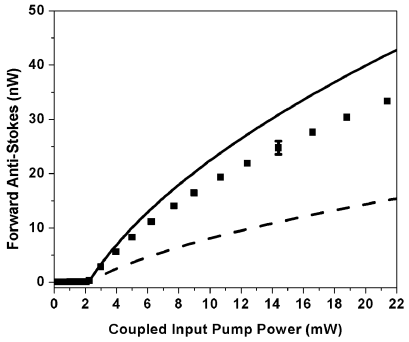

(c) Anti-Stokes power.

Figure 5.9: Output powers as functions of input power at 50.75 psi (3.45 atm) on gain line-center. Data are shown as squares and theory as lines.

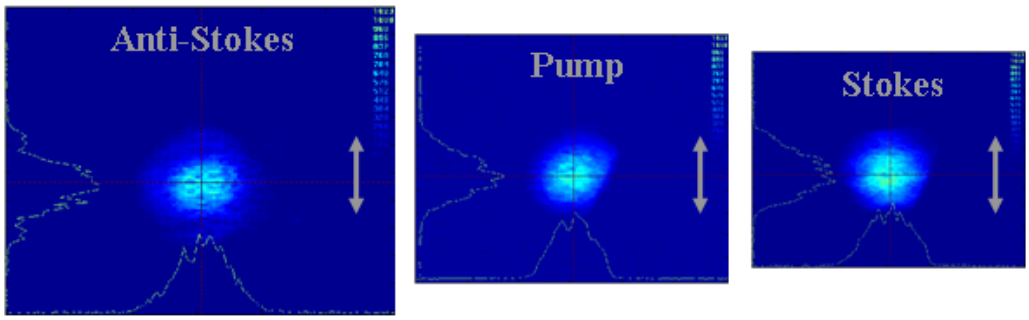

Figure 5.10: Spatial profiles of the pump, Stokes, and anti-Stokes at 21.18 psi (1.44 atm). The profiles have been rescaled to account for the different path lengths from the cavity to the camera, as outlined in Appendix N. The arrow is 2.3-mrad long.

Comparison of Data: A possible source of the slight disagreement between the theory and data in Figure 5.6 is due the desire to use a single set of reflectivities and transmittivities for all three data sets. Essentially, this is saying the mirrors are the mirrors. The set of reflectivities and transmittivities in Table 5.1 were chosen by repeatedly fitting the data shown in Figures 5.6, 5.9, and 5.12 to determine the values or R and T that best fit all three data sets. Slight adjustments to R and T will improve the fit for Figure 5.6 but worsen the fit for Figures 5.9 and 5.12. In reality, the data sets are taken as near to line-center as it is possible to determine with the experimental apparatus. Therefore, the fits might be able to be improved with a slight change to the Raman gain to account for this small detuning. However, it is hard to determine with of the three sets is slightly detuned. Therefore, they were all assumed to be line-center and the data and theory disagree in places.

As pressure decreases, the Raman gain decreases due to a decrease in the number density, as shown in Figure 4.11. Also, as pressure is decreased, the Raman linewidth decreases as shown in Figure 4.10. These two effects are both apparent in the three data sets above. The decrease in the Raman gain is evident in the increase in both input pump power needed to reach threshold and the above-threshold pump clamp

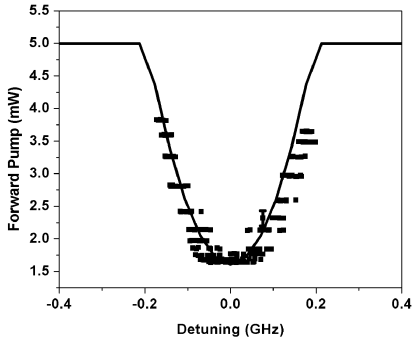

(a) Pump power.

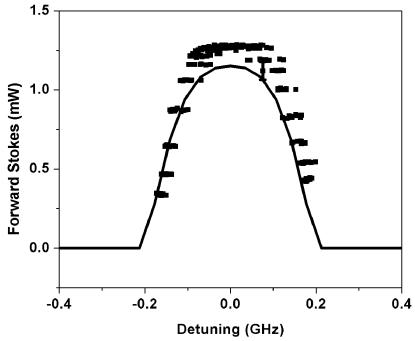

(b) Stokes power.

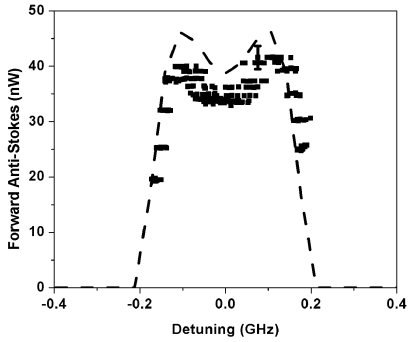

(c) Anti-Stokes power.

Figure 5.11: Output powers as functions of detuning at 21.18 psi (1.44 atm). This data was taken at a coupled input power of 17.79 mW.

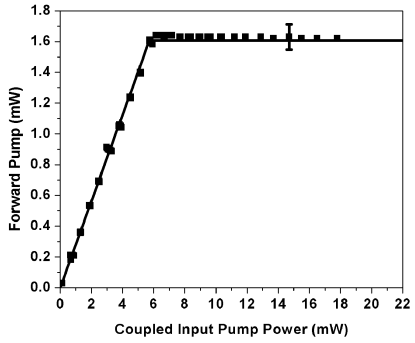

(a) Pump power.

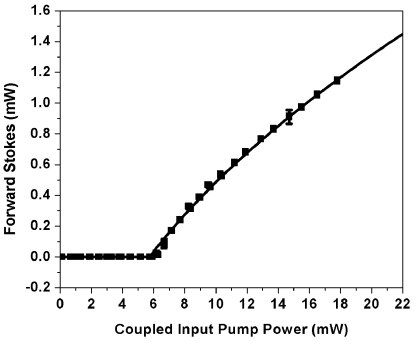

(b) Stokes power.

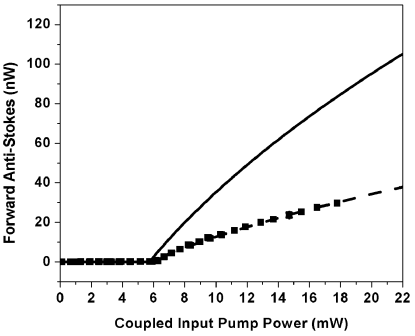

(c) Anti-Stokes power.

Figure 5.12: Output powers as functions of input power at 21.18 psi (1.44 atm) on gain line-center.

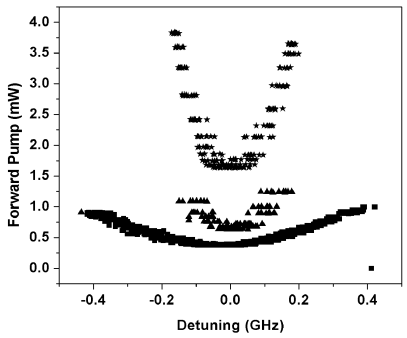

Figure 5.13: Forward pump power as a function of detuning. The squares are data at 141.23 psi (9.61 atm), the triangles at 50.75 psi (3.45 atm) and the stars at 21.18 psi (1.44 atm). These data are repeated from Figures 5.5a, 5.8a, and 5.11a, respectively.

level. The threshold at 141.23 psi (9.61 atm) is 1.6 mW and the pump clamp level is 0.37 mW. At 21.18 psi (1.44 atm), the threshold has increased to 6.3 mW and the pump clamp level is 1.6 mW.

The decrease in the linewidth is most easily seen from the pump tuning curves in Figures 5.5a, 5.8a, and 5.11a because the pump follows the same curve regardless of how far above threshold the tuning curve was taken (as shown in Figure 3.11a. Figure 5.13 shows the forward pump powers as a function of detuning for the three pressures. The squares are at 141.23 psi (9.61 atm), the triangles are at 50.75 psi (3.45 atm), and the stars are at 21.18 psi (1.44 atm). The curve at 141.23 psi (9.62 atm) is much broader than the curve at 21.18 psi (1.44 atm). The change in the gain is also evident in the increase in the line-center value as pressure decreases.

A comparison of the amount of anti-Stokes produced at the three pressures is not very enlightening because the anti-Stokes falls at different locations within the bounds of the Airy function. Because of this, there is more anti-Stokes measured at 50.75 psi (3.45 atm) than at 21.18 psi (1.44 atm). However, about twice as much could theoretically be produced at 21.18 psi (1.44 atm) if the anti-Stokes optical frequency

were closer to a cavity resonance frequency.

Measurements as a Function of Pressure

The three data sets presented in the last section are typical of the data taken during this dissertation work. Many other data sets were taken over pressures from 21.18 psi (1.44 atm) to 155.68 psi (10.59 atm). This subsection looks at *all* the data as a function of pressure. First, the forward pump, Stokes, and anti-Stokes powers are shown as functions of pressure at coupled input pump powers between 8 and 11 mW. Then, the forward pump power data is converted to measurements of the Raman gain and linewidth as functions of pressure. The Raman linewidth is compared to Bischel's measurements [44].

It was known that the gain and linewidth would be pressure dependent. However, before the data was taken, it was more-or-less expected that these effects would not be seen until pressures of about 1-2 atm. The data was taken from high pressures to low. As a surprise, the increase in the pump clamp level was readily apparent by a pressure of 5 atm, long before it was expected.

Data as a Function of Pressure: Figure 5.14 shows the forward pump, Stokes and anti-Stokes powers as functions of pressure (all at gain line-center). The data (squares) corresponds to coupled input powers between 8 and 11 mW. It was necessary to take a range of coupled input powers because there was not always a data point at a specific coupled input pump power. (Partially, this is because the data is initially taken as a function of an input pump monitor. This makes it very hard to know exactly what the coupled input pump power is while taking the data.) The three circled data points correspond to [points from the three data sets presented in the previous section.

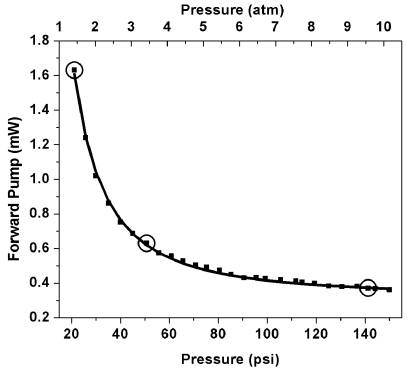

(a) Pump power.

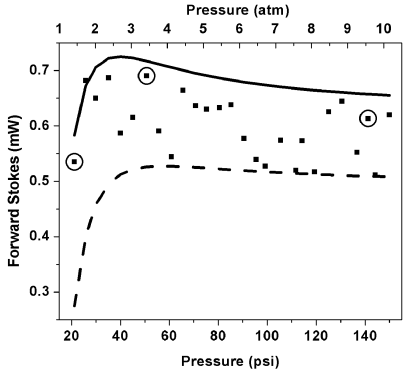

(b) Stokes power.

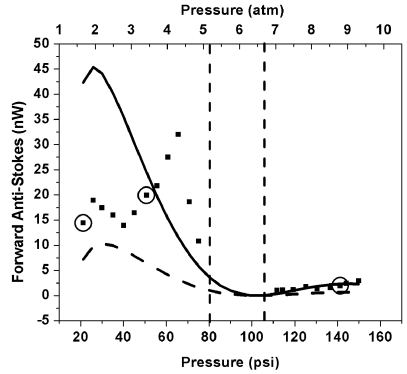

(c) Anti-Stokes power.

Figure 5.14: Output powers as functions of pressure.

Since the pump clamps above threshold, only one theoretical line is shown on Figure 5.14a. The Stokes and anti-Stokes plots show two theoretical lines. In Figure 5.14b, the upper (solid) theoretical line corresponds to the amount of Stokes produced at a coupled input pump power of 11 mW and the lower (dashed) theoretical line corresponds to 8 mW. To minimize confusion, theoretical lines corresponding to coupled input pump powers between 8 and 11 mW were not included in the figure. In general, the agreement between the Stokes theory and Stokes data is very good over the entire range. At the most, they disagreed by $\sim 10\%$. Figure P.9b in Appendix P shows one of the worst cases of disagreement between data and theory. This much disagreement occurred in less than 1/4 of the data shown in Figure 5.14b.

In Figure 5.14c, the upper (solid) theoretical line corresponds to a coupled input pump power of 11 mW while the lower (dashed) theoretical line corresponds to the anti-Stokes produced at coupled input pump power of 8 mW multiplied by the minimum value of the Airy function, 0.36 (from Figure 4.4). Also in Figure 5.14c, there are two vertical dashed lines at 80 psi (5.4 atm) and 105 psi (7.14 atm). In between these lines, the anti-Stokes mode was not TEM_{00}. These vertical lines surround the region where it is predicted that the anti-Stokes should not occur on a TEM_{00} mode because the overlap integral, V_{FWM} goes through zero (as shown in Figure H.3 on page 255). Often times, it was a superposition of anti-Stokes modes. Some of the data corresponding to pressures in between the two vertical lines is presented in the next chapter. Because the anti-Stokes reflectivity is low, the pump and Stokes data between these pressures is still valid and, therefore, is displayed in Figures 5.14a and b.

In Figure 5.14c, there are a five points between 55 psi (3.7 atm) and 75 psi (5.1 atm) where the data is higher than the maximum predicted. It is unclear why this is occurring. It is possible that there is some mode competition between HOM

that is causing more anti-Stokes to be produced. However, the anti-Stokes spatial patterns at all five points appeared to be TEM_{00}. A more likely possibility is that something is improving the phase-matching at these pressures. If the phase-matching were improved, the theoretical value would increase because V_{FWM} would increase. However, the reason that the phase-matching would improve is unclear. This is further discussed in Appendix R.

Raman Gain as a Function of Pressure : Since the above-threshold pump power clamps, it is the best data to use when investigating the Raman gain, G. Luckily, the clamped pump power depends on the gain in a fairly simple manner. In the undepleted pump limit, the theoretical value of the above threshold intracavity pump clamp field magnitude is (from equation 3.44)

$$A_{p\,ss} = \sqrt{\frac{\gamma_{cs} V_{ps\,o}}{2GV_{ps}}}. \tag{5.2}$$

Thus, G, can be found from

$$G = \frac{\gamma_{cs} V_{ps\,o}}{2V_{ps}} \frac{1}{A_{p\,ss}^2}. \tag{5.3}$$

Finally, recall that the forward pump power can be calculated from the intracavity field magnitude by (using equations 3.16 and 3.21)

$$\mathcal{P}_{p2} = T_{p2} \left(\frac{\pi w_{op}^2 n_o}{16} \sqrt{\frac{\varepsilon_o}{\mu_o}} \right) A_{p\,ss}^2, \tag{5.4}$$

where $A_{p\,ss}^2$ has been substituted for $|E_p|^2$ in equation 3.16. Given this, the Raman gain, G, in terms of the transmitted power is

$$G = \frac{T_{p2}}{\mathcal{P}_{p2}} \left(\frac{\pi w_{op}^2 n_o}{16} \sqrt{\frac{\varepsilon_o}{\mu_o}} \right) \frac{\gamma_{cs} V_{ps\,o}}{2V_{ps}}. \tag{5.5}$$

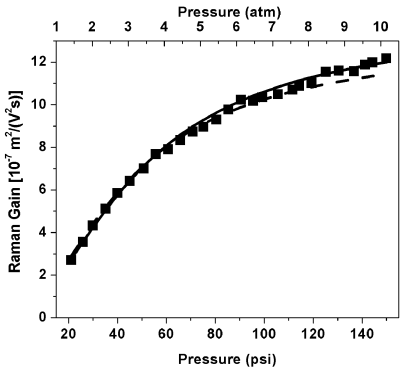

Figure 5.15: Raman gain, G, as a function of pressure.

Figure 5.15 shows a graph of the Raman gain as a function of pressure. The squares are the data obtained from the forward pump power. The dashed line is the theoretical gain calculated using Bischel's linewidth [44] and the solid line is the gain calculated using a linewidth modified to better fit the data. The functional form of the Raman linewidth is discussed next.

Raman Linewidth as a Function of Pressure : In his paper [44], Bischel presents data on the Raman linewidth as a function of the H_2 density. He also gives a functional form for the linewidth based on a least-squares fit to the data using the diffusion model (which is discussed in the reference). This functional form is not valid at low pressures because it does not properly incorporate the Doppler linewidth. However, it is valid at the pressures used in this dissertation.

The functional form for the Raman linewidth presented in Bischel

$$\gamma_{13} \quad = \quad \frac{A}{\rho} + B\rho, \tag{5.6}$$

where A and B are constants determined by the least-squares fit and ρ is the H_2 density in amagats. Bischel's data was taken using a pump laser at 488 nm which results in Stokes emission at 612 nm. The data taken in this dissertation used a pump laser at 532 nm, giving Stokes emission at 683 nm. Therefore, for Bischel's values

of A and B to be valid at the wavelengths of this dissertation, the Raman linewidth needs to be multiplied by the ratio of the Stokes wavelengths (which is 0.89). This adjustment factor agrees with the factor Bischel used in reference [54].

(The H_2 pressure needs to be converted to H_2 density. The Table 4h-19 in the AIP handbook [55] gives relative density of H_2 as a function of pressure and temperature. The data at 300 K was used to find a relationship between the pressure and density. That relationship is

$$\rho = 0.8613P + 0.4041, \tag{5.7}$$

where ρ is in amagats and P is in atm. Equation 5.7 is valid over pressures from 1 to 10 atm.)

The values of A and B as determined by Bischel are

$$A = 309 \pm 11 \text{ MHz amagat} \tag{5.8}$$

$$B = 52.2 \pm 0.5 \text{ MHz/amagat.} \tag{5.9}$$

As can be seen in Figure 5.15, these values for the linewidth did not lead to a gain (dashed line) that agreed exceptionally well with the data taken during this experiment. Thus, the values of A and B were modified to better fit the data (solid line). The modified values are

$$A = 350 \text{ MHz amagat} \tag{5.10}$$

$$B = 49 \text{ MHz/amagat.} \tag{5.11}$$

Both values, as modified are outside the error bars of Bishell's measurements. These modified values were used when numerically fitting all the data and theory presented in this dissertation.

Experiment 2

The original goal of this experiment had been to increase the reflectivity to $R_a > 0.999$ by changing both of the old mirrors in the Raman cavity out for new mirrors designed to be highly-reflective at all three wavelengths. However, there were two problems that prohibited that experiment. The first was that the new mirrors were very lossy, making it very hard for the Raman threshold to be reached. The second was that the pressure fluctuations within the Raman cavity due to ambient temperature fluctuations were too large to be controlled by the system as currently designed. The fluctuations would have caused the anti-Stokes resonance to be lost (assuming it could be found in the first place). Thus, a compromise was made: one old mirror and one new mirror were used, effectively doubling the anti-Stokes reflectivity of the cavity.

Experimental Layout

The first part of the experimental layout for this experiment is very similar to experiment 1. Because the old mirror was placed on the input side of the cavity, the primary Stokes and anti-Stokes transmission was in the backward direction. This required some changes to the layout. Of the forward propagating fields, only the pump was measured since the backward pump is used to generate the error signal.

The backward Stokes and anti-Stokes beams travel back along the input pump path, through the QWP (at the pump wavelength) to the PBS. At this point, interesting polarization effects were discovered on the Stokes and anti-Stokes which warrant further investigation. The majority of the backward Stokes is transmitted through the PBS continuing along the path back toward the laser. In order to separate the Stokes from the input pump, the turning mirror nearest the cavity was replaced by a dichroic mirror. The backward Stokes is transmitted through this mirror while

Parameter	Value	Parameter	Value
R_{p1}	0.9998	R_{p2}	0.99992
T_{p1}	1.06×10^{-4}	T_{p2}	7.9×10^{-6}
R_{s1}	0.99983	R_{s2}	0.99981
T_{s1}	1.50×10^{-4}	T_{s2}	26×10^{-5}
R_{a1}	0.25	R_{a2}	0.999
T_{a1}	0.75	T_{a2}	20×10^{-5}

Table 5.2: Parameters used to fit theory to data for the second experiment.

the input pump is reflected by it, as shown in Figure 5.16. The HWP was moved to before the turning mirror so that it could be adjusted (to change the input pump power) without affecting the backward Stokes beam.

The majority of the backward anti-Stokes was reflected by the PBS and followed the reflected pump light along the error signal path. A Pellin-Broca prism was placed in this path to separate the reflected pump and the anti-Stokes. A turning mirror is used to direct the reflected pump to the error signal detector. The anti-Stokes continues to a power meter.

Because of the complexity of this diagram, the camera is not shown. It is shown in the more detailed versions in Appendices N and O (Figures N.5 and O.2, respectively).

Experimental Parameters

Table 5.2 lists the reflectivities and transmittivities used to fit all the data for this experiment. Since, the mirrors in the cavity are not matched in this experiment, two values of the reflectivity and transmittivity are given for each wavelength. The subscript 1 indicates the front (input) mirror and the subscript 2 indicates the back mirror. The values associated with the front mirror are the same as those used in experiment 1 (Table 5.1), with the exception of the Stokes transmittivity. However, the Stokes transmittivity is within the manufacturer's specifications as given on page 127. The values of the Raman-dependent parameters (such as the population

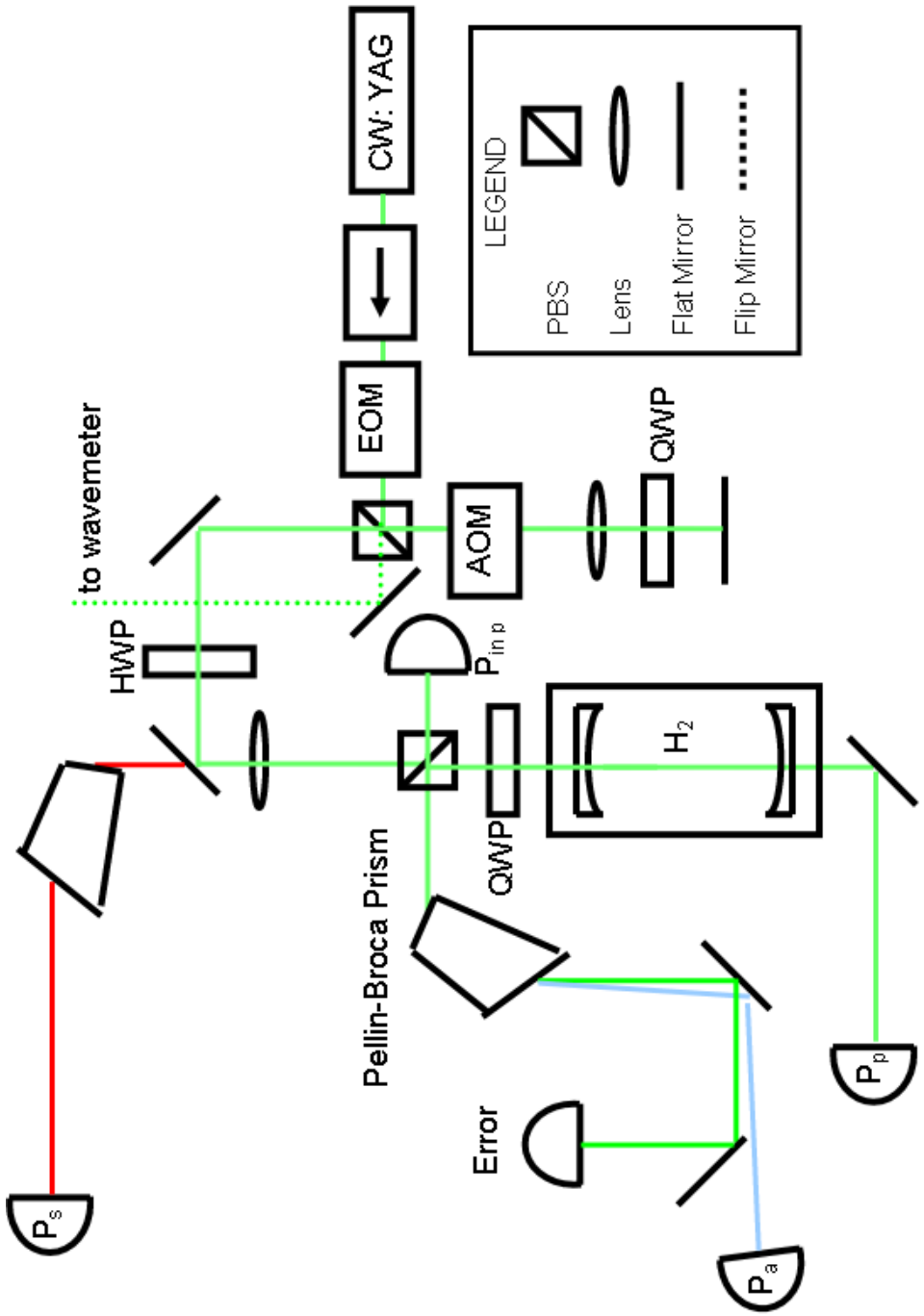

Figure 5.16: Experimental layout for the second set of experiments.

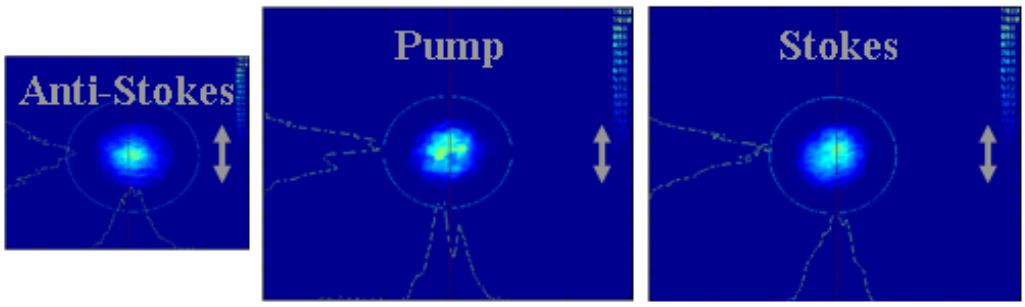

Figure 5.17: Spatial profiles of the pump, Stokes, and anti-Stokes at 45.7 psi (3.1 atm). The profiles have been rescaled to account for the different path lengths from the cavity to the camera, as outlined in Appendix N. The arrow is 2.3-mrad long.

decay rate and the plane-wave gain coefficient) are the same as in Table 3.1, with the exception of the Raman linewidth because it is pressure dependent. The Raman linewidth as a function of pressure is given in equation 5.6.

The manufacturer's (Advanced Thin Films) specifications for the new set of mirrors are $T_p = 6$ ppm, $T_s = 11$ ppm, and $T_a = 15$ ppm. The manufacturer did not specify the reflectivities. The pump reflectivity was measured by ringdown to be 0.999909. The parameters in Table 5.2 were determined by fitting the theory to the data.

Experiment 2 data

The data for Experiment 1 covered a large pressure range. It was not felt that this needed to be investigated again in Experiment 2. Therefore, only one data set is going to be looked at from this experiment. It will be compared to a data set taken in Experiment 1, which is in Appendix P.

This data set was taken at 45.7 psi (3.1 atm). Figure 5.17 shows the spatial mode profiles for this experiment. The structure in the pump spatial mode is due to interference fringes from a NB filter.

Figure 5.18 shows the forward pump power and backward Stokes and anti-Stokes powers as functions of input power when the Stokes frequency is on gain line-center. The agreement between theory (lines) and data (squares) for the pump and Stokes is excellent, as shown in Figures 5.18a and b. The threshold for this system is 1.2 mW. The pump clamp level is 51 μW.

As can be seen in Figure 5.18c, the measured anti-Stokes power is approximately twice as large as theoretically predicted by the maximum of the Airy function. (The minimum of the Airy function is not plotted.) Data at this pressure was taken multiple times (including with an additional NB filter in front of the anti-Stokes power meter to rule out possible leakage from either the pump or Stokes) and was consistent. It is thought that this discrepancy might be due to improved phase-matching, which would increase the value of the V_{FWM} overlap integral and therefore increase the theoretically predicted value. However, the reason the phase-matching would be improved is unclear. Appendix R contains some additional thoughts regarding phase-matching and this data set.

Comparison of Experiment 1 and Experiment 2 Data

Because of the different thresholds (at the same pressure) for the two experiments, it does not seem valid to compare anti-Stokes powers at a given input pump power. Instead, comparisons are going to be made at the same pump rate. (Pump rate is, by definition, the input power divided by the power needed to reach threshold. For example, if the threshold for is 1.2 mW, a pump rate of 3 would correspond to an input power of 3.6 mW or 3 times the threshold power.)

The Experiment 1 data at ∼45 psi (3 atm) is shown in Appendix P on page 365. At a pump rate of 3 (corresponding to 7.5 mW of coupled input pump power), the anti-Stokes measured in Experiment 1 was $\sim$ 11 nW and the maximum theoretically

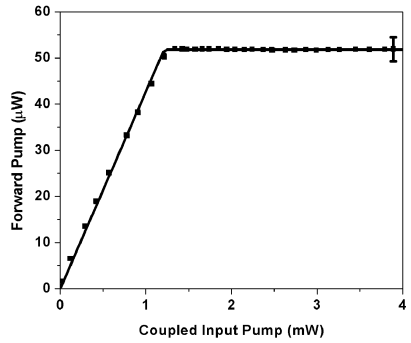

(a) Pump power.

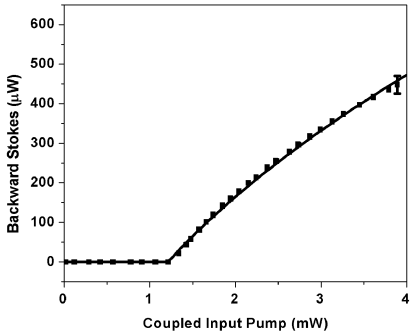

(b) Stokes power.

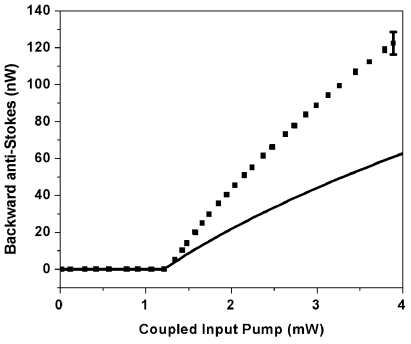

(c) Anti-Stokes power.

Figure 5.18: Output powers as functions of input power at 45.7 psi (3.1 atm) on gain line-center.

predicted value was $\sim$ 20 nW. The measured Experiment 2 data at $\sim$ 45 psi (3 atm) and a pump rate of 3 (corresponding to 3.6 mW of coupled input pump power) was $\sim$112 nW. (Theoretically, it was only 55 nW). Thus, this modest increase in the anti-Stokes reflectivity from 0.25 to 0.5 had dramatic results on the anti-Stokes power generated by the CW Raman laser. Theoretically, the maximum amount produced almost tripled. The experimentally measured power increased by a factor of 10.

Concluding Thoughts

This chapter has focused on the pump, Stokes and anti-Stokes TEM_{00} mode combination. In Experiment 1, the anti-Stokes generated by the CW Raman laser was investigated as functions of input power, detuning, and pressure. As a bonus, during this experiment, it was also possible to look at the pressure dependence of the Raman gain and linewidth. The Raman linewidth was then compared to results presented in the literature. Two methods of increasing the amount of anti-Stokes generation found: the input pump power could be increased and, for some pump rates, the Stokes could be detuned from gain line-center.

Experiment 2 focused exclusively on the anti-Stokes produced as a function of input power, which was then compared to the results from Experiment 1. It was found that the modest increase in the cavity's reflectivity at the anti-Stokes from 0.25 to 0.5 had a dramatic effect on the amount of anti-Stokes produced by the system.

The next chapter will look at HOM combinations and will compare them to the results from this chapter.

HIGHER-ORDER MODE EXPERIMENTS

This chapter will present experiments performed while investigating HOM combinations. Since the anti-Stokes mode profile can change from one pressure to the next, the mode combinations taken are grouped under their pump and Stokes modes only.

While tuning curves are not presented in this chapter, all the data was taken with the Stokes on gain line-center. In addition, in many cases, the data as a function of input power for the pump and Stokes are not shown. When this occurs, for reference, the complete data set as a function of input power has been included in, for Experiment 1, Appendix P or, for Experiment 2, Appendix Q. For all data sets, attempts were made to fit data and theory, with varying degrees of success, using the parameters in Tables 5.1 and 5.2 for Experiment 1 and Experiment 2, respectively.

The chapter begins by presenting some of the data from Experiment 1 with the pump and Stokes on TEM_{00} modes when the anti-Stokes was not. This data falls at pressures in between the dashed vertical lines on Figure 5.14c. Next, other HOM combinations are presented. Most of the data presented is from Experiment 1. However, there are two HOM combinations from Experiment 2 presented. The first is for pump TEM_{00} and Stokes HG TEM_{10} and the second is pump TEM_{00} and Stokes LG TEM_{10}. For these mode combinations, the structure of the anti-Stokes profile is investigated.

After samples of each set of modes, there will be some general discussion and comparison of the various mode combinations for the two experiments. The chapter finishes with some concluding remarks.

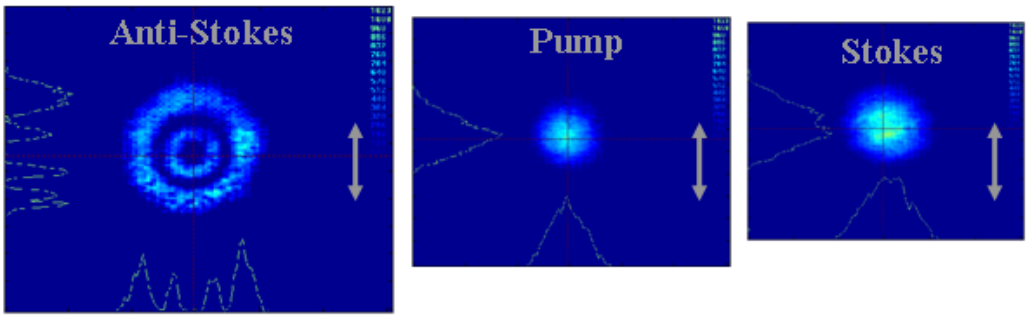

Figure 6.1: Spatial profiles of the pump, Stokes, and anti-Stokes at 99.26 psi (6.8 atm). The profiles have been rescaled to account for the different path lengths from the cavity to the camera, as outlined in Appendix N. The grey arrow is 2.3-mrad long. The anti-Stokes mode profile is not well-defined in any symmetry.

Pump and Stokes TEM_{00}

Both data sets in this section are from Experiment 1. They represent the mode combinations that occurred when the pump TEM_{00}, Stokes TEM_{00}, and anti-Stokes TEM_{00} mode combination could not occur due to the zero in the V_{FWM} overlap integral for that combination (as shown in Figure H.3 on page 255). The pressures over which the anti-Stokes did not occur on a TEM_{00} mode, as shown by the vertical bars on Figure 5.14c, are 80 to 105 psi (5.4 to 7.1 atm). Two sets of modes in that pressure range were chosen for discussion in this chapter. The first, at 99.26 psi (6.8 atm), is interesting because the anti-Stokes spatial pattern cannot be anything other than a superposition of modes. The second, at 90.48 psi (6.2 atm) was chosen because it is more typical of the data in that pressure region.

99.26 psi (6.8 atm)

The spatial mode profiles at this pressure (from Experiment 1) are shown in Figure 6.1. The pump and Stokes modes are clearly TEM_{00} modes. The anti-Stokes

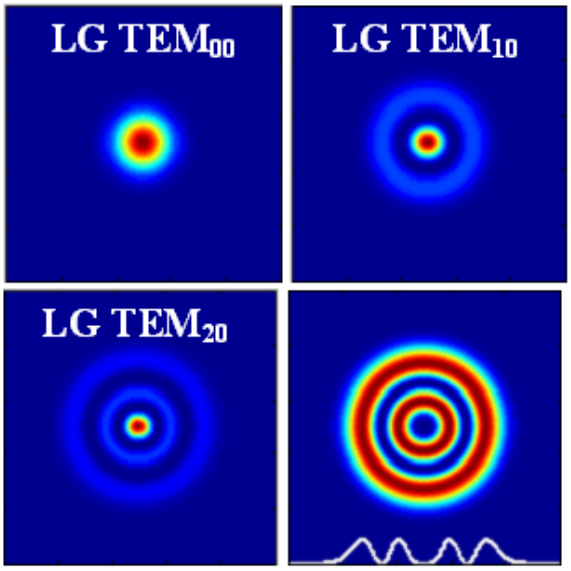

Figure 6.2: Clockwise from top left the spatial profiles are: LG TEM_{00}, LG TEM_{10}, LG TEM_{20} and a superposition, in fields. The superposition is given by $(-0.2 \times TEM_{00} - 0.4 \times TEM_{10} + 0.6 \times TEM_{20})$ and is characterized by two concentric rings. Blue areas are the least intense and red areas are the most intense.

profile is not a well-defined mode in any symmetry. But, this profile *can* occur as a superposition of other well-defined spatial modes.

By superposing fields, it was possible to find a mode combination that produces a spatial profile similar to the anti-Stokes profile in Figure 6.1, characterized by two concentric rings with a dark center. Figure 6.2 shows the three LG modes that were superposed $(-0.2 \times TEM_{00} - 0.4 \times TEM_{10} + 0.6 \times TEM_{20})$ and the result of the superposition.

Also shown on the bottom right profile in Figure 6.2 as a white line is the intensity profile of a horizontal cut through the center of the profile. This line can be compared to the faint white line at the bottom of the anti-Stokes profile in Figure 6.1, which is the intensity distribution along the horizontal line through the center of the profile. The two look very similar. Thus, this is a reasonable guess as to what modes compose this anti-Stokes spatial profile.

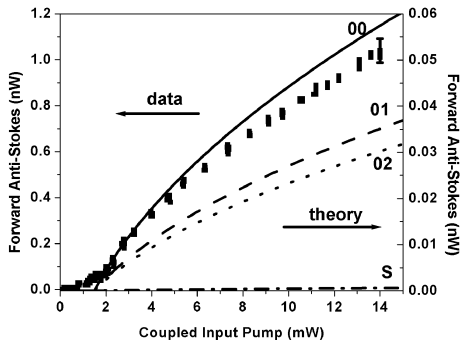

Figure 6.3: Forward anti-Stokes power as a function of the coupled input power on line-center at 99.26 psi (6.8 atm). The left axis shows the scale for the data (squares). The right axis shows the scale for the theory. There are four theoretical lines. The solid line corresponds to the theory if the anti-Stokes was on the LG TEM_{00} mode, the dashed line to LG TEM_{10} mode, the dotted line to LG TEM_{20}, and the dash-dot line to the power obtained by a superposition of fields given by $(-0.2 \times \mathrm{TEM}_{00} - 0.4 \times \mathrm{TEM}_{10} + 0.6 \times \mathrm{TEM}_{20})$.

But, can the LG TEM_{00}, LG TEM_{10}, and LG TEM_{20} modes all be simultaneously resonant within the cavity? All three modes are allowed, given the rules for allowable mode combinations in cylindrical symmetry given in Appendix H on page 259. As can be seen in Figure 4.6a, the modes can all be resonant in the cavity. (For reference, the LG TEM_{00} mode would follow curve A, the LG TEM_{10} mode would follow curve B, and the LG TEM_{20} mode would follow curve C on Figure 4.6a.) It is thought, ignoring any possible mode competition, that the weighting factors used in the superposition are dependent on both the value of V_{FWM} for each mode combination and the strength of the Airy function for that anti-Stokes mode.

Figure 6.3 shows the measured anti-Stokes power as a function of the coupled input pump power along with four theoretical fits. The data in Figure 6.3 is shown as squares. Its power should be read off the left scale. Below threshold, the anti-Stokes power is slowly increasing. This is due to scattered forward pump power reaching the power meter. Since the forward pump power clamps above threshold

but the data above threshold shows the characteristic above threshold behavior of the Stokes and anti-Stokes emission from the CW Raman laser, it is felt that the readings above threshold are due to anti-Stokes reaching the detector. While it is possible that scattered forward Stokes power could also be reaching the anti-Stokes power meter and, therefore, artificially inflating the anti-Stokes reading, it is felt that this is not the case based on observation of the system while the data was being taken. However, the measured anti-Stokes is so small that this possibility cannot be completely discounted. Shortly after this data set, the anti-Stokes NB filter was mounted to the front of the power meter to help prevent stray light from reaching the detector.

There are four theoretical lines on Figure 6.3. Because the theoretical result is numerically much smaller than the data, its scale is on the right axis. The solid line assumes that the anti-Stokes mode is LG TEM_{00}, the dashed line assumes LG TEM_{10} and the dotted line LG TEM_{20}. The final theoretical line (dash dot) assumes a superposition of fields as found by trying to match the observed spatial profile (i.e. the fields superposed according to $[-0.2 \times TEM_{00} - 0.4 \times TEM_{10} + 0.6 \times TEM_{20}]$). This superposition assumes that all the fields were at the maximum of their Airy functions (which is not physically possible). As can be seen, the theory is numerically much smaller than the data, regardless of whether the anti-Stokes is assumed to be on a single spatial mode or a superposition. This could be indicative of the spatial modes augmenting each other. It could also be a sign that the phase-matching is better than thought. Further investigation is needed.

90.48 psi (6.2 atm)

Figure 6.4 shows the spatial mode profiles from Experiment 1 at this pressure . The pump and Stokes are TEM_{00}.

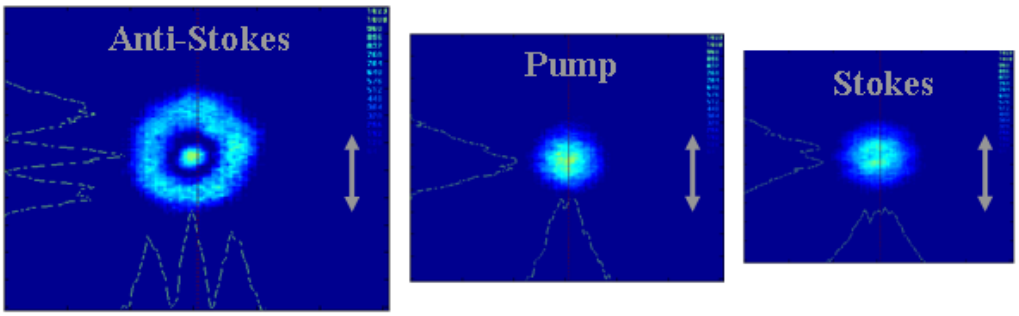

Figure 6.4: Spatial profiles of the pump, Stokes, and anti-Stokes at 90.48 psi (6.2 atm). The pump and Stokes are TEM_{00} and the anti-Stokes appears to be LG TEM_{10}. The profiles have been rescaled to account for the different path lengths from the cavity to the camera, as outlined in Appendix N. The grey arrow is 2.3 mrad long.

The anti-Stokes appears to be a LG TEM_{10} mode. Figure 6.5a shows a cross-section of the anti-Stokes mode profile. This cross-section was taken horizontally through the middle of the anti-Stokes profile. (For reference, there is another cross-section on the anti-Stokes profile in Figure 6.4. That cross-section was taken 1 pixel below the cross section in Figure 6.4, along the dashed horizontal line.) Figure 6.5b shows a horizontal cross-section of a LG TEM_{10} mode. Figures 6.5a and b are not on the same horizontal scale and both have been rescaled such that the peak intensity is 1. A comparison of Figures 6.5a and b shows that the measured anti-Stokes mode profile is not simply a LG TEM_{10} mode. Specifically, there is too much power in the outer ring relative to the peak.

On the other hand, the angular placement of the outer ring of the anti-Stokes spatial mode in Figure 6.4 is consistent with a LG TEM_{10} mode. Figure 6.6 again shows the measured anti-Stokes spatial mode. The cursors aligned with the outer peaks of the horizontal cross-section in Figure 6.6b are separated by 132 pixels. As outlined in Appendix N, 132 pixels corresponds to a separation of $\sim$343 μm. At the center of the cavity, the theoretical separation between the lobes of the outer ring of the LG TEM_{10} mode is 333.4 μm. This separation at 96 cm from the center of the

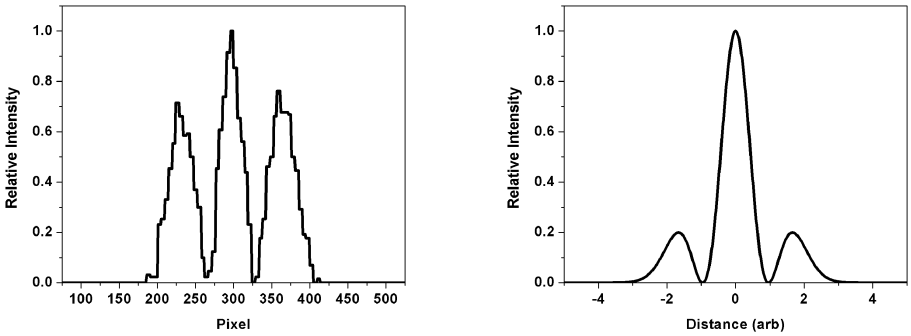

(a) Measured Cross-Section. (b) Theoretical Cross-Section.

Figure 6.5: Cross-sections of the measured anti-Stokes profile shown in Figure 6.4 and the theoretical LG TEM_{10} mode. The measured cross-section does not have the same distribution of energy as the theoretical profile. Both profiles have been rescaled so that their peak intensities are 1. They are not on the same horizontal scale.

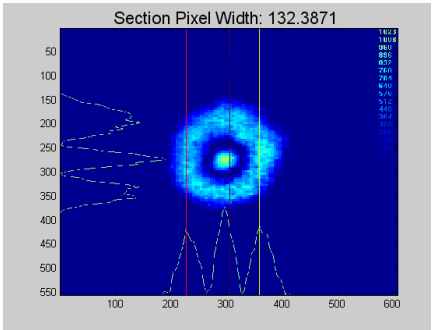

Figure 6.6: Anti-Stokes spatial mode profile showing the peak-to-peak width of the outer ring in pixels.

cavity is 2.36 mm and was found by using the ratio of the cavity waist (from equation N.6) to the spot size at 96 cm (from equation N.9). This method is valid because the ratio of the various mode properties will be constant. As measured by the camera, it is 330 μm. The measured separation and the theoretical separation are not identical but are very close. (This discrepancy could be due to errors in the calibration of the pictures.) Thus, even though the intensity distribution is not correct for the measured anti-Stokes mode to be LG TEM_{10}, it seems that that mode is consistent in other ways. (For reference, the diameter of the anti-Stokes cone-angle, from equation 4.8, as measured by the camera would be 537.6 μm.)

It appears that a superposition of modes is contributing to the measured anti-Stokes mode. Since there is no apparent structure to the measured anti-Stokes mode beyond the outer ring, it would be impossible for any higher HOM to contribute to the mode. Lower order modes could contribute. However, since the measured mode shows circular symmetry, modes with non-zero values of m cannot contribute because they would break the symmetry. This leaves the superposition to be between the LG TEM_{10} mode and the TEM_{00} mode. A superposition of these two modes given by $(-0.184 \times TEM_{00} + 0.5 \times TEM_{10})$ seems to give the proper distribution of energy between the main mode and outer ring, as shown in Figure 6.7b. (Figure 6.7a is the same as Figure 6.5a. It is repeated so that the intensity distribution of the superposition can easily be compared to the measured mode.)

In the same way that the distance between the lobes of the LG TEM_{10} mode was determined, the distance between the lobes of the outer ring of the superposition can be determined. It was calculated to be 308 μm, as measured by the camera. This is $\sim$90% of the measured separation.

Figure 6.8 shows a plot of the forward anti-Stokes power as a function of the coupled input pump power. The data is shown as squares and the theory as lines.

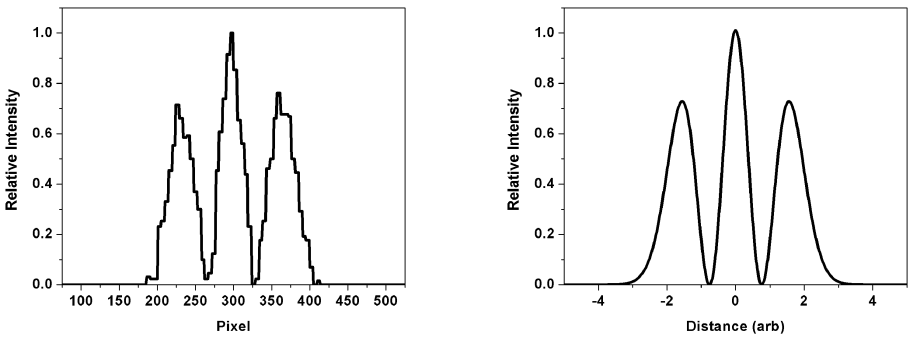

(a) Measured Cross-Section. (b) Theoretical Cross-Section.

Figure 6.7: Cross-sections of the measured anti-Stokes profile shown in Figure 6.4 and a theoretical superposition. The superposition, performed on the fields, is given by $(-0.184 \times \mathrm{TEM}_{00} + 0.5 \times \mathrm{TEM}_{10})$. The distribution of energy in the measured profile is very similar to the distribution of the theoretical superposition. Both profiles have been rescaled so that their peak intensities are 1. They are not on the same horizontal scale.

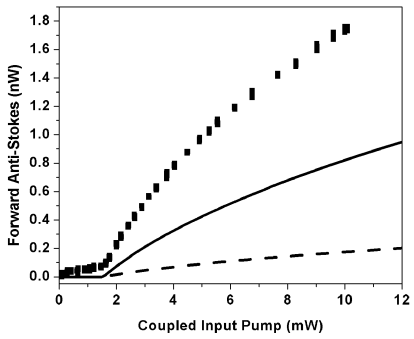

Figure 6.8: Forward anti-Stokes power as a function of the coupled input power on line-center at 90.48 psi (6.2 atm). Data are shown as squares and theory as lines. The solid line assumes that the anti-Stokes mode is a pure TEM_{00} mode and the dashed line assumes the mode is a pure LG TEM_{10} mode. The theory is smaller than the data in both cases.

There are two theoretical lines, neither of which fits the data well. The solid line assumes that the anti-Stokes mode is a pure TEM_{00} mode and the dashed line assumes a pure LG TEM_{10} mode. Neither assumption is valid, as discussed above, but they do provide a basis of comparison for the data. (In Figure 6.8, the measured anti-Stokes data below threshold does rise gradually due to pump leakage onto the anti-Stokes power meter.)

Pump TEM_{00}, Stokes HG TEM_{10}

There are two data sets with this mode combination, one for each of the two experiments.

Experiment 1

There are several anti-Stokes mode profiles that were observed with the pump and Stokes confined to TEM_{00} and HG TEM_{10} modes, respectively. Figure 6.9 shows three such mode combinations taken at 120.51 psi (8.20 atm), 66.56 psi (4.53 atm), and 25.97 psi (1.77 atm). The anti-Stokes profile at 120.51 psi (8.20 atm) is most similar to an LG TEM_{21}. The profile at 66.56 psi (4.53 atm) could be either HG TEM_{10} or LG TEM_{01}. The profile at 25.97 psi (1.77 atm) is not readily identifiable as any particular mode but might be a superposition of LG TEM_{01} and LG TEM_{11}.

Figure 6.10 plots the forward anti-Stokes power as a function of the coupled input power for the profiles at 66.56 psi (4.53 atm) shown in 6.9b. The theory is a bit of a victory and a bit of a failure. The victory is that the threshold agrees even though the Stokes is no longer on the fundamental mode. (As shown in Appendix P, the pump and the Stokes agree quite well with the theory modified to include HOM.)

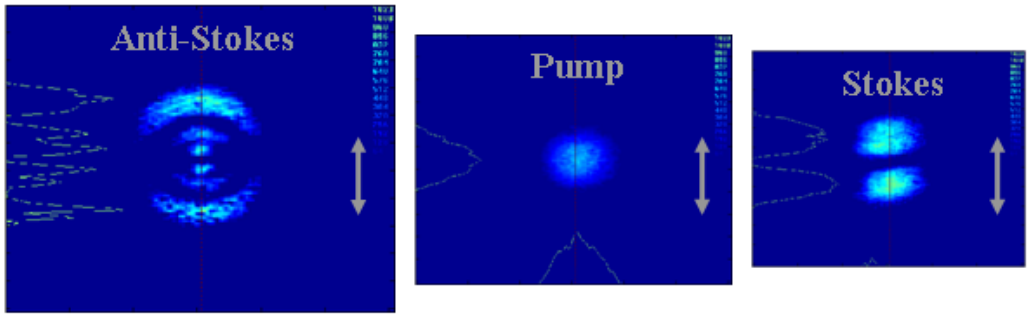

(a) 120.51 psi (8.2 atm)

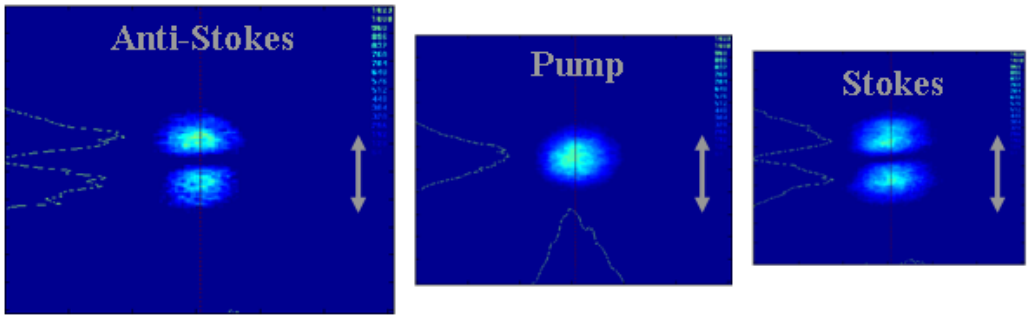

(b) 66.56 psi (4.53 atm)

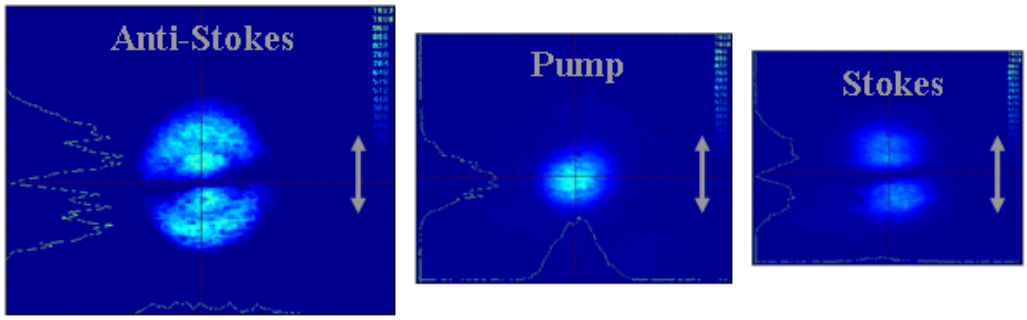

(c) 25.97 psi (1.77 atm)

Figure 6.9: Spatial profiles of the pump, Stokes, and anti-Stokes at three different pressures. The observed anti-Stokes profile varies significantly. The profiles have been rescaled to account for the different path lengths from the cavity to the camera, as outlined in Appendix N. The grey arrow is 2.3-mrad long.

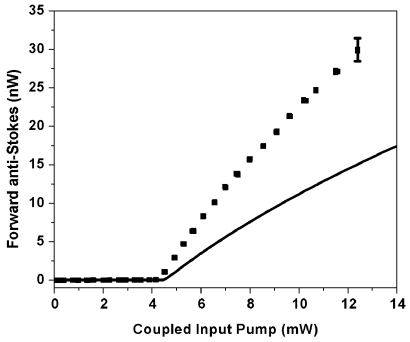

Figure 6.10: Forward anti-Stokes power as a function of the coupled input power on line-center at 66.56 psi (4.53 atm). Data are shown as squares and theory as a line. The measured and theoretical thresholds are the same but the theory is a factor of 2 smaller than the data.

The failure is that the anti-Stokes theory is again smaller than the data (by a factor of 2).

Experiment 2

The pump on TEM_{00} and Stokes on HG TEM_{10} mode was also observed for Experiment 2, as shown in Figure 6.11. In this case, the anti-Stokes was on a mode similar to LG TEM_{11}. However, the distribution of energy is incorrect – there should be more power in the center two spots and less in the outer ones. (For comparison, see Figure D.1.) This mode combination was taken at 45.39 psi (3.08 atm).

Figure 6.12 shows the forward anti-Stokes power as a function of the coupled input pump power. For this set of modes, the data and theory do not agree. The measured threshold is $\sim$2.4 mW while the theoretical threshold is closer to 2.7 mW. However, since the theory worked for the Experiment 1 data for this same pump and Stokes mode combination, the discrepancy between the measured and theoretical thresholds might be due to a calibration error. Appendix R contains some additional thoughts regarding phase-matching and this data set.

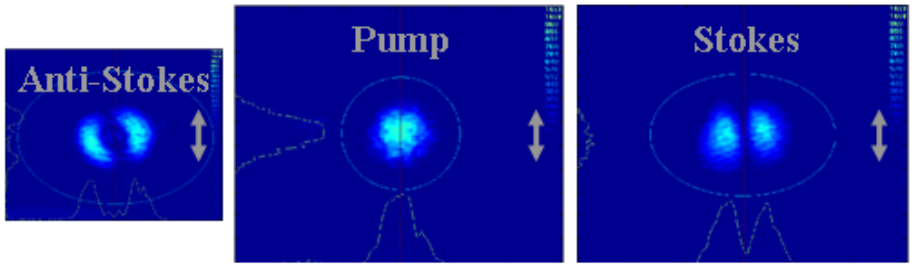

Figure 6.11: Spatial profiles of the pump, Stokes, and anti-Stokes at 45.39 psi (3.08 atm). The anti-Stokes profile looks similar to an LG TEM_{11} mode but does not have the correct distribution of energy. The profiles have been rescaled to account for the different path lengths from the cavity to the camera, as outlined in Appendix N. The grey arrow is 2.3-mrad long.

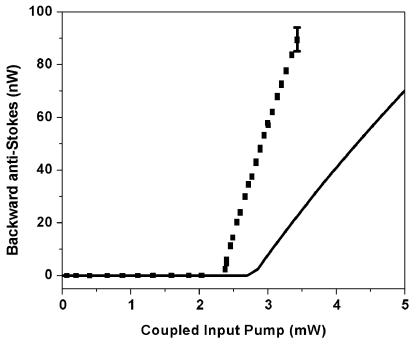

Figure 6.12: Forward anti-Stokes power as a function of the coupled input power on line-center at 45.39 psi (3.08 atm). Data are shown as squares and theory as a line.

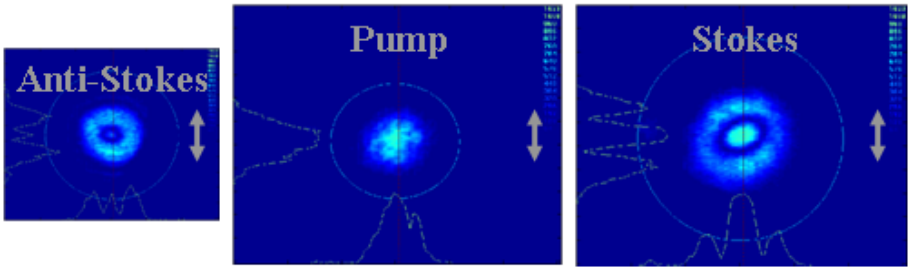

Figure 6.13: Spatial profiles of the pump, Stokes, and anti-Stokes at 45.72 psi (3.11 atm). The pump is TEM_{00} while both the Stokes and anti-Stokes resemble LG TEM_{10} modes. The profiles have been rescaled to account for the different path lengths from the cavity to the camera, as outlined in Appendix N. The grey arrow is 2.3-mrad long.

Pump TEM_{00}, Stokes LG TEM_{10}

This is Experiment 2 data taken at 45.72 psi (3.11 atm). The pump is on a TEM_{00} mode. The Stokes and anti-Stokes both appear to be LG TEM_{10}. In this case, it is necessary to show that both the Stokes and anti-Stokes are LG TEM_{10} modes. This will be done following the same procedure used to look at the pump and Stokes TEM_{00} mode and anti-Stokes LG TEM_{10} mode combination above. First, a comparison of the intensity distributions of the energy in central spot and ring to a true LG TEM_{10} mode, shown in Figure 6.5b. Figure 6.14a shows a cross-section of the anti-Stokes mode shown in Figure 6.13 and Figure 6.14b shows a cross-section of the Stokes mode. Both profiles have been rescaled such that the peak intensity is 1. The ratio between the peak intensity and the maximum intensity of the outer ring for a true LG TEM_{10} mode is ~ 0.2 (from Figure 6.5b). For the measured anti-Stokes mode (in Figure 6.14a), the peak to outer ring ratio is greater than 1. This is indicative that it is not an LG TEM_{10} mode. For the measured Stokes mode (in Figure 6.14b), the peak to side-lobe ratio is 0.48, which is closer to being the desired

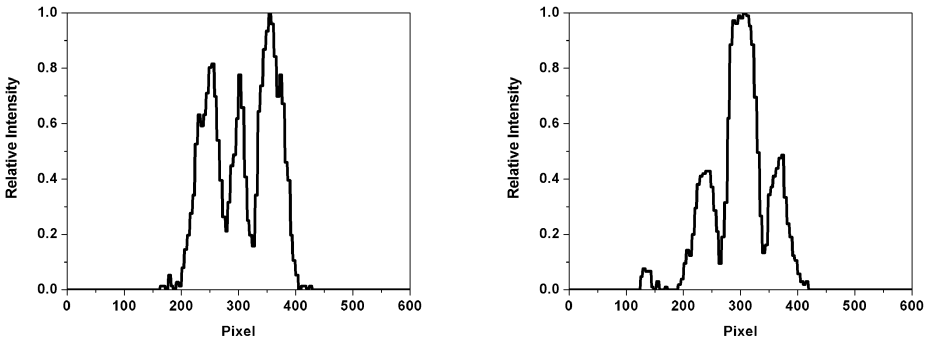

(a) Anti-Stokes Cross-Section. (b) Stokes Cross-Section.

Figure 6.14: Cross-sections of the measured anti-Stokes and Stokes profiles shown in Figure 6.13. Neither profile agrees perfectly with the LG TEM_{10}cross-section shown in Figure 6.5b. Both profiles have been rescaled so that their peak intensities are 1.

0.2 ratio but is not close enough. Therefore, neither the Stokes or anti-Stokes modes are LG TEM_{10} modes.

The semi-classical theory (as presented in Chapter 2) assumes that the Stokes mode is a pure mode profile. Therefore, even though the Stokes mode is not a pure LG TEM_{10} mode, for the theory, it is going to be assumed that both it, and the anti-Stokes mode, are LG TEM_{10} modes. Figure 6.15 plots the forward anti-Stokes power as a function of the coupled input pump power for this mode combination based on these assumptions. The data are shown as squares and the theory as a line. The measured and theoretical thresholds are in good agreement at 2.4 mW. But, the theoretical amount of anit-Stokes produced is again much lower than the data. This time the data is a factor of 4 times bigger than the theory. The measured forward anti-Stokes power for this mode combination is the second largest seen in these experiments. Appendix R contains some additional thoughts regarding phase-matching and this data set.

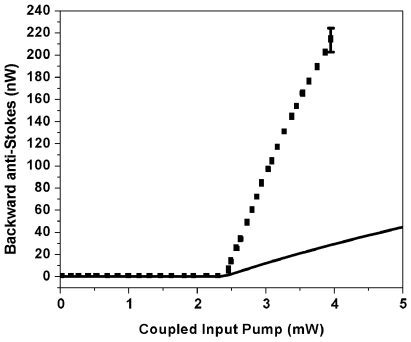

Figure 6.15: Forward anti-Stokes power as a function of coupled input pump power on line-center at 45.72 psi (3.11 atm). The measured and theoretical thresholds are both 2.4 mW. Data are shown as squares and theory as a line.

Pump TEM_{00}, Stokes HG TEM_{20}

The observed anti-Stokes mode when the pump was TEM_{00} and the Stokes was HG TEM_{20} in Experiment 1 varied. Of the nine data sets that were taken with this pump and Stokes mode combination, the anti-Stokes was seen with five different spatial profiles, some resembling various HG and LG modes but with incorrect intensity distributions. Figure 6.16 shows three of these five different spatial profiles.

In Figure 6.16b, the Stokes profile appears rotated relative to the horizontal and vertical axes of the picture but does not in Figures 6.16a and c. It is unclear what determines the cavity's symmetry, though it is most likely related to the mirrors. Whatever the process is, the symmetry axes of the spatial profiles from the cavity are canted with respect to the horizontal plane of the optics table. In Figure 6.16b, the horizontal axis of the pictures was aligned with the horizontal plane defined by the table and thus the Stokes profile appears at an angle. In Figures 6.16a and c, the camera had been rotated to better align with the axes defined by the profile resulting in the profiles not appearing at an angle. Rotated profiles will be observed

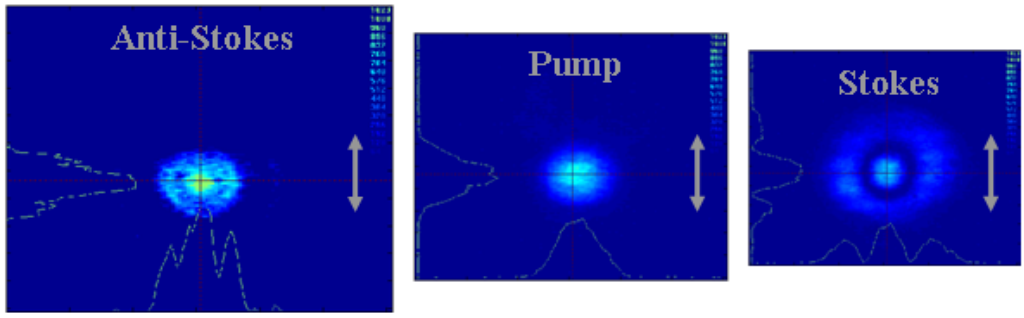

(a) 149.97 psi (10.2 atm)

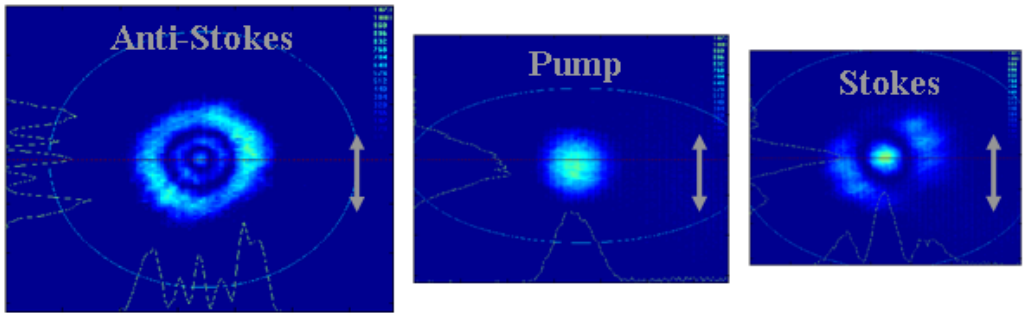

(b) 113.6 psi (7.73 atm)

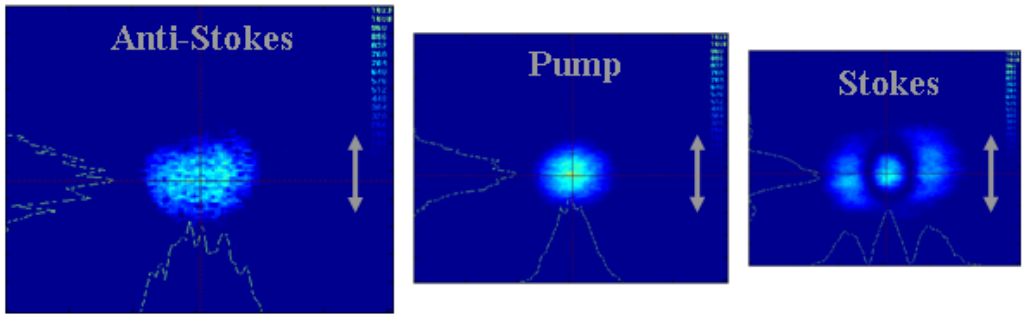

(c) 65.77 psi (4.47 atm)

Figure 6.16: Spatial profiles of the pump, Stokes, and anti-Stokes at three different pressures. The anti-Stokes profiles differ significantly from each other. The profiles have been rescaled to account for the different path lengths from the cavity to the camera, as outlined in Appendix N. The grey arrow is 2.3-mrad long.

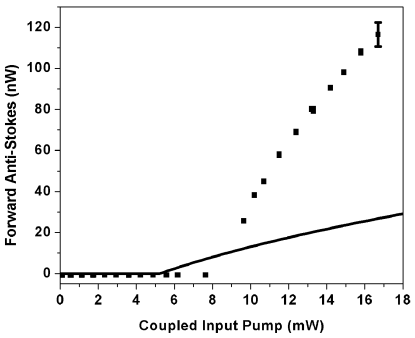

Figure 6.17: Forward anti-Stokes power as a function of coupled input pump power on line-center at 65.77 psi (4.47 atm). The measured threshold is ∼65% higher than the calculated threshold. Data are shown as squares and theory as a line.

occasionally throughout the rest of the chapter.

Figure 6.17 shows the forward anti-Stokes power as a function of the coupled input pump power at 65.77 psi (4.47 atm) corresponding to the spatial profiles in Figure 6.16c. In fitting the theory and data, the anti-Stokes was assumed to be a TEM_{00} mode (though, clearly, it is not). The calculated threshold is lower than the measured threshold by ∼3 mW. Or, in other words, the measured threshold is ∼65% higher than the calculated threshold. Not surprisingly given that the anti-Stokes profile shows that it is not a pure TEM_{00}, the measured anti-Stokes power is larger than the theoretical.

One possible reason for the threshold being incorrect is the assumption that the Stokes mode is HG TEM_{20}. Figure 6.18 shows the measured Stokes cross-section and a theoretical cross-section for a pure HG TEM_{20} mode. This indicates that the Stokes mode is probably not a pure HG TEM_{20} because of the intensity distribution between the central peak and the side-lobes.

This is the second time that the Stokes mode has been arguably not on a pure cavity mode. There are undoubtedly many possibilities that could explain

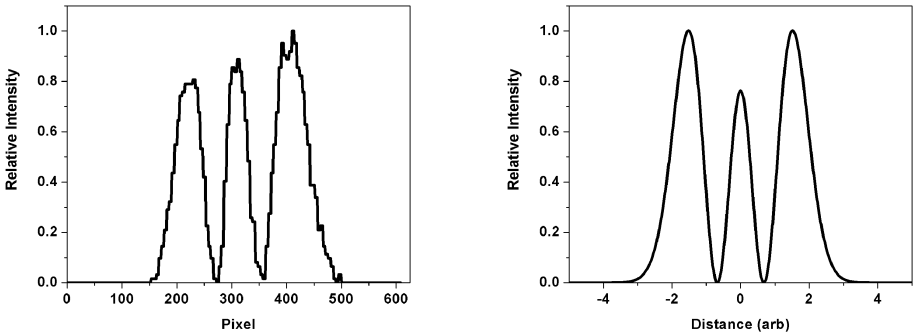

(a) Measured Cross-Section. (b) Theoretical Cross-Section.

Figure 6.18: Cross-sections of the measured Stokes profile and a pure HG TEM_{20} mode. The intensity distribution of the measured profile is not quite the same as in the theoretical cross-section. Both profiles have been rescaled so that their peak intensities are 1. They are not on the same horizontal scale.

this behavior, but only three will be presented here. First, it is possible that the "cold" cavity modes are being modified by the "hot" Raman medium. These effects have been observed in other systems [76, 77, 78] and lead to the non-Hermitian (nonorthogonal) modes. However, in those systems, the Raman medium is pumped much harder than in CW Raman system, so it is questioned how likely it is that this is occurring.

Second, the discrepancy could also indicate that more than one Stokes mode is lasing, which would require the modes to have nearly equal gain. This does not seem as likely since, when such effects were experimentally observed, it was impossible to stably frequency-lock the system, because of mode-switching. Also, if it were multiple modes running simultaneously, then a change in the profile should have been observed during tuning along with a corresponding jump in the output pump power because, at the least, the pump clamp level depends on the mode combination.

A third possibility is that the Stokes mode is not a HG mode but possibly an IG mode. Recall that as the ellipticity goes to zero (infinity), the IG mode becomes an LG

(HG) mode. This is significant because the HG modes have more of their intensity in the outer bands of the profile while the LG modes have their intensity more confined to the central spot. Therefore, as the ellipticity is increased from zero, the intensity must move from the center of the profile to the outer lobes. Figure 6.19 shows mode profiles of the IG TEM^{e}_{20} (rotated 90^{o} from the mode profile shown in Figure E.1) at a couple of ellipticities. Also shown on each profile are cross-sections from a horizontal slice through the middle of the profile. The ellipticities were chosen to best show how the mode evolves from one extreme to the other. Ellipticities between 3 and 6 appear to be better matches to the observed anti-Stokes cross-section in Figure 6.18. (For reference, the IG TEM^{e}_{20} appears to have potential for explaining the observed Stokes mode in Figure 6.13 with an ellipticity of $\sim$0.5. The ellipticity for the mode at 45.72 psi (3.11 atm) can differ from the mode in Figure 6.16c because they were taken with Experiments 2 and 1, respectively.) The most likely cause of ellipticity in the CW Raman laser system is the Raman mirrors. Perhaps, they are not perfectly spherical either due to their polishing or the deposition of the coating layers. Regrettably, the V_{FWM} overlap integral cannot easily be evaluated in elliptic symmetry. The IG modes can be written as sums of either the LG or HG modes[51]; however, this was not undertaken.

Pump TEM_{00}, Stokes HG TEM_{30}

This was an interesting Experiment 1 data set taken at 75.54 psi (5.14 atm). Partially through taking the data as a function of input power, the Stokes mode-hopped. Figure 6.20a shows a picture of the initial mode combination while Figure 6.20b shows the post-hop mode combination. A fair bit of effort was put into trying to keep the data set on one of the two mode-combinations. It should be noted that

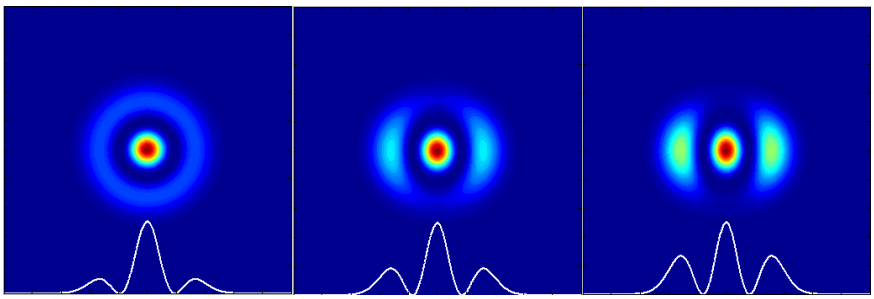

(a) 0. (b) 0.5. (c) 1.

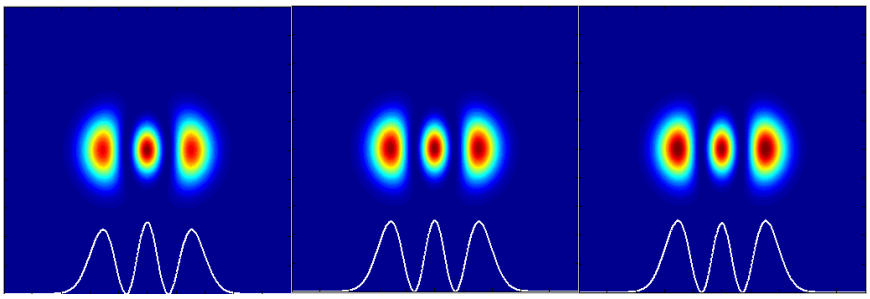

(d) 3. (e) 4. (f) 5.

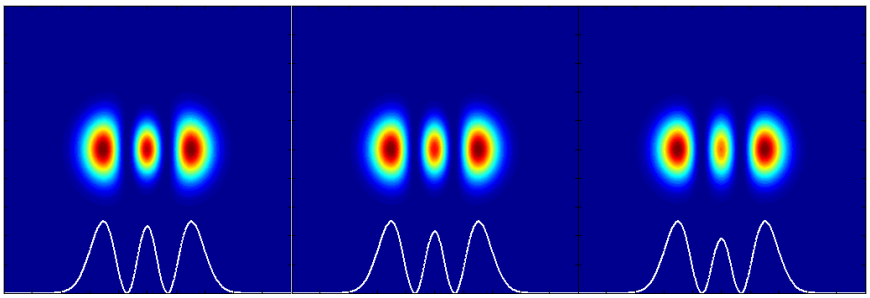

(g) 6. (h) 10. (i) Infinite.

Figure 6.19: IG TEM^{e}_{20} mode profiles taken at various ellipticities, as indicated by the sub-captions. When the ellipticity is zero, the IG TEM^{e}_{20} mode is equivalent to the LG TEM_{10} mode and when the ellipticity is infinite, it is equivalent to the HG TEM_{20} mode. Red areas are the most intense and blue are the least.

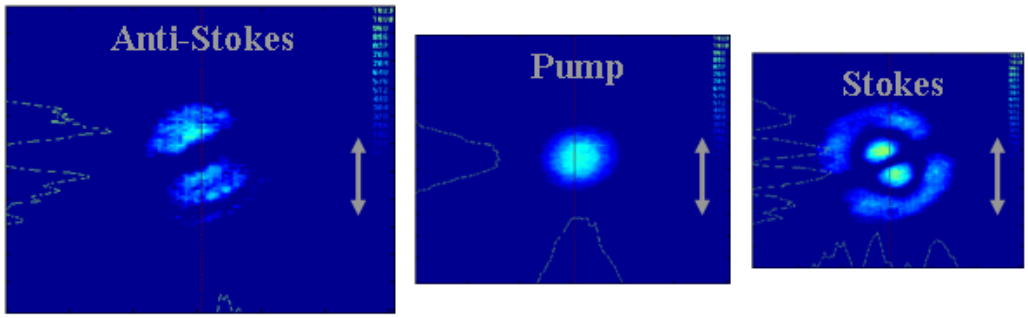

(a) Pre-hop.

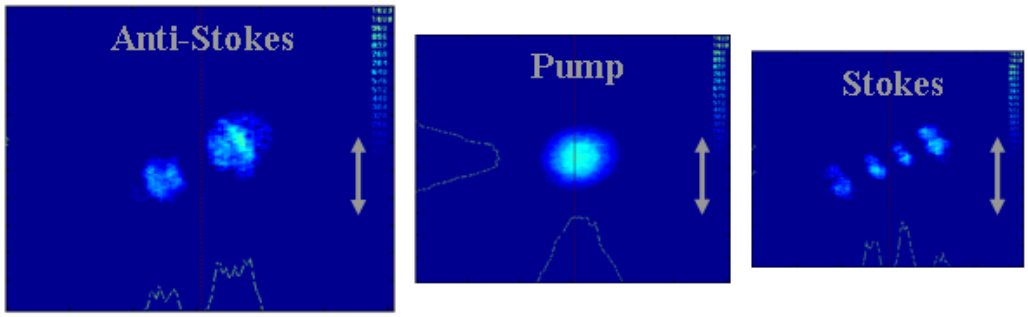

(b) Post-hop.

Figure 6.20: Spatial profiles of the pump, Stokes, and anti-Stokes before and after a mode-hop. The profiles have been rescaled to account for the different path lengths from the cavity to the camera, as outlined in Appendix N. The grey arrow is 2.3-mrad long. Both profiles were taken during a single data set at 75.54 psi (5.14 atm).

the initial mode-combination was verified to be on line-center while the final was not. It is thought that the symmetry of this system should be cylindrical but, as discussed in the previous section, there is some evidence that the symmetry might be elliptical. (In fact, the pre-hop Stokes mode looks a great deal like the IG TEM_{31} mode with ellipticity of 2 in Figure E.2 based on the bright spots at the end of the upper curve.) The pre- and post-hop anti-Stokes profiles are both unrecognizable as pure HG or LG spatial mode profiles. However, since both pre- and post-hop, the modes can be viewed as having three dark stripes in one axis and none in the other, it was thought that the mode that best characterized both modes was the HG TEM_{30}.

A puzzle that remains is what breaks the symmetry of the cavity – perhaps it is an asymmetry in the mirrors. Theoretically, modes with the same Gouy phase-shift should resonate at the same cavity length. However, it has been observed experimentally that the HG TEM_{10} mode resonates at a slightly different cavity length than the HG TEM_{01} mode. Because of this, if the frequency of the pump were such that the Stokes HG TEM_{10} mode were on line-center, then the HG TEM_{01} would not be exactly on line-center. It is thought that the pre-hop and post-hop modes shown in Figures 6.20a and b are modes of the same Gouy phase-shift, like the HG TEM_{10} and HG TEM_{01} modes. Therefore, it is thought that the post-hop modes shown in Figure 6.20 are most likely not on line-center.

Because there are some interesting features in all three output power versus input power curves, they will all be shown in Figure 6.21. In fitting the theory and the data, both the Stokes and anti-Stokes are assumed to be HG TEM_{30} modes. (This is a reasonable assumption for the Stokes (especially post-hop) but is more questionable for the anti-Stokes. However, the overlap integrals had already been performed for that combination, so it was used. A better assumption for the anti-Stokes profile might have been HG TEM_{10}.) Figure 6.21a shows the forward pump power as a

function of coupled input pump power. The behavior of the forward pump power below threshold is consistent with the theory. However, above threshold, the measured forward pump power does not immediately clamp. From experience, it is thought that this is due to the gain of the frequency locking system being improperly adjusted. Most likely, the gain is too high. The mode-hop can be seen at a coupled input pump power ∼12 mW. Theory and data are not in agreement.

Figure 6.21b shows the forward Stokes power as a function of coupled input pump power. The mode-hop is clearly visible around ∼12 mW. If the data from input pump powers ¿12 mw is extrapolated to the x-axis, it appears that the threshold would have been around 8 mW. However, because of the hop, the measured threshold was closer to 10 mW. The theoretical threshold is 6 mW.

Figure 6.21c shows the forward anti-Stokes power as a function of coupled input pump power. The mode-hop is least visible in this data set. If the assumption that the post-hop data is not on line-center is correct, then the anti-Stokes might not exhibit a drop in power for the reasons discussed in Chapter 3 regarding the tuning behavior of the system (on page 76).

Pump TEM_{00}, Stokes HG TEM_{40}

This mode combination was also often observed in Experiment 1. It was recorded a total of seven times over pressures from 40.83 psi (2.78 atm) to 95.53 psi (6.5 atm). With the exception of the data set at 99.26 psi (6.8 atm) (shown in Figure 6.1) where the anti-Stokes was not a recognizable mode in any symmetry, all of the previous mode combinations were obviously allowable. This is not the case with this mode combination. Assuming the symmetry of the system is rectangular, then allowable anti-Stokes modes will be those with both indices even. This requires that

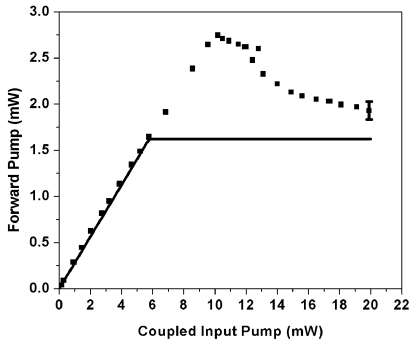

(a) Pump power.

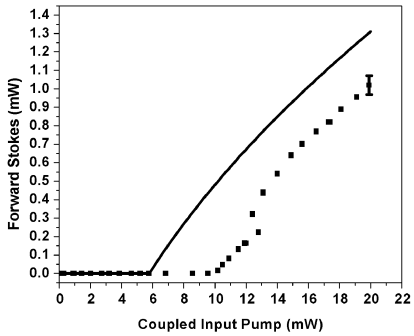

(b) Stokes power.

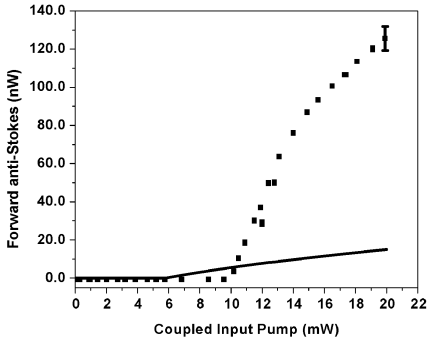

(c) Anti-Stokes power.

Figure 6.21: Forward pump, Stokes and anti-Stokes powers as functions of coupled input pump power on line-center at 75.54 psi (5.14 atm). The Stokes mode-hopped at a coupled input pump power of ∼12 mW. Data are shown as squares and theory as a line.

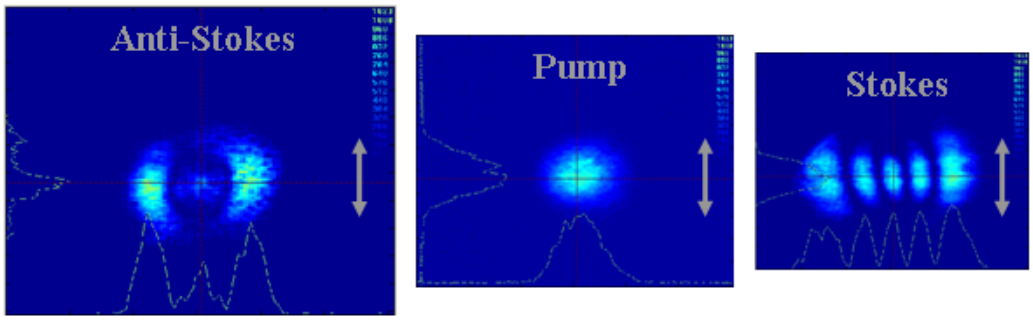

(a) 40.83 psi (2.78 atm)

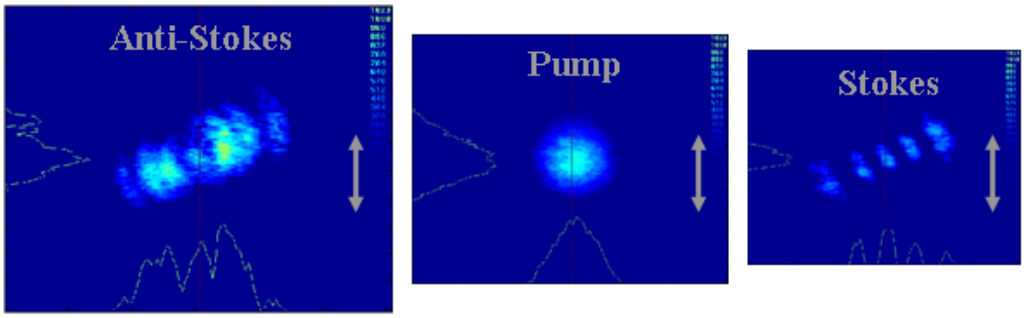

(b) 90.74 psi (6.17 atm)

Figure 6.22: Allowable spatial profiles of the pump, Stokes, and anti-Stokes at two different pressures. These anti-Stokes modes are considered allowable because they are bright centers like the Stokes profile. The profiles have been rescaled to account for the different path lengths from the cavity to the camera, as outlined in Appendix N. The grey arrow is 2.3-mrad long.

the anti-Stokes profile have a bright central spot. (The allowable mode combinations for rectangular symmetry are discussed on page 250.) Of the seven recorded mode combinations, five met this requirement. Two did not.

Figure 6.22 shows two of the five profiles that are consistent with the requirement. Figure 6.22a looks like a HG TEM_{20} but, again, the intensity distribution is incorrect. This mode combination was recorded three times. Figure 6.22b is an unrecognizable blur and was recorded twice.

Figure 6.23 shows the two profiles that appear to violate the rules regarding allowable mode combinations. The anti-Stokes profile in Figure 6.23a looks a bit

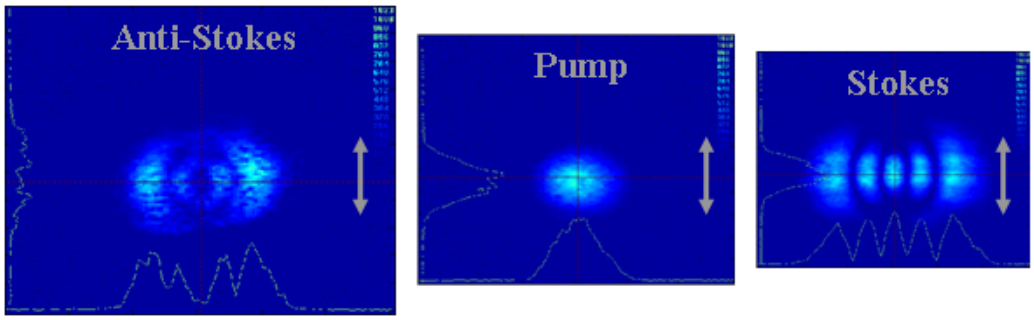

(a) 46.6 psi (3.17 atm)

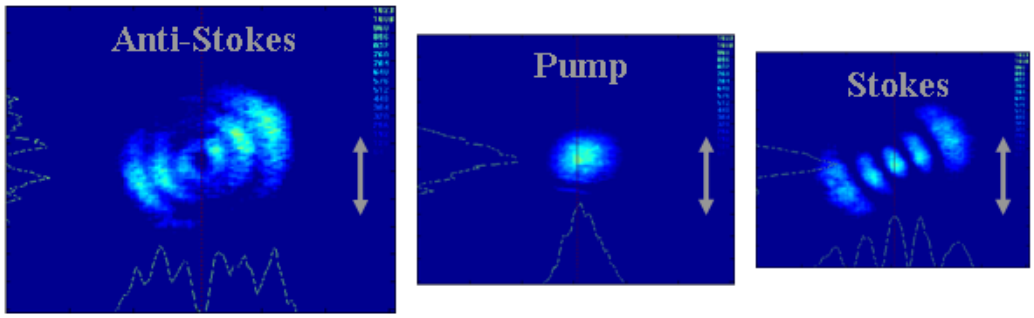

(b) 75.39 psi (5.13 atm)

Figure 6.23: Spatial profiles of the pump, Stokes, and anti-Stokes at two different pressures that appear to violate the rules for allowable mode combinations. Since the Stokes profile is bright at the center, the anti-Stokes profiles should be, too. The profiles have been rescaled to account for the different path lengths from the cavity to the camera, as outlined in Appendix N. The grey arrow is 2.3-mrad long.

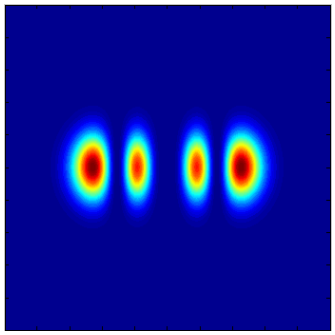

Figure 6.24: Superposition of modes that looks similar to the anti-Stokes mode in Figure 6.23a. The superposition is formed by the following mode combination $(-0.17 \times \mathrm{TEM}_{00} + 0.1 \times \mathrm{TEM}_{20} + 0.4 \times \mathrm{TEM}_{40})$, all of which would be allowable modes given the Stokes profile in Figure 6.23a.

like either an LG TEM_{11} or an HG TEM_{30} while the anti-Stokes profile in Figure 6.23b looks most like an LG TEM_{12}. However, the lobes in Figure 6.23b appear to be too close together to truly be an LG TEM_{12}. In both cases, the distribution of the intensity is incorrect.

In this dissertation, two methods of modeling the distribution of energy within a spatial profile have been investigated. The first looked at superpositions of either HG or LG modes. The second assumed that the modes were IG with an ellipticity somewhere between 0 and ∞. However, in this case, there is no known IG mode that would have the profile shown in either Figure 6.23a or b. Therefore, a superposition is going to be tried in order to show that the observed anti-Stokes mode is a combination of allowed modes.

Figure 6.24 shows a superposition of three HG modes that appears to give the correct structure when compared to the anti-Stokes mode in Figure 6.23a. The superposition has a central dark region with two bright lobes to either side of it. It was formed by adding and subtracting the fields of three HG modes, as given by $(-0.17 \times \mathrm{TEM}_{00} + 0.1 \times \mathrm{TEM}_{20} + 0.4 \times \mathrm{TEM}_{40})$. All three of the modes contributing to the superposition would be allowable modes!

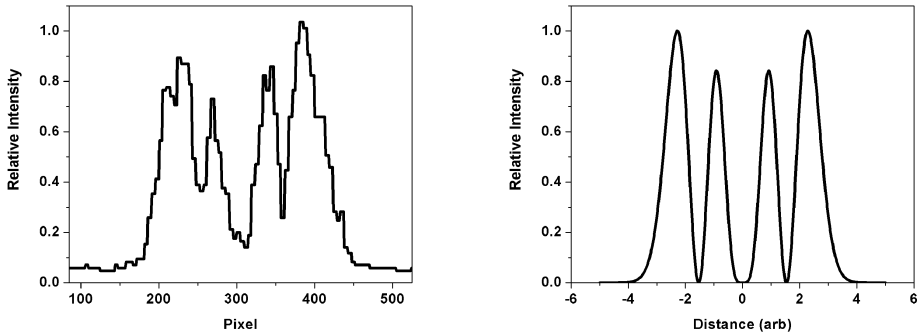

(a) Measured Cross-Section. (b) Theoretical Cross-Section.

Figure 6.25: Cross-sections of the measured anti-Stokes profile and a theoretical superposition of three HG modes given by $(-0.17 \times \mathrm{TEM}_{00} + 0.1 \times \mathrm{TEM}_{10} + 0.4 \times \mathrm{TEM}_{40})$. The distribution of energy in the theoretical cross-section is similar to the distribution in the measured cross-section. Both profiles have been rescaled so that their peak intensities are 1. They are not on the same horizontal scale.

Figure 6.25 shows cross-sections taken horizontally through the middle of the measured anti-Stokes profile in Figure 6.23a and the theoretical superposition in Figure 6.24. Both cross-sections have been rescaled such that the maximum intensity is 1. The intensity distribution in the theoretical superposition is comparable to the measured distribution. Using the same methods employed when investigating the anti-Stokes mode at 90.48 psi (6.2 atm), the width of the theoretical superposition can be compared to the width of the measured profile. The measured width between the maxima of the outer lobes is 155.4 pixels which corresponds to 404 μm and the calculated width is (as measured by the camera) $\sim$451 μm. The measured width is 90% of the calculated width. Since the measured anti-Stokes profile is angled slightly with respect to the axis of the cavity, it is conceivable that the measured width is small. Presumably, a superposition could also be found that reasonably approximates the anti-Stokes mode in Figure 6.23b.

Figure 6.26 shows the forward anti-Stokes power as a function of the coupled input

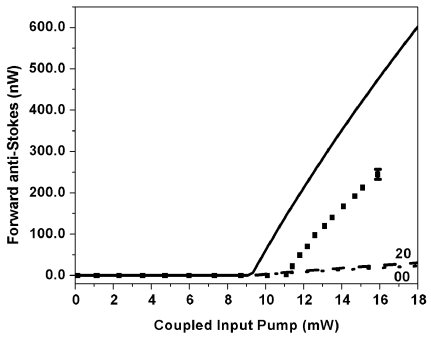

Figure 6.26: Forward anti-Stokes power as a function of coupled input pump power on line-center at 46.6 psi (3.17 atm). Data are shown as squares and theory as lines. The solid line assumes the anti-Stokes mode is HG TEM_{40}, the dashed assumes HG TEM_{20} and the dotted assumes HG TEM_{00}. The latter two are nearly indistinguishable.

pump power at 46.6 psi (3.17 atm), corresponding to the mode profiles in Figure 6.23b. The data is shown as squares and the theory as lines. There are three theoretical lines corresponding to the anti-Stokes mode being HG TEM_{40} (solid), HG TEM_{20} (dashed), and TEM_{00}(dotted). The Stokes mode was assumed to be HG TEM_{40}. The theoretical threshold again does not fit the data. The theoretical threshold is 9.2 mW and the measured threshold is 11.1 mW (or 1.2 $\times$the theoretical threshold). For this mode set, unlike the previous sets, the theoretical prediction, assuming the anti-Stokes is HG TEM_{40}, is larger than the data. Additionally, the measured anti-Stokes power is the largest seen in these experiments.

Pump HG TEM_{10}, Stokes HG TEM_{10}

To obtain this mode combination, in Experiment 1, the pump was mode-matched into the HG TEM_{10} mode instead of the HG TEM_{00} mode. Because the input pump mode profile is a well-defined TEM_{00} mode, it is very hard to mode-match into the HG TEM_{10} mode. When this data set was taken, their were about equal powers

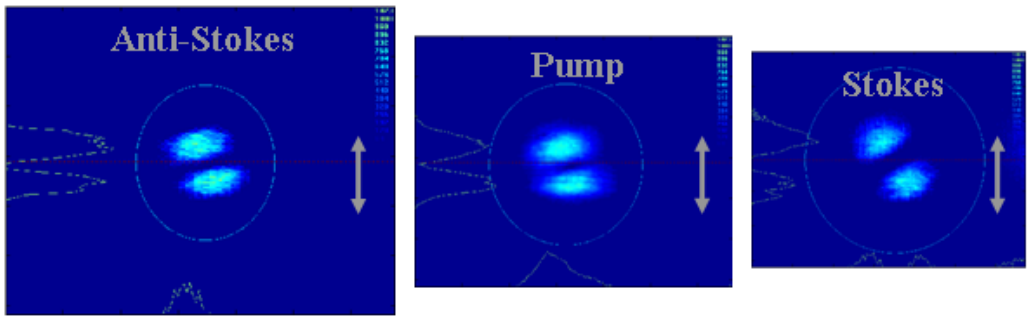

Figure 6.27: Spatial profiles of the pump, Stokes, and anti-Stokes at 154.65 psi (10.52 atm). Amazingly, all three profiles appear to have different axes of symmetry. The profiles have been rescaled to account for the different path lengths from the cavity to the camera, as outlined in Appendix N. The grey arrow is 2.3-mrad long.

coupled into the TEM_{00} and HG TEM_{10} modes. As such, the coupling efficiency into both modes was poor. Therefore, when taking the data, threshold was barely reached before the input pump power was maxed out. The data also looks like there might have been frequency locking issues, though there were no notes regarding any difficulties. Figure 6.28 shows the forward anti-Stokes power as a function of coupled input pump power.

The spatial profiles are shown in Figure 6.27. Interestingly, the symmetry axes for the three modes do not appear to be identical. Between the cavity and the camera, for each beam, there is only the Pellin-Broca, a couple of mirrors, the camera lens, and, possibly, a NB filter. None of these elements could rotate one beam profile relative to another. Therefore, it is thought that the observed rotation results from something associated with their generation in the Raman cavity, though the exact mechanism is unknown.

This mode combination is also interesting from an allowable mode combination perspective. In rectangular symmetry, the allowable anti-Stokes modes are determined only by the Stokes mode. As such, it is possible for the Stokes and anti-Stokes modes to be HG TEM_{10} regardless of the pump mode. In Figure 6.9b, the Stokes

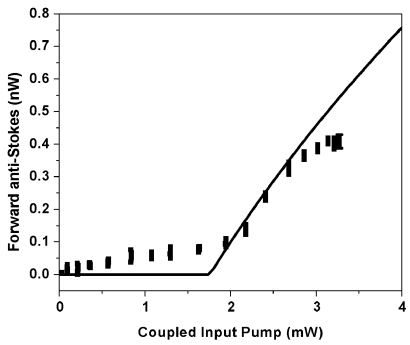

Figure 6.28: Forward anti-Stokes power as a function of coupled input pump power on line-center at 154.65 psi (10.52 atm). The slope of the data below threshold is due to scattered pump reaching the anti-Stokes power meter. Data are shown as squares and theory as a line.

and anti-Stokes are HG TEM_{10} but the pump is TEM_{00}.

The calculated threshold is 1.74 mW and the measured threshold is ∼2.2 mW (or 1.3 ×the calculated threshold). If a better data set was taken, it appears that the theory and data might agree for all three fields.

Discussion and Comparison

Comparison of the Amount of Anti-Stokes Generated

A great deal of data has now been presented. In order to properly compare the data, the pressure must be kept relatively constant among the data sets in order to keep the Raman gain constant. Luckily, there are two groups of three mode combinations at ∼46 psi (3.13 atm), one from each experiment. Table 6.1 provides cross-references to these modes, their mode-pictures and data sets. When the anti-Stokes spatial mode is not well-defined, the cell is left empty.

Figures 6.29a, c, and e show, from Experiment 1, the forward pump, Stokes, and anti-Stokes powers, respectively, as functions of the coupled input pump power while

Pressure	Pump	Stokes	Anti-Stokes	Mode Profiles	Data
45.11 psi (3.07 atm)	TEM_{00}	TEM_{00}	TEM_{00}	P.1	P.2
46.60 psi (3.17 atm)	TEM_{00}	HG TEM_{40}		6.23a	6.26
45.14 psi (3.07 atm)	TEM_{00}	HG TEM_{10}	HG TEM_{10}	P.3	P.4
45.70 psi (3.11 atm)	TEM_{00}	TEM_{00}	TEM_{00}	5.17	5.17
45.72 psi (3.11 atm)	TEM_{00}	LG TEM_{10}	LG TEM_{10}	6.13	6.15
45.39 psi (3.09 atm)	TEM_{00}	HG TEM_{10}	HG TEM_{10}	6.11	6.12

Table 6.1: Cross-references of data in Figure 6.29 with the mode structure and the figures that contain the pictures of the mode profiles and the data. When the anti-Stokes mode is not well-defined, the cell is left blank.

Figures 6.29b, d, and f show, from Experiment 2, the forward pump and backward Stokes and anti-Stokes powers as functions of the coupled input pump power. In each subplot, there are three curves representing three different mode combinations. They are labeled by the pressure they were taken at and can be cross-referenced using Table 6.1. Theoretical fits to the data in Figure 6.29 are not shown since they have been shown elsewhere in the dissertation and would clutter the figure.

From Chapter 3, in the undepleted pump limit, the above threshold pump field amplitude is given by equation 3.44, which is restated here:

$$A_{p\,ss} = \sqrt{\frac{\gamma_{cs} V_{ps\,o}}{2GV_{ps}}}. \tag{6.1}$$

Moving from one mode combination to the next in the same experiment at the same pressure, will only change the value of V_{ps}. The three HOM combinations in Figure 6.29a have very disparate values of V_{ps} while two of the three modes in Figure 6.29b have similar values.

The behavior of the forward pump, as V_{ps} changes, looks like the behavior seen when detuning the system (as shown in Figure 3.9). Namely, the threshold increase causes the pump clamp level to increase. However, when tuning, the value of G was changing, whereas, here, it is constant because all three data sets in Figures 6.29a

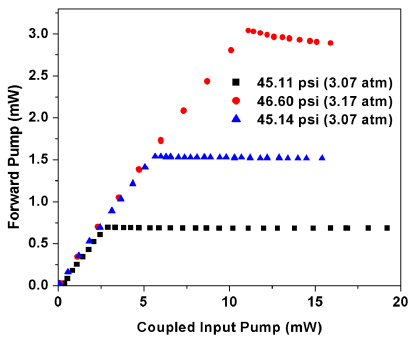

(a) Experiment 1 pump.

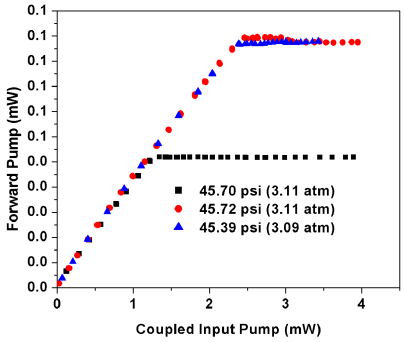

(b) Experiment 2 pump.

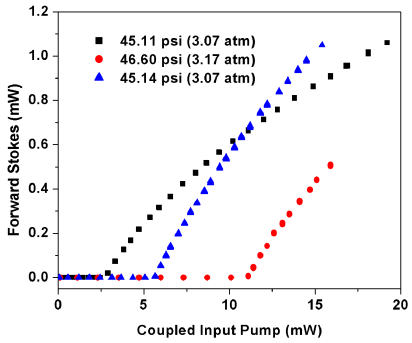

(c) Experiment 1 Stokes.

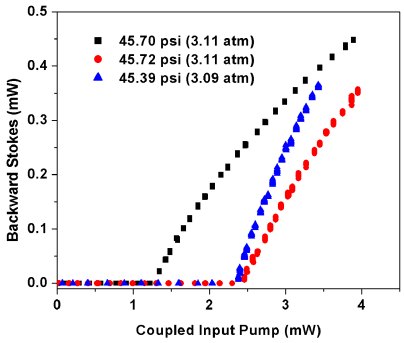

(d) Experiment 2 Stokes.

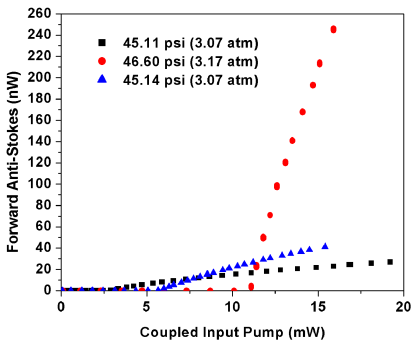

(e) Experiment 1 anti-Stokes.

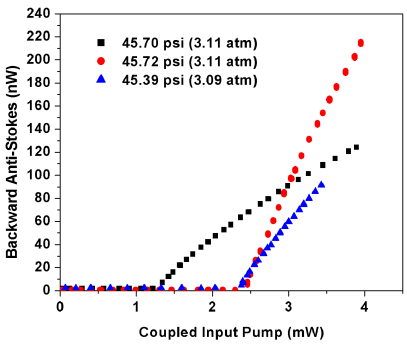

(f) Experiment 2 anti-Stokes.

Figure 6.29: Powers as functions of coupled input pump power on line-center for each experiment at three different pressures. The squares are for the fundamental combination of modes while the circles and triangles are different HOM combinations.

and b were taken on line-center at almost the same pressure. An effective gain, G_{eff} can be defined that takes into consideration the particulars of the mode combination, in addition to changes in pressure and detuning:

$$G_{eff} \equiv \frac{GV_{ps}}{V_{ps\,o}}. \tag{6.2}$$

Equation 3.45 governs the above threshold behavior of the Stokes field. It is restated here in terms of G_{eff}.

$$A_{s\,ss} = \sqrt{\frac{2V_p\omega_s}{V_s\omega_p G_{eff}\gamma_{cp}}\left(\frac{\gamma_{in\,p}A_{in\,p}}{\gamma_{cp}A_{p\,ss}} - 1\right)}. \tag{6.3}$$

Changing G_{eff} by switching from one mode-combination to another is effectively the same as detuning the system. As seen in the tuning discussion on page 76 of Chapter 3, the amount of Stokes produced is going to depend on the total amount of energy available to the system at any given coupled input pump power, leading to more Stokes being produced for HOM combinations than for the fundamental combination. This occurs in Figure 6.29c where two of the curves cross and almost occurs in d. It is unclear, theoretically, why the two HOM Stokes combinations in Figure 6.29d are not more similar, since the pump clamp levels for the same mode combinations are nearly identical.

The amount of anti-Stokes generated in the undepleted pump limit is given by equation on page 91, which is restated here, in terms of G_{eff}, for convenience.

$$A_{a\,ss} = -\frac{2}{\gamma_{ca}}\frac{\omega_a}{\omega_s}G_{eff}\,A_{p\,ss}^2 A_{s\,ss}\frac{V_s V_{FWM}^R}{V_a V_{ps}} \tag{6.4}$$

It is not quite as easy, here, to make parallels to the tuning discussion because as the system moves from one mode combination to the next, G_{eff}, $A_{p\,ss}$, $A_{s\,ss}$, V_{FWM}^R, and V_{ps} all change. However, the quantity $G_{eff}A_{p\,ss}$ is constant because it is the gain for the Stokes transition. As was done in the tuning discussion, it is now going to

be assumed that the amount of Stokes produced by the two mode combinations is equal. This leaves the question of how the ratio of V_{FWM}^{R} to V_{ps} changes from one mode-combination to the next. This is hard to determine because the theory did not always agree with the data.

However, the data in Figures 6.29e and f, looks a great deal like the results found when detuning (as shown in Figure 3.9). There, it was seen that the detuned anti-Stokes would cross the line-center anti-Stokes at an input power below that at which the detuned Stokes crossed the line-center Stokes. In Figures 6.29e and f, the anti-Stokes generated in the HOM combinations (circles and triangles) crosses (or nearly crosses) the fundamental combination (squares) at coupled input pump powers below those at which the Stokes crosses. This suggests that the ratio of V_{FWM}^{R} to V_{ps} is greater for these HOM combinations than for the fundamental combination.

Comparison of Pump Clamp Levels

There are two HOM combinations from Experiment 1 for which a comparison between the pump clamp level and Raman gain can be made, as was done for the fundamental mode combination. Because Experiment 1 is in the undepleted pump limit (meaning that the generated anti-Stokes is not strong enough to effect the pump and Stokes), only the pump and Stokes modes matter to this analysis.

Figure 6.30 shows the pump clamp level as a function of pressure for five mode combinations, including the data for the fundamental mode combination from Figure 5.14a. On the figure, there is both data (symbol) and theory (line) for each mode combination. The legend in the upper right corner indicates the Stokes mode. The pump mode is always TEM_{00}. As expected theoretically, the pump clamp level increases from the fundamental mode combination to the HOM combinations at a given pressure. Though the data is noisier when the Stokes is TEM_{20}, TEM_{30}, TEM_{40}

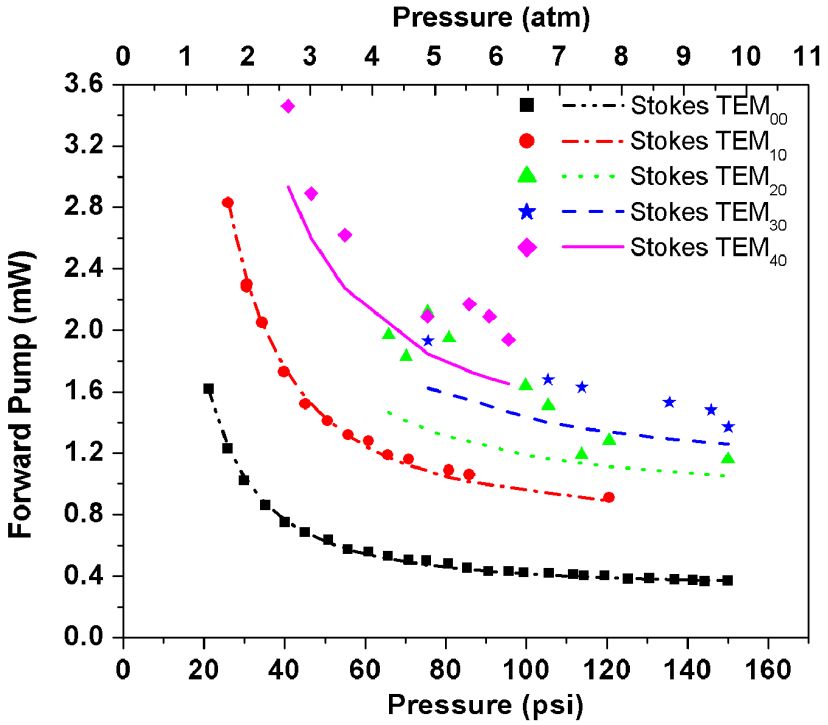

Figure 6.30: Forward pump power as a function of pressure for five different mode combinations. The pump mode is TEM_{00} for all the mode combinations and the Stokes mode designation is given in the upper right corner. The symbol is the data for that mode combination and the line is the associated theory. For a given pressure, the pump clamps at a higher power level as the Stokes order increases.

than when it is TEM_{00} and TEM_{10}, it also appears that the clamp level increases as the order of the Stokes mode increases.

Concluding Thoughts

This chapter focused on HOM combinations. It began by looking at the mode structure of the anti-Stokes profiles. Both the distribution of the intensity and the width of the profile were used as tools to help identify the mode. When necessary, superpositions of theoretically allowed modes were assembled to match mode profiles that were either not well-defined modes or were not obviously allowed modes. At times, the modes appeared to be IG instead of HG or LG.

An attempt to fit the theory to the data was made for every observed mode combination, with varying degrees of success. In general, theory and data matched better for lower order mode combinations. It is thought that this is partially because the Stokes and anti-Stokes mode profiles are not exactly the profiles assumed when calculating the theory.

A comparison was also made among three mode combinations for each experiment at comparable pressures. The effect on the pump, Stokes, and anti-Stokes data as the mode combination was switched was found to be very similar to the effect on them as the system was detuned. This led to the definition of an effective gain which took into consideration the effects of detuning, pressure, and mode combination. With this new definition, the behavior of the pump and Stokes as the mode combination was switched became very easy to explain because it was completely analogous to their behavior when detuned. The anti-Stokes behavior was harder to explain theoretically. Thus, the last point needed in understanding the anti-Stokes behavior was extrapolated from the data. The data showed that more anti-Stokes could be produced for HOM

combinations than for the fundamental above certain values of the coupled input pump power.

Finally, the behavior of the pump clamp level as a function of pressure was briefly examined. The pump clamp level increased as pressure decreased and as the Stokes mode increased in order.

CONCLUSION

Summary

The focus of this dissertation has been understanding anti-Stokes generation in a CW Raman laser. It began with a brief discussion of the operation of a CW Raman laser, including some of the differences in the system that arise when generating anti-Stokes versus Stokes. The historical development of the CW Raman laser was presented next, to place the work of this dissertation into context.

Chapter 2 presented a semi-classical theory, extended to include HOM combinations. The result was a set of three coupled time-dependent differential equations governing the pump, Stokes, and anti-Stokes produced by the laser. These were numerically integrated in Chapter 3 so that the behavior of the three fields could be investigated as functions of time, input pump power, and detuning. Based on the numerically integrated results, two analytic steady-state solutions to the time-dependent CW Raman laser equations were derived. Both solutions are valid only on line-center. One of the solutions is valid only when the anti-Stokes generated by the system is not strong enough to significantly affect the generated pump and Stokes while the other is valid for any amount of generated anti-Stokes.

When trying to generate anti-Stokes with a CW Raman laser, additional experimental difficulties that arise which had posed no problems for Stokes generation. The goal of Chapter 4 was to clarify these difficulties, most of which are related to the index of refraction of the H_2, and discuss how to overcome them. Also discussed in Chapter 4 was the behavior of the optical powers as the pressure within the system was changed.

The experimental results from these studies of anti-Stokes generation are presented

in Chapters 5 and 6. Chapter 5 focused on the fundamental mode combination (with pump, Stokes and anti-Stokes on the TEM_{00} mode). It compared data and theory as functions of input pump power, detuning, pressure, and anti-Stokes reflectivity. Data and theory compared well. Chapter 6 looked at other mode combinations involving any of the three fields on HOM. The produced anti-Stokes mode was compared to theoretical modes. Often, the measured mode was found to look similar to the theoretical modes but did not have the proper distribution of intensity throughout the profile to be the theoretical mode. In addition, the amount of anti-Stokes produced as a function of input pump power was compared to theory. Comparisons were also made among the various mode combinations.

In this dissertation, five ways were found to increase the amount of anti-Stokes produced. They are:

1. Increase the input pump power. For a given mode, at a given pressure, increasing the input pump power will lead to more anti-Stokes being emitted. However, since, above threshold, the anti-Stokes is dependent on the square root of the input pump power, at some point increasing the input pump power will lead to minimal gain in the generated anti-Stokes.

2. Detune from gain line-center. This only works for input pump powers greater than three times the line-center threshold for that mode combination at a given pressure. But, if the input pump power is large enough, this can lead to significant increases in the amount of anti-Stokes produced.

3. Decrease the pressure. As the pressure is decreased, the phase-matching for the anti-Stokes improves, leading to more anti-Stokes generation.

4. Increase the anti-Stokes reflectivity of the cavity mirrors. Increasing the reflectivity, increases the amount of anti-Stokes that can build-up within the optical cavity and, thus, the amount emitted. Even a modest increase in the reflectivity can lead to much more anti-Stokes generation, as seen when switching from Experiment 1 to Experiment 2.

5. Use a HOM. The anti-Stokes produced for a HOM combination can exceed the amount produced for the fundamental combination. As with detuning (and for the similar reasons), this will only work at some input pump powers. The powers it will work at are dependent on the particular mode combination.

Thoughts for the Future

There are many subjects in this dissertation that would benefit from further investigation. In many ways, there seem to be more questions raised as a result of this work than were answered.

A first pass at a theory for the CW Raman laser which included the possibility of HOM's was made. This theory worked fairly well for lower HOM combinations, such as the combination with the pump a TEM_{00} mode and the Stokes and anti-Stokes HG TEM_{10} modes. But, it seemed to become more and more discrepant from the data as the order of the Stokes mode was increased. Possibly, this is due to the modes not being HG or LG, for which the overlap integrals can easily be calculated, but IG. If this is the case, it is possible that the problem with the theory for HOM combinations stems from not being able to calculate the overlap integrals in elliptic coordinates. Thus, further development of the IG modes and their integration might be beneficial.

The theory also did not easily cover the possibility of the anti-Stokes being a superposition of modes. Often when superpositions were seen, it seemed that the

predicted anti-Stokes power was far smaller than that measured. This could be evidence that the anti-Stokes modes are somehow augmenting each other.

There seems to be some evidence that the symmetry of the CW Raman laser system is elliptical instead of cylindrical or rectangular. Perhaps, the cause of the asymmetry in the system is due to the polishing of the mirrors or the deposition of the mirror coatings. A measurement of the curvature of the mirrors might help illuminate this mystery.

And, lastly, it was not possible, given the losses of the mirrors, to perform an experiment with both cavity mirrors highly-reflective at the anti-Stokes. It is felt that the system will have to be much more pressure and temperature stable than the existing system in order to achieve resonance. But, if resonance can be achieved, the theoretical amount of anti-Stokes generated could be near the quantum-limit.

APPENDICES

APPENDIX A

ACRONYMS

Below is an alphabetical list of the acronyms used throughout this thesis along with their meanings.

Acronym	Meaning
AFA	Adibatic Following Approximation
AOM	Acousto-Optic Modulator
CW	Continuous-Wave
CWRLE	Continuous-Wave Raman Laser Equation
EOM	Electro-Optic Modulator
FOR	Far-Off Resonance
FSR	Free Spectral Range
FWM	Four-Wave Mixing
HFC	High Finesse Cavity
HG	Hermite-Gaussian
HWP	Half-Wave Plate
IG	Ince-Gaussian
LG	Laguerre-Gaussian
NB	Narrow Band
PBS	Polarizing Beam Splitter

ppm	parts per million
QWP	Quarter-Wave Plate
SVAA	Slowly Varying Amplitude Approximation
SVEA	Slowly Varying Envelope Approximation
TDSE	Time-Dependent Shrodinger Equation

APPENDIX B

VARIABLES AND NOTATION

Below is a list of the mathematical notation used in this thesis. The first column gives the general symbol, without any of the subscripts that might be associated with it. The second column gives the meaning of that variable, the units (in standard MKS units), and any other associated versions of it, usually due to additional subscripts. The list is organized alphabetically with the Greek symbols following the Roman symbols. Regrettably, some symbols are used more than once, but, in most cases, the context of the usage will indicate which meaning is appropriate. Also included in the list are the physical constants used throughout the thesis and the meanings of the various subscripts.

Subscripts that are numbers can have a variety of meanings. In the case of frequencies, like ω_1 or ω_{23}, or elements of the interaction potential or dipole matrix (V_{12} or μ_{23}respectively), they are referring to molecular energy levels. They can be mode indices, like TEM_{11} mode. They can also refer to the front or back of the cavity, like R_{p1} and R_{p2} which are the power reflectivities for the front (input) and back cavity mirrors at the pump wavelength. Again, usage context should indicate which meaning is appropriate.

Variable	Meaning. (*Units*) [Associated forms]
A	Electric field amplitude. (V/m) $[A_q,\ A_p,\ A_s,\ A_a,\ A_{in\,p},\ A_{p\,ss},\ A_{s\,ss}]$
A	Absorption (and all other losses in an optical cavity). (*unitless*)
A_T	Transverse Area. (m^2)
a_q	Coefficient of the AC Stark shift associated with molecular level 1. ($V^2 s/m^2$) $[a_p,\ a_s,\ a_a]$
a	Subscript – Quantity is dependent on the anti-Stokes wavelength.

a Eigenvalue associated with IG modes. (*unitless*)

$\overrightarrow{B}$ Magnetic field. (*tesla*)

b Constant associated with Ince polynomials. (*unitless*) $[b_0, b_1]$

b_q Coefficient of the AC Stark shift associated with molecular level 3. (V^2s/m^2) $[b_p, b_s, b_a]$

b Subscript – Indicates light traveling in the backward direction, i.e. in the opposite direction of the input field, from an optical cavity.

C_n Wavefunction amplitude. (*unitless*) $[C'_n, C_1, C_2, C_3]$

c Constant – speed of light in vacuum. (m/s)

c Subscript – Associated with the cavity.

$\overrightarrow{D}$ Electric displacement field. (C/m^2)

D Population difference between ground state and first excited vibrational state. (*unitless*) $[D_{eq}]$

d_q Coefficient of the two-photon Rabi frequency. (V^2s/m^2) $[d_p, d_s, d_o]$

$\overrightarrow{E}(\overrightarrow{r}, t)$ Complex electric field. (V/m)

$\overline{E}(\overrightarrow{r}, t)$ Complex electric field envelope. (V/m) $[\overline{E}_q, \overline{E}_p, \overline{E}_s, \overline{E}_a, \overline{E}_{in}]$

$E(t)$ Complex electric field envelope. (V/m) $[E_q, E_p, E_s, E_a, E_{in}]$

e Superscript – Even.

eq Subscript – Equilibrium value.

$\mathcal{F}$ Finesse. (*unitless*)

f Frequency – could be either an optical frequency or a cavity resonance frequency. (Hz) $[f_p,\ f_{plc},\ f_c]$

f Subscript – Indicates light transmitted in the forward direction, i.e. in the same direction as the input field, from an optical cavity.

G Raman gain. ($m^2/(V^2 s)$) $[G_{eff}]$

$\overrightarrow{H}$ Magnetic field. (A/m)

HM Subscript – Half-maximum.

H Hamiltonian. (J)

$\hbar$ Constant – Plank's constant ($J\ s$)

I Subscript or superscript – Indicates the imaginary part of the given quantity.

in Subscript – Associated with an input field.

$\overrightarrow{J_f}$ Free current. (C/s)

k Wave number. ($1/m$) $[k_p,\ k_s,\ k_a]$

L Cavity length. (m)

l Spatial mode index. (*unitless*)

lc Subscript – Line center.

$\overrightarrow{M}$ Magnetization. (A/m)

m Subscript – Spatial mode profile/index.

m Subscript – Electronic energy level.

m Subscript – Measured quantity.

N Number density. (*unitless*)

N_A Constant – Avogadro's number. (*molecules/mole*)

n Index of refraction. (*unitless*) $[n_{nl}]$

n Energy level. (*unitless*)

n Subscript – Spatial mode profile/index.

n Subscript – Electronic energy level.

nl Subscript – Non-linear.

o Subscript – Initial condition.

o Superscript – Odd.

$\overrightarrow{P}(\overrightarrow{r},t)$ Polarization. ($C^2\,V/(N\,m^3)$)

$\overline{P}(\overrightarrow{r},t)$ Polarization envelope. ($C^2\,V/(N\,m^3)$) $[\overline{P}_q, \overline{P}_p, \overline{P}_s, \overline{P}_a]$

$P(t)$ Polarization envelope. ($C^2\,V/(N\,m^3)$) $[P_q, P_p, P_s, P_a]$

P Pressure. (atm)

$\mathcal{P}$ Power external to the cavity. (W) $[\mathcal{P}_{p1}, \mathcal{P}_{p2}, \mathcal{P}_{s1}, \mathcal{P}_{s2}, \mathcal{P}_{a1}, \mathcal{P}_{a2}]$

p Subscript – Quantity is dependent on the pump wavelength.

q Transverse mode index. (*unitless*) $[q_p, q_s, q_a]$

q Subscript – Quantity is wavelength dependent.

R Mirror power reflectivity. (*unitless*) $[R_1, R_2, R_{p1}, R_{p2}, R_{s1}, R_{s2}, R_{a1}, R_{a2}]$

R Subscript or superscript – Indicates the real part of the given quantity.

R_c Mirror (or field) radius of curvature. (m)

r Radial direction.

$\overrightarrow{r}$ Three-dimensional position. (m)

rel Subscript – Indicative of a relative quantity.

r_p Pump rate. (*unitless*)

S Scale factor for pictures. (*unitless*) $[S_s, S_a]$

s Subscript – Quantity is dependent on the Stokes wavelength.

ss Subscript – Steady-state value.

T Mirror power transmittivity. (*unitless*) $[T_1, T_{p1}, T_{p2}, T_{s1}, T_{s2}, T_{a1}, T_{a2}]$

T Temperature. (K)

t Time. (s)

th Superscript – Threshold value.

$u(\overrightarrow{r})$ Spatial dependence of electric field. (*unitless*) $[u_n, u_q, u_p, u_s, u_a]$

V Interaction potential. (J) $[V_{mn},\ V_{12},\ V_{23},\ V_{13}\ ]$

V Mode overlap volume. (m^3) $[V_q,\ V_p,\ V_s,\ V_a\ ]$

$V_{q\,q'}$ Overlap volume. (m^3) $[V_{ps},\ V_{pa},\ V_{ps\,o}]$

V_{FWM} Overlap volume. (m^3)

v Speed of light in a medium. (m/s)

w_o Minimum beam waist. (m) $[w_{oq},\ w_{op},\ w_{os},\ w_{oa}\ ]$

w Beam radius. (m) $[w_q,\ w,\ w_s,\ w_a\ ]$

x Direction perpendicular to propagation direction.

x Arbitrary cavity length. (m)

y Direction perpendicular to propagation direction.

z Direction parallel to propagation direction.

z_o Rayleigh range. (m)

α_g Plane-wave gain coefficient. $(C^2 s/(N\,V^2))$

α_{go} Small-signal gain coefficient. $(\,V^2 s^2\,C^4/(m^5 N))$

β Ratio of steady-state anti-Stokes field amplitude to steady-state Stokes field amplitude when $\delta = 0$. $(unitless)$ $[\beta_+,\ \beta_-\ ]$

Γ_{31} Population decay rate. (rad/s)

γ_{in} Input coupling coefficient. (rad/s) $[\gamma_{in\,p}]$

γ_{13} Cavity loss coefficient. (rad/s) $[\gamma_{cq},\ \gamma_{cp},\ \gamma_{cs},\ \gamma_{ca}\ ]$

δ Detuning from Raman resonance. (rad/s)

ϵ Ellipticity of IG modes. ($unitless$)

ε_o Constant – permittivity of free space. (N/A^2)

ε Permittivity in a medium. (N/A^2)

ζ By definition, $\zeta = \frac{\omega_a V_s \gamma_{cs}}{\omega_s V_a \gamma_{ca}}$. Used in the steady-state solution of the CWRLE when $\delta = 0$. ($unitless$)

η Conversion efficiency. ($unitless$) $[\eta_s, \eta_a]$

η Angular coordinate in elliptic geometry.

η Ratio of the power before an optic to the power after. ($unitless$) $[\eta_q, \eta_p, \eta_s, \eta_a]$

θ Azimuthal direction in cylindrical coordinates.

θ_{cone} Anti-Stokes cone angle. ($unitless$)

κ Wavenumber. ($1/m$)

λ Wavelength. (m) $[\lambda_q, \lambda_p, \lambda_s, \lambda_a]$

μ Electric dipole moment matrix element. ($C\ m$) $[\mu_{mn}, \mu_{12}, \mu_{23}]$

μ_o Constant – permeability of free space. ($C^2/(N\ m^2)$)

ξ Radial coordinate in elliptic geometry.

Π Intracavity power. (W)

ϖ Arbitrary sum of angular frequencies. (rad/s)

ϖ In V_{FWM} calculations, it is used to define sums of beam radii. (m) [ϖ_o]

ρ Electric charge. (C) [ρ_f, ρ_b]

ρ Number density. (*unitless*) [ρ_o]

ρ_{mn} Coherence between molecular levels. (*unitless*) [$\tilde{\rho}_{mn}$, ρ_{13}, ρ_{12}, ρ_{32}]

ρ_{mm} Population of molecular levels. (*unitless*)

σ Conductivity. (*1/(Ωm)*)

Υ Argument of the Gaussian portion of V_{FWM} integrand. ($1/m^2$)

ϕ Electric field phase. (*rad/s*) [ϕ_q, ϕ_p, ϕ_s, ϕ_a]

$\chi^{(1)}$ Linear electric susceptibility. (*unitless*)

$\chi^{(3)}$ Third order electric susceptibility. (m^2/V^2)

ψ Wavefunction. (*unitless*)

Ω_{13} Two-photon Rabi frequency. (*rad/s*)

Ω_{nn} AC Stark shift. (*rad/s*) [Ω_{11}, Ω_{33}]

ω Optical frequency. (*rad/s*) [ω_q, ω_p, ω_s, ω_a]

ω_c Cavity resonance frequency. (*rad/s*) [ω_{cq}, ω_{cp}, ω_{cs}, ω_{ca}]

ω_n Frequency associated with the energy of a molecular energy level. (*rad/s*) [ω_1, ω_2, ω_3]

ω_{mn} Frequency separation of molecular energy levels. (*rad/s*) [ω_{31}, ω_{32}, ω_{21}]

APPENDIX C

HERMITE-GAUSSIAN MODES

The rectangularly symmetric laser cavity modes are the Hermite-Gaussian (HG) modes [47, 46]. This is only one of the three possible symmetries discussed in this dissertation, but is the most well-known and most likely to be fully presented in optics texts [47, 46].

The functional form of the HG modes is

$$\begin{aligned} u(\overrightarrow{r}) &= u(x,y,z) \\ &= \frac{w_o}{w(z)}\sqrt{\frac{1}{2^{l+m}l!m!}}\exp\left[-i(l+m+1)\arctan\left[\frac{z}{z_o}\right]\right]\mathrm{H}_l\left[\frac{\sqrt{2}x}{w(z)}\right] \\ &\quad \mathrm{H}_m\left[\frac{\sqrt{2}y}{w(z)}\right]\exp\left[\left(-\frac{ik}{2R_c(z)}-\frac{1}{w^2(z)}\right)\left(x^2+y^2\right)\right]\sin\left[kz\right] \end{aligned} \tag{C.1}$$

where w_o is the ($1/e$ radius in field) beam waist, $w(z)$ is the spot size (again, $1/e$ radius in field) at a distance z from the waist, l and m are the spatial mode indices, z_o is the Rayleigh range, H_l and H_m are Hermite polynomials, $R_c(z)$ is the wavefront radius of curvature at z, and k is the wavenumber. From [46] page 83,

$$w_o = \left(\frac{\lambda z_o}{\pi}\right)^{\frac{1}{2}} \tag{C.2}$$

$$w(z) = w_o\left[1+\left(\frac{z}{z_o}\right)^2\right]^{\frac{1}{2}} \tag{C.3}$$

$$R_c(z) = z\left[1+\left(\frac{z_o}{z}\right)^2\right] \tag{C.4}$$

The Rayleigh range, z_o, is calculated using equation C.4 by setting $z = L/2$ and R_c to the cavity mirror's radius of curvature. The Hermite functions are standard orthogonal polynomials that can be found in most math tables (for example, reference [79] section 6.10). The factor $\exp\left[-i(l+m+1)\arctan\left[\frac{z}{z_o}\right]\right]$ in equation C.1 is known as the Gouy phase factor which is responsible for shifting the resonance frequency of the higher-order modes away from the resonance of the fundamental mode. The lowest order mode, for which $l = m = 0$, is known as the fundamental (or TEM_{00}) mode and takes the same form regardless of the symmetry of the cavity.

This functional form of the HG modes differs from the form presented in some of the standard textbooks in a couple of ways, as can be seen by a comparison to the forms on page 644 in Siegman [47] and on page 124 in Yariv [53].

1. The functional form of $u(\overrightarrow{r})$ in Siegman has units of 1/m whereas the above form is unitless. As discussed below equation 2.18, this change was necessary so that $E(t)$ would still have units of electric field. This change was accomplished by multiplying the $u(\overrightarrow{r})$ by w_o. Also due to this change in normalization, Siegman's form is multiplied by $\frac{1}{\sqrt{\pi}}$ whereas the above form is not. These changes agree with Yariv's form.

2. Siegman's form is not proportional to either $\exp(ikz)$ like Yariv's nor $\sin(kz)$ as in equation C.1. The former indicates a traveling wave in the z-direction. The latter is more indicative of standing waves within the optical cavity.

Figure C.1 shows pictures of the intensity distributions, $|u(\overrightarrow{r})|^2$, of the lowest order modes – red indicating the most intense portions and blue being the least. The following parameters were used in the calculation of the profiles in Figure C.1: z_o= 13.3 cm (cavity length of 7.62 cm and mirror radius of curvature of 50 cm), λ= 435 nm, and $z = 0$. As can be seen from the figure, in this symmetry, the indices l and m of the TEM_{lm} modes indicate the number of nulls in the mode profiles in the x and y-directions, respectively. For example, the TEM_{21} mode has two nulls in the x-direction (horizontal) and one in the y-direction (vertical).

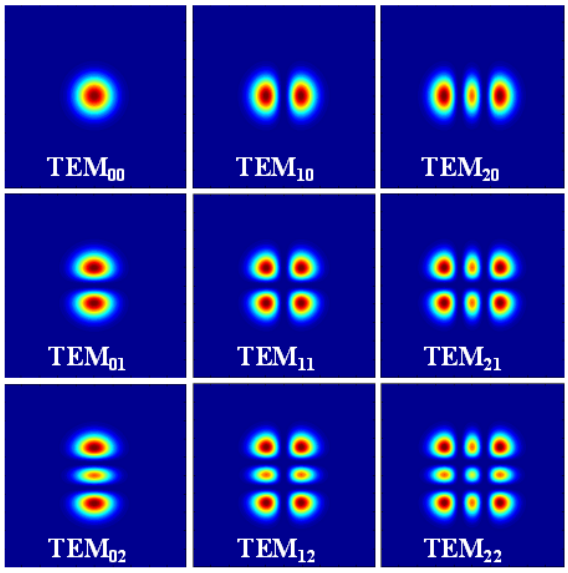

Figure C.1: Intensity distributions of the lowest order HG modes. The profiles are shaded such that the most intense portions are red and the least are blue.

APPENDIX D

LAGUERRE-GAUSSIAN MODES

The cylindrically symmetric laser cavity modes are known as the Laguerre-Gaussian (LG) modes [46, 47]. Of the three symmetries discussed in this dissertation, it is likely to be mentioned in optics texts, but in general, not be as fully discussed as the Hermite-Gaussian (HG) modes. For example, Saleh and Teich [46] has only one paragraph (on page 104) regarding the LG modes. On page 647, Siegman [47] gives a functional form, similar to the one below.

The functional form of these modes is

$$\begin{aligned} u(\overrightarrow{r}) &= u(r,\theta,z) \\ &= \frac{w_o}{w(z)}\sqrt{\frac{2l!}{(1+\delta_{0,m})(l+m)!}}\left(\frac{\sqrt{2}r}{w(z)}\right)^m \exp\left[-i(2l+m+1)\arctan\left[\frac{z}{z_o}\right]\right] \\ &\quad \mathrm{L}_l^m\left[\frac{2r^2}{w^2(z)}\right]\exp\left[\left(-\frac{ik}{2R_c(z)}-\frac{1}{w^2(z)}\right)r^2\right]\cos\left[m\theta\right]\sin\left[kz\right] \end{aligned} \tag{D.1}$$

where w_o is the ($1/e$ radius in field) beam waist, $w(z)$ is the spot size (again, $1/e$ radius in field) at a distance z from the waist, l and m are the spatial mode indices, z_o is the Rayleigh range, L_l^m is a Laguerre polynomial, $R_c(z)$ is the wavefront radius of curvature at z, and k is the wavenumber. From [46] page 83,

$$w_o = \left(\frac{\lambda z_o}{\pi}\right)^{\frac{1}{2}} \tag{D.2}$$

$$w(z) = w_o\left[1+\left(\frac{z}{z_o}\right)^2\right]^{\frac{1}{2}} \tag{D.3}$$

$$R_c(z) = z\left[1+\left(\frac{z_o}{z}\right)^2\right] \tag{D.4}$$

The Rayleigh range, z_o, is calculated using equation D.4 by setting $z = L/2$ and R_c to the cavity mirror's radius of curvature. Laguerre polynomials are standard orthogonal polynomials that can be found in most math tables (for example, reference [79] section 6.10). The factor $\exp\left[-i(2l+m+1)\arctan\left[\frac{z}{z_o}\right]\right]$ in equation D.1 is known as the Gouy phase factor which is responsible for shifting the resonance frequency of the

higher-order modes away from the resonance of the fundamental mode. The lowest order mode for which $l = m = 0$ is known as the fundamental (or TEM_{00}) mode and takes the same form regardless of the symmetry of the system.

Figure D.1 shows pictures of the intensity distributions, $|u(\overrightarrow{r})|^2$, of the lowest order modes – red indicating the most intense portions and blue being the least. The

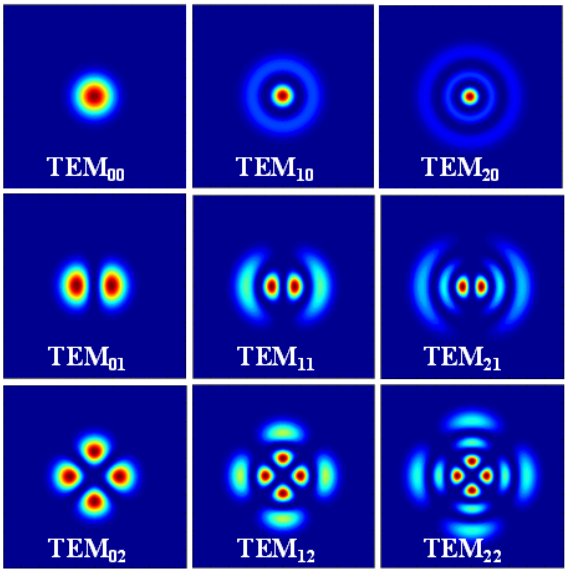

Figure D.1: Intensity distributions of the lowest order LG modes. The profiles are shaded such that the most intense portions are red and the least are blue.

following parameters were used in the calculation of the profiles in Figure D.1: z_o= 13.3 cm (cavity length of 7.62 cm and mirror radius of curvature of 50 cm), λ= 435 nm, and $z = 0$. As can be seen in the figure, in this symmetry, the indices l and m of the TEM_{lm} modes indicate the number of nulls in the mode profiles in the radial and azimuthal directions, respectively. There are l radial nulls and $2m$ azimuthal nulls. For example, the TEM_{21}mode has two radial nulls and two angular nulls, as opposed to the TEM_{12} mode which has one radial null and four angular nulls.

APPENDIX E

INCE-GAUSSIAN MODES

Ince-Gaussian (IG) modes are cavity modes for a laser cavity whose symmetry is neither rectangularly nor cylindrically symmetric. Instead, the symmetry is somewhere in between – elliptical. Unlike the Laguerre-Gaussian (LG) and Hermite-Gaussian (HG) modes, the IG modes are rarely mentioned in optics texts. There are a couple of papers in the literature regarding them [51, 52, 50].

These modes are written in terms of elliptical spatial coordinates where ξ (an element of $[0, \infty]$) and is the radial coordinate and η is the angular coordinate (an element of $[0, 2\pi]$). Rectangular coordinates can be written in terms of the elliptical co-ordinates as follows [51]:

$$x = f(z)\cosh[\xi]\cos[\eta] \tag{E.1}$$

$$y = f(z)\sinh[\xi]\sin[\eta] \tag{E.2}$$

where $f(z) = {f_o w(z)}/{w_o}$is the semi-focal separation and f_o is the semi-focal separation at the waist plane.

Unlike the HG or LG modes, the IG modes can have two possible functional forms, denoted as $u^e(\overrightarrow{r}, \epsilon)$ and $u^o(\overrightarrow{r}, \epsilon)$, dependent on whether the symmetry of the Ince polynomials is even or odd. And, in addition to their dependence on the spatial coordinates, the IG modes are also dependent on the ellipticity of the system. As found in reference [50] (with some of the notation changed to match the rest of this

dissertation), they are:

$$
\begin{aligned}
u(\overrightarrow{r},\epsilon) &= u(\xi,\eta,z,\epsilon) \\
u^e(\overrightarrow{r},\epsilon) &= C\frac{w_o}{w(z)}\mathrm{C}_l^m[i\xi,\epsilon]\mathrm{C}_l^m[\eta,\epsilon]exp\left[-\frac{r^2}{w^2(z)}\right] \\
&\quad exp\left[i\left(\frac{kr^2}{2R_c(z)}-(l+1)\arctan\left[\frac{z}{z_o}\right]\right)\right]\sin\left[kz\right] \qquad \text{(E.3)} \\
u^o(\overrightarrow{r},\epsilon) &= S\frac{w_o}{w(z)}\mathrm{S}_l^m[i\xi,\epsilon]\mathrm{S}_l^m[\eta,\epsilon]exp\left[-\frac{r^2}{w^2(z)}\right] \\
&\quad exp\left[i\left(\frac{kr^2}{2R_c(z)}-(l+1)\arctan\left[\frac{z}{z_o}\right]\right)\right]\sin\left[kz\right] \qquad \text{(E.4)}
\end{aligned}
$$

where C and S are normalization constants,w_o is the ($1/e$ radius in field) beam waist, $w(z)$ is the spot size (again, $1/e$ radius in field) at a distance z from the waist, l and m are the spatial mode indices, z_o is the Rayleigh range, C_l^m and S_l^m are, respectively, the even and odd Ince polynomials, $R_c(z)$ is the wavefront radius of curvature at z, k is the wavenumber, and $r^2 = \cosh^2[\xi]\cos^2[\eta] + \sinh^2[\xi]\sin^2[\eta]$. Because the field inside the cavity is not a traveling wave but a standing wave, the e^{ikz} dependence of the IG modes in reference [50] has been changed to $\sin[kz]$.

From [46] page 83,

$$
\begin{aligned}
w_o &= \left(\frac{\lambda z_o}{\pi}\right)^{\frac{1}{2}} \qquad \text{(E.5)} \\
w(z) &= w_o\left[1+\left(\frac{z}{z_o}\right)^2\right]^{\frac{1}{2}} \qquad \text{(E.6)} \\
R_c(z) &= z\left[1+\left(\frac{z_o}{z}\right)^2\right]. \qquad \text{(E.7)}
\end{aligned}
$$

The Rayleigh range, z_o, is calculated using equation E.7 by setting $z = L/2$ and R_c to the cavity mirror's radius of curvature. The factor $\exp\left[-i(l+1)\arctan\left[\frac{z}{z_o}\right]\right]$ in equations E.3 and E.4 is known as the Gouy phase factor which is responsible for shifting the resonance frequency of the higher-order modes away from the resonance of the fundamental mode. The lowest order mode for which $l = m = 0$ is known as

the Gaussian mode and takes the same form regardless of the symmetry of the mode though it is hard to see in this symmetry.

The Ince polynomials are non-standard orthogonal polynomials, and, as such, are not included in common math tables. The best reference for them found during this dissertation work was in reference [50], but even there only the recurrence relations were included. As such, Table E.1 contains the first few functions found by those recurrence relations in terms of an unknown constant, A_o, along with the associated eigenvalue, a. (The polynomials are given in terms of η. The polynomials in terms of ξ can be found by replacing η with $i\xi$.) As can be seen from the recurrence relations, not all possible values of l and m are possible.

Figure E.1 shows pictures of the intensity distributions, $|u(\overrightarrow{r})|^2$, of the lowest order even (top six) and odd (bottom six) modes with red indicating the most intense portions and blue being the least. The following parameters were used in

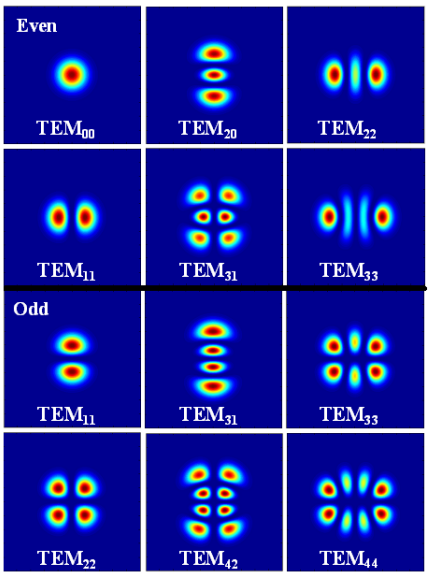

Figure E.1: Intensity distributions of the lowest order IG modes. The top six profiles are for even IG modes and the bottom six are odd IG modes. The profiles are shaded such that the most intense portions are red and the least are blue.

l	m	Constants	Eigenvalue	Constants	Polynomial
0	0				$\mathrm{C}_0^0[\eta] = A_o$
2	0		$a = 2\left(1 - \sqrt{(1+\epsilon^2}\right)$	$A_1 = \frac{aA_o}{2\epsilon}$	$\mathrm{C}_2^0[\eta] = A_o + A_1 \cos[2\eta]$
2	2		$a = 2\left(1 + \sqrt{(1+\epsilon^2}\right)$	$A_1 = \frac{aA_o}{2\epsilon}$	$\mathrm{C}_2^0[\eta] = A_o + A_1 \cos[2\eta]$
1	1		$a = 2(1+\epsilon)$		$\mathrm{C}_1^1[\eta] = A_o \cos[\eta]$
3	1	$b_o = -10 - 2\epsilon$ $b_1 = 9 + 18\epsilon - 3\epsilon^2$	$a = -b_1 - \frac{\sqrt{b_1^2 - 4b_o}}{2}$	$A_1 = \frac{A_o\epsilon}{(a-9)}$	$\mathrm{C}_3^1[\eta] = A_o \cos[\eta] + A_1 \cos[3\eta]$
3	3	$b_o = -10 - 2\epsilon$ $b_1 = 9 + 18\epsilon - 3\epsilon^2$	$a = -b_1 + \frac{\sqrt{b_1^2 - 4b_o}}{2}$	$A_1 = \frac{A_o\epsilon}{(a-9)}$	$\mathrm{C}_3^3[\eta] = A_o \cos[\eta] + A_1 \cos[3\eta]$
1	1				$\mathrm{S}_1^1[\eta] = A_o \sin[\eta]$
1	3	$b_o = 9 - 18\epsilon - 3\epsilon^2$ $b_1 = -10 + 2\epsilon$	$a = -b_1 - \frac{\sqrt{b_1^2 - 4b_o}}{2}$	$A_1 = \frac{A_o\epsilon}{(a-9)}$	$\mathrm{S}_3^1[\eta] = A_o \sin[\eta] + A_1 \sin[3\eta]$
3	3	$b_o = 9 - 18\epsilon - 3\epsilon^2$ $b_1 = -10 + 2\epsilon$	$a = -b_1 + \frac{\sqrt{b_1^2 - 4b_o}}{2}$	$A_1 = \frac{A_o\epsilon}{(a-9)}$	$\mathrm{S}_3^3[\eta] = A_o \sin[\eta] + A_1 \sin[3\eta]$
2	2				$\mathrm{S}_2^2[\eta] = A_o \sin[2\eta]$
4	2	$b_o = 64 - 4\epsilon^2$ $b_1 = -20$	$a = -b_1 - \frac{\sqrt{b_1^2 - 4b_o}}{2}$	$A_1 = \frac{(a-4)A_o}{4\epsilon}$	$\mathrm{S}_4^2[\eta] = A_o \sin[2\eta] + A_1 \sin[4\eta]$
4	4	$b_o = 64 - 4\epsilon^2$ $b_1 = -20$	$a = -b_1 + \frac{\sqrt{b_1^2 - 4b_o}}{2}$	$A_1 = \frac{(a-4)A_o}{4\epsilon}$	$\mathrm{S}_4^4[\eta] = A_o \sin[2\eta] + A_1 \sin[4\eta]$

Table E.1: Ince polynomials.

the calculation of the profiles in Figure E.1, z_o= 13.3 cm (cavity length of 7.62 cm and mirror radius of curvature of 50 cm), λ= 435 nm, ϵ =4 and $z = 0$. As can be seen in Figure E.1, in this symmetry, the indices l and m of the TEM$_{lm}$ modes indicate the number of nulls in the mode profiles in the radial and azimuthal directions, respectively. In this geometry, the nulls take the form of hyperbolae and ellipses, though this behavior is sometimes hard to see in the lower order modes. Unlike the HG and LG modes where the indices l and m directly indicate the number of nulls in a given profile, for the IG modes, there are m hyperbolic nulls and $^{(l-m)}/_2$ elliptic nulls lines (excluding the line at $\xi = 0$ for the odd modes).

For the same parameters as in Figure E.1, Figure E.2 shows the even TEM$_{31}$IG mode with the ellipticity varied from 0 to ∞, along with the LG TEM$_{11}$ mode and the HG TEM$_{12}$ mode that correspond to the IG mode when $\epsilon = 0$ and ∞, respectively. The values of ϵ in Figure E.2 were chosen to best display the evolution of the mode

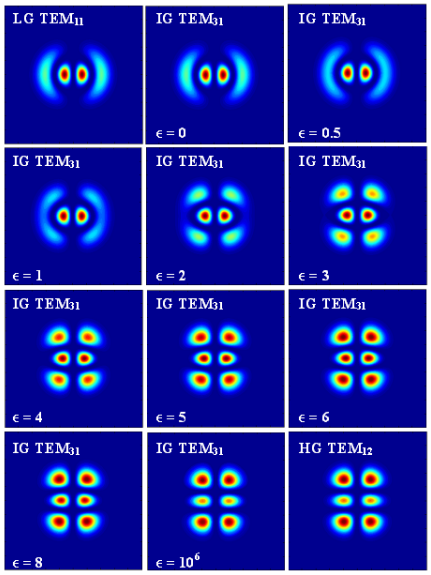

Figure E.2: Intensity distributions of the IG TEM$_{31}$ mode with variation of the ellipticity, ϵ, from 0 to ∞, along with the corresponding LG TEM$_{11}$ and HG TEM$_{12}$ modes for either extreme in ϵ. The profiles are shaded such that the most intense portions are red and the least are blue.

from one extreme to the other.

The Gouy phase shift of the IG TEM_{31} mode is independent of ϵ. Therefore the shift for the LG $TEM_{11}$and HG TEM_{12} modes must be the same as the IG TEM_{31} mode (and the same as each other) since they represent the IG TEM_{31} mode at either extreme of the ellipticity.

APPENDIX F

TYPE 1 OVERLAP VOLUME

The type 1 overlap integral, V_q, is the normalization volume for the cavity modes. This integral was defined in equation 2.19 and restated in equation 2.129. Adding the wavelength dependence explicitly to the definition with the subscript q, the type 1 overlap integral is:

$$\int_{cav} u_{q\,n}(\overrightarrow{r})\, u^*_{q\,n'}(\overrightarrow{r})\, dcav = \begin{cases} V_q & n = n' \\ 0 & n \neq n' \end{cases}. \tag{F.1}$$

Because the spatial mode profiles are orthogonal, the integral is zero unless both $u's$ are both the same spatial mode profile, as indicated by the subscript n. Thus,

$$V_q \;=\; \int_{cav} |u_q(\overrightarrow{r})|^2\, dcav \tag{F.2}$$

Rectangular Symmetry

As defined in Appendix C, explicitly adding the wavelength dependence, the magnitude of the Hermite-Gaussian (HG) spatial mode function is

$$\begin{aligned} |u_q(\overrightarrow{r})|^2 \;=\; & \frac{w_{oq}^2}{w_q^2(z)} \left(\frac{1}{2^{l+m} l!m!}\right) \mathrm{H}_l^2 \left[\frac{\sqrt{2}x}{w_q(z)}\right] \mathrm{H}_m^2 \left[\frac{\sqrt{2}y}{w_q(z)}\right] \\ & \exp\left[\left(-\frac{2}{w_q^2(z)}\right)\left(x^2+y^2\right)\right] \sin^2\left[k_q z\right]. \end{aligned} \tag{F.3}$$

In this symmetry,

$$dcav \;=\; dxdydz \tag{F.4}$$

Thus,

$$V_q \;= \int_{-L/2}^{L/2} dz \int_{-\infty}^{\infty} dy \;\; \int_{-\infty}^{\infty} dx\, |u_q(\overrightarrow{r})|^2. \tag{F.5}$$

From the form of $|u_q|^2$in equation G.3, it can be seen that the x and y-integrals in equation G.5 are independent of each other, though not independent of z. Following are a couple of specific examples for this symmetry.

$\underline{l = m = 0}$

The lowest order Hermite polynomial, $\mathrm{H}_0[x] = 1$.

$$\begin{aligned} V_q &= \int_{-L/2}^{L/2} dz \int_0^{\infty} dy \int_0^{\infty} dx \, |u_q(\overrightarrow{r})|^2 \\ &= \int_{-L/2}^{L/2} dz \frac{w_{oq}^2}{w_q^2(z)} \sin^2[k_q z] \int_{-\infty}^{\infty} dx \exp\left[\left(-\frac{2}{w_q^2(z)}\right) x^2\right] \\ &\quad \int_{-\infty}^{\infty} dy \exp\left[\left(-\frac{2}{w_q^2(z)}\right) y^2\right] \end{aligned} \tag{F.6}$$

The x and y-integrals are functionally identical. This integral is twice the value of integral #643 in the CRC math tables [79]. Thus,

$$\begin{aligned} V_q &= \int_{-L/2}^{L/2} dz \frac{w_{oq}^2}{w_q^2(z)} \sin^2[k_q z] \left(\frac{w_q(z)\sqrt{\pi}}{\sqrt{2}}\right)\left(\frac{w_q(z)\sqrt{\pi}}{\sqrt{2}}\right) \\ &= \frac{\pi w_{oq}^2}{2} \int_{-L/2}^{L/2} dz \sin^2[k_q z]. \end{aligned} \tag{F.7}$$

The remaining z-integral is integral #279 in the CRC math tables [79] and results in

$$\begin{aligned} V_q &= \frac{\pi w_{oq}^2}{2}\left(\frac{z}{2} - \frac{1}{4k_q}\sin[2k_q z]\right)\Bigg|_{-L/2}^{L/2} \\ &= \frac{\pi w_{oq}^2 L}{4} \end{aligned} \tag{F.8}$$

where it has been assumed that $\sin\left[2k_q\frac{L}{2}\right] = 0$ because $k_q = \frac{2\pi n_q}{\lambda_q}$ and $L = \frac{q\lambda_q}{2}$. V_q in equation F.8 looks like the volume of a cylinder of radius w_{oq}, the ($1/e^2$ radius) beam waist, and length L divided by four. The x and y integrals can also be easily calculated with *Mathematica*.

$\underline{l = 1 \text{ and } m = 2}$

The necessary Hermite polynomials in this case are

$$\mathrm{H}_1[x] = 2x \tag{F.9}$$

$$\mathrm{H}_2[y] = -2 + 4y^2. \tag{F.10}$$

Evaluating the x-integral of equation G.5 using integral #648 from the CRC math table [79]:

$$\begin{aligned}
&\int_{-\infty}^{\infty} dx\, \mathrm{H}_1^2\left[\frac{\sqrt{2}x}{w_q(z)}\right] \exp\left[\left(-\frac{2}{w_q^2(z)}\right)x^2\right] \\
&= \int_{-\infty}^{\infty} dx\, \left(\frac{2\sqrt{2}x}{w_q(z)}\right)^2 \exp\left[\left(-\frac{2}{w_q^2(z)}\right)x^2\right] \\
&= 2\sqrt{\frac{\pi w_q^2(z)}{2}}. \qquad \text{(F.11)}
\end{aligned}$$

The y-integral is evaluated using the same integral as the x. It is:

$$\begin{aligned}
&\int_{-\infty}^{\infty} dy\, \mathrm{H}_2^2\left[\frac{\sqrt{2}y}{w_q(z)}\right] \exp\left[\left(-\frac{2}{w_q^2(z)}\right)y^2\right] \\
&= \int_{-\infty}^{\infty} dy\, \left(2 - 4\left(\frac{\sqrt{2}y}{w_q(z)}\right)^2\right)^2 \exp\left[\left(-\frac{2}{w_q^2(z)}\right)y^2\right] \\
&= 8\sqrt{\frac{\pi w_q^2(z)}{2}}. \qquad \text{(F.12)}
\end{aligned}$$

The results of the x and y-integrals in equations F.11 and F.12 can now be plugged back into the remaining z-integral.

$$\begin{aligned}
V_q &= \int_{-L/2}^{L/2} dz \left(\frac{1}{2^3 1!2!}\right) \frac{w_{oq}^2}{w_q^2(z)} \sin^2\left[k_q z\right] \left(2\sqrt{\frac{\pi w_q^2(z)}{2}}\right)\left(8\sqrt{\frac{\pi w_q^2(z)}{2}}\right) \\
&= \frac{\pi w_{oq}^2}{2} \int_{-L/2}^{L/2} dz\, \sin^2\left[k_q z\right] \qquad \text{(F.13)}
\end{aligned}$$

The remaining integral is the same that remained for the $l = m = 0$ case (equation F.7). Therefore, the value of V_q is the same for this case ($l = 1$ and $m = 2$) as it was for the $l = m = 0$.

This result might seem surprising, at first, since higher-order modes have a larger spatial distribution than the fundamental and therefore it seems that their mode volume should be larger. However, in the other common normalization scheme – in

which the cavity spatial mode function is not unitless – the type 1 integral is

$$\int_{cav} u_{q\,n}(\overrightarrow{r})\, u^{*}_{q\,n'}(\overrightarrow{r})\, dcav \;=\; \begin{cases} 1 & n = n' \\ 0 & n \neq n' \end{cases}, \tag{F.14}$$

regardless of the specific mode-structure of the u's. The goal of normalization is to define the u's such that the integral in equation F.1 (or F.14) is a constant. That constant could be 1 or it could be a specific number. Either way, the function is said to be normalized though the specific functional form will vary depending on what normalization scheme is used. An example of this was outlined in Appendix C.

Cylindrical Symmetry

As defined in Appendix D, the Laguerre-Gaussian (LG) modes are

$$\begin{aligned} |u_q(\overrightarrow{r})|^2 \;=\; & \frac{w_{oq}^2}{w_q^2(z)} \left(\frac{2l!}{(1+\delta_{0,m})(l+m)!} \right)^2 \left(\frac{\sqrt{2}r}{w_q(z)} \right)^{2m} \left(\mathrm{L}_l^m \left[\frac{2r^2}{w_q^2(z)} \right] \right)^2 \\ & \exp\left[\left(-\frac{2}{w_q^2(z)} \right) r^2 \right] \cos^2\left[m\theta\right] \sin^2\left[k_q z\right] \end{aligned} \tag{F.15}$$

In this symmetry,

$$dcav \;=\; r dr d\theta dz \tag{F.16}$$

Thus,

$$V_q \;=\; \int_{-L/2}^{L/2} dz \int_0^{\infty} dr \int_0^{2\pi} d\theta\, r |u_q(\overrightarrow{r})|^2. \tag{F.17}$$

From the form of $|u_q|^2$in equation G.28, it can be seen that the r and θ-integrals in equation F.17 are independent of each other, though not independent of z. Following are a couple of specific examples in this symmetry.

$\underline{l = m = 0}$

The necessary Laguerre polynomial is

$$\mathrm{L}_0^0[r] \;=\; 1 \tag{F.18}$$

and

$$\begin{aligned} V_q &= \int_{-L/2}^{L/2} dz \int_0^{\infty} dr \int_0^{2\pi} d\theta\, r \frac{w_{oq}^2}{w_q^2(z)} \exp\left[\left(-\frac{2}{w_q^2(z)}\right) r^2\right] \sin^2\left[k_q z\right] \\ &= 2\pi \int_{-L/2}^{L/2} dz \int_0^{\infty} dr\, r \frac{w_{oq}^2}{w_q^2(z)} \exp\left[\left(-\frac{2}{w_q^2(z)}\right) r^2\right] \sin^2\left[k_q z\right] \\ &= 2\pi \int_{-L/2}^{L/2} dz\, \frac{w_{oq}^2}{w_q^2(z)} \left(\frac{w_q^2(z)}{4}\right) \sin^2\left[kz\right] \\ &= \frac{\pi w_{oq}^2 L}{4} \end{aligned} \tag{F.19}$$

where the r-integral was done with CRC math tables integral #649 and the z-integral is the same as in equation F.7. The result of this integral is the same as was found for the rectangular symmetric modes.

$\underline{l = 2 \text{ and } m = 1}$

When $l = 2$ and $m = 1$,

$$\mathrm{L}_2^1[r] \;=\; \frac{1}{2}\left(6 - 6r + r^2\right) \tag{F.20}$$

and

$$\begin{aligned} V_q &= \int_{-L/2}^{L/2} dz \int_0^{\infty} dr \int_0^{2\pi} d\theta\, r \frac{2}{12} \frac{w_{oq}^2}{w_q^2(z)} \left(\frac{\sqrt{2}r}{w_q(z)}\right)^2 \exp\left[\left(-\frac{2}{w_q^2(z)}\right) r^2\right] \\ &\quad \left[6 - 6\left(\frac{2r^2}{w_q^2(z)}\right) + \left(\frac{2r^2}{w_q^2(z)}\right)^2\right]^2 \cos^2\left[\theta\right] \sin^2\left[k_q z\right]. \end{aligned} \tag{F.21}$$

The integral over θ is the easiest. It is

$$\int_0^{2\pi} d\theta\, \cos^2\left[\theta\right] \;=\; \pi \tag{F.22}$$

When expanded out, $\left(\mathrm{L}_2^1\left[\frac{2r^2}{w_q^2(z)}\right]\right)^2$ yields terms that are proportional to r^0, r^2, r^4, r^6, and r^8. Combining this with the additional factor of r^3 in the integrand of equation F.21, the general form of the r-dependent integral is $\int_0^\infty dr\, r^n \exp\left[\left(-\frac{2}{w_q^2(z)}\right) r^2\right]$ where n= 3, 5, 7, 9, or 11. This is integral #649 in the CRC math tables [79] (beware the difference in notation!) or can be done with *Mathematica*. For example,

$$\begin{aligned}\int_0^\infty dr\, r^7 \exp\left[\left(-\frac{2}{w_q^2(z)}\right) r^2\right] &= \frac{3!}{2}\left(\frac{w_q^2(z)}{2}\right)^4 \\ &= \frac{3}{16} w_q^8(z). \end{aligned} \tag{F.23}$$

After the r-integrals, the remaining z-integral is

$$V_q = \frac{\pi w_{oq}^2}{2}\int_{-L/2}^{L/2} dz\, \sin^2\left[k_q z\right]. \tag{F.24}$$

which is, again, the integral in equation F.7. Thus, for this higher-order mode, V_q is $\frac{\pi w_{oq}^2 L}{4}$.

Elliptical Symmetry

As defined in Appendix E, the Ince-Gaussian (IG) modes are,

$$|u_q^e(\overrightarrow{r})|^2 = C^2 \frac{w_{oq}^2}{w_q^2(z)} \left(\mathrm{C}_l^m\left[i\xi,\epsilon\right]\mathrm{C}_l^m\left[\eta,\epsilon\right]\right)^2 exp\left[-\frac{2r^2}{w^2(z)}\right]\sin^2\left[k_q z\right] \tag{F.25}$$

and

$$|u_q^o(\overrightarrow{r})|^2 = S^2 \frac{w_{oq}^2}{w_q^2(z)} \left(\mathrm{S}_l^m\left[i\xi,\epsilon\right]\mathrm{S}_l^m\left[\eta,\epsilon\right]\right)^2 exp\left[-\frac{2r^2}{w^2(z)}\right]\sin^2\left[k_q z\right]. \tag{F.26}$$

where $r^2 = \cosh^2\left[\xi\right]\cos^2\left[\eta\right] + \sinh^2\left[\xi\right]\sin^2\left[\eta\right]$. In this symmetry,

$$dcav = f^2(z)\left(\sinh^2\left[\xi\right] + \sin^2\left[\eta\right]\right) d\xi d\eta \tag{F.27}$$

Thus,

$$V_q = \int_{-L/2}^{L/2} dz \int_0^\infty d\xi \int_0^{2\pi} d\eta\, f^2(z)\left(\sinh^2\left[\xi\right] + \sin^2\left[\eta\right]\right)|u_q(\overrightarrow{r})|^2, \tag{F.28}$$

where, in this case, $|u_q(\overrightarrow{r})|^2$ could refer to either an even or odd IG mode.

The functional form of $|u_q(\overrightarrow{r})|^2$ is not precisely known (as it was for the HG and LG modes). There are two unknown constants (that could be combined into one but have not been). The first constant, C (S), in the even (odd) mode is visible above in equation F.25 (F.26). The second, A_o, is not visible in the above equations because it is hidden within the Ince polynomials (see Table E.1). Since the normalization volume is known from the other two symmetries, these constants can be found by calculating the integrals in F.28.

In rectangular symmetry, it was possible to perform the x and y-integrals independent of each other. The same was true in cylindrical symmetry with the r and θ-integrals. However, in elliptic symmetry, it is not possible to independently calculate the ξ and η- integrals This makes F.28 much harder to calculate. Attempts were made at both analytically and numerically calculating this integral but no results were obtained. Although more integrals (and some algebra) are involved, if these modes are needed, it might probably be easier to rewrite the IG modes in terms of either the HG or LG modes (as outlined in [50]) and then doing the necessary integrals in one of the other two symmetries.

APPENDIX G

TYPE 2 OVERLAP VOLUME

The type 2 overlap volume is defined in equation 2.132. It is

$$V_{q\,q'} \;=\; \int_{cav} |u_q(\overrightarrow{r})|^2\,|u_{q'}(\overrightarrow{r})|^2\,dcav. \tag{G.1}$$

This integral will depend on the wavelengths of the two fields and their mode structure. As can be seen from equations 2.158 – 2.160, the only two combinations of wavelengths that will be needed are V_{ps} and V_{pa}. This integral can be found analytically and will be functionally the same when the second mode is either the Stokes or the anti-Stokes. Therefore, the results will be left in terms of q so that later, they can be used for either the Stokes or anti-Stokes wavelengths.

In the evaluation of these integrals, the following definition is needed [46].

$$w_q(z) \;\equiv\; w_{oq}\left[1+\left(\frac{z}{z_o}\right)^2\right]^{\frac{1}{2}} \tag{G.2}$$

The Rayleigh range, z_o, is independent of wavelength because it is determined strictly from the cavity parameters (length and mirror radius of curvature).

Rectangular Symmetry

As defined in Appendix C and explicitly including the wavelength dependence, the functional form of $|u_q(\overrightarrow{r})|^2$ for the Hermite-Gaussian (HG) modes is

$$\begin{aligned}|u_q(\overrightarrow{r})|^2 \;=\;& \frac{w_{oq}^2}{w_q^2(z)}\left(\frac{1}{2^{l+m}l!m!}\right)\mathrm{H}_l^2\left[\frac{\sqrt{2}x}{w_q(z)}\right]\mathrm{H}_m^2\left[\frac{\sqrt{2}y}{w_q(z)}\right]\\ &\exp\left[\left(-\frac{2}{w_q^2(z)}\right)\left(x^2+y^2\right)\right]\sin^2\left[k_q z\right].\end{aligned} \tag{G.3}$$

In this symmetry,

$$dcav \;=\; dxdydz \tag{G.4}$$

Thus,

$$V_{pq} = \int_{-L/2}^{L/2} dz \int_{-\infty}^{\infty} dy \int_{-\infty}^{\infty} dx \, |u_p(\overrightarrow{r})|^2 |u_q(\overrightarrow{r})|^2. \quad \text{(G.5)}$$

From the form of $|u_q|^2$ in equation G.3, it can be seen that the x and y-integrals in equation G.5 are independent of each other, though not independent of z. Following are a couple of specific examples for this symmetry and a table with additional results.

Pump TEM_{00} and q TEM_{00}

The lowest order Hermite polynomial, $\mathrm{H}_0[x] = 1$.

$$\begin{aligned} V_{pq} = & \int_{-L/2}^{L/2} dz \int_{-\infty}^{\infty} dy \int_{-\infty}^{\infty} dx \\ & \left(\frac{w_{op}^2}{w_p^2(z)} \exp\left[\left(-\frac{2}{w_p^2(z)} \right) (x^2 + y^2) \right] \sin^2[k_p z] \right) \\ & \left(\frac{w_{oq}^2}{w_q^2(z)} \exp\left[\left(-\frac{2}{w_q^2(z)} \right) (x^2 + y^2) \right] \sin^2[k_q z] \right) \end{aligned} \quad \text{(G.6)}$$

The x and y-integrals above have the same form. Evaluating the x-integral yields:

$$\int_{-\infty}^{\infty} dx \, \exp\left[\left(-\frac{2}{w_p^2(z)} - \frac{2}{w_q^2(z)} \right) x^2 \right] = \sqrt{\frac{\pi w_p^2(z) w_q^2(z)}{2\left(w_p^2(z) + w_q^2(z)\right)}} \quad \text{(G.7)}$$

where integral # 643 from the CRC math tables has been used [79]. Alternatively, the integral can be done with *Mathematica*. The remaining z-integral is

$$V_{pq} = \int_{-L/2}^{L/2} dz \, \frac{w_{op}^2}{w_p^2(z)} \frac{w_{oq}^2}{w_q^2(z)} \left(\frac{\pi w_p^2(z) w_q^2(z)}{2\left(w_p^2(z) + w_q^2(z)\right)} \right) \sin^2[k_p z] \sin^2[k_q z] \quad \text{(G.8)}$$

To perform this integral, the functional forms of $w_p^2(z)$ and $w_q^2(z)$ need to be substituted in using equation G.2. After this substitution,

$$V_{pq} = \left(\frac{\pi w_{op}^2 w_{oq}^2}{2\left(w_{op}^2 + w_{oq}^2\right)} \right) \int_{-L/2}^{L/2} dz \, \frac{1}{\left(1 + \left(\frac{z}{z_o} \right)^2 \right)} \sin^2[k_p z] \sin^2[k_q z] \quad \text{(G.9)}$$

This integral requires a bit of manipulation before it can be integrated. Using this trig identity

$$\sin[x] \;=\; \frac{1-\cos[2x]}{2} \tag{G.10}$$

the trig functions in integral G.9 can be rewritten such that

$$\begin{aligned} V_{pq} \;=\; & \left(\frac{\pi w_{op}^2 w_{oq}^2}{8\left(w_{op}^2+w_{oq}^2\right)}\right)\int_{-L/2}^{L/2} dz\,\frac{1}{\left(1+\left(\frac{z}{z_o}\right)^2\right)} \\ & \left(1-\cos\left[2k_p z\right]-\cos\left[2k_q z\right]\right. \\ & \left.+\frac{1}{2}\cos\left[2\left(k_p-k_q\right)z\right]+\frac{1}{2}\cos\left[2\left(k_p+k_q\right)z\right]\right) \end{aligned} \tag{G.11}$$

There are now five integrals but only the first integral (which is not proportional to a cosine) is significant. Looking at the other four integrals first, they can all be written in the same general form:

$$\begin{aligned} & \int_{-L/2}^{L/2} dz\,\frac{\cos\left[2kz\right]}{\left(1+\left(\frac{z}{z_o}\right)^2\right)} \\ & \quad\approx \int_{-L/2}^{L/2} dz\;\cos\left[2kz\right]\left(1-\left(\frac{z}{z_o}\right)^2+\left(\frac{z}{z_o}\right)^4-\ldots\right), \end{aligned} \tag{G.12}$$

where k is any of the wavenumber combinations in G.11 and the expansion is found on page 40 of the CRC math tables [79]. The expansion is valid when $\left(\frac{z}{z_o}\right)^2 < 1$. This quantity will be at its largest at either limit of integration. Given a cavity length of 7.62 cm and a Rayleigh range of 13.2 cm (given mirror radius of curvature of 50 cm), then the maximum value of $\left(\frac{z}{z_o}\right)^2 \sim 0.08$.

Looking at the first term of G.12,

$$\int_{-L/2}^{L/2} dz\;\cos\left[2kz\right] \;=\; \left.\frac{\sin\left[2kz\right]}{2k}\right|_{-L/2}^{L/2} \tag{G.13}$$

This integral will be zero because $k = {}^{2\pi}/_{\lambda}$ and $L = {}^{q\lambda}/_{2}$ where q is an integer.

The next term of equation G.12 is

$$\int_{-L/2}^{L/2} dz \left(\frac{z}{z_o}\right)^2 \cos\left[2kz\right] = \frac{1}{z_o^2}\left(\frac{z\cos\left[2kz\right]}{2k^2} + \frac{(-1+2k^2z^2)\sin\left[2kz\right]}{4k^3}\right)\Bigg|_{-L/2}^{L/2} \tag{G.14}$$

The second term of this integral is zero for the same reasons as equation G.13. Once the limits of integration are applied, the first term of this integral is proportional to $L/4k^2zo^2$. Given L= 7.62 cm, z_o =13.2 cm, and $k_p = 2\pi/532$ nm^{-1}, then $L/4k^2zo^2 \sim 10^{-12}$. (When $k \neq k_p$ in equation G.12, then the value of $L/4k^2zo^2 < 10^{-12}$.) While not zero, this term will be small when compared to the remaining, dominant, term of equation G.11.

The dominant term of equation G.11 is

$$V_{pq} = \frac{1}{4}\int_{-L/2}^{L/2} dz \left(\frac{\pi w_{op}^2 w_{oq}^2}{2\left(w_{op}^2 + w_{oq}^2\right)}\right) \frac{1}{\left(1+\left(\frac{z}{z_o}\right)^2\right)} \tag{G.15}$$

Integrating with *Mathematica* yields

$$V_{pq} = \frac{L}{4}\left(\frac{\pi w_{op}^2 w_{oq}^2}{2\left(w_{op}^2 + w_{oq}^2\right)}\right) F[\frac{1}{2},\, 1,\, \frac{3}{2},\, \frac{-L}{4z_o^2}] \tag{G.16}$$

where $F[\frac{1}{2},\, 1,\, \frac{3}{2},\, \frac{-L}{4z_o^2}]$ is a special case of a hypergeometric function and is defined on page 508 of the CRC math tables [79] as

$$F[\frac{1}{2},\, 1,\, \frac{3}{2},\, \frac{-L^2}{4z_o^2}] = \frac{2z_o}{L}\arctan[\frac{L}{2z_o}]. \tag{G.17}$$

Thus,

$$V_{pq} = \frac{\pi}{4}\left(\frac{w_{op}^2 w_{oq}^2}{\left(w_{op}^2 + w_{oq}^2\right)}\right) z_o \arctan[\frac{L}{2z_o}]. \tag{G.18}$$

A special case of this integral needed in Chapter 2 for the definition of the Raman gain (equation 2.157) is when q represents the Stokes wavelength. This case is the

named integral

$$V_{ps\,o} = \frac{\pi}{4}\left(\frac{w_{op}^2 w_{os}^2}{\left(w_{op}^2+w_{os}^2\right)}\right) z_o \arctan[\frac{L}{2z_o}]. \tag{G.19}$$

Pump TEM_{00} and q TEM_{12}

The necessary Hermite polynomials in this case are

$$\mathrm{H}_1[x] = 2x \tag{G.20}$$

$$\mathrm{H}_2[y] = -2+4y^2. \tag{G.21}$$

In this case,

$$\begin{aligned} V_{pq} = & \int_{-L/2}^{L/2} dz \int_{-\infty}^{\infty} dy \int_{-\infty}^{\infty} dx \\ & \left(\frac{1}{16}\frac{w_{oq}^2}{w_q^2(z)}\mathrm{H}_1^2\left[\frac{\sqrt{2}x}{w_q(z)}\right]\mathrm{H}_2^2\left[\frac{\sqrt{2}y}{w_q(z)}\right]\exp\left[\left(-\frac{2}{w_q^2(z)}\right)\left(x^2+y^2\right)\right]\sin^2\left[k_q z\right]\right) \\ & \left(\frac{w_{op}^2}{w_p^2(z)}\exp\left[\left(-\frac{2}{w_p^2(z)}\right)\left(x^2+y^2\right)\right]\sin^2\left[k_p z\right]\right) \end{aligned} \tag{G.22}$$

Looking at the x-integral first,

$$\begin{aligned} & \int_{-\infty}^{\infty} dx\, \mathrm{H}_1^2\left[\frac{\sqrt{2}x}{w_q(z)}\right]\exp\left[\left(-\frac{2}{w_q^2(z)}-\frac{2}{w_p^2(z)}\right)x^2\right] \\ & = \int_{-\infty}^{\infty} dx \left(2\frac{\sqrt{2}x}{w_q(z)}\right)^2 \exp\left[\left(-\frac{2}{w_q^2(z)}-\frac{2}{w_p^2(z)}\right)x^2\right] \\ & = \frac{\sqrt{2\pi}w_p^3(z)w_q(z)}{\left(w_q^2(z)+w_p^2(z)\right)^{3/2}} \end{aligned} \tag{G.23}$$

where the integral was done using integral # 648 in the CRC math tables [79].

Proceeding with the evaluation of the y-integral,

$$\begin{aligned}
&\int_{-\infty}^{\infty} dy\, \mathrm{H}_2^2\left[\frac{\sqrt{2}y}{w_q(z)}\right] \exp\left[\left(-\frac{2}{w_q^2(z)}-\frac{2}{w_p^2(z)}\right)y^2\right] \\
&\quad = \int_{-\infty}^{\infty} dx \left[-2+4\left(\frac{\sqrt{2}y}{w_q(z)}\right)^2\right]^2 \exp\left[\left(-\frac{2}{w_q^2(z)}-\frac{2}{w_p^2(z)}\right)y^2\right] \\
&\quad = \int_{-\infty}^{\infty} dx \left(4-\frac{32y^2}{w_q^2(z)}+\frac{64y^4}{w_q^4(z)}\right) \exp\left[-2\left(\frac{w_p^2(z)+w_q^2(z)}{w_p^2(z)w_q^2(z)}\right)y^2\right] \quad \text{(G.24)}
\end{aligned}$$

This integral is also evaluated using integral #648 in the CRC math tables [79]. It results in

$$\begin{aligned}
&\int_{-\infty}^{\infty} dy\, \mathrm{H}_2^2\left[\frac{\sqrt{2}y}{w_q(z)}\right] \exp\left[\left(-\frac{2}{w_q^2(z)}-\frac{2}{w_p^2(z)}\right)y^2\right] \\
&\quad = \frac{2\sqrt{2\pi}w_p(z)w_q(z)\left(2w_p^4(z)+w_q^4(z)\right)}{\left(w_p^2(z)+w_q^2(z)\right)^{5/2}}. \quad \text{(G.25)}
\end{aligned}$$

The results of the x and y-integrals can now be plugged back into equation G.22.

$$\begin{aligned}
V_{pq} &= \int_{-L/2}^{L/2} dz \left(\frac{1}{16}\frac{w_{oq}^2 w_{op}^2}{w_q^2(z)w_p^2(z)}\sin^2[k_q z]\sin^2[k_p z]\right)\left(\frac{\sqrt{2\pi}w_p^3(z)w_q(z)}{\left(w_q^2(z)+w_p^2(z)\right)^{3/2}}\right) \\
&\quad \left(\frac{2\sqrt{2\pi}w_p(z)w_q(z)\left(2w_p^4(z)+w_q^4(z)\right)}{\left(w_p^2(z)+w_q^2(z)\right)^{5/2}}\right) \\
&= \int_{-L/2}^{L/2} dz\, \frac{\pi}{4}\sin^2[k_q z]\sin^2[k_p z]\, w_{oq}^2 w_{op}^2 \frac{w_p^2(z)\left(2w_p^4(z)+w_q^4(z)\right)}{\left(w_q^2(z)+w_p^2(z)\right)^4} \\
&= \frac{\pi}{4}\frac{w_{oq}^2 w_{op}^4\left(2w_{op}^4+w_{oq}^4\right)}{\left(w_{oq}^2+w_{op}^2\right)^4}\int_{-L/2}^{L/2} dz\, \frac{1}{\left(1+\left(\frac{z}{z_o}\right)^2\right)}\sin^2[k_q z]\sin^2[k_p z] \quad \text{(G.26)}
\end{aligned}$$

where equation G.2 has been substituted in. The remaining integral in equation G.26 is the same as the integral in equation G.9. Immediately applying the result of that integration yields:

$$V_{pq} = \tfrac{\pi}{8} \quad \frac{w_{oq}^2 w_{op}^4\left(2w_{op}^4+w_{oq}^4\right)}{\left(w_{oq}^2+w_{op}^2\right)^4} z_o \arctan[\frac{L}{2z_o}] \quad \text{(G.27)}$$

All the mode combinations calculated in this dissertation work came down to the evaluation of the same z-integral as seen in equations G.9 and G.26.

l_p	m_p	l_q	m_q	V_{pq}
0	0	0	0	$\frac{\pi}{4}\left(\frac{w_{op}^2 w_{oq}^2}{\left(w_{op}^2+w_{oq}^2\right)}\right) z_o \arctan[\frac{L}{2z_o}]$
0	0	1	2	$\frac{\pi}{8}\left(\frac{w_{oq}^2 w_{op}^4\left(2w_{op}^4+w_{oq}^4\right)}{\left(w_{oq}^2+w_{op}^2\right)^4}\right) z_o \arctan[\frac{L}{2z_o}]$
0	0	1	0	$\frac{\pi}{4}\left(\frac{w_{oq}^2 w_{op}^4}{\left(w_{oq}^2+w_{op}^2\right)^2}\right) z_o \arctan[\frac{L}{2z_o}]$
1	0	1	0	$\frac{3\pi}{4}\left(\frac{w_{oq}^4 w_{op}^4}{\left(w_{oq}^2+w_{op}^2\right)^3}\right) z_o \arctan[\frac{L}{2z_o}]$
1	1	1	0	$\frac{3\pi}{4}\left(\frac{w_{oq}^6 w_{op}^4}{\left(w_{oq}^2+w_{op}^2\right)^4}\right) z_o \arctan[\frac{L}{2z_o}]$
1	1	1	1	$\frac{9\pi}{4}\left(\frac{w_{oq}^6 w_{op}^6}{\left(w_{oq}^2+w_{op}^2\right)^5}\right) z_o \arctan[\frac{L}{2z_o}]$
0	0	3	0	$\frac{\pi}{8}\left(\frac{w_{oq}^2 w_{op}^4\left(2w_{op}^4+3w_{oq}^4\right)}{\left(w_{oq}^2+w_{op}^2\right)^4}\right) z_o \arctan[\frac{L}{2z_o}]$
0	1	0	0	$\frac{\pi}{4}\left(\frac{w_{op}^2 w_{oq}^4}{\left(w_{oq}^2+w_{op}^2\right)^2}\right) z_o \arctan[\frac{L}{2z_o}]$

Table G.1: Results of calculating the Type 2 overlap integral in rectangular coordinates.

Table of Values

Table G.1 contains the above two results and some additional results for V_{pq} calculated in this symmetry. They are labeled by the spatial mode indices for the pump, l_p and m_p, and the other mode, l_q and m_q. There are also additional results in Appendix I within the *Matlab* subroutines entitled V_{ps} and V_{pa}.

Cylindrical Symmetry

As defined in Appendix D, the Laguerre-Gaussian (LG) modes are

$$|u_q(\overrightarrow{r})|^2 = \frac{w_{oq}^2}{w_q^2(z)}\left(\frac{2l!}{(1+\delta_{0,m})(l+m)!}\right)^2\left(\frac{\sqrt{2}r}{w_q(z)}\right)^{2m}\left(\mathrm{L}_l^m\left[\frac{2r^2}{w_q^2(z)}\right]\right)^2 \exp\left[\left(-\frac{2}{w_q^2(z)}\right)r^2\right]\cos^2[m\theta]\sin^2[k_q z] \quad \text{(G.28)}$$

In this symmetry,

$$dcav \;=\; rdrd\theta dz \tag{G.29}$$

Thus,

$$V_{pq} \;=\; \int_{-L/2}^{L/2} dz \int_0^{\infty} dr \int_0^{2\pi} d\theta\, r|u_p(\overrightarrow{r})|^2|u_q(\overrightarrow{r})|^2. \tag{G.30}$$

From the form of $|u_q|^2$ in equation G.28, it can be seen that the r and θ-integrals in equation G.30 are independent of each other, though not independent of z. Following are a couple of specific examples in this symmetry.

Pump TEM_{00} and q TEM_{00}

The necessary Laguerre polynomial is $L_0^0[r] = 1$. Thus,

$$\begin{aligned} V_{pq} \;=\; & \int_{-L/2}^{L/2} dz \int_0^{\infty} dr \int_0^{2\pi} d\theta\, r \\ & \left(\frac{w_{op}^2}{w_p^2(z)} \exp\left[\left(-\frac{2}{w_p^2(z)}\right) r^2\right] \sin^2\left[k_p z\right]\right) \\ & \left(\frac{w_{oq}^2}{w_q^2(z)} \exp\left[\left(-\frac{2}{w_q^2(z)}\right) r^2\right] \sin^2\left[k_q z\right]\right). \end{aligned} \tag{G.31}$$

The integral over θ in equation G.31 is easy since the integrand does not depend on θ. The integral over r is integral #649 in the CRC math tables [79] and yields

$$\int_0^{\infty} dr\, r \exp\left[\left(-\frac{2}{w_p^2(z)} - \frac{2}{w_q^2(z)}\right) r^2\right] \;=\; \frac{1}{4} \frac{w_p^2(z) w_q^2(z)}{\left(w_p^2(z) + w_q^2(z)\right)} \tag{G.32}$$

The result of equation G.32 can be plugged back into equation G.31. The remaining z-integral is

$$\begin{aligned} V_{pq} \;&=\; \frac{\pi}{2} \int_{-L/2}^{L/2} dz\, \frac{w_{op}^2(z) w_{oq}^2(z)}{\left(w_p^2(z) + w_q^2(z)\right)} \sin^2\left[k_p z\right] \sin^2\left[k_q z\right] \\ &=\; \frac{\pi}{4} \left(\frac{w_{op}^2 w_{oq}^2}{\left(w_{op}^2 + w_{oq}^2\right)}\right) z_o \arctan[\frac{L}{2z_o}] \end{aligned} \tag{G.33}$$

where equation G.2 was substituted in yielding the same z-integral as in equation G.9, the result of which was applied. Reassuringly, this result agrees with the result obtained in cylindrical symmetry (equation G.19).

Pump TEM_{00} and q TEM_{12}

The Laguerre polynomial when $l = 1$ and $m = 2$ is

$$\mathrm{L}_1^2[r] \;=\; 3 - r \tag{G.34}$$

Thus, for this combination of modes,

$$\begin{aligned} V_{pq} \;=\; & \int_{-L/2}^{L/2} dz \int_0^{\infty} dr \int_0^{2\pi} d\theta\, r \\ & \left(\frac{w_{op}^2}{w_p^2(z)} \exp\left[\left(-\frac{2}{w_p^2(z)} \right) r^2 \right] \sin^2\left[k_p z\right] \right) \\ & \left(\frac{1}{9} \frac{w_{oq}^2}{w_q^2(z)} \left(\frac{\sqrt{2}r}{w_q(z)} \right)^4 \left(3 - \frac{2r^2}{w_q^2(z)} \right)^2 \right. \\ & \left. \exp\left[\left(-\frac{2}{w_q^2(z)} \right) r^2 \right] \cos^2\left[2\theta\right] \sin^2\left[k_q z\right] \right). \end{aligned} \tag{G.35}$$

Evaluating the integral over θ first,

$$\int_0^{2\pi} d\theta \cos^2\left[2\theta\right] \;=\; \pi \tag{G.36}$$

by integral #285 in the CRC math tables [79].

Moving on to the r-integral,

$$\begin{aligned} & \int_0^{\infty} dr\, r \exp\left[\left(-\frac{2}{w_p^2(z)} - \frac{2}{w_q^2(z)} \right) r^2 \right] \left(\frac{\sqrt{2}r}{w_q(z)} \right)^4 \left(3 - \frac{2r^2}{w_q^2(z)} \right)^2 \\ & \quad = \frac{4}{w_q^4(z)} \int_0^{\infty} dr\, r^5 \left(3 - \frac{2r^2}{w_q^2(z)} \right)^2 \exp\left[-2 \left(\frac{w_p^2(z) + w_q^2(z)}{w_p^2(z) w_q^2(z)} \right) r^2 \right] \end{aligned} \tag{G.37}$$

Given that

$$r^5 \left(3 - \frac{2r^2}{w_q^2(z)} \right)^2 \;=\; 9r^5 - \frac{12r^7}{w_q^2(z)} + \frac{4r^9}{w_q^4(z)}, \tag{G.38}$$

the r-integrals can be solved using integral #649 in the CRC math tables [79]. For example,

$$\int_0^\infty dr\, r^5 \exp\left[-2\left(\frac{w_q^2(z)+w_q^2(z)}{w_p^2(z)w_q^2(z)}\right)r^2\right] = \frac{w_p^6(z)w_q^6(z)}{8\left(w_p^2(z)+w_q^2(z)\right)^3}. \quad \text{(G.39)}$$

Thus, the result of the r-integral in equation G.37 is

$$\frac{4}{w_q^4(z)}\int_0^\infty dr\, r^5\left(3-\frac{2r^2}{w_q^2(z)}\right)^2 \exp\left[-2\left(\frac{w_p^2(z)+w_q^2(z)}{w_p^2(z)w_q^2(z)}\right)r^2\right]$$
$$= \frac{3}{2}\left(\frac{w_p^6(z)w_q^2(z)\left(w_p^4(z)+3w_q^4(z)\right)}{(w_p^2(z)+w_q^2(z))^5}\right). \quad \text{(G.40)}$$

Equations G.36 and G.40 can now be plugged back into equation G.35.

$$V_{pq} = \frac{\pi}{6}w_{op}^2 w_{oq}^2 \int_{-L/2}^{L/2} dz \left(\frac{w_p^4(z)\left(w_p^4(z)+3w_q^4(z)\right)}{(w_p^2(z)+w_q^2(z))^5}\right)\sin^2\left[k_p z\right]\sin^2\left[k_q z\right] \quad \text{(G.41)}$$

Once equation G.2 is plugged-in, the resulting z-integral is again the same as in equation G.9. Thus, the Type 2 overlap volume for $l = 1$ and $m = 2$ in cylindrical symmetry is

$$V_{pq} = \frac{\pi}{12}\left(\frac{w_{op}^6 w_{oq}^2\left(w_{op}^4+3w_{oq}^4\right)}{(w_{op}^2+w_{oq}^2)^5}\right) z_o \arctan[\frac{L}{2z_o}] \quad \text{(G.42)}$$

There are a couple of additional results for this mode symmetry in Appendix I within the *Matlab* subroutines entitled V_{ps} and V_{pa}.

Elliptical Symmetry

Please see the discussion in Appendix F regarding integration in elliptical symmetry.

APPENDIX H

TYPE 3 OVERLAP VOLUME

The type 3 overlap volume is defined in equation 2.135. It is

$$V_{FWM} = \int_{cav} u_p^{*2}\, u_s\, u_a\, dcav \tag{H.1}$$

This integral will depend on all three wavelengths and mode structures. Unlike the first two types of overlap volumes, V_{FWM} is not a real quantity. It also cannot be calculated analytically without first approximating the spatial mode structure of the three fields. This appendix will begin with that approximation and then proceed with calculations in rectangular and circularly symmetric modes. For modes with elliptic symmetry, please see Appendix E.

As a reminder, the functional dependence of the spot size $w_q(z)$ and wavefront radius of curvature $R_c(z)$ are [46]

$$w_q(z) = w_{oq}\left[1+\left(\frac{z}{z_o}\right)^2\right]^{\frac{1}{2}} \tag{H.2}$$

$$R_c(z) = z\left[1+\left(\frac{z_o}{z}\right)^2\right]. \tag{H.3}$$

Also, a note of caution: *Mathematica* was initially used exclusively (after verification by hand of the simplest mode combination) to calculate the x- and y-integrals in V_{FWM}, as these integrals can become quite complicated . However, during one calculation *Mathematica* made an error, not in the integration, but in the simplification of the result. After that discovery, the integrals, as cumbersome as they are, were calculated both by hand and by *Mathematica*, with the results cross-checked to verify accuracy.

Collimated Beam Approximation

In the collimated beam approximation, it is assumed that the cavity mode is TEM_{00} and that $w_q(z) = w_{oq}$. In other words, the spot size is constant along the

direction of propagation. As a result of this, the Rayleigh range, z_o, is infinite as is R_c, the field's radius of curvature. In this approximation, the functional form of the cavity mode structures simplifies (from either C.1 or D.1) to

$$u_q(\overrightarrow{r}) \;=\; \exp\left[-\frac{r^2}{w_{oq}^2}\right]\sin\left[k_q z\right], \tag{H.4}$$

where, if in rectangular symmetry, $r^2 = x^2 + y^2$. Equation H.4 can now be plugged into equation H.1, yielding

$$V_{FWM} \;=\; \int_{cav} dcav\,\left(\exp\left[-\frac{2r^2}{w_{op}^2}\right]\sin^2\left[k_p z\right]\right)\left(\exp\left[-\frac{r^2}{w_{os}^2}\right]\sin\left[k_s z\right]\right)\times \left(\exp\left[-\frac{r^2}{w_{oa}^2}\right]\sin\left[k_a z\right]\right). \tag{H.5}$$

As can be seen from equation H.5, in this approximation, V_{FWM} will be a real quantity. Though the result would be the same in rectangular symmetry, it is easiest to work this integral in cylindrical symmetry because in cylindrical symmetry, one of the integrals is trivial. Thus, let

$$dcav \;=\; r dr d\theta dz \tag{H.6}$$

and

$$V_{FWM} \;=\; \int_{-L/2}^{L/2} dz \int_0^{\infty} dr \int_0^{2\pi} d\theta\, r\, \exp\left[-\left(\frac{2}{w_{op}^2}+\frac{1}{w_{os}^2}+\frac{1}{w_{oa}^2}\right)r^2\right]\times \sin^2\left[k_p z\right]\sin\left[k_s z\right]\sin\left[k_a z\right]. \tag{H.7}$$

The θ-integral is trivial. The r-integral is # 649 in the CRC math tables [79]. After performing both,

$$V_{FWM} \;=\; \pi\varpi_o^2 \int_{-L/2}^{L/2} dz\, \sin^2\left[k_p z\right]\sin\left[k_s z\right]\sin\left[k_a z\right] \tag{H.8}$$

where

$$\frac{1}{\varpi_o^2} \;\equiv\; \left(\frac{2}{w_{op}^2}+\frac{1}{w_{os}^2}+\frac{1}{w_{oa}^2}\right). \tag{H.9}$$

The remaining z-integral in equation H.8 is not easily calculated as written. Instead, rewrite the integral using trig identities as

$$\begin{aligned} V_{FWM} &= \frac{\pi \varpi_o^2}{8} \int_{-L/2}^{L/2} dz \; (2\cos\left[(k_s - k_a)\, z\right] - 2\cos\left[(k_s + k_a)\, z\right] \\ &\quad - \cos\left[(2k_p - k_s + k_a)\, z\right] - \cos\left[(2k_p + k_s - k_a)\, z\right] \\ &\quad + \cos\left[(2k_p + k_s + k_a)\, z\right] + \cos\left[(2k_p - k_s - k_a)\, z\right]) \end{aligned} \tag{H.10}$$

There are now six integrals but each is very easy to evaluate. The result of the basic integral is

$$\int_{-L/2}^{L/2} dz \; \cos\left[\Delta\kappa\, z\right] = \frac{\sin\left[\Delta\kappa\, z\right]}{\Delta\kappa}\Bigg|_{-L/2}^{L/2}, \tag{H.11}$$

where $\Delta\kappa$ is any of the six possible combinations of wave numbers in equation H.10. Given $c = \lambda f$ and $\omega = 2\pi f$ then $k_q = {}^{2\pi n_q}/_{\lambda_q} = {}^{n_q \omega_q}/_{c}$. Given a pump wavelength of 532 nm and the index of refraction of hydrogen from the AIP handbook [55] (see equation H.20) and using equations 2.29 and 2.30 (which, on line-center, are $\omega_s = \omega_p - \omega_{31}$ and $\omega_a = \omega_p + \omega_{31}$) to determine the Stokes and anti-Stokes frequencies relative to the pump, then the values of $\Delta\kappa$, in rad/m, are at 10 atm and 298 K.

$$|k_s - k_a| \simeq 5 \times 10^6 \tag{H.12}$$

$$|k_s + k_a| \simeq 2 \times 10^7 \tag{H.13}$$

$$|2k_p - k_s + k_a| \simeq 3 \times 10^7 \tag{H.14}$$

$$|2k_p + k_s - k_a| \simeq 2 \times 10^7 \tag{H.15}$$

$$|2k_p + k_s + k_a| \simeq 5 \times 10^7 \tag{H.16}$$

$$|2k_p - k_s - k_a| \simeq 1 \times 10^2. \tag{H.17}$$

Because, equation H.11 is proportional to $\Delta\kappa^{-1}$, the dominant term in equation H.10 will be the one proportional to the smallest value of $\Delta\kappa$. Thus, define

$$\Delta k \equiv 2k_p - k_s - k_a, \tag{H.18}$$

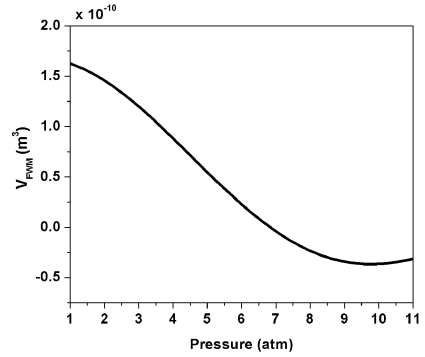

(a)

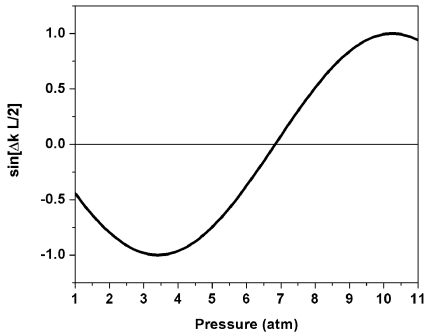

(b)

Figure H.1: (a) Graph of V_{FWM} as a function of pressure as calculated in the collimated beam approximation and (b) the corresponding value of $\sin\left[\frac{\Delta k\, L}{2}\right]$.

which is the standard phase matching definition for Raman scattering and

$$V_{FWM} \;=\; \frac{\pi \varpi_o^2}{4\Delta k} \sin\left[\frac{\Delta k\, L}{2}\right] \tag{H.19}$$

Since k_q depends on the index of refraction (i.e. $k_q = {}^{2\pi n_q}/_{\lambda_q}$), V_{FWM} will be dependent on the indices of refraction, which are in turn dependent on pressure. Figure H.1a shows the calculated value of V_{FWM}, and Figure H.1b shows the value of $\sin\left[\frac{\Delta k\, L}{2}\right]$, both as functions of pressure. The parameters used in making these plot are $\lambda_p = 532$ nm, $L \sim$7.62 cm, and $T = 293$ K. The Stokes frequency was determined by the cavity mode closest to gain line center, and the anti-Stokes frequency was $2f_p - f_s$. Of particular importance is that V_{FWM} goes through zero at a pressure of 7

atm because $\sin\left[\frac{\Delta k\, L}{2}\right]$ goes through zero at that pressure. Because V_{FWM} is zero, no anti-Stokes can be produced at that pressure (as can be seen from equation 2.160), for this mode combination in this approximation.

(To find the index of refraction as a function of frequency, temperature, and pressure, a polynomial fit (proportional to f^2) was first made to the index data in the AIP Handbook [55]. The data in the AIP handbook is at standard temperature and pressure (0^o C and 1 atm). Since an increase in pressure should increase the index, to adjust the index for pressure changes, the fit parameters were multiplied by the desired pressure and divided by the standard pressure (in atm). Temperature increases should decrease the index of refraction. Therefore, the fit parameters were multiplied by the standard temperature and divided by the desired temperature (in Kelvin) in order to adjust for temperature changes. The formula used in the *Matlab* code of Appendix I was originally found by Roos and later reverified. It is

$$n - 1 \;=\; n_o \frac{273P}{T} + b_o \frac{273P}{T} f + c_o \frac{273P}{T} f^2 \qquad \text{(H.20)}$$

where $n_o = 1.36075 \times 10^{-4}$, $b_o = 2.69852 \times 10^{-22}$, and $c_o = 1.16021 \times 10^{-35}$ for P in atm, T in K, and f in Hz.)

The collimated beam approximation is beneficial because it leads to an analytic solution for V_{FWM}. However, in making the collimated beam approximation, much of the z-dependence of the V_{FWM} integrand is dropped. As will be seen in the next section, if the pump, Stokes, and anti-Stokes are all TEM_{00}, then the collimated beam approximation is a fairly good approximation to the actual behavior of V_{FWM}. But, for HOM combinations, the collimated beam approximation will be less applicable. Therefore, it is necessary to proceed with non-approximated calculations.

Rectangular Symmetry

From Appendix C, the Hermite-Gaussian (HG) cavity spatial mode profile in rectangular symmetry is

$$u_q(\overrightarrow{r}) = \frac{w_{oq}}{w_q(z)}\sqrt{\frac{1}{2^{l_q+m_q}l_q!m_q!}}\exp\left[-i(l_q+m_q+1)\arctan\left[\frac{z}{z_o}\right]\right]\mathrm{H}_{l_q}\left[\frac{\sqrt{2}x}{w_q(z)}\right] \mathrm{H}_{m_q}\left[\frac{\sqrt{2}y}{w_q(z)}\right]\exp\left[\left(-\frac{ik_q}{2R_c(z)}-\frac{1}{w_q^2(z)}\right)\left(x^2+y^2\right)\right]\sin\left[k_q z\right]. \quad \text{(H.21)}$$

In this symmetry,

$$dcav = dxdydz \quad \text{(H.22)}$$

Thus,

$$V_{FWM} = \int_{-L/2}^{L/2} dz \int_{-\infty}^{\infty} dy \int_{-\infty}^{\infty} dx\, u_p^{*2}\, u_s\, u_a. \quad \text{(H.23)}$$

From the form of $u_q(\overrightarrow{r})$ in equation H.21, it can be seen that the x- and y-integrals in equation G.5 are independent of each other, though not independent of z.

Allowable Mode Combinations

Unlike the first two types of overlap integrals, the integrand for V_{FWM} is not inherently even overall. If the integrand is odd, V_{FWM} will be zero. Therefore, there are mode combinations that will not be allowed because they lead to odd integrands. Since the functional form of the x- and y-integrals is identical, the allowable mode combinations for this symmetry can be found by looking at only one of them and

then applying the same conclusions to the other.

$$\int_{-\infty}^{\infty} dx \; \exp\left[\left(\frac{ik_p}{R_c(z)} - \frac{2}{w_p^2(z)}\right)x^2\right] \mathrm{H}_{l_p}^2\left[\frac{\sqrt{2}x}{w_p(z)}\right] \exp\left[\left(-\frac{ik_s}{2R_c(z)} - \frac{1}{w_s^2(z)}\right)x^2\right] \mathrm{H}_{l_s}\left[\frac{\sqrt{2}x}{w_s(z)}\right] \exp\left[\left(-\frac{ik_a}{2R_c(z)} - \frac{1}{w_a^2(z)}\right)x^2\right] \mathrm{H}_{l_a}\left[\frac{\sqrt{2}x}{w_a(z)}\right] \tag{H.24}$$

The gaussian functions are inherently even, as is the Hermite polynomial associated with the pump mode because it is squared. Therefore, the allowed mode combinations will be independent of the pump mode.

This leaves the Stokes and anti-Stokes Hermite polynomials to determine the symmetry of the integrand. A general property of the Hermite polynomials is that $\mathrm{H}_l[x]$ is an even function when l is even and $\mathrm{H}_l[x]$ is odd when l is odd. For example, the first few Hermite polynomials are:

$$\mathrm{H}_0[x] = 1 \tag{H.25}$$

$$\mathrm{H}_1[x] = 2x \tag{H.26}$$

$$\mathrm{H}_2[x] = 4x^2 - 2 \tag{H.27}$$

$$\mathrm{H}_3[x] = 8x^3 - 12x \tag{H.28}$$

Therefore, the x-integral in V_{FWM} will be non-zero only when the Stokes and anti-Stokes mode indices (l_s and l_a, respectively) are both even or both odd. The same will be true for the y-indices, m_s and m_a.

Figure H.2a shows the intensity profile of the TEM_{12} mode. Figure H.2b shows pictures of some allowable anti-Stokes modes given the Stokes mode of TEM_{12} while Figure H.2c is pictures of some non-allowed modes. The possible allowed anti-Stokes modes shown in Figure H.2b are TEM_{10}, TEM_{12}, and TEM_{32} because the first index

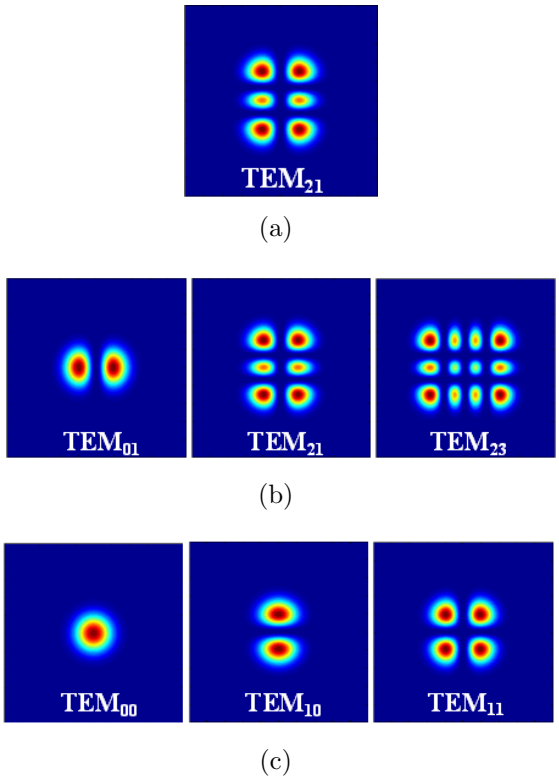

Figure H.2: Intensity profiles for various HG modes showing allowed and non-allowed anti-Stokes modes, given a possible Stokes mode. In this symmetry, the allowed anti-Stokes modes are independent of the pump. The Stokes mode is shown in subplot a. Subplots b and c show allowed and non-allowed anti-Stokes modes, respectively. Red is the most intense and blue is the least.

is always even and the second index is always odd. Anti-Stokes modes that would not be allowed (Figure H.2c) are TEM_{00}, TEM_{01}, and TEM_{11}. Red in the intensity profiles is the most intense and blue is the least.

As can be seen from Figure H.2, physically, having both the Stokes and anti-Stokes mode indices (l_s and l_a or m_s and m_a, respectively) both even or both is odd results in a symmetry in the modes. When the index, l_s (or l_a), is odd, the intensity pattern is zero along the y-axis. When it is even, the intensity pattern is not necessarily a global maximum of the intensity pattern but is a local maximum. The index, m_s (or m_a), will result in either a zero or local maximum along the y-axis if the index is odd or even, respectively. By requiring the Stokes and anti-Stokes mode indices to be either both even or both odd, it is requiring the modes to have the same symmetry around the x- and y-axes.

Following are a couple of specific examples for this symmetry.

Pump, Stokes, and anti-Stokes TEM_{00}

The lowest order Hermite polynomial is $\mathrm{H}_0[x] = 1$. Plugging H.21 into equation H.23 and simplifying yields:

$$\begin{aligned} V_{FWM} &= \int_{-L/2}^{L/2} dz \int_{-\infty}^{\infty} dy \int_{-\infty}^{\infty} dx \, \frac{w_{op}^2 w_{os} w_{oa}}{w_p^2(z) w_s(z) w_a(z)} \times \\ &\qquad \exp\left[\left(\frac{i\Delta k}{R_c(z)} - \frac{1}{\varpi^2(z)}\right)\left(x^2+y^2\right)\right] \times \\ &\qquad \sin^2[k_p z] \sin[k_s z] \sin[k_a z] \end{aligned} \tag{H.29}$$

where the definition of Δk from equation H.18 has been used and

$$\frac{1}{\varpi^2(z)} \equiv \left(\frac{2}{w_p^2(z)} + \frac{1}{w_s^2(z)} + \frac{1}{w_a^2(z)}\right) \tag{H.30}$$

which is an obvious extension to the definition in equation H.9. The x- and y-integrals are identical and can be solved using integral #643 in the CRC math tables [79]. The

x-integral is

$$\int_{-\infty}^{\infty} dx\ \exp\left[\left(\frac{i\Delta k}{R_c(z)} - \frac{1}{\varpi^2(z)}\right)x^2\right] \;=\; \sqrt{\frac{\pi\varpi^2(z)R_c(z)}{(i\Delta k\varpi^2(z) - R_c(z))}}. \quad \text{(H.31)}$$

The remaining z-integral in equation H.29 is

$$V_{FWM} \;=\; \pi\int_{-L/2}^{L/2} dz\ \frac{w_{op}^2 w_{os} w_{oa}}{w_p^2(z)w_s(z)w_a(z)}\left(\frac{\varpi^2(z)R_c(z)}{(i\Delta k\varpi^2(z) - R_c(z))}\right) \sin^2[k_p z]\sin[k_s z]\sin[k_a z] \quad \text{(H.32)}$$

As in the collimated beam approximation, the product of the sine functions can be rewritten with the aid of trig identities and only the term proportional to $\cos(\Delta k z)$ will be retained.

$$V_{FWM} \;=\; \frac{\pi}{8}\int_{-L/2}^{L/2} dz\ \frac{w_{op}^2 w_{os} w_{oa}}{w_p^2(z)w_s(z)w_a(z)} \times \left(\frac{\varpi^2(z)R_c(z)}{(i\Delta k\varpi^2(z) - R_c(z))}\right)\cos(\Delta k z) \quad \text{(H.33)}$$

This integral cannot be calculated analytically. Therefore, a *Matlab* code was written to solve it numerically. This code is available in Appendix I.

Figures H.3a and b show the calculated values of the real and imaginary parts of V_{FWM} (as denoted by the superscripts R and I), respectively, as functions of pressure. Also plotted as dots on Figure H.3a is the result for the collimated beam approximation which agrees very well with the numerically calculated result for this mode combination. Since there is no net Gouy phase shift for this mode combination, V_{FWM}^R goes through zero at ∼7 atm, the same pressure as the collimated beam approximation result. As will be seen in the next example, when there is a net Gouy phase shift, V_{FWM}^R will pass through zero at a pressure other than 7 atm. The imaginary part of V_{FWM} is very small compared to the real part. The oscillations at larger pressures are likely due to numerics. Figure H.3 was made using the same parameters as Figure H.1.

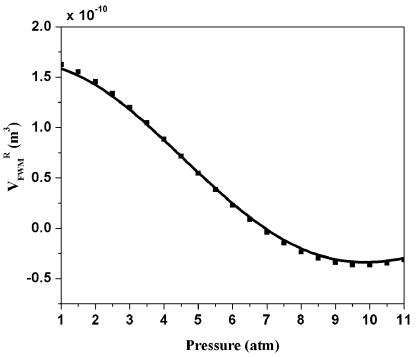

(a) Real part.

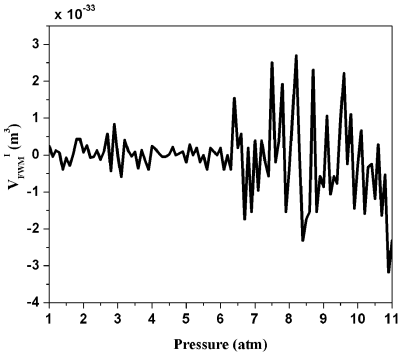

(b) Imaginary part.

Figure H.3: Graphs of the real and imaginary parts of V_{FWM} as functions of pressure for the pump, Stokes and anti-Stokes all on HG TEM_{00} modes. The dots on subplot a are from the collimated beam approximation.

Pump TEM_{00}, Stokes TEM_{20}, and anti-Stokes TEM_{20}

The two Hermite polynomials needed for this case are

$$\mathrm{H}_0[x] = 1 \tag{H.34}$$

$$\mathrm{H}_2[x] = 4x^2 - 2. \tag{H.35}$$

After plugging in H.21 into equation H.23 and simplifying

$$\begin{aligned} V_{FWM} = \sqrt{\frac{1}{8}} \int_{-L/2}^{L/2} dz \int_{-\infty}^{\infty} dy \int_{-\infty}^{\infty} dx \, \frac{w_{op}^2 w_{os} w_{oa}}{w_p^2(z) w_s(z) w_a(z)} \exp\left[-4i \arctan\left[\frac{z}{z_o}\right]\right] \times \\ \mathrm{H}_2\left[\frac{\sqrt{2}x}{w_s(z)}\right] \exp\left[\left(\frac{i\Delta k}{R_c(z)} - \frac{1}{\varpi^2(z)}\right)(x^2+y^2)\right] \times \\ \mathrm{H}_2\left[\frac{\sqrt{2}x}{w_a(z)}\right] \sin^2[k_p z] \sin[k_s z] \sin[k_a z] \end{aligned} \tag{H.36}$$

where the definitions of Δk and ϖ have again been applied from equations H.18 and H.9, respectively.

The x-integral is

$$\begin{aligned} \int_{-\infty}^{\infty} dx \, \mathrm{H}_2\left[\frac{\sqrt{2}x}{w_s(z)}\right] \mathrm{H}_2\left[\frac{\sqrt{2}x}{w_a(z)}\right] \exp\left[\left(\frac{i\Delta k}{R_c(z)} - \frac{1}{\varpi^2(z)}\right)x^2\right] \\ = \int_{-\infty}^{\infty} dx \, \left(4 - 16\frac{x^2}{w_s^2(z)} - 16\frac{x^2}{w_a^2(z)} + \frac{x^4}{w_s^2(z) w_a^2(z)}\right) \times \\ \exp\left[\left(\frac{i\Delta k}{R_c(z)} - \frac{1}{\varpi^2(z)}\right)x^2\right] \end{aligned} \tag{H.37}$$

There are now four integrals. However, they can all be calculated using integral # 648 in the CRC math tables [79]. For example,

$$\begin{aligned} \int_{-\infty}^{\infty} dx \, 16\frac{x^2}{w_s^2(z)} \exp\left[\left(\frac{i\Delta k}{R_c(z)} - \frac{1}{\varpi^2(z)}\right)x^2\right] \\ = \frac{8\sqrt{\pi}}{w_s^2(z)} \left(\frac{\varpi^2(z) R_c(z)}{(i\Delta k \varpi^2(z) - R_c(z))}\right)^{\frac{3}{2}} \end{aligned} \tag{H.38}$$

After performing all four integrals, the result of the x-integral is

$$\int_{-\infty}^{\infty} dx\, \mathrm{H}_2\left[\frac{\sqrt{2}x}{w_s(z)}\right] \mathrm{H}_2\left[\frac{\sqrt{2}x}{w_a(z)}\right] \exp\left[\left(\frac{i\Delta k}{R_c(z)} - \frac{1}{\varpi^2(z)}\right) x^2\right]$$
$$= \frac{4\sqrt{\pi}}{w_s^2(z)w_a^2(z)} \frac{\left(12 + \Upsilon^2 w_s^2(z)w_a^2(z) - 2\Upsilon\left(w_s^2(z) + w_a^2(z)\right)\right)}{\Upsilon^{5/2}} \qquad \text{(H.39)}$$

where

$$\Upsilon = \left(\frac{i\Delta k\varpi^2(z) - R_c(z)}{R_c(z)\varpi^2(z)}\right) \qquad \text{(H.40)}$$

is from the argument of the gaussian.

The y-integral is the same integral evaluated in equation H.31. Restating that result in terms of Υ yields

$$\int_{-\infty}^{\infty} dy\, \exp\left[\left(\frac{i\Delta k}{R_c(z)} - \frac{1}{\varpi^2(z)}\right) y^2\right] = \sqrt{\frac{\pi}{\Upsilon}}. \qquad \text{(H.41)}$$

After again simplifying the product of the sine functions in equation H.36 as in the collimated beam approximation and combining the results of the x- and y-integrals, the remaining z-integral is

$$V_{FWM} = \frac{\pi}{2}\sqrt{\frac{1}{8}} \int_{-L/2}^{L/2} dz\, \frac{w_{op}^2 w_{os} w_{oa}}{w_p^2(z)w_s^3(z)w_a^3(z)} \exp\left[-4i \arctan\left[\frac{z}{z_o}\right]\right] \cos\left[\Delta k\, z\right]$$
$$\left(\frac{\left(12 + \Upsilon^2 w_s^2(z)w_a^2(z) - 2\Upsilon\left(w_s^2(z) + w_a^2(z)\right)\right)}{\Upsilon^3}\right). \qquad \text{(H.42)}$$

This integral cannot be calculated analytically. Therefore, a *Matlab* code was written to solve it numerically. This code is available in Appendix I.

Figures H.4a and b show the calculated values of the real and imaginary parts of V_{FWM}, respectively, as functions of pressure. As shown in Figure H.4a, the real part of V_{FWM} passes through zero at just over ~ 8.2 atm, as opposed to 7 atm calculated for the pump, Stokes, and anti-Stokes TEM_{00} mode combination (as seen in Figure H.3). This means that at pressures where the anti-Stokes cannot be generated with all

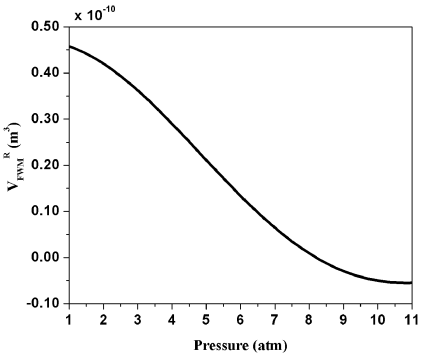

(a) Real part.

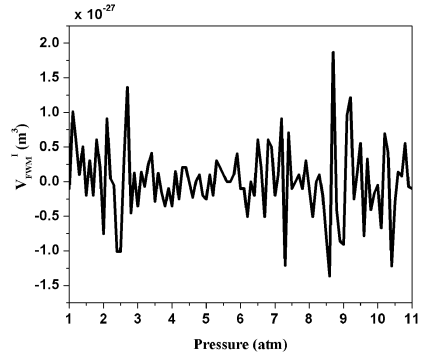

(b) Imaginary part.

Figure H.4: Graphs of the real and imaginary parts of V_{FWM} as functions of pressure for the mode combination: pump HG TEM_{00}, Stokes HG TEM_{20}, and anti-Stokes HG TEM_{20}.

the fields on TEM_{00} modes, it may be possible to generate anti-Stokes on other mode combinations. This difference between the two cases is due to the Gouy phase shift. The imaginary part of V_{FWM}, shown in Figure H.4b, is still small compared to the real part. (However, the ratio of the real and imaginary parts for this mode combination is seven orders of magnitude smaller than the same ratio for the fundamental mode combination.) Figure H.4 was made using the same parameters as Figure H.1.

Cylindrical Symmetry

As defined in Appendix D, the Laguerre-Gaussian (LG) modes are

$$\begin{aligned} u_q(\overrightarrow{r}) &= \frac{w_{oq}}{w_q(z)}\sqrt{\frac{2l_q!}{(1+\delta_{0,m_q})(l_q+m_q)!}}\left(\frac{\sqrt{2}r}{w_q(z)}\right)^{m_q} \\ &\quad \exp\left[-i(2l_q+m_q+1)\arctan\left[\frac{z}{z_o}\right]\right] \mathrm{L}_{l_q}^{m_q}\left[\frac{2r^2}{w_q^2(z)}\right] \\ &\quad \exp\left[\left(-\frac{ik_q}{2R_c(z)}-\frac{1}{w_q^2(z)}\right)r^2\right]\cos\left[m_q\theta\right]\sin\left[k_q z\right] \end{aligned} \tag{H.43}$$

In this symmetry,

$$dcav = r dr d\theta dz \tag{H.44}$$

Thus,

$$V_{FWM} = \int_{-L/2}^{L/2} dz \int_0^{\infty} dr \int_0^{2\pi} d\theta \, r u_p^{*2} \, u_s \, u_a. \tag{H.45}$$

Allowable Mode Combinations

As in rectangular symmetry, there are some modes that are not going to be allowed. The allowable modes will be determined by the r- and θ-integrals.

As complicated as the radial dependence of equation H.45 is, the r-integral will be non-zero regardless of the relationships of the mode indices. Since only the radial

integral is dependent on the radial mode indices, all combinations of the radial indices are allowable.

The θ-integral is

$$\begin{aligned}
&\int_0^{2\pi} d\theta\ \cos^2\left[m_p\theta\right]\cos\left[m_s\theta\right]\cos\left[m_a\theta\right] \\
&\quad = \frac{1}{8}\int_0^{2\pi} d\theta\,(2\cos\left[(m_s-m_a)\theta\right] + 2\cos\left[(m_s+m_a)\theta\right] \\
&\qquad + \cos\left[(2m_p-m_s+m_a)\theta\right] + \cos\left[(2m_p+m_s-m_a)\theta\right] \\
&\qquad + \cos\left[(2m_p+m_s+m_a)\theta\right] + \cos\left[(2m_p-m_s-m_a)\theta\right]) \qquad \text{(H.46)}
\end{aligned}$$

Since the integral of cosine over a period is zero, each of the six integrals above will be zero unless the argument of its cosine is zero. Since m_q is a non-negative integer, only four combinations of m_p, m_s, and m_a can meet this requirement. This condition will be met if one or more of the four following equations is satisfied.

$$2m_p = m_s + m_a \qquad \text{(H.47)}$$

$$2m_p = m_s - m_a \qquad \text{(H.48)}$$

$$2m_p = -m_s + m_a \qquad \text{(H.49)}$$

$$m_s = m_a \qquad \text{(H.50)}$$

These four cases include the special case where $m_p = m_s = m_a = 0$ and require that m_s and m_a be either both even or odd. Unlike rectangular symmetry, where the allowable anti-Stokes modes depended only on the Stokes mode, in cylindrical symmetry, the allowed anti-Stokes modes can depend on the pump, in addition to the Stokes.

Figure H.5 shows the intensity profiles of three allowed pump, Stokes and anti-Stokes mode combinations. Areas shaded red are more intense than areas shaded blue.

Following are a couple of specific examples for this symmetry.

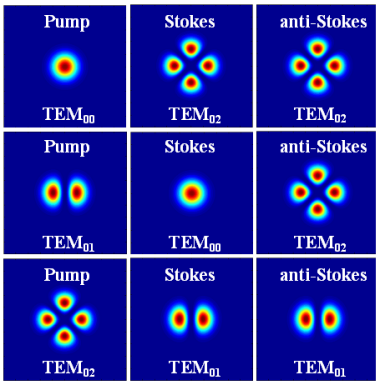

Figure H.5: Intensity profiles of three sets of allowed LG modes. Red areas are more intense than blue.

Pump, Stokes, and anti-Stokes TEM_{00}

The Laguerre polynomial for this combination is $\mathrm{L}_0^0[r] = 1$. Thus, after simplification,

$$V_{FWM} = \int_{-L/2}^{L/2} dz \int_0^\infty dr \int_0^{2\pi} d\theta \, r \frac{w_{op}^2 w_{os} w_{oa}}{w_p^2(z) w_s(z) w_a(z)} \times \exp\left[\Upsilon r^2\right] \sin^2\left[k_p z\right] \sin\left[k_s z\right] \sin\left[k_a z\right] \tag{H.51}$$

where the definition of Υ has been employed from equation H.40. The θ-integral is trivial. The r-integral is integral #649 in the CRC math tables [79]. It results in

$$\int_0^\infty dr \, r \exp\left[\Upsilon r^2\right] = \frac{1}{2\Upsilon} \tag{H.52}$$

The remaining z-integral is

$$V_{FWM} = \pi \int_{-L/2}^{L/2} dz \, r \frac{w_{op}^2 w_{os} w_{oa}}{w_p^2(z) w_s(z) w_a(z)} \frac{1}{\Upsilon} \sin^2\left[k_p z\right] \sin\left[k_s z\right] \sin\left[k_a z\right] \tag{H.53}$$

Equation H.53 is identical to the rectangularly symmetric result in equation H.32. Therefore, the result in circular symmetry is the same as the result in rectangular symmetry.

Pump TEM_{00}, Stokes TEM_{02}, and anti-Stokes TEM_{02}

The necessary Laguerre polynomials are

$$\mathrm{L}_0^0[r] = 1 \tag{H.54}$$

$$\mathrm{L}_0^2[r] = 1. \tag{H.55}$$

After simplification, V_{FWM}, for this mode combination, is

$$V_{FWM} = \int_{-L/2}^{L/2} dz \int_0^\infty dr \int_0^{2\pi} d\theta\, r \frac{w_{op}^2 w_{os} w_{oa}}{w_p^2(z) w_s(z) w_a(z)} \exp\left[-i4 \arctan\left[\frac{z}{z_o}\right]\right] \sin^2[k_p z] \sin[k_s z] \sin[k_a z] \cos[2\theta] \cos[2\theta] \left(\frac{\sqrt{2}r}{w_s(z)}\right)^2 \left(\frac{\sqrt{2}r}{w_a(z)}\right)^2 \exp\left[\Upsilon r^2\right] \tag{H.56}$$

The θ-integral is

$$\int_0^{2\pi} d\theta \cos[2\theta] \cos[2\theta] = \pi. \tag{H.57}$$

The radial integral is

$$\int_0^\infty dr\, r \left(\frac{\sqrt{2}r}{w_s(z)}\right)^2 \left(\frac{\sqrt{2}r}{w_a(z)}\right)^2 \exp\left[\Upsilon r^2\right] = \frac{4}{w_s^2(z) w_a^2(z)} \int_0^\infty dr\, r^5 \exp\left[\Upsilon r^2\right] = \frac{4}{w_s^2(z) w_a^2(z) \Upsilon^3}. \tag{H.58}$$

It was evaluated using integral #649 from the CRC math tables [79]. The remaining z-integral is

$$V_{FWM} = 4\pi \int_{-L/2}^{L/2} dz\, \frac{w_{op}^2 w_{os} w_{oa}}{w_p^2(z) w_s^3(z) w_a^3(z) \Upsilon^3} \exp\left[-i4 \arctan\left[\frac{z}{z_o}\right]\right] \times \sin^2[k_p z] \sin[k_s z] \sin[k_a z] \tag{H.59}$$

The product of the sine functions in equation H.36 can be simplified as in the collimated beam approximation. The resulting z-integral integral cannot be calculated analytically. Therefore, a *Matlab* code was written to solve it numerically. This code is available in Appendix I.

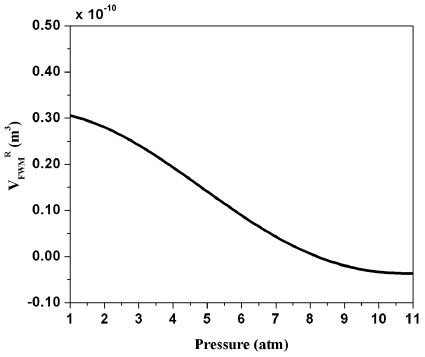

(a) Real part.

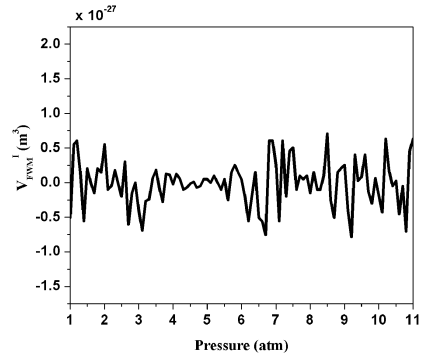

(b) Imaginary part.

Figure H.6: Graphs of the real and imaginary parts of V_{FWM} as functions of pressure for the pump LG TEM_{00}, Stokes LG TEM_{02}, and anti-Stokes LG TEM_{02} mode combination.

Figures H.6a and b show the calculated values of the real and imaginary parts of V_{FWM}, respectively, as functions of pressure. As shown in Figure H.6a, the real part of V_{FWM} goes through zero at ~ 8.2 atm. This is the same pressure at which the real part of V_{FWM} for the second set of rectangular modes (Figure H.4) went through zero because both mode combinations have the same Gouy phase shift. The imaginary part is much smaller than the real part, as shown in Figure H.6b.

Figure H.6 was made using the same parameters as Figure H.1.

Allowable Mode Combinations

There appears to be a conflict between the allowable mode combinations in rectangular and cylindrical symmetry, since in rectangular symmetry, the allowed combinations are independent of the pump and in cylindrical, they depend on the pump. To reiterate the allowed combinations in each symmetry:

1. Rectangular symmetry: l_p and m_p arbitrary. If l_s is odd (even) then l_a must be odd (even). If m_s is odd (even) then m_a must be odd (even).

2. Cylindrical symmetry: l_p, l_s, and l_a arbitrary. m_p, m_s, and m_a must satisfy one of four equations.

$$2m_p = m_s + m_a \tag{H.60}$$

$$2m_p = m_s - m_a \tag{H.61}$$

$$2m_p = -m_s + m_a \tag{H.62}$$

$$m_s = m_a \tag{H.63}$$

These equations require m_s and m_a to either both be even or both be odd.

There are two possible ways to try and resolve this conflict. The first is by looking at the mode combinations, using elliptic symmetry to evolve the LG mode into its corresponding HG mode. The second is by writing the LG modes as sums of HG modes.

... and Elliptic Symmetry.

Elliptic symmetry can be used to investigate this dichotomy because, as seen in Appendix E, the rectangular and cylindrical modes are the elliptical modes with the ellipticity taken to zero and infinity, respectively. Table H.1 gives an elliptic Ince-Gaussian (IG) mode along with the corresponding rectangular, HG, and cylindrical,

LG, modes at either extreme. Interestingly, both the IG TEM^{e}_{22} and the IG TEM^{o}_{22}

IG	LG	HG		IG	LG	HG
TEM^{e}_{11}	TEM_{01}	TEM_{01}		TEM^{o}_{11}	TEM_{01}	TEM_{10}
TEM^{e}_{31}	TEM_{03}	TEM_{03}		TEM^{o}_{31}	TEM_{11}	TEM_{30}
TEM^{e}_{33}	TEM_{11}	TEM_{21}		TEM^{o}_{33}	TEM_{03}	TEM_{12}
TEM^{e}_{22}	TEM_{02}	TEM_{20}		TEM^{o}_{22}	TEM_{02}	TEM_{11}
TEM^{e}_{00}	TEM_{00}	TEM_{00}		TEM^{o}_{42}	TEM_{12}	TEM_{31}
TEM^{e}_{20}	TEM_{10}	TEM_{02}		TEM^{o}_{44}	TEM_{04}	TEM_{13}

Table H.1: IG modes and the corresponding HG and LG modes for either extreme of the ellipticity. The LG modes are the IG modes with ϵ=0 and the HG modes are IG modes with $\epsilon = \infty$. The superscripts, e and o, on the IG modes represent whether the IG mode is even or odd.

appear to evolve to the same LG mode but to different HG modes. The same appears to be true for IG TEM^{e}_{11} and IG TEM^{o}_{11}. Figure H.7 illustrates this effect by showing the intensity profiles of the various modes with red being the brightest and blue being the weakest. In Figure H.7a, the IG TEM^{e}_{22} is shown for $\varepsilon = 4$ on the left and $\varepsilon = 0$ on the right. Figure H.7b shows IG TEM^{o}_{22} for $\varepsilon = 4$ on the left and $\varepsilon = 0$ on the right. Figure H.7c is the LG TEM_{02} mode. As can be seen, IG TEM^{o}_{22} evolves into a mode that is characterized by four angular nulls but is rotated 45^o from the LG TEM_{02}. If the LG modes had been chosen to be proportional to $\sin[m\theta]$ instead of to $\cos[m\theta]$, the LG TEM_{02}would be rotated 45^o as well.

Using this Table H.1, the choice of allowed combinations made in the above two sections can be investigated. The first set of rectangular modes was pump, Stokes and anti-Stokes on HG TEM_{00} modes. As already shown, the circular symmetric modes with pump, Stokes, and anti-Stokes LG TEM_{00} yield the same value of V_{FWM}.

The second set of rectangular symmetric modes was pump HG TEM_{00}, Stokes HG TEM_{20} and anti-Stokes HG TEM_{20}. This mode combination corresponds to the following set of cylindrical modes: pump LG TEM_{00}, Stokes LG TEM_{02}, and anti-Stokes LG TEM_{02}, respectively, which is the second set of modes calculated in the

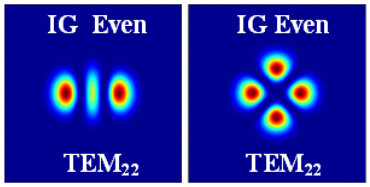

(a) Even IG mode.

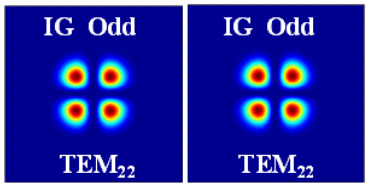

(b) Odd IG mode.

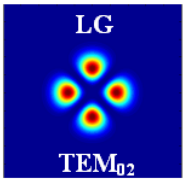

(c) LG mode.

Figure H.7: Intensity profiles for the IG $\mathrm{TEM}^{\mathrm{e}}_{22}$, IG $\mathrm{TEM}^{\mathrm{o}}_{22}$, and LG TEM_{02} modes with red being the most intense and blue being the least. The left IG mode is for $\epsilon = 4$ and the right is for $\epsilon = 0$.

cylindrically symmetric section. V_{FWM} calculated in the two cases is not the same. However, since the Ince polynomials are dependent on the ellipticity, the two values should represent the extremes of V_{FWM} calculated in elliptic symmetry.

Another possible combination is the circularly symmetric modes: pump LG TEM_{01}, Stokes LG TEM_{00}, and anti-Stokes LG TEM_{02}. The corresponding rectangular mode for the pump is either HG TEM_{01} or HG TEM_{10}. However, in rectangular symmetry, the pump mode does not matter. Therefore, it does not matter which pump mode is chosen. There is only one possibility for the Stokes mode. It is HG TEM_{00}. The anti-Stokes mode has two possibilities, HG TEM_{20} and HG TEM_{11}, because both the IG TEM^{e}_{22} and IG TEM^{o}_{22} evolve to an LG mode that should be labeled TEM_{02}, as shown in Figure H.7. The HG TEM_{20} would be an allowed mode, the second would not. However, it might not be a coincidence that the mode that works for the anti-Stokes is connected to the LG TEM_{02} mode through an even IG mode, since the connection for the Stokes modes is through an even IG mode.

This method of looking at the mode combinations helps, but does not resolve all the issues.

... and Sums of Modes

The LG modes can be written in terms of sums of the HG modes (and vice versa) [80]. The only HG modes that will contribute to a given LG mode are HG modes that have the same Gouy phase shift as the LG mode. For example, the LG TEM_{20} mode has a Gouy phase shift of 5, because, in cylindrical coordinates, the size of the Gouy phase shift is determined by $(2l + m + 1)$. The size of the Gouy phase shift in rectangular coordinates is determined by $(l + m + 1)$. Therefore, HG modes that might contribute to forming the LG TEM_{20} mode are any where $l + m = 4$.

LG	HG
TEM_{00}	TEM_{00}
TEM_{01}	TEM_{10}
TEM_{10}	$\frac{\sqrt{2}}{2}\mathrm{TEM}_{20} + \frac{\sqrt{2}}{2}\mathrm{TEM}_{02}$
TEM_{11}	$\frac{\sqrt{3}}{2}\mathrm{TEM}_{30} + \frac{1}{2}\mathrm{TEM}_{12}$
TEM_{20}	$\frac{\sqrt{6}}{4}(\mathrm{TEM}_{40} + \mathrm{TEM}_{04}) + \frac{1}{2}\mathrm{TEM}_{22}$
TEM_{02}	$\frac{\sqrt{2}}{2}\mathrm{TEM}_{20} - \frac{\sqrt{2}}{2}\mathrm{TEM}_{02}$
TEM_{12}	$\frac{\sqrt{2}}{2}\mathrm{TEM}_{40} - \frac{\sqrt{2}}{2}\mathrm{TEM}_{04}$
TEM_{21}	$\frac{1}{2}\mathrm{TEM}_{32} + \frac{\sqrt{2}}{4}\mathrm{TEM}_{14} + \frac{\sqrt{10}}{4}\mathrm{TEM}_{50}$

Table H.2: An LG mode and the sum of HG modes that is equivalent to that LG mode.

Table H.2 gives some LG modes and their corresponding expressions as sums of HG modes.

The set of modes in the last section that were still unresolved was pump LG TEM_{01}, Stokes LG TEM_{00}, and anti-Stokes LG TEM_{02}. From Table H.2, it can be seen that in the corresponding HG modes are pump HG TEM_{10}, Stokes HG TEM_{00} and anti-Stokes HG $\left(\frac{\sqrt{2}}{2}\mathrm{TEM}_{20} - \frac{\sqrt{2}}{2}\mathrm{TEM}_{02}\right)$. These are all allowable mode combinations.

Another possibility is pump LG TEM_{11}, Stokes LG TEM_{01}, and anti-Stokes LG TEM_{11}. The corresponding HG modes are pump HG $\left(\frac{\sqrt{3}}{2}\mathrm{TEM}_{30} + \frac{1}{2}\mathrm{TEM}_{12}\right)$, Stokes HG TEM_{01}, and anti-Stokes HG $\left(\frac{\sqrt{3}}{2}\mathrm{TEM}_{30} + \frac{1}{2}\mathrm{TEM}_{12}\right)$. This combination of HG modes, as written, is not allowed. However, if the LG modes had been written in terms of $\sin[m\theta]$ instead of $\cos[m\theta]$, then the LG TEM_{01} would be the HG TEM_{10} mode because the sine function goes through zero 90^o after the cosine. With this change, the mode combination is allowable in both symmetries.

Again, this method of looking at the allowable modes helps, but is not resolved. This issue is still under investigation.

APPENDIX I

MATLAB CODE

This appendix contains the *Matlab* code used to numerically integrate the CWRLE for Chapter 3. This code is limited to higher pressures (around 10 atm) because it does not contain the necessary modifications to the linewidth and gain for use at lower pressures. The main code is presented first. It is called "front_end". It calls several sub-routines for the calculation of the frequencies and overlap integrals.

At the time of writing this code, unnecessary care was given to making sure that the pump and Stokes frequencies were resonant with a given cavity length. The result of this is that the line-center pump frequency input into the main code has many decimal places in order to ensure that both it and the Stokes are resonant with the cavity length and the detuning of the Stokes frequency from gain line-center is zero. The pump frequency is then detuned from the line-center frequency, tuning the Stokes and anti-Stokes frequencies.

Main Code "front-end"

This section presents the main code, called "front_end", for the calculations in Chapter 3. Here is how the code works:

1. Set parameters specific to the mode combination and pressures that are being considered. These include the parameters Q, Q_a, and Q_b which will be used to determine the values of the overlap integrals. It is also includes setting the pressure, temperature, the pump frequency that will lead to the Stokes being on line-center (fp_lc), the pump transverse mode index (q_p), and the spatial mode indices for all three fields.

2. Set constants including the plane-wave gain coefficient, Raman linewidth (g_ab) the two-photon Rabi frequency, and population decay rate.

3. Define reflectivities, transmittivities, and absorptions at all three wavelengths.

4. Subroutine “frequency” is called. It calculates the specific values of the cavity length, Stokes frequency, anti-Stokes frequency, indices of refraction, etc.

5. Subroutines “vfwm”, “vps”, and “vpa” are called. They give the results of the overlap integrals, either analytic or calculated.

6. The specific result of $V_{ps\,o}$ (in the code it is called Vps00) is then entered because the value from subroutine “vps” may not be for the fundamental mode combination. As a reminder, $V_{ps\,o}$ is needed in the definition of the Raman gain.

7. The cavity loss and coupling coefficients are determined.

8. The line-center Raman gain is defined.

9. The line-center full steady-state solutions are calculated so that the line-center threshold can be determined.

10. The next step is to set the desired detuning. Plots of powers vs. detuning can be made by setting up a for-loop for the parameter v.

11. Steps 4 – 6 and 8 are repeated for the desired detuning.

12. The input pump power is set. Plots of power vs. input power can be made by setting up a for-loop for the parameter u.

13. A group of parameters is then combined into one array called “values” which will be passed to the subroutine containing the CWRLE.

14. The numerical integration routine is now called. It is possible to choose either method 1 or method 2 (as discussed in Chapter 3 on page 63). Comment or uncomment the desired section. It is also necessary to comment and uncomment

the desired method in the subroutine containing the CWRLE which is at the bottom of "front_end".

15. If plots vs. time are desired, uncomment the next section.

16. Following are some definitions if plots vs. detuning or input power are desired. The two steady-state solutions are next. If plots of any of these are desired, the plot calls need to be added to the code. This is the end of the main code.

17. Belows the main code is the subroutine that contains the CWRLE that are called during the numerical integration routines. At the beginning of the subroutine, the array of values is unfolded into its components. Then the CWRLE for method 1 are coded followed by the CWRLE for method 2.

Here is the main code:

```
function front_end
format long
global L wop wos woa dk x wo_sq zo values uo b Q Qa Qb
% % Set parameters
T = 293;
P = 10;
fp_lc = 563161.827754377*10^9;
qp = 286392;
mp = 0;
lp = 0;
ms = 0;
ls = 0;
```

```
ma = 0;

la = 0;

Q = 1;

Qa = 1;

Qb = 1;

% Define constants

uo = 4*pi*10^-7;

c = 3*10^8; % Speed of light in vacuum (m/s)

eo = 8.854*10^-12;

ago = 2.5*10^-11; % Plane-wave gain coefficient (m/W)

g_ab = 2*pi*250*10^6; % Linewidth (rad/s)

W_ab = 2*pi*1.5*10^5; % 2-photon Rabi frequency, approximate

G_ba = 2*pi*10^4; % Population decay rate (rad/s)

% Set cavity parameters – R = Reflectivity, T = Transmitivity,

% and A = Absorption

% Index 1 is for the front mirror. Index 2 is for the back mirror.

R1p = 0.9999;

R2p = R1p;

Ap = 50*10^-6;

T1p = 1 - R1p - Ap;

T2p = 1 - R2p - Ap;

R1s = 0.9998;

R2s = R1s;

As = 150*10^-6;

T1s = 1 - R1s - As;
```

```
T2s = 1 - R2s - As;

R1a = 0.999;

R2a = R1a;

Aa = 100*10^-6;

T1a = 1 - R1a - Aa;

T2a = 1 - R2a - Aa;

zo = 0.133; % Cavity Rayleigh Range (m)

b = 2*zo; % Confocal parameter

% Calculate the line-center values

y1 = frequency(mp,lp,ms,ls,ma,la,P,T,fp_lc,qp);

Lp = y1(1); % Wavelength (m)

Ls = y1(2);

La = y1(3);

% delta = y1(4)

wp = y1(5); % Frequency (rad/s)

ws = y1(6);

wa = y1(7);

np = y1(8);

ns = y1(9);

na = y1(10);

kp = 2*pi*np/Lp; % wavenumbers in medium

ks = 2*pi*ns/Ls;

ka = 2*pi*na/La;

sk = 2*kp + ks + ka;

dk = 2*kp - ks - ka;
```

```
% % Calculate the overlap integrals
% % First calculate Vfwm.
y2 = vfwm;
Vfwm = y2(1);
% % Next calculate Vps.
y3 = vps;
Vps = y3(1);
% % Next calculate Vpa.
y4 = vpa;
Vpa = y4(1);
% % Finally calculate Vp, Vs, and Va.
% % These are independent of the mode indices.
Vp = pi*(wopˆ2)*L/4;
Vs = pi*(wosˆ2)*L/4;
Va = pi*(woaˆ2)*L/4;
% % In general, Vps00 does not equal Vps_mn
% % Therefore, it is necessary to calculate Vps00 separately while not
% % necessary to calculate Vs_00.
Vps00 = pi*(wopˆ2)*(wosˆ2)*zo*atan(L/(2*zo))/(4*(wopˆ2 + wosˆ2));
% % Determine the cavity loss and coupling coefficients
g_cp = -c*log(sqrt(R1p*R2p))/(np*L); % Pump cavity loss
g_cs = -c*log(sqrt(R1s*R2s))/(ns*L); % Stokes cavity loss
g_ca = -c*log(sqrt(R1a*R2a))/(na*L); % Anti-Stokes cavity loss
g_inp = 2*c*sqrt(T1p)/(np*L); % Pump cavity coupling
% Set the line-center gain
```

```
d = 0; % line center detuning is zero
ag = ago*(g_abˆ2)/((dˆ2) + (g_abˆ2)*(1 + 4*(W_abˆ2)/(G_ba*g_ab)));
G_lc =0.25*ag*ns*np*(cˆ2)*eo*Vps00/Vs;

% Determine the line center threshold
x1p = wp*Vs*Vps*G_lc/(ws*Vp*Vps00);
x2p = wp*Vs*Vpa*G_lc/(ws*Vp*Vps00);
x3p = wp*Vs*Vfwm*G_lc/(ws*Vp*Vps);
x1s = G_lc*Vfwm/Vps00;
x2s = G_lc*Vps/Vps00;
x1a = wa*Vs*Vpa*G_lc/(ws*Va*Vps00);
x2a = wa*Vs*conj(Vfwm)*G_lc/(ws*Va*Vps00);
xp = 0; xs = -real(x1s);
xa = -real(x2a);
A = g_cs*real(x2a);
B = -g_cs*x1a - g_ca*x2s;
C = g_ca*real(x1s);
beta = (-B + sqrt((Bˆ2)-4*A*C))/(2*A);
kappa = sqrt(g_cs*beta/(2*(-real(x1s) + x2s*beta)));
Epth_lc = (g_cp/g_inp)*kappa;

% Determine pump frequency – this determines the detuning of the
% Stokes from gain line center
v = 26; %˜gain line center %
v = 19; %detuned by ˜248 MHz %
v = 13; %detuned by ˜447 MHz
fpo = fp_lc - 4*10ˆ9; % Initial pump frequency in Hz
```

```
fp = fpo + (v-1)*0.16*10^9;

% First calculate the wavelengths, cavity length, frequencies, indices
% of refraction, etc... for the 3 frequencies
y1 = frequency(mp,lp,ms,ls,ma,la,P,T,fp,qp);
Lp = y1(1); % Wavelength (m)
Ls = y1(2);
La = y1(3);
delta = y1(4);
d = y1(4)*2*pi; % Detuning of Stokes from line center
wp = y1(5); % Frequency (rad/s)
ws = y1(6);
wa = y1(7);
np = y1(8); % Indices of refraction
ns = y1(9);
na = y1(10);
wcp = y1(11); % Cavity resonance frequency
wcs = y1(12);
wca = y1(13);

kp = 2*pi*np/Lp; % wavenumbers in medium
ks = 2*pi*ns/Ls;
ka = 2*pi*na/La;
sk = 2*kp + ks + ka;
dk = 2*kp - ks - ka;

% % First calculate Vfwm.
y2 = vfwm;
```

```
Vfwm = y2(1);
% % Next calculate Vps.
y3 = vps;
Vps = y3(1);
% % Next calculate Vpa.
y4 = vpa;
Vpa = y4(1);
% % Finally calculate Vp, Vs, and Va.
% % These are independent of the mode indices.
Vp = pi*(wopˆ2)*L/4;
Vs = pi*(wosˆ2)*L/4;
Va = pi*(woaˆ2)*L/4;
% % In general, Vps00 does not equal Vps_mn
% % Therefore, it is necssary to calculate Vps00 seperately while not
% % necessary to calculate Vs_00.
Vps00 = pi*(wopˆ2)*(wosˆ2)*zo*atan(L/(2*zo))/(4*(wopˆ2 + wosˆ2));
% Define G – the Raman gain
ag = ago*(g_abˆ2)/((dˆ2) + (g_abˆ2)*(1 + 4*(W_abˆ2)/(G_ba*g_ab)));
G = 0.25*ag*ns*np*(cˆ2)*eo*Vps00/Vs;
u = 41;
Epin = sqrt(4)*Epth_lc;
values = [Lp,Ls,wp,ws,wa,g_cp,g_cs,g_ca,g_inp,...
G,Vpa,Vps,Vfwm,Vs,Va,Epin,d,g_ab,np,ns,na,wcp,wcs,wca,Vps00,Vp];
% Solve time dependent equations
tstart = 0;
```

```
tstop = 5*10^-3;

% Initial conditions and call numerical integration routine

% For integration by method 1

s0 = [10^-10,10^-10,0];

[t,s] = ode45(@g,[tstart tstop],s0);

pp = (abs(s(:,1).^2))*pi*b*T2p/(16*wp*uo);

ps = (abs(s(:,2).^2))*pi*b*T2s/(16*ws*uo);

pa = (abs(s(:,3).^2))*pi*b*T2a/(16*wa*uo);

phi_p = angle(s(:,1));

phi_s = angle(s(:,2));

phi_a = angle(s(:,3));

%%%%%%%%%%%%%%%%%%%%%%%%%%%%%%%%%%%%

% For integration by method 2

% s0 = [0,10^-10,10^-10,pi/4,pi/6,pi/7];

% [t,s] = ode45(@g,[tstart tstop],s0);

% pp = (abs(s(:,1).^2))*pi*b*T2p/(16*wp*uo);

% ps = (abs(s(:,2).^2))*pi*b*T2s/(16*ws*uo);

% pa = (abs(s(:,3).^2))*pi*b*T2a/(16*wa*uo);

% phi_p = s(:,4);

% phi_s = s(:,5);

% phi_a = s(:,6);

%%%%%%%%%%%%%%%%%%%%%%%%%%%%%%%%%%%%

t1 = t;

No = size(s);

N = No(1,1);
```

```
%% UNCOMMENT THIS SECTION FOR PLOTS VS. TIME
xmin = tstart;
xmax = tstop;
figure subplot(3,1,1)
plot(t1,pp, 'g')
ylabel('Pp')
xlim([xmin xmax])
subplot(3,1,2)
plot(t1,ps,'r')
ylabel('Ps')
xlim([xmin xmax])
subplot(3,1,3)
plot(t1,pa,'b')
ylabel('Pa')
xlabel('time')
xlim([xmin xmax])

figure
subplot(3,1,1)
plot(t1,phi_p)
ylabel('phip')
xlim([xmin xmax])
subplot(3,1,2)
plot(t1,phi_s)
ylabel('phis')
xlim([xmin xmax])
```

```
subplot(3,1,3)
plot(t1,phi_a)
ylabel('phia')
xlabel('time')
xlim([xmin xmax])

DPhi = (2*phi_p - phi_s - phi_a);
figure
plot(t1,DPhi)
xlabel('time')
ylabel('dphi')
xlim([xmin xmax])
%%%%%%%%%%%%%%%%%%%%%%%%%%%%%%%%%%%

% ppth = (Epth_lcˆ2)*pi*b/(4*wp*uo);
% ppin = (abs(Epin)ˆ2)*pi*b/(4*wp*uo);
% ppump = pp(N,1);
% pstokes = ps(N,1);
% pantistokes = pa(N,1);
% phip = phi_p(N,1);
% phis = phi_s(N,1);
% phia = phi_a(N,1);

%%UNCOMMENT THIS FOR PLOTS VS. INPUT PUMP POWER
% Ppin(u,1) = ppin;
% Pp(u,1) = ppump;
% Ps(u,1) = pstokes;
% Pa(u,1) = pantistokes;
```

```
% Pptrans = ppump;
% Ppa(u,1) = R1p*ppin + Pptrans -2*sqrt(R1p*ppin*Pptrans);
% Psa(u,1) = pstokes;
% Paa(u,1) = pantistokes;
% Ppb(u,1) = ppump;
% Pp_noncon(u,1) = (((g_inp/g_cp)*Epin)^2)*pi*b*T1p/(16*wp*uo);
\% Ps_con(u,1) = pstokes/ppin;
% Pa_con(u,1) = pantistokes/ppin;
% p_p(u,1) = phip;
% p_s(u,1) = phis;
% p_a(u,1) = phia;
% DPHI(u,1) = 2*phip - phis - phia;
%%%%%%%%%%%%%%%%%%%%%%%%%%%%%%%%%%%%
%%%%%% UNCOMMENT THIS FOR PLOTS VS. DETUNING
% Delta(v,1) = delta;
% Pp(v,1) = ppump;
% Ps(v,1) = pstokes;
% Pa(v,1) = pantistokes;
% Ps_con(v,1) = pstokes/ppin;
% Pa_con(v,1) = pantistokes/ppin;
% phip = phi_p(N,1);
% phis = phi_s(N,1);
% phia = phi_a(N,1);
% p_p(v,1) = phip;
% p_s(v,1) = phis;
```

```
% p_a(v,1) = phia;
% DPHI(v,1) = 2*phip - phis - phia;
%%%%%%%%%%%%%%%%%%%%%%%%%%%%%%%%%%%%
%% LINE-CENTER STEADY-STATE SOLUTIONS
%% FULL THEORY
% eta = wa*Vs*g_cs/(ws*Va*g_ca);
% beta = (-eta*Vpa - Vps)/(2*real(Vfwm))-...
% 0.5*sqrt(((-eta*Vpa - Vps)/(real(Vfwm)))^2-4*eta);
% Epss1 = sqrt(Vps00*g_cs/(2*G*(Vps+beta*real(Vfwm))));
% Esss1 = sqrt(ws*Vp*Vps00*g_cp*(g_inp*Epin/(g_cp*Epss1)-1)...
% /(wp*Vs*2*G*(Vps+Vpa*beta^2)));
% Eass1 = beta*Esss1;
% Eth1 = g_cp*Epss1/g_inp;
% ppth1 = (abs(Eth1)^2)*pi*b/(4*wp*uo);
% if Epin ¡ abs(Eth1); %
Pptrans = (((g_inp/g_cp)*Epin)^2)*pi*b*T1p/(16*wp*uo);
% Ppss1a(u,1) = R1p*ppin + Pptrans -2*sqrt(R1p*ppin*Pptrans);
% Psss1a(u,1) = 0;
% Pass1a(u,1) = 0;
% Ppss1b(u,1) = (((g_inp/g_cp)*Epin)^2)*pi*b*T2p/(16*wp*uo);
% Psss1b(u,1) = 0;
% Pass1b(u,1) = 0;
% else
% Pptrans = (abs(Epss1)^2)*pi*b*T1p/(16*wp*uo);
% Ppss1a(u,1) = R1p*ppin + Pptrans -2*sqrt(R1p*ppin*Pptrans);
```

```
% Psss1a(u,1) = (abs(Esss1)^2)*pi*b*T1s/(16*ws*uo);
% Pass1a(u,1) = (abs(Eass1)^2)*pi*b*T1a/(16*wa*uo);
% Ppss1b(u,1) = (abs(Epss1)^2)*pi*b*T2p/(16*wp*uo);
% Psss1b(u,1) = (abs(Esss1)^2)*pi*b*T2s/(16*ws*uo);
% Pass1b(u,1) = (abs(Eass1)^2)*pi*b*T2a/(16*wa*uo);
% end

%%%%%%%%%%%%%%%%%%%%%%%%%%%%%%%%%%%%%%%%%%%%
%%%%%UNDEPLETED PUMP APPROXIMATION
% Epss2 = sqrt(g_cs*Vps00/(2*G*Vps));
% Esss2 = sqrt(Vp*Vps00*ws*g_cp*(g_inp*Epin/(g_cp*Epss2)-1)...
% /(2*Vps*Vs*wp*G));
% Eass2 = -2*wa*G*(Epss2^2)*Esss2*Vs*real(Vfwm)/(g_ca*ws*Va*Vps00);
% Eth2 = g_cp*Epss2/g_inp;
% ppth2 = (Eth2^2)*pi*b/(4*wp*uo);
% if Epin ¡ Eth2; % Ppss2(u,1) = (((g_inp/g_cp)*Epin)^2)*pi*b*T2p/(16*wp*uo);
% Psss2(u,1) = 0;
% Pass2(u,1) = 0;
% else
% Ppss2(u,1) = (abs(Epss2)^2)*pi*b*T2p/(16*wp*uo);
% Psss2(u,1) = (abs(Esss2)^2)*pi*b*T2s/(16*ws*uo);
% Pass2(u,1) = (abs(Eass2)^2)*pi*b*T2a/(16*wa*uo);
% end

%%%%%%%%%%%%%%%%%%%%%%%%%%%%%%%%%%%%%%%%%%%%

%%%%%%%%%%%%%%%%%%%%%%%%%%%%%%%%%%%%%%%%%%%%
function dsdt = g(t,s)
```

```
global L wop wos woa dk x wo_sq zo values uo b Q Qa Qb
% Parameters needed for solving
Lp = values(1);
Ls = values(2);
wp = values(3);
ws = values(4);
wa = values(5);
g_cp = values(6);
g_cs = values(7);
g_ca = values(8);
g_inp = values(9);
G = values(10);
Vpa = values(11);
Vps = values(12);
Vfwm = values(13);
Vs = values(14);
Va = values(15);
Epin = values(16);
d = values(17);
g_ab = values(18);
np = values(19);
ns = values(20);
na = values(21);
wcp = values(22);
wcs = values(23);
wca = values(24);
```

```
Vps00 = values(25);
Vp = values(26);

% for method 1 – uncomment the function dsdt below
% pump, stokes, and anti-stokes – complex
% s(1) = pump
% s(2) = stokes
% s(3) = anti-stokes
dsdt = [(-(g_cp/2)*s(1) + (g_inp/2)*Epin*s(1)/abs(s(1))...
- wp*G*Vps*Vs*(1+i*d/g_ab)*s(1)*(abs(s(2))^2)/(Vp*ws*Vps00)...
+ Vs*wp*G*(1-i*d/g_ab)*s(1)*(abs(s(3))^2)*Vpa/(Vp*ws*Vps00)...
- 2*i*Vs*wp*G*d*conj(s(1))*s(2)*s(3)*Vfwm/(Vp*ws*Vps00*g_ab));
(-(g_cs/2)*s(2) + G*(1-i*d/g_ab)*Vps*s(2)*(abs(s(1))^2)/(Vps00)...
+ G*(1-i*d/g_ab)*s(1)*s(1)*conj(s(3))*Vfwm/(Vps00));
(-(g_ca/2)*s(3) ...
-wa*Vs*(1+i*d/g_ab)*G*(abs(s(1))^2)*s(3)*Vpa/(ws*Va*Vps00)...
-wa*Vs*(1+i*d/g_ab)*G*s(1)*s(1)*conj(s(2))*conj(Vfwm)/(ws*Va*Vps00));];
%%%%%%%%%%%%%%%%%%%%%%%%%%%%%%%%%%%%

% for method 2 – uncomment everything below the definition of dphi
% pump, Stokes, and anti-Stokes only, phase separate
% s(1) = pump
% s(2) = stokes
% s(3) = anti-stokes
% s(4) = pump phase
% s(5) = stokes phase
% s(6) = anti-stokes phase
```

```
% d_phi = 2*s(4)-s(5)-s(6);

% x1p = wp*Vs*Vps*G/(ws*Vp*Vps00);

% x2p = wp*Vs*Vpa*G/(ws*Vp*Vps00);

% x3p = wp*Vs*Vfwm*G/(ws*Vp*Vps);

% x1s = G*Vfwm/Vps00;

% x2s = G*Vps/Vps00;

% x1a = wa*Vs*Vpa*G/(ws*Va*Vps00);

% x2a = wa*Vs*conj(Vfwm)*G/(ws*Va*Vps00);

% xp = d*(real(x3p)*sin(d_phi) - imag(x3p)*cos(d_phi))/g_ab;

% xs = real(x1s)*cos(d_phi) + real(x1s)*d*sin(d_phi)/g_ab ...

% -imag(x1s)*sin(d_phi) + imag(x1s)*d*cos(d_phi)/g_ab;

% xa = real(x2a)*cos(d_phi) - real(x2a)*d*sin(d_phi)/g_ab ...

% -imag(x2a)*sin(d_phi) - imag(x2a)*d*cos(d_phi)/g_ab;

% yp = d*(real(x3p)*cos(d_phi) + imag(x3p)*sin(d_phi))/g_ab;

% ys = real(x1s)*sin(d_phi) - real(x1s)*d*cos(d_phi)/g_ab ...

% +imag(x1s)*cos(d_phi) + imag(x1s)*d*sin(d_phi)/g_ab;

% ya = real(x2a)*sin(d_phi) + real(x2a)*d*cos(d_phi)/g_ab ...

% +imag(x2a)*cos(d_phi) - imag(x2a)*d*sin(d_phi)/g_ab;

% dsdt = [(-(g_cp/2)*s(1) + (g_inp/2)*Epin -x1p*s(1)*s(2)*s(2)...

% + x2p*s(1)*s(3)*s(3) - 2*xp*s(1)*s(2)*s(3));

% (-(g_cs/2)*s(2) + xs*s(1)*s(1)*s(3) + x2s*s(1)*s(1)*s(2));

% (-(g_ca/2)*s(3) - x1a*s(1)*s(1)*s(3) - xa*s(1)*s(1)*s(2));

% (-x1p*d*s(2)*s(2)/g_ab - x2p*d*s(3)*s(3)/g_ab - 2*yp*s(2)*s(3));

% (ys*s(1)*s(1)*s(3)/s(2) - x2s*d*s(1)*s(1)/g_ab);

% (0 - x1a*d*s(1)*s(1)/g_ab - ya*s(1)*s(1)*s(2)/s(3));];
```

Subroutine “frequency”

The first subroutine called in the main code is called “frequency”. Passed into this program from the main program are the pump frequency, pump transverse mode index, spatial mode indices for all three fields, pressure, and temperature. It returns the wavelengths, angular frequencies, indices of refraction, detuning, and the cavity resonance frequencies. This program assumes modes with rectangular symmetry. Therefore, if modes with symmetry other than rectangular are used, substitute mode indices that give the correct Gouy phase shift need to be used.

Here is how this code works:

1. The first step is to calculate parameters related to the pump frequency. These include the index of refraction and wavelength.

2. The cavity length is then calculated using the pump frequency and pump transverse mode index. This formula is an approximation to equation on page 105, in order to allow that equation to be solved for the cavity length.

3. The line-center Stokes frequency is then calculated, followed by the index of refraction at the line-center Stokes frequency. It is assumed that the index of refraction at the Stokes frequency equals the line-center index, i.e. the index of refraction is constant near the Stokes frequency.

4. The transverse cavity mode index closest to the line-center Stokes frequency is then calculated. This in turn is used to calculate the Stokes frequency, wavelength, etc...

5. The anti-Stokes frequency is then calculated based on the pump and Stokes frequencies, followed by anti-Stokes index of refraction, wavelength, etc...

6. A couple of additional parameters are calculated, and then the wavelengths, angular frequencies, indices of refraction, detuning and cavity resonant frequencies are passed back to the main program.

Here is the code:

```
function result = frequency(mp,lp,ms,ls,ma,la,P,T,fp,qp)
format long
global L wop wos woa dk x wo_sq zo values uo b Q Qa Qb sk

% Set constants
% Constants associated with the index of refraction
% This method of calculating the index was developed by Pete Roos.
no = 0.000136075; % Index at zero frequency, 1 atm, and 273 K
bo = 2.69852 * 10^-22; % Linear correction coefficient
co = 1.16021 * 10^-35; % Quadratic correction coefficient
% The index of refraction takes on the following form:
% n = A + B*f + % C*f^2 where A, B, and C are definded by:
an = 1 + no*P*273/T;
bn = bo*P*273/T;
cn = co*P*273/T;

% Determine pump wavelength
c = 3*10^8; % Speed of light in vacuum (m/s)
Lp = c/fp; % Pump wavelength (m)
np = an + bn*fp + cn*fp^2; % Pump index of refraction
Lpm = Lp/np; % Pump wavelength in medium (m)
kpm = 2*pi/Lpm; % Pump wavenumber in medium (1/m)
```

```
kp = 2*pi/Lp; % Pump wavenumber in vacuum (1/m)

% Determine physical cavity length (m)
L = c*qp/(2*np*(fp - (lp + mp + 1)*c/(2*pi*zo)));

% Set Raman shift – for vibrational shift in H2, this is 4155 1/cm
kR = 4.155 * 10^5; % Raman shift (1/m)
fR = c*kR; % Raman shfit (Hz)

% Determine Stokes wavelength
fslc = fp - fR; % Line center stokes frequency (Hz)
% Assumption – the index of refraction at the line center is the same
% as the index of refraction at the actual Stokes frequency
ns = an + bn*fslc + cn*fslc^2; % Stokes index of refraction
% Stokes mode index
qs = round((2*ns*L/c)*(fslc - (ls + ms + 1)*c/(2*pi*zo)));
% Stokes frequency
fs = (qs*c/(2*ns*L)) + (ls + ms + 1)*(c/(2*pi*zo));
Ls = c/fs; % Stokes wavelength in vacuum
Lsm = Ls/ns; % Stokes wavelength in medium
ksm = 2*pi/Lsm; % Stokes wavenumber in medium (1/m)
ks = 2*pi/Ls; % Stokes waveneumber in vacuum (1/m)
delta = fs - fslc; % Stokes detuning from gain line center

% Determine anti-Stokes wavelength
fa = 2*fp - fs; % Anti-Stokes frequency (Hz)
na = an + bn*fa + cn*fa^2;
% Anti-Stokes index La = c/fa;
% Anti-Stokes vacuum wavelength (m)
```

```
Lam = La/na; % Anti-Stokes wavelength in medium (m)
ka = 2*pi/La; % Anti-Stokes wavenumber in vacuum (1/m)
kam = 2*pi/Lam; % Anti-Stokes wavenumber in medium (1/m)

% % % And a couple more parameters...
wop = sqrt(b/kpm); % Pump beam min. waist (m)
wos = sqrt(b/ksm); % Stokes beam min. waist (m)
woa = sqrt(b/kam); % Anti-Stokes beam min. waist (m)
dk = 2*kpm-ksm-kam;
sk = 2*kpm+ksm+kam;
wo_sq = b/sk;
x = dk*wo_sq;
ws = 2*pi*fs;
wp = 2*pi*fp;
wa = 2*pi*fa;

% These are the cold cavity resonant frequencies (medium ignored)
% as defined in Saleh and Teich pg 336
wcp = 2*pi*(qp*c/(2*L) + (lp + mp + 1)*2*atan(L/zo)*c/(2*pi*L));
wcs = 2*pi*(qs*c/(2*L) + (ls + ms + 1)*2*atan(L/zo)*c/(2*pi*L));
wca = 2*pi*(qa*c/(2*L) + (la + ma + 1)*2*atan(L/zo)*c/(2*pi*L));

% Beta is the anti-Stokes cone angle -
w1 = 2*pi*fs; w2 = 2*pi*fp; w3 = 2*pi*fa;
beta = acos(((w1*ns)^2 - 4*(w2*np)^2 - (w3*na)^2)/(-4*w3*w2*na*np));

result = [Lp, Ls, La, delta, wp, ws, wa, np, ns, na, wcp, wcs, wca];
```

Sub-routine "vfwm"

This subroutine numerically calculates the z-integral of the V_{FWM} overlap integral starting with the analytic results of the x- and y-integrals. At the top of the code is a list that matches the values of Q to different possible mode combinations. The program numerically integrates the code twice, using two different *Matlab* integration routines and then takes the average. The rest of this code is a list of the analytically calculated results of the x- and y-integrals.

Here is the code:

```
function result = vfwm(Q,L,wop,wos,woa,dk,x,wo_sq,zo)
% % This program numerically evaluates the z-dependent integral that
% % results from the overlap of the pump, Stokes, and anti-Stokes
% % modes
% % Vfwm = Integral over the cavity (up*^2 us uas)
% % The x and y integrals are done analytically. This leaves
% % only the z-integral still to be evaluated.
% % Determine which set of modes is being evaluated
% % Unless otherwised noted by an LG for Laguerre-Gaussian, all
% % modes indexes are assumed to indicate rectangular symmetry
% % Q = 1 P = 00 S = 00 A = 00
% % Q = 2 P = 00 S = 00 A = 00 (collimated beam approximation)
% % Q = 3 P = 00 S = 10 A = 10
% % Q = 4 P = 11 S = 11 A = 11
% % Q = 5 P = 11 S = 10 A = 10
% % Q = 6 P = 10 S = 10 A = 10
```

% % Q = 7 P = 20 S = 10 A = 10

% % Q = 8 P = 20 S = 20 A = 40

% % Q = 9 P = 00 S = 20 A = 40

% % Q = 10 P = 00 S = 30 A = 30

% % Q = 11 P = 00 S = 20 A = 04

% % Q = 12 P = 00 S = 11 (LG) A = 11 (LG)

% % Q = 13 P = 00 S = 10 (LG) A = 20 (LG)

% % Q = 14 P = 01 S = 00 A = 00

% % Q = 15 P = 00 S = 20 A = 20

% % Q = 16 P = 00 S = 00 A = 20

% % Q = 17 P = 00 S = 00 A = 40

% % Q = 18 P = 00 S = 40 A = 00

% % Q = 19 P = 00 S = 40 A = 20

% % Q = 20 P = 00 S = 40 A = 40

% % Q = 21 P = 00 S = 00 A = 22

% % Q = 22 P = 00 S = 00 A = 10 (LG)

% % Q = 23 P = 00 S = 00 A = 20 (LG)

% % Q = 24 P = 00 S = 02 (LG) A = 02 (LG)

format long

global L wop wos woa dk x wo_sq zo values uo b Q Qa Qb sk

Lc = L;

% % Integrate

Vfwma = quadl(@fun,-Lc/2,Lc/2);

Vfwmb = quad(@fun,-Lc/2,Lc/2);

result = (Vfwma + Vfwmb)/2;

```
%%%%%%%%%%%%%%%%%%%%%%%%%%%%%%%%%

function y = fun(z)
global L wop wos woa dk x wo_sq zo values uo b Q Qa Qb sk

if Q == 1
% % For pump, Stokes, and anti-Stokes on TEM00
a1 = (2*pi*zo^4)./(zo^2 + z.^2);
b1 = cos(dk*z)/8;
c1 = i*wo_sq*(-x.*z - i*2*zo^2)./(x^2*z.^2 + 4*zo^4);
y = a1.*b1.*c1;

elseif Q == 2
% % collimated beam approximation results
d = wo_sq/2;
e = cos(dk*z)/8;
y = 2*pi*d.*e;

elseif Q == 3
% % For pump on TEM00, and Stokes and anti-Stokes on TEM10
phi = 2*atan(z./zo);
A = x*z;
B = 2*zo^2;
a1 = (8*pi*(wo_sq^2)*zo^6)./(woa*wos*(zo^2 + z.^2));
b1 = (cos(phi)+i*sin(phi));
c1 = cos(dk*z)/8;
d1 = -A.^2 + B^2 + 2*i.*A*B;
e1 = (-A.^2 + B^2).^2 + (2.*A*B).^2;
y = a1.*b1.*c1.*d1./e1;
```

```
elseif Q == 4
% % For the pump, Stokes, and anti-Stokes on TEM11;
A = x*z;
B = 2*zoˆ2;
a1 = 4608*pi*(wo_sqˆ5)*(zoˆ12)./((woaˆ2)*(wopˆ4)*(wosˆ2)*...
(zoˆ2 + z.ˆ2));
b1 = cos(dk*z)/8;
c1 = (5*(A.ˆ4)*B - 10*(A.ˆ2)*(Bˆ3) + Bˆ5 - i*(A.ˆ5 -10*(A.ˆ3)*...
(Bˆ2) + 5*A.*Bˆ4)) ;
d1 = (5*(A.ˆ4)*B - 10*(A.ˆ2)*(Bˆ3) + Bˆ5).ˆ2 + (A.ˆ5 -10*(A.ˆ3)...
*(Bˆ2) + 5*A.*Bˆ4).ˆ2;
y = a1.*b1.*c1./d1;

elseif Q == 5
% % For pump on TEM11, and Stokes and anti-Stokes on TEM10
phi = 2*atan(z./zo);
A = x*z;
B = 2*zoˆ2;
A1 = (384*pi*(wo_sqˆ4)*(zoˆ10))./(woa*wos*(wopˆ4)*(zoˆ2 + z.ˆ2));
B1 = (cos(phi)-i*sin(phi));
C1 = cos(dk*z)/8;
D1 = (A.ˆ4) - 6*(A.*B).ˆ2 + (B.ˆ4) - 4*i*(-A.*(B.ˆ3) + 4*(A.ˆ3).*B);
E1 = ((A.ˆ4) - 6*(A.*B).ˆ2 + (B.ˆ4)).ˆ2 + (-4*(A.*(B.ˆ3) + 4*(A.ˆ3).*B)).ˆ2;
y = A1.*B1.*C1.*D1./E1;

elseif Q == 6
% % For pump, Stokes and anti-Stokes on TEM10
```

```
A1 = 96*pi*(wo_sq^3)*(zo^8);
B1 = cos(dk*z)/8;
C1 = woa*(wop^2)*wos*((z.^2) + (zo)^2);
D1 = (i*x*z + 2*zo^2).^3;
y = (A1.*B1)./(C1.*D1);

elseif Q == 7
% % For pump on TEM20 and Stokes and anti-Stokes on TEM10
% % Ra is 1/R where R is the beam's radius of curvature.
% % By using this, a 1/0 error is avoided.
Ra = z./(zo^2 + z.^2);
wa = woa*((zo^2 + z.^2)/zo^2).^0.5;
wp = wop*((zo^2 + z.^2)/zo^2).^0.5;
ws = wos*((zo^2 + z.^2)/zo^2).^0.5;
A = x*z;
B = 2*zo^2;
phi = 2*atan(z./zo);
A1 = 4*pi*(wo_sq^4)*(zo^18)./((woa^5)*(wop^4)*(wos^5)...
*((zo^2 + z.^2).^5).*(-i*A + B).^4);
B1 = (cos(phi)-i*sin(phi));
C1 = cos(dk*z)/8;
D1 = ((dk*(wa.*wp.*ws).^4).*(Ra.^2)) + ...
(4*i*dk*((wa.*wp.*ws).^2).*((wp.*ws).^2 + (wp.*wa).^2 -4*(wa.*ws).^2).*Ra)...
+ 4*((wp.*ws).^4 + 2*((wa.*wp.*ws).^2).*(wp.^2 - 4*ws.^2) + ...
(wa.^4).*(wp.^4 - 8*(wp.*ws).^2 + 40*ws.^4));
y = A1.*B1.*C1.*D1;
```

```
elseif Q == 8
% % For pump and Stokes on TEM20 and anti-Stokes on TEM40
% % Ra is 1/R where R is the beam's radius of curvature.
% % By using this, a 1/0 error is avoided.
Ra = z./(zo^2 + z.^2);
wa = woa*((zo^2 + z.^2)/zo^2).^0.5;
wp = wop*((zo^2 + z.^2)/zo^2).^0.5;
ws = wos*((zo^2 + z.^2)/zo^2).^0.5;
phi = 2*atan(z/zo);
ca = (wp.^2).*(ws.^2) + (wa.^2).*((wp.^2) + 2*(ws.^2));
cb = (ws.^2).*(wp.^2).*(wa.^2);
a1 = -4*sqrt(12)*pi*(wo_sq^6)*(zo^14);
b1 = cos(phi) + i*sin(phi);
c1 = cos(dk*z)/8;
d1 = (woa^4)*(wop^4)*(wos^2)*((z.^2) + (zo^2)).*(i*x*z + 2*zo^2).^6;
e1 = -10080;
f1 = 10*((3*(wa.^4) + (wp.^4) + 2*(wp.^2).*(ws.^2) + ...
6*(wa.^2).*(2*(wp.^2) + (ws.^2))).*(-dk*cb.*Ra + 2*i*ca).^2)./(cb.^2);
g1 = -((2*(wp.^2).*(ws.^2) + (wa.^2).*((wp.^2) + ...
2*(ws.^2))).*(-dk*cb.*Ra + 2*i*ca).^4)./(8*(cb.^3).*(ws.^2));
h1 = 280*((6*(wa.^2) + 2*(wp.^2) + (ws.^2)).*(i*dk*cb.*Ra + 2*ca))./cb;
i1 = (((wp.^4).*(ws.^2) + 3*(wa.^4).*(2*(wp.^2) + ...
(ws.^2)) + 6*(wa.^2).*((wp.^4) + 2*(wp.^2).*(ws.^2))).*...
(i*dk*cb.*Ra + 2*ca).^3)./(2*cb.^3);
j1 = ((i*dk*cb.*Ra + 2*ca).^5)./(32*(cb.^3).*(ws.^2));
```

```
k1 = e1 + f1 + g1 + h1 + i1 + j1;
y = (a1.*b1.*c1./d1).*k1;

elseif Q == 9
% For pump on TEM00, Stokes on TEM20 and anti-Stokes on TEM40
% % Ra is 1/R where R is the beam's radius of curvature.
% %By using this, a 1/0 error is avoided.
Ra = z./(zo^2 + z.^2);
wa = woa*((zo^2 + z.^2)/zo^2).^0.5;
wp = wop*((zo^2 + z.^2)/zo^2).^0.5;
ws = wos*((zo^2 + z.^2)/zo^2).^0.5;
phi = 6*atan(z./zo);
A = dk*Ra/2;
B = (2./(wp.^2) + 1./(ws.^2) + 1./(wa.^2));
C = (i*A + B);
x0 = 192./(wa.^2) + 96./(ws.^2);
x1 = -128./(wa.^4) - 768./((ws.^2).*(wa.^2));
x2 = 512./((ws.^2).*(wa.^4));
a1 = pi*(wop^2)*wos*woa./(32*sqrt(3)*(wp.^2).*ws.*wa);
b1 = cos(phi) + i*sin(phi);
c1 = 24./C + x0./(2*C.^2) + 3*x1./(4*C.^3) + 15*x2./(8*C.^4);
d1 = (cos(dk*z)/8);
y = a1.*b1.*c1.*d1;

elseif Q == 10
% For pump on TEM00 and Stokes and anti-Stokes on TEM30
% % Ra is 1/R where R is the beam's radius of curvature.
```

```
% % By using this, a 1/0 error is avoided.
Ra = z./(zo^2 + z.^2);
wa = woa*((zo^2 + z.^2)/zo^2).^0.5;
wp = wop*((zo^2 + z.^2)/zo^2).^0.5;
ws = wos*((zo^2 + z.^2)/zo^2).^0.5;
phi = 6*atan(z./zo);
a1 = -4*pi*((wa.*wp.*ws).^2).*(woa*wos)*(wop^2);
b1 = -24*i*dk*Ra.*((wa.*ws).^4).*wp.^2 ...
- 3*(dk^2)*(Ra.^2).*(wa.*wp.*ws).^4 + 4*(-14*(wp.^4).*...
(ws.*wa).^2 + 3*(wp.*ws).^4 + 3*(wa.*wp).^4 - 12*(wa.*ws).^4);
c1 = cos(phi) + i*sin(phi);
d1 = cos(dk*z)/8;
e1 = (-i*dk*Ra.*(wa.*ws.*wp).^2 - 2*((wp.*ws).^2 + (wp.*wa).^2 ...
+ 2*(wa.*ws).^2)).^4;
y = a1.*b1.*c1.*d1./e1;

elseif Q == 11
% For pump on TEM00, Stokes on TEM20 and anti-Stokes on TEM04
% which is only slightly different from Q = 9.
% % Ra is 1/R where R is the beam's radius of curvature.
% % By using this, a 1/0 error is avoided.
Ra = z./(zo^2 + z.^2);
wa = woa*((zo^2 + z.^2)/zo^2).^0.5;
wp = wop*((zo^2 + z.^2)/zo^2).^0.5;
ws = wos*((zo^2 + z.^2)/zo^2).^0.5;
phi = 6*atan(z./zo);
```

```
A1 = -sqrt(3)*pi*wa*woa.*(wop^2)*wos.*ws;
B1 = cos(phi)+ i*sin(phi);
C1 = i*dk*Ra.*(wa.^2).*(ws.^2).*(wp.^2) ...
+ 2*(wp.*ws).^2 - 2*(wa.^2).*((wp.^2) - 2*(ws.^2));
D1 = (-i*dk*Ra.*(wa.^2).*(ws.^2).*(wp.^2) ...
- 2*(-(wp.*ws).^2 + (wa.^2).*((wp.^2)+2*(ws.^2)))).^2;
E1 = (cos(dk*z)/8);
F1 = 2*(-i*dk*Ra.*(wa.^2).*(ws.^2).*(wp.^2) ...
- 2*((wp.*ws).^2 + (wa.^2).*((wp.^2)+2*(ws.^2)))).^4;
y = A1.*B1.*C1.*D1.*E1./F1;

elseif Q == 12
% For pump on TEM00, and Stokes and anti-Stokes on Laguerre-
% Gaussian TEM11 which is only slightly different from Q = 10.
% Ra is 1/R where R is the beam's radius of curvature.
% By using this, a 1/0 error is avoided.
Ra = z./(zo^2 + z.^2);
wa = woa*((zo^2 + z.^2)/zo^2).^0.5;
wp = wop*((zo^2 + z.^2)/zo^2).^0.5;
ws = wos*((zo^2 + z.^2)/zo^2).^0.5;
phi = 6*atan(z./zo);
Aa = (dk*Ra/2);
Bb = (2./wp.^2) + (1./ws.^2)+(1./wa.^2);
a1 = 8*pi*(wop^2)*wos*woa;
b1 = 1./(2*(i*Aa+Bb).^2)-(((wa.^2)+(ws.^2))./(((i*Aa+Bb).^3).*(wa.*ws).^2))...
+3./(((wa.*ws).^2).*(i*Aa+Bb).^4);
```

```
c1 = cos(phi) - i*sin(phi);
d1 = cos(dk*z)/8;
e1 = (wp.*ws.*wa).^2;
y = a1.*b1.*c1.*d1./e1;

elseif Q == 13
% For pump on TEM00, and Stokes on Laguerre-Gaussian (LG) TEM20
% and anti-Stokes on LG TEM40, which is only slightly different from
% Q = 9 and 11.
% Ra is 1/R where R is the beam's radius of curvature.
% By using this, a 1/0 error is avoided.
Ra = z./(zo^2 + z.^2);
wa = woa*((zo^2 + z.^2)/zo^2).^0.5;
wp = wop*((zo^2 + z.^2)/zo^2).^0.5;
ws = wos*((zo^2 + z.^2)/zo^2).^0.5;
phi = -6*atan(z./zo);
Aa = (dk*Ra/2);
Bb = (2./wp.^2) + (1./ws.^2) + (1./wa.^2);
a1 = 2*pi*(wop^2)*wos*woa;
b1 = 1./(2*(i*Aa+Bb))...
-((wa.^2)+(2*ws.^2))./(((i*Aa+Bb).^2).*(wa.*ws).^2)...
+ ((8*wa.^4)+(2*(wa.*ws).^2))./((wa.^6).*(ws.^2).*(i*Aa+Bb).^3)...
-12./(((wa.^4).*(ws.^2)).*(i*Aa+Bb).^4);
c1 = cos(phi) + i*sin(phi);
d1 = cos(dk*z)/8; e1 = (wp.^2).*ws.*wa;
```

```
y = a1.*b1.*c1.*d1./e1;

elseif Q == 14
% % For pump on TEM01 and Stokes and anti-Stokes on TEM00
% % Ra is 1/R where R is the beam's radius of curvature
% % By using this, a 1/0 error is avoided.
Ra = z./(zo^2 + z.^2);
wa = woa*((zo^2 + z.^2)/zo^2).^0.5;
wp = wop*((zo^2 + z.^2)/zo^2).^0.5;
ws = wos*((zo^2 + z.^2)/zo^2).^0.5;
phi = -2*atan(z./zo);
Aa = (dk*Ra/2);
Bb = (2./wp.^2) + (1./ws.^2) + (1./wa.^2);
a1 = 2*pi*woa*(wop^2)*wos./(wa.*ws.*(wp.^4));
b1 = cos(phi) + i*sin(phi);
c1 = cos(dk*z)/8;
d1 = (i*Aa - Bb).^2;
y = a1.*b1.*c1./d1;

elseif Q == 15
% % For pump on TEM00 and Stokes and anti-Stokes on TEM20
% % Ra is 1/R where R is the beam's radius of curvature.
% % By using this, a 1/0 error is avoided.
Ra = z./(zo^2 + z.^2);
wa = woa*((zo^2 + z.^2)/zo^2).^0.5;
wp = wop*((zo^2 + z.^2)/zo^2).^0.5;
ws = wos*((zo^2 + z.^2)/zo^2).^0.5;
```

```
phi = 4*atan(z./zo);
Aa = (dk*Ra/2);
Bb = (2./wp.^2) + (1./ws.^2) + (1./wa.^2);
a1 = i*pi*wop^2*wos*woa./(8*(wa.^5).*(wp.^6).*(ws.^5));
b1 = -8*i*dk*Ra.*((wa.*ws).^4).*(wp.^2) - ...
(dk^2)*(Ra.^2).*((wa.*ws.*wp).^4) + ...
4*(-10*((wa.*ws).^2).*(wp.^4) + (wp.*ws).^4 + (wa.*wp).^4 - 4*(wa.*ws).^4);
c1 = cos(phi) + i*sin(phi); d1 = cos(dk*z)/8; e1 = (-Aa + i*Bb).^3;
y = a1.*b1.*c1.*d1./e1;

elseif Q == 16
% % For pump and Stokes on TEM00 and anti-Stokes on TEM20
% % Ra is 1/R where R is the beam's radius of curvature.
% % By using this, a 1/0 error is avoided.
Ra = z./(zo^2 + z.^2);
wa = woa*((zo^2 + z.^2)/zo^2).^0.5;
wp = wop*((zo^2 + z.^2)/zo^2).^0.5;
ws = wos*((zo^2 + z.^2)/zo^2).^0.5;
phi = 2*atan(z./zo);
Aa = (dk*Ra);
Bb = (wa.*wp.*ws).^2;
Cc = -(wp.*ws).^2 + (wa.*wp).^2 + 2*(wa.*ws).^2;
Dd = (wp.*ws).^2 + (wa.*wp).^2 + 2*(wa.*ws).^2;
a1 = -sqrt(2)*pi*wa*woa*(wop^2)*wos.*ws;
b1 = i*Aa.*Bb + 2*Cc;
c1 = cos(phi) + i*sin(phi);
```

```
d1 = cos(dk*z)/8;
e1 = (-i*Aa.*Bb - 2*Dd).^2;
y = a1.*b1.*c1.*d1./e1;

elseif Q == 17
% % For pump and Stokes on TEM00 and anti-Stokes on TEM40
% % Ra is 1/R where R is the beam's radius of curvature.
% % By using this, a 1/0 error is avoided.
Ra = z./(zo^2 + z.^2);
wa = woa*((zo^2 + z.^2)/zo^2).^0.5;
wp = wop*((zo^2 + z.^2)/zo^2).^0.5;
ws = wos*((zo^2 + z.^2)/zo^2).^0.5;
phi = 4*atan(z./zo);
Aa = (dk*Ra);
Bb = (wa.*wp.*ws).^2;
Cc = -(wp.*ws).^2 + (wa.*wp).^2 + 2*(wa.*ws).^2;
Dd = (wp.*ws).^2 + (wa.*wp).^2 + 2*(wa.*ws).^2;
a1 = sqrt(3/2)*pi*wa*woa*(wop^2)*wos.*ws;
b1 = (-i*Aa.*Bb - 2*Cc).^2;
c1 = cos(phi) + i*sin(phi);
d1 = cos(dk*z)/8;
e1 = (i*Aa.*Bb + 2*Dd).^3;
y = a1.*b1.*c1.*d1./e1;

elseif Q == 18
% % For pump on TEM00, Stokes on TEM40 and anti-Stokes
% % on TEM00
```

```
% % Ra is 1/R where R is the beam's radius of curvature.
% % By using this, a 1/0 error is avoided.
Ra = z./(zo^2 + z.^2);
wa = woa*((zo^2 + z.^2)/zo^2).^0.5;
wp = wop*((zo^2 + z.^2)/zo^2).^0.5;
ws = wos*((zo^2 + z.^2)/zo^2).^0.5;
phi = 4*atan(z./zo);
Aa = (dk*Ra);
Bb = (wa.*wp.*ws).^2;
Cc = (wp.*ws).^2 - (wa.*wp).^2 + 2*(wa.*ws).^2;
Dd = (wp.*ws).^2 + (wa.*wp).^2 + 2*(wa.*ws).^2;
a1 = sqrt(3/2)*pi*wa*woa*(wop^2)*wos.*ws;
b1 = (i*Aa.*Bb + 2*Cc).^2;
c1 = cos(phi) + i*sin(phi);
d1 = cos(dk*z)/8;
e1 = (i*Aa.*Bb + 2*Dd).^3;
y = a1.*b1.*c1.*d1./e1;

elseif Q == 19
% % For pump on TEM00, Stokes on TEM40 and anti-Stokes
% % on TEM20
% % Ra is 1/R where R is the beam's radius of curvature.
% % By using this, a 1/0 error is avoided.
Ra = z./(zo^2 + z.^2);
wa = woa*((zo^2 + z.^2)/zo^2).^0.5;
wp = wop*((zo^2 + z.^2)/zo^2).^0.5;
```

```
ws = wos*((zo^2 + z.^2)/zo^2).^0.5;
phi = 6*atan(z./zo);
Aa = (dk*Ra);
Bb = (wa.*wp.*ws).^2;
Cc = 2*(wp.*ws).^2 - 2*(wa.*wp).^2 + 4*(wa.*ws).^2;
Dd = (wp.*ws).^2 + (wa.*wp).^2 + 2*(wa.*ws).^2;
a1 = -0.5*sqrt(3)*pi*wa*woa*(wop^2)*wos.*ws;
b1 = i*Aa.*Bb + Cc;
c1 = 8*Aa.*Bb.*(wa.*ws).^2 - (Aa.^2).*Bb.^2 ...
- 4*(-18*Bb.*wp.^2 + (wp.*ws).^4 + (wa.*wp).^4 - 4*(wa.*ws).^4);
d1 = cos(phi) + i*sin(phi);
e1 = cos(dk*z)/8;
f1 = (-i*Aa.*Bb - 2*Dd).^4;
y = a1.*b1.*c1.*d1.*e1./f1;

elseif Q == 20
% % For pump on TEM00, Stokes on TEM40 and anti-Stokes
% % on TEM40
% % Ra is 1/R where R is the beam's radius of curvature.
% % By using this, a 1/0 error is avoided.
Ra = z./(zo^2 + z.^2); wa = woa*((zo^2 + z.^2)/zo^2).^0.5;
wp = wop*((zo^2 + z.^2)/zo^2).^0.5;
ws = wos*((zo^2 + z.^2)/zo^2).^0.5;
phi = 8*atan(z./zo);
Aa = (dk*Ra);
Bb = (wa.*wp.*ws).^2;
```

```
Cc = (wp.*ws).^2 + (wa.*wp).^2 + 2*(wa.*ws).^2;
a1 = 4*pi*woa*(wop^2)*wos;
b1 = 560+3*((wa.^4)+12*(wa.*ws).^2+ ...
(ws.^4)).*((-i*Aa.*Bb-2*Cc).^2)./(Bb.^2);
c1 = 3*((i*Aa.*Bb - 2*Cc).^4)./(16*(wa.^4).*(wp.^8).*(ws.^4));
d1 = -120*((wa.^2)+(ws.^2)).*(i*Aa.*Bb + 2*Cc)./Bb;
e1 = -3*((wa.^2)+(ws.^2)).*((i*Aa.*Bb + ...
2*Cc).^3)./(2*(wa.^4).*(wp.^6).*(ws.^4));
f1 = cos(phi) + i*sin(phi);
g1 = cos(dk*z)/8;
h1 = (wa.^5).*(wp.^2).*(ws.^5).*(-i*Aa.*Bb + (2./wa.^2)+...
(4./wp.^2)+(2./ws.^2)).^5;
y = a1.*(b1 + c1 + d1 + e1).*f1./h1;

elseif Q == 21
% % For pump on TEM00, Stokes on TEM00 and anti-Stokes
% % on TEM22
% % Ra is 1/R where R is the beam's radius of curvature.
% % By using this, a 1/0 error is avoided.
Ra = z./(zo^2 + z.^2);
wa = woa*((zo^2 + z.^2)/zo^2).^0.5;
wp = wop*((zo^2 + z.^2)/zo^2).^0.5;
ws = wos*((zo^2 + z.^2)/zo^2).^0.5;
phi = 4*atan(z./zo);
Aa = (dk*Ra);
Bb = (wa.*wp.*ws).^2;
```

```
Cc = (wp.*ws).^2 + (wa.*wp).^2 + 2*(wa.*ws).^2;
Dd = -(wp.*ws).^2 + (wa.*wp).^2 + 2*(wa.*ws).^2;
a1 = pi*wa*woa*(wop^2)*wos.*ws;
b1 = (-i*Aa.*Bb - 2*Dd).^2;
c1 = cos(phi) + i*sin(phi);
d1 = cos(dk*z)/8; e1 = (i*Aa.*Bb + 2*Cc).^3;
y = a1.*b1.*c1.*d1./e1;

elseif Q == 22
% % For pump on TEM00, Stokes on TEM00 and anti-Stokes
% % on LG TEM10
% % Ra is 1/R where R is the beam's radius of curvature.
% % By using this, a 1/0 error is avoided.
Ra = z./(zo^2 + z.^2);
wa = woa*((zo^2 + z.^2)/zo^2).^0.5;
wp = wop*((zo^2 + z.^2)/zo^2).^0.5;
ws = wos*((zo^2 + z.^2)/zo^2).^0.5;
phi = -2*atan(z./zo);
Aa = (dk*Ra);
Bb = (wa.*wp.*ws).^2;
Cc = (wp.*ws).^2 + (wa.*wp).^2 + 2*(wa.*ws).^2;
Dd = -(wp.*ws).^2 + (wa.*wp).^2 + 2*(wa.*ws).^2;
a1 = 2*pi*wa*woa*(wop^2)*wos.*ws;
b1 = (i*Aa.*Bb + 2*Dd);
c1 = cos(phi) + i*sin(phi);
d1 = cos(dk*z)/8;
```

```
e1 = (-i*Aa.*Bb - 2*Cc).^2;
y = a1.*b1.*c1.*d1./e1;

elseif Q == 23
% % For pump on TEM00, Stokes on TEM00 and anti-Stokes
% % on LG TEM20
% % Ra is 1/R where R is the beam's radius of curvature.
% % By using this, a 1/0 error is avoided.
Ra = z./(zo^2 + z.^2);
wa = woa*((zo^2 + z.^2)/zo^2).^0.5;
wp = wop*((zo^2 + z.^2)/zo^2).^0.5;
ws = wos*((zo^2 + z.^2)/zo^2).^0.5;
phi = -4*atan(z./zo);
Aa = (dk*Ra);
Bb = (wa.*wp.*ws).^2;
Cc = (wp.*ws).^2 + (wa.*wp).^2 + 2*(wa.*ws).^2;
Dd = -(wp.*ws).^2 + (wa.*wp).^2 + 2*(wa.*ws).^2;
a1 = 2*pi*wa*woa*(wop^2)*wos.*ws;
b1 = (-i*Aa.*Bb - 2*Dd).^2;
c1 = cos(phi) + i*sin(phi);
d1 = cos(dk*z)/8;
e1 = (i*Aa.*Bb + 2*Cc).^3;
y = a1.*b1.*c1.*d1./e1;

elseif Q == 24
% % For pump on TEM00, Stokes on LG TEM02 and anti-Stokes
% % on LG TEM02
```

```
% % Ra is 1/R where R is the beam's radius of curvature.
% % By using this, a 1/0 error is avoided.
Ra = z./(zo^2 + z.^2);
wa = woa*((zo^2 + z.^2)/zo^2).^0.5;
wp = wop*((zo^2 + z.^2)/zo^2).^0.5;
ws = wos*((zo^2 + z.^2)/zo^2).^0.5;
phi = -4*atan(z./zo);
Aa = (wa.^2).*(wp.^2).*(ws.^2);
Bb = (i*dk.*Aa.*Ra);
Cc = 2*((wp.^2).*(ws.^2) + (wa.^2).*(wp.^2)+ 2*(wa.^2).*(ws.^2));
a1 = 32*pi*(wop^2)*wos*woa.*(wa.^3).*(ws.^3).*(wp.^4);
b1 = (Bb+Cc).^3;
c1 = cos(phi) + i*sin(phi); d1 = cos(dk*z)/8;
y = a1.*c1.*d1./b1;
end
```

Sub-routines "vps" and "vpa"

These two subroutines are identical with the exception of two lines. In order to calculate "vpa," change the name of the subroutine and change "woq = wos" to "woq = woa" and "Qq = Qa" (for Stokes) to "Qq = Qb" for anti-Stokes. This program contains a grocery list of analytically calculated results of the Type 2 overlap integral with the parameter "Qq" determining which one is returned to the main code. At the top of the code, is a list of the possible mode combinations.

Here is the code:

```
function result = vps
```

% % This program calculates the value of the overlap integral of the

% % pump mode with the stokes mode. The integrals were

% % calculate completely analytically.

% % Vps = Integral over the cavity (—up—ˆ2 —us—ˆ2)

% % The mode indexes here are all for rectangularly symmetric TEMmn

% % modes unless otherwise noted with an LG for Laguerre-Gaussian

% % Determine which set of modes to be evaluated

% % Qq = 1 P = 00 q = 00

% % Qq = 2 P = 00 q = 10

% % Qq = 3 P = 10 q = 10

% % Qq = 4 P = 11 q = 10

% % Qq = 5 P = 11 q = 11

% % Qq = 6 P = 20 q = 10

% % Qq = 7 P = 20 q = 20

% % Qq = 8 P = 20 q = 40

% % Qq = 9 P = 00 q = 30

% % Qq = 10 P = 00 q = 20

% % Qq = 11 P = 00 q = 40

% % Qq = 12 P = 01 q = 00

% % Qq = 13 P = 00 q = 22

% % Qq = 14 P = 00 q = 10 (LG)

% % Qq = 15 P = 00 q = 20 (LG)

format long

global L wop wos woa dk x wo_sq zo values uo b Q Qa Qb

```
woq = wos;
Qq = Qa;
if Qq == 1
% % For pump on 00 and q on 00
Vpq = pi*(wop^2)*(woq^2)*zo*atan(L/(2*zo))/(4*(wop^2 + woq^2));
elseif Qq == 2
% % For pump on 00 and q on 10
Vpq = pi*(wop^4)*(woq^2)*zo*atan(L/(2*zo))/(4*(wop^2 + woq^2)^2);
elseif Qq == 3
% % For pump on 10 and q on 10
Vpq = 3*pi*(wop^4)*(woq^4)*zo*atan(L/(2*zo))/(4*(wop^2 + woq^2)^3);
elseif Qq == 4
% % For pump on 11 and q on 10
Vpq = 3*pi*(wop^4)*(woq^6)*zo*atan(L/(2*zo))/(4*(wop^2 + woq^2)^4);
elseif Qq == 5
% % For pump on 11 and q on 11
Vpq = 9*pi*(wop^6)*(woq^6)*zo*atan(L/(2*zo))/(4*(wop^2 + woq^2)^5);
elseif Qq == 6
% % For pump on 20 and q on 10
a = wop^4 - 4*(wop^2)*(woq^2) + 10*woq^4;
Vpq = pi*(wop^4)*(woq^2)*a*zo*atan(L/(2*zo))/(8*(wop^2 + woq^2)^4);
elseif Qq == 7
% % For pump on 20 and q on 20
a = 2*wop^8 - 16*(wop^6)*(woq^2) + 69*(wop^4)*(woq^4)...
```

```
- 16*(wop^2)*(woq^6) + 2*woq^8;
Vpq = pi*(wop^2)*(woq^2)*a*zo*atan(L/(2*zo))/(16*(wop^2 + woq^2)^5);
elseif Qq == 8 % %
For pump on 20 and q on 40
a = 8*wop^12 - 128*(wop^10)*(woq^2) +1064*(wop^8)*(woq^4)
- 1344*(wop^6)*(woq^6)+ 819*(wop^4)*(woq^8) -...
96*(wop^2)*(woq^10) + 6*woq^12;
Vpq = pi*(wop^2)*(woq^2)*a*zo*atan(L/(2*zo))/(64*(wop^2 + woq^2)^7);
elseif Qq == 9
% % For pump on 00 and q on 30
a = (wop^2)*(2*(wop^4) + 3*(woq^4));
Vpq = pi*(wop^2)*(woq^2)*a*zo*atan(L/(2*zo))/(8*(wop^2 + woq^2)^4);
elseif Qq == 10
% % For pump on 00 and q on 20
a = (2*(wop^4) + (woq)^4);
Vpq = pi*(wop^2)*(woq^2)*a*zo*atan(L/(2*zo))/(8*(wop^2 + woq^2)^3);
elseif Qq == 11
% % For pump on 00 and q on 40
a = (8*(wop^8) + 24*(wop^4)*(woq^4) + 3*(woq^8));
Vpq = pi*(wop^2)*(woq^2)*a*zo*atan(L/(2*zo))/(32*(wop^2 + woq^2)^5);
elseif Qq == 12
% % For pump on 01 and q on 00
a = woq^2;
Vpq = pi*(wop^2)*(woq^2)*a*zo*atan(L/(2*zo))/(4*(wop^2 + woq^2)^2);
```

```
elseif Qq == 13
% % For pump on 00 and q on 22
a = (2*(wopˆ4)+ (woqˆ4))ˆ2;
Vpq = pi*(wopˆ2)*(woqˆ2)*a*zo*atan(L/(2*zo))/(16*(wopˆ2 + woqˆ2)ˆ5);
elseif Qq == 14
% % For pump on 00 and q on LG 10
a = ((wopˆ4)+(woqˆ4));
Vpq = pi*(wopˆ2)*(woqˆ2)*a*zo*atan(L/(2*zo))/(4*(wopˆ2 + woqˆ2)ˆ3);
elseif Qq == 15
% % For pump on 00 and q on LG 20
a = ((wopˆ8)+ 4*(wopˆ4)*(woqˆ4)+(woqˆ8));
Vpq = pi*(wopˆ2)*(woqˆ2)*a*zo*atan(L/(2*zo))/(4*(wopˆ2 + woqˆ2)ˆ5);
end
result = Vpq;
```

APPENDIX J

COMPARISON FIGURES

As discussed in Chapter 3 on page 63, the CWRLE can be numerically integrated with two methods. The first method integrates the equations as written at the end of Chapter 2 (equations 2.158 – 2.160). The second method integrates the equations after they have been separated into amplitude and phase equations (equations 3.2 – 3.7). The second method has the advantage of being able to set the initial phases. However, integration by the first method should give the same results as the second method. In this appendix, the results from integration method 1, equivalent to Figures 3.2 and 3.3, are shown.

When integrating with method 1, the initial phases cannot be set. The initial values for the fields were 10^{-10} V/m for the pump and Stokes and 0 for the anti-Stokes.

Figure J.1 recreates the result of numerically integrating the CWRLE using method 1 using the parameters in Table on page 65 (with the exception of the initial conditions). Figures J.1a, c, and e are the forward pump, Stokes, and anti-Stokes powers, respectively, as functions of time. Also shown on Figures J.1a, c, and e, for comparison, as squares, are the results shown in Figure 3.2 as calculated by method 2. (The temporal spacings between successive points of the method 2 data are not equal. Points were chosen to best show the trends.) The amplitudes calculated by both methods agree perfectly.

Figures J.1b, d, and f of Figure J.1 show the pump, Stokes and anti-Stokes phases, respectively, as a function of time. The phases calculated by the two methods do not look the same. In part, this is due to the choice of initial phases for the calculation by method 2. The Stokes and anti-Stokes phases both show oscillations between 0 and π below threshold (these oscillations could be the result of numerics) but appear constant above threshold. The pump phase in steady-state is slowly evolving. Since the pump phase is slowly evolving, in order for the phase mismatch, $\Delta\phi$, to be constant, either the Stokes or anti-Stokes (or both) must also be slowly evolving.

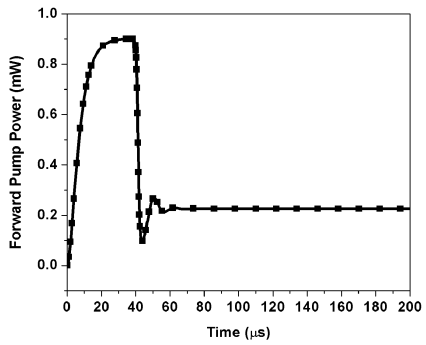

(a) Pump power.

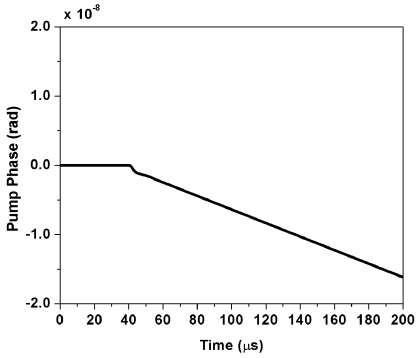

(b) Pump phase.

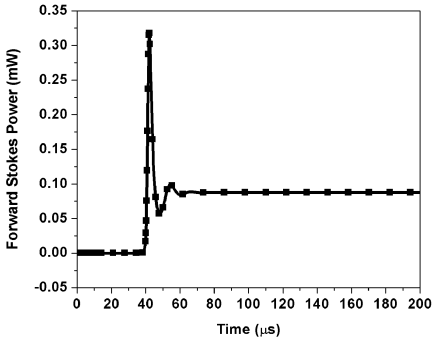

(c) Stokes power.

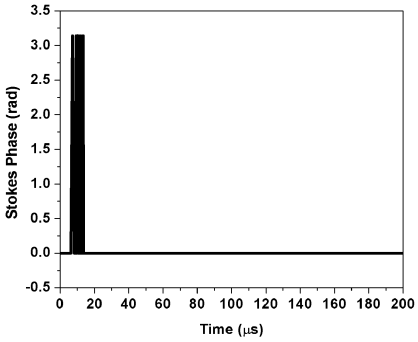

(d) Stokes phase.

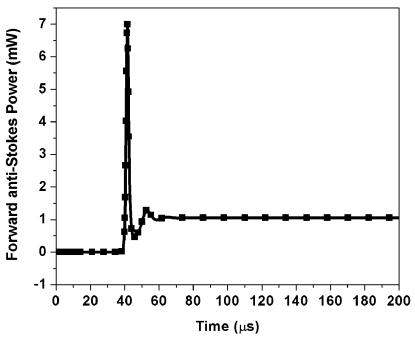

(e) Anti-Stokes power.

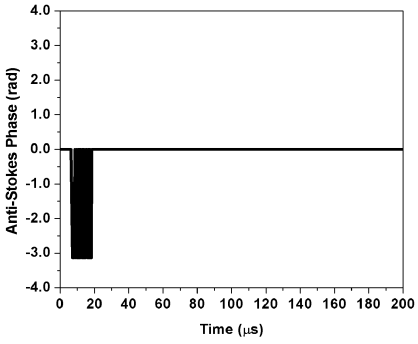

(f) Anti-Stokes phase.

Figure J.1: Forward powers and phases as a function of time when $\delta = 0$, with conditions specified in Table 3.1. On subplots a, c and e, the solid line is the result of integration by method 1 and the squares are the results of integration by method 2. Subplots b, d, and f only show the results calculated by method 1.

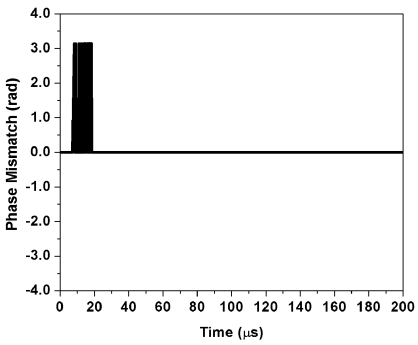

Figure J.2: Phase mismatch as a function of time when $\delta = 0$, with conditions specified in Table 3.1, as calculated by integration method 1.

However, zooming in on both the Stokes and anti-Stokes phases shows that only the Stokes is evolving.

Figure J.2 shows the phase mismatch as a function of time as calculated by method 1. The steady-state value of the phase-mismatch is constant at zero, as calculated by method 2 and shown in Figure 3.3.

APPENDIX K

CHOICE OF SIGN OF BETA

In Chapter 3, a full-steady state solution, valid only on line-center, was derived. In that process, it was found that the anti-Stokes field magnitude was proportional to the Stokes field magnitude. This ratio is given in equation 3.30. That equation is:

$$\frac{A_{a\,ss}}{A_{s\,ss}} = \frac{-\left(\zeta V_{pa} + V_{ps}\right)}{2V_{FWM}^{R}} \pm \frac{1}{2}\sqrt{\frac{\left(\zeta V_{pa} + V_{ps}\right)^{2}}{V_{FWM}^{R\,2}} - 4\zeta}. \tag{K.1}$$

There are two possible choices for the constant of proportionality based on the sign of the square root. Let the two possibilities be β_+ and β_-, with the subscripts indicating the choice of sign. Physically, the anti-Stokes magnitude cannot exceed the Stokes magnitude. Therefore, the ratio of $A_{a\,ss}/A_{s\,ss}$ cannot be greater than one, a fact which will determine which sign of the proportionality constant to choose.

Using the numerical parameters from Chapter 3 (Table 3.1), values of the two possibilities can be determined, as shown in Figure K.1. Figure K.1a shows the calculated value of β_- over a pressure range from 1.5 to 10 atm. The spike around 7 atm is due to V_{FWM}^{R} going through zero at that pressure, as shown in Figure H.1. $|\beta_-|$ is physical only for pressures above the spike at 7 atm. Figure K.1c also shows β_- but on a much smaller vertical scale in order to get an idea of the numerical value of β_- in the pressure region where it is physical. Figure K.1b shows the calculated value of β_+. It is physical for pressures below the spike at 7 atm. Figure K.1d shows the value of β_+ on a smaller vertical scale in order to give an idea of its magnitude in the region where it is physical.

The choice of sign of β depends on the pressure where the theory is being calculated, as shown in Figure K.1. The reason that the sign of β depends on pressure is due to phase matching (Δk) causing the sign of V_{FWM}^{R} to flip from positive to negative. At pressures above $\sim$ 7 atm, the negative sign should be chosen whereas for pressures below $\sim$ 7 atm, the positive sign should be chosen. At pressures very

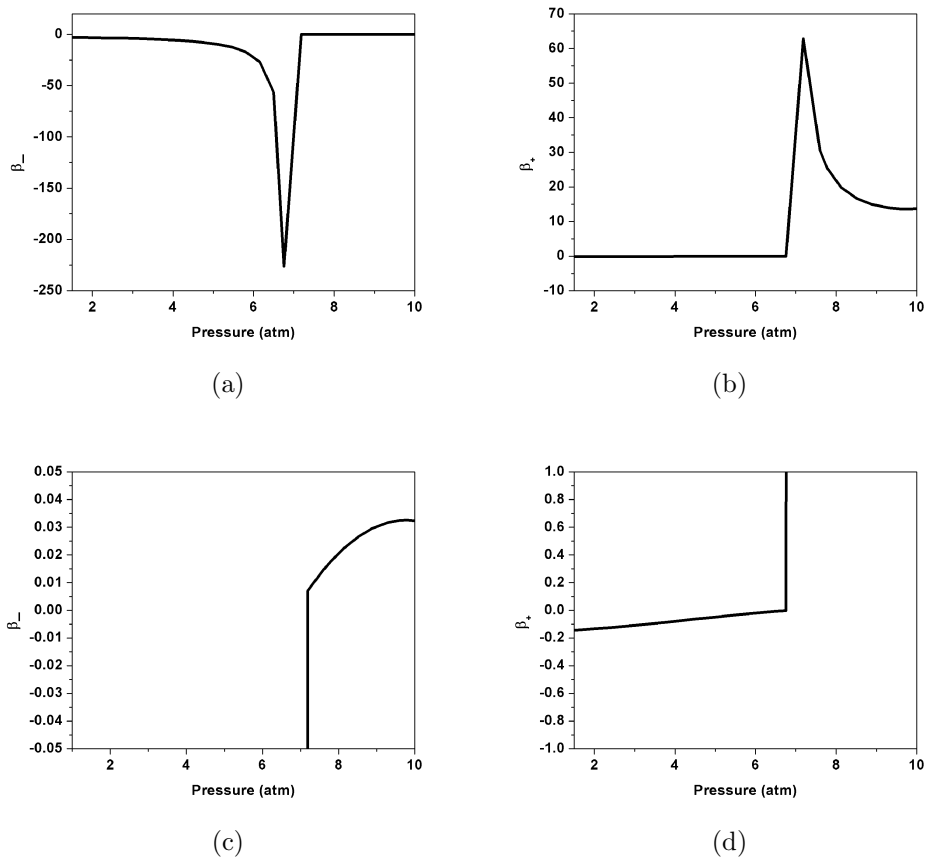

Figure K.1: Graphs of the two possibilities for the sign of β. Sublots a and c are the calculated values of β_- while subplots b and d are the values of β_+. Subplots c and d are zoomed in versions of subplots a and b showing the region in pressure where the values of β_- and β_+ are physical.

near to 7 atm, V^R_{FWM} is predicted to be zero (whenever the pump, Stokes and anti-Stokes have no net Guoy phase shift as discussed in Appendix H), and therefore the theory should predict that no anti-Stokes is produced.

APPENDIX L

FABRY-PEROT CAVITY 1

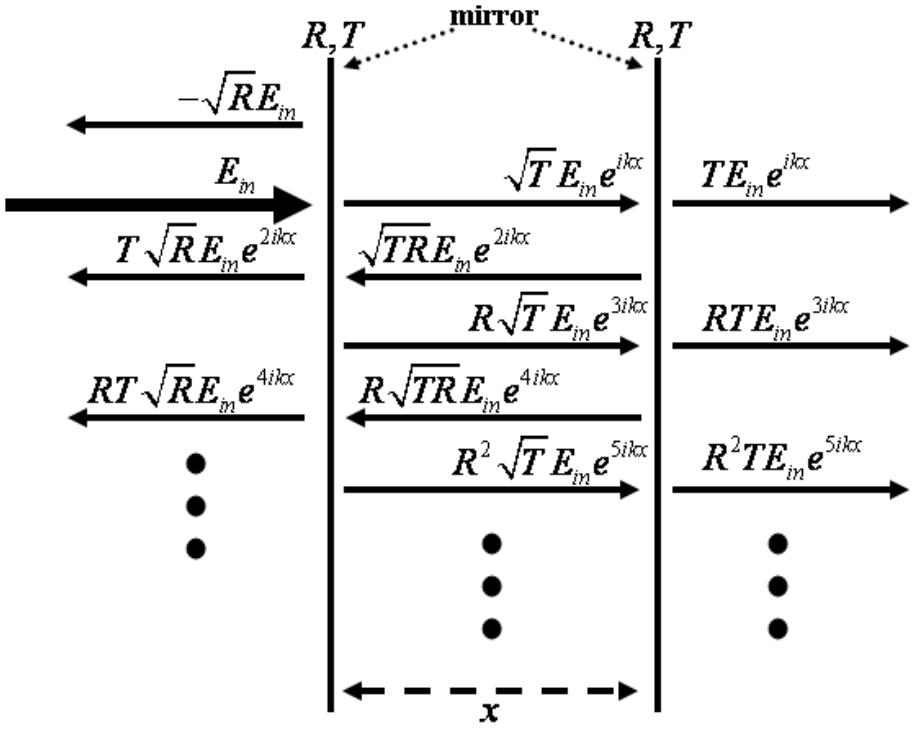

Figure L.1: Schematic of the first few terms of the steady-state electric field inside and outside of an optical cavity. The terms have been displaced vertically for ease of viewing. In reality, they are all collinear.

Just as a musical instrument only resonates certain frequencies, optical cavities are only resonant for certain optical frequencies. For an optical cavity composed of two flat mirrors ($R_c \to \infty$), these resonant frequencies are easily found by simply summing the fields both inside and outside the cavity, assuming it has reached steady-state. This process is shown in Figure L.1, given an electric field of magnitude E_{in} (at an arbitrary wavelength) incident on a matched cavity whose mirrors have power reflectivities, R, and transmittivities, T, such that

$$R + A + T \;=\; 1, \tag{L.1}$$

where A is the mirror's losses due to absorption, scattering, etc. The minus sign on the initial reflection is due to a 180^o phase shift. In Figure L.1, the distance between

the mirrors (otherwise known as the cavity length) is x, $k = {}^{2\pi n}/_{\lambda}$ is the wavenumber (where n is the index of refraction) and the quantity kx is the phase accumulated by the beam after traveling through a distance x. For simplicity, this analysis ignores any additional phase effects that might be accumulated due to the coating layers, etc. It also assumes that the phase of the input field is zero.

Light transmitted through the first mirror back along the input path is said to travel in the "backward" direction. Light transmitted out the side opposite the input side (i.e. traveling in the same direction as the input) is in the "forward" direction.

In the forward direction, the steady-state field sums to:

$$\begin{aligned} E_f &= E_{in}\left(Te^{ikx} + RTe^{3ikx} + R^2Te^{5ikx} + ...\right) \\ &= E_{in}Te^{ikx}(1 + Re^{2ikx} + ...) \\ &= \frac{E_{in}Te^{ikx}}{1 - Re^{2ikx}}, \end{aligned} \tag{L.2}$$

where the subscript, f, indicates the forward direction and the series (from page 40 of reference [79])

$$(1-a)^{-1} = 1 + a + a^2 + a^3... \tag{L.3}$$

(which is valid when $|a| < 1$) has been used to simplify equation L.2. The power transmitted by the cavity can be found using equation 3.16. Thus, the power transmitted by the cavity is

$$\mathcal{P}_f = \frac{\mathcal{P}_{in}T^2}{1 + R^2 - 2R\cos[2kx]}, \tag{L.4}$$

where $\mathcal{P}_{in}$ is the input power which equals

$$\mathcal{P}_{in} = \left(\frac{\pi w_o^2}{4}\sqrt{\frac{\varepsilon_o}{\mu_o}}\right)|E_{in}|^2. \tag{L.5}$$

(As a reminder, w_o in equation L.5 is the ($1/e$ radius in field) beam waist.) The maximum of $\mathcal{P}_f$ occurs when $\cos[2kx] = 1$ which requires that

$$x = \frac{qn\lambda}{2} \tag{L.6}$$

where q is an integer. Equation L.6 determines the resonant cavity lengths for a given wavelength of light. The maximum value of $\mathcal{P}_f$ is

$$\mathcal{P}_{f\,max} = \frac{\mathcal{P}_{in}T^2}{1+R^2-2R}, \tag{L.7}$$

When the mirrors are lossless, i.e. $A = 0$, then equation L.7 simplifies to

$$\mathcal{P}_{f\,max} = \mathcal{P}_{in}. \tag{L.8}$$

Physically, in this on-resonance, lossless case, through interference, the maximum value transmitted by the cavity equals the amount of power input on the system. By conservation of energy, in this special case, there can be no energy traveling backward along the direction of the input pump.

Dividing equation L.4 by equation L.7 gives the relative power transmitted in the forward direction by the cavity as a function of x. It is

$$\begin{aligned} \mathcal{P}_{rel} &= \frac{\mathcal{P}_f}{\mathcal{P}_{f\,max}} \\ &= \frac{(1+R^2-2R)}{(1+R^2-2R\cos[2k_a x])}. \end{aligned} \tag{L.9}$$

This result will be referred to in Appendix M.

In the backward direction, the steady-state field sums to

$$\begin{aligned} E_b &= E_{in}\left(-\sqrt{R} + T\sqrt{R}e^{2ikx} + RT\sqrt{R}e^{4ikx} + ...\right) \\ &= -\sqrt{R}E_{in} + E_{in}T\sqrt{R}e^{2ikx}(1 + Re^{2ikx} + ...) \\ &= -\sqrt{R}E_{in} + \frac{E_{in}T\sqrt{R}e^{2ikx}}{1-Re^{2ikx}}, \end{aligned} \tag{L.10}$$

where the subscript, b, indicates the backward direction and the series in equation L.3 has again been used. Because of interference between the initial reflected field and the transmitted field, the power in the backward direction is more complicated than the power in the forward direction. It is

$$\mathcal{P}_b = \frac{\mathcal{P}_{in} R \left(1 - 2\cos[2kx]\,(R+T) + (R+T)^2\right)}{1 + R^2 - 2R\cos[2kx]}. \tag{L.11}$$

On resonance, equation L.11 simplifies to (applying equation L.6)

$$\mathcal{P}_b = \frac{\mathcal{P}_o R \left(1 - 2\,(R+T) + (R+T)^2\right)}{1 + R^2 - 2R}. \tag{L.12}$$

In the special case discussed above, (on-resonance and lossless mirrors), $\mathcal{P}_b$ is zero! (This is easily seen by applying $T = 1 - R$ to the numerator.) The transmitted field has perfectly canceled the initial reflection. As discussed above, this was necessary because, in this special case, the transmitted power equals the input power (equation L.8).

Inside the cavity, the fields moving right and left must be summed at a common location. Let this position be an arbitrary position located a distance x' from the left mirror ($x' < x$). As such, Figure L.1 needs to be modified slightly, but that will be left up to the reader. The field inside the cavity moving to the right at x' is

$$\begin{aligned} E_{right} &= E_{in}\left(\sqrt{T}e^{ikx'} + R\sqrt{T}e^{ik(2x+x')} + R^2\sqrt{T}e^{ik(4x+x')} + ...\right) \\ &= E_{in}\sqrt{T}e^{ikx'}(1 + Re^{2ikx} + R^2e^{2ikx} + ...) \\ &= \frac{E_{in}\sqrt{T}e^{ikx'}}{1 - Re^{2ikx}}, \end{aligned} \tag{L.13}$$

where equation L.3 has been applied. The field inside the cavity moving to the left at x' is

$$\begin{aligned} E_{left} &= E_{in}\left(\sqrt{TR}e^{ik(2x-x')} + R\sqrt{TR}e^{ik(4x-x')} + R^2\sqrt{TR}e^{ik(6x-x')} + ...\right) \\ &= E_{in}\sqrt{TR}e^{ik(2x-x')}(1 + Re^{2ikx} + R^2e^{2ikx} + ...) \\ &= \frac{E_{in}\sqrt{TR}e^{ik(2x-x')}}{1 - Re^{2ikx}}, \end{aligned} \tag{L.14}$$

where equation L.3 has, again, been applied. The total field within the cavity is the sum of the left bound and right bound moving pieces. It is

$$\begin{aligned} E_{inside} &= \frac{E_{in}\sqrt{T}e^{ikx'}}{1 - Re^{2ikx}} + \frac{E_{in}\sqrt{TR}e^{ik(2x-x')}}{1 - Re^{2ikx}} \\ &= \frac{E_{in}\sqrt{T}}{1 - Re^{2ikx}}\left(e^{ikx'} + \sqrt{R}e^{ik(2x-x')}\right). \end{aligned} \tag{L.15}$$

The magnitude of the field inside, squared, is

$$|E_{inside}|^2 = \frac{|E_{in}|^2 T}{1 + R^2 - 2R\cos\left[2kx\right]}\left(1 + 2\sqrt{R}\cos\left[2k(x - x')\right] + R\right). \tag{L.16}$$

The maximum value will occur when the cavity length satisfies equation L.6 and the observation point, x', is located at an anti-node of the standing wave within the cavity, making

$$\cos\left[2k(x - x')\right] = -1. \tag{L.17}$$

The maximum value of $|E_{inside}|^2$ is

$$|E_{inside}|^2 = |E_{in}|^2\left(\frac{T\left(1 - \sqrt{R}\right)^2}{(1 - R)^2}\right). \tag{L.18}$$

Figure L.2 plots the ratio of $|E_{inside}|^2$ to $|E_{in}|^2$. The ratio is 1 when $R = 0$ and increases as R increases. The fact that $|E_{inside}|^2$ can exceed $|E_{in}|^2$ is what makes the CW Raman laser possible.

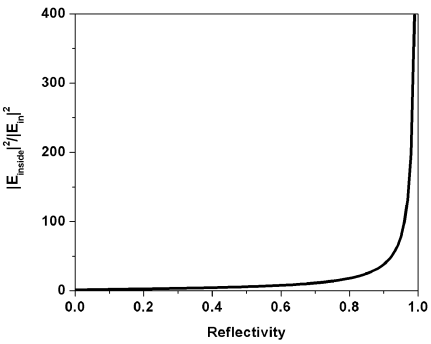

Figure L.2: Graph of the ratio of $|E_{inside}|^2$ to $|E_{in}|^2$ as a function of reflectivity.

APPENDIX M

FABRY-PEROT CAVITY 2

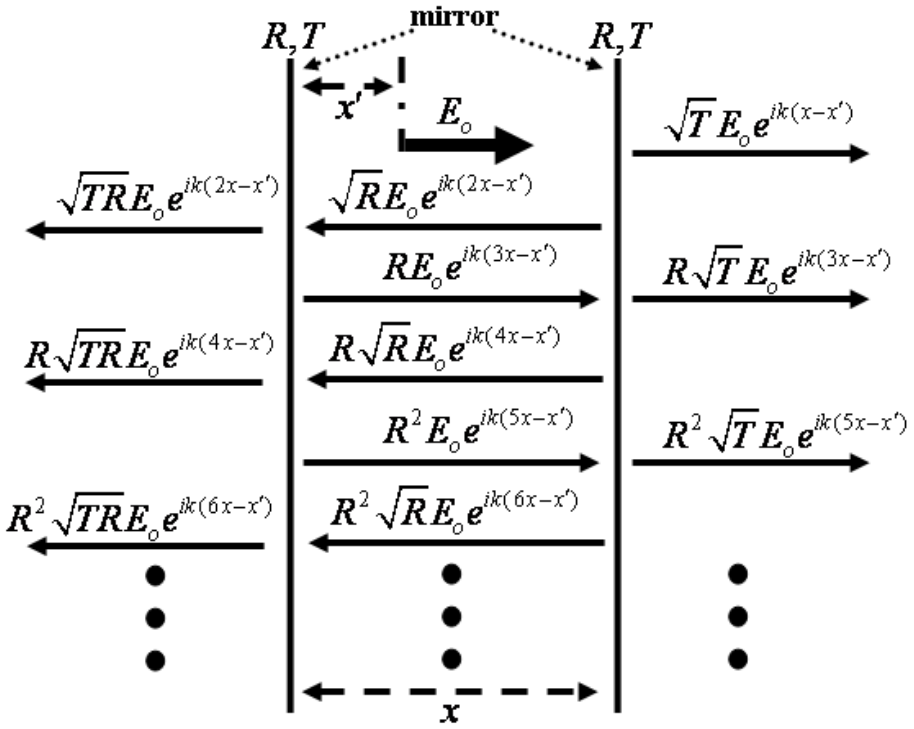

Figure M.1: Schematic of the first few terms of the steady-state electric field inside and outside of an optical cavity with the source inside the cavity. The terms have been displaced vertically for ease of viewing. In reality, they are all collinear.

Appendix L considers a flat-flat Fabry-Perot interferometer with a source external to the cavity. That situation is valid for both the pump and Stokes fields because both have an external field. In the case of the pump, the external source is the input field. For the Stokes, the external source is the vacuum field.

The anti-Stokes, however, does not need an external source field in order to grow within the cavity. It grows due to interactions of the medium with the pump and Stokes fields. Therefore, the results of Appendix L are not necessarily applicable. This appendix covers the case of a Fabry-Perot with the source inside the cavity.

Figure M.1 shows a schematic of a flat-flat Fabry-Perot. The matched mirrors have power reflectivities and trasmittivities, R and T, respectively. The distance between

the mirrors is x. At a position x' from the left mirror is the location of the source, E_o. (Note, E_o will not be the magnitude of the field at x'.) $k = {}^{2\pi n}/_{\lambda}$ is the wavenumber (where n is the index of refraction). The phase accumulated by the beam as it travels is equal to k multiplied by the distance traveled. While actually collinear, the fields in Figure M.1 have been displaced vertically for ease of viewing. For simplicity, this analysis ignores any additional phase effects that might be accumulated due to the coating layers, etc. It also assumes that the phase of the input field is zero.

For consistency with Appendix L, light transmitted through the left mirror is said to travel in the backward direction. Light transmitted through the right mirror is in the forward direction.

The field transmitted in the backward direction is:

$$\begin{aligned} E_b &= E_o\left(\sqrt{TR}e^{ik(2x-x')} + R\sqrt{TR}e^{ik(4x-x')} + R^2\sqrt{TR}e^{ik(6x-x')} + ...\right) \\ &= E_o\sqrt{TR}e^{ik(2x-x')}\left(1 + Re^{2ikx} + R^2e^{4ikx} + ...\right) \\ &= \frac{E_o\sqrt{TR}e^{ik(2x-x')}}{1 - Re^{2ikx}}, \end{aligned} \tag{M.1}$$

where the subscript, b, indicates the backward direction and the series (from page 40 of reference [79])

$$(1-a)^{-1} = 1 + a + a^2 + a^3... \tag{M.2}$$

(which is valid when $|a| < 1$) has been used to simplify equation M.1.

The field transmitted in the forward direction is

$$\begin{aligned} E_f &= E_o\left(\sqrt{T}e^{ik(x-x')} + R\sqrt{T}e^{ik(3x-x')} + R^2\sqrt{T}e^{ik(5x-x')} + ...\right) \\ &= E_o\sqrt{T}e^{ik(x-x')}\left(1 + Re^{2ikx} + R^2e^{4ikx} + ...\right) \\ &= \frac{E_o\sqrt{T}e^{ik(x-x')}}{1 - Re^{2ikx}}, \end{aligned} \tag{M.3}$$

where the subscript, f, indicates the forward direction and the series in equation M.2 has again been used to simplify equation M.3.

The power transmitted by the cavity can be found using equation 3.16. Thus, the power transmitted in the backward direction is

$$\mathcal{P}_b = \frac{\mathcal{P}_o T R}{1 + R^2 - 2R\cos[2kx]}, \tag{M.4}$$

where $\mathcal{P}_o$ is the input power which is defined as

$$\mathcal{P}_o = \left(\frac{\pi w_o^2 n}{4}\sqrt{\frac{\varepsilon_o}{\mu_o}}\right)|E_{in}|^2. \tag{M.5}$$

(As a reminder, w_o in equation M.5 is the [$1/e$ radius in field] beam waist.) The power transmitted in the forward direction is

$$\mathcal{P}_f = \frac{\mathcal{P}_o T}{1 + R^2 - 2R\cos[2kx]}, \tag{M.6}$$

The maximum values of $\mathcal{P}_b$ and $\mathcal{P}_f$ occur when $\cos[2kx] = 1$ which requires that

$$x = \frac{qn\lambda}{2} \tag{M.7}$$

where q is an integer. This is the same resonance condition found in Appendix L (equation L.6). The maximum value of $\mathcal{P}_b$ is

$$\mathcal{P}_{b\,max} = \frac{\mathcal{P}_o T R}{1 + R^2 - 2R}. \tag{M.8}$$

The maximum value of $\mathcal{P}_f$ is

$$\mathcal{P}_{f\,max} = \frac{\mathcal{P}_o T}{1 + R^2 - 2R}. \tag{M.9}$$

In the special case where there is no absorption or scattering from the mirrors, A is zero so that $T = 1 - R$, the maximum values simplify to

$$\mathcal{P}_{b\,max} = \frac{\mathcal{P}_o R}{(1 - R)}. \tag{M.10}$$

$$\mathcal{P}_{f\,max} = \frac{\mathcal{P}_o}{(1 - R)}. \tag{M.11}$$

When $R \sim 1$, equations M.10 and M.11 are approximately equal. Of more concern is that it appears that more power is transmitted by the cavity than is contained in the source field, i.e. $\mathcal{P}_{b\,max} > \mathcal{P}_o$ and $\mathcal{P}_{f\,max} > \mathcal{P}_o$. Thus, it appears that conservation of energy has been violated. However, while E_o is the source field for this analysis, nowhere in the analysis has the source of E_o been considered. In other words, what caused the field E_o within the cavity? In the case of anti-Stokes generation, E_o would be caused by radiating dipoles. This case is important but not the easiest to consider because characterizing the exact nature of E_o based on the pump and Stokes radiation is complicated. Instead, consider the case where $E_o = \sqrt{T}E_{in}$ and $x' = 0$, where E_{in} is an external source field. This case is exactly the situation in Appendix L. Converting E_o to power and plugging into equations M.10 and M.11 returns the results found in Appendix L. Namely, the power transmitted in the forward direction is $\mathcal{P}_o$ and the power transmitted in the backward direction is $R\mathcal{P}_o$, which will cancel the initial reflection that must have occurred. In this special case, it is clear that conservation of energy is not violated.

In anti-Stokes generation, a collection of dipoles within the cavity would be emitting. Equation on page 332 would represent one dipole emitting to the right at the anti-Stokes wavelength ($k = k_a$). To make a collection of dipoles emitting within the cavity, dipoles radiating to the left would have to be included, too. Outside the cavity, the forward traveling field from one dipole at a position x' with emission equal E_o to the right and left is:

$$\begin{aligned} E_f &= \frac{E_o\sqrt{T}e^{ik_a(x-x')}}{1-Re^{2ik_ax}} + \frac{E_o\sqrt{RT}e^{ik_a(x+x')}}{1-Re^{2ik_ax}} \\ &= \frac{E_o\sqrt{T}e^{ik_ax}\left(e^{-ik_ax'} + \sqrt{R}e^{ik_ax'}\right)}{1-Re^{2ik_ax}} \end{aligned} \tag{M.12}$$

A good first approximation to a system of dipoles is multiplying equation M.12 by a

function that would represent a standing wave distribution of dipoles caused by the pump and Stokes and then integrating over x'. This function representing the dipole distribution is $\sin[k'x']$ where $k' = 2k_p - k_s$. This is a first approximation and ignores effects such as the focusing of the fields within the cavity and the relative sizes of the anti-Stokes waist and the waist of the dipole distribution created by the interaction of the medium with the pump and Stokes fields. Integrating yields

$$\begin{aligned} E_f &= \frac{E_o\sqrt{T}e^{ik_a x}}{1-Re^{2ik_a x}}\int_{-L/2}^{L/2} dx' \left(e^{-ik_a x'} + \sqrt{R}e^{ik_a x'}\right)\sin[k'x'] \\ &= \frac{E_o\sqrt{T}e^{ik_a x}}{2i\,(1-Re^{2ik_a x})}\int_{-L/2}^{L/2} dx' \left(e^{-i(k_a-k')x'} - e^{-i(k_a+k')x'}\right. \\ &\qquad \left. +\sqrt{R}e^{i(k_a+k')x'} + \sqrt{R}e^{i(k_a-k')x'}\right). \end{aligned} \tag{M.13}$$

$k_a + k' = 2k_p - k_s + k_a$ and $k_a - k' = -2k_p + k_s + k_a$. As discussed in Appendix H H.12, $(k_a - k')$ will be much smaller than $(k_a + k')$. Therefore, the integral over pieces containing $(k_a - k')$ will dominate. Thus, equation M.13 is

$$E_f = \frac{E_o\sqrt{T}e^{ik_a x}}{i\,(1-Re^{2ik_a x})}\frac{2(1+\sqrt{R})}{(k_a-k')}\sin\left[\frac{(k_a-k')L}{2}\right]. \tag{M.14}$$

In terms of power, this is

$$\mathcal{P}_f = \frac{4\mathcal{P}_o T(1+\sqrt{R})^2}{(k_a-k')^2\,(1+R^2-2R\cos[2k_a x])}\sin^2\left[\frac{(k_a-k')L}{2}\right]. \tag{M.15}$$

The maximum value is

$$\mathcal{P}_{f\,max} = \frac{4\mathcal{P}_o T}{(k_a-k')^2\,(1+R^2-2R)}\sin^2\left[\frac{(k_a-k')L}{2}\right]. \tag{M.16}$$

$k_a - k' = -2k_p + k_s + k_a$ is the standard phase-matching definition for anti-Stokes scattering (as discussed in Chapter 4 on page 108). If $\mathcal{P}_{f\,max}$ is multiplied and divided by $(L/2)^2$, then it is proportional to $\mathrm{sinc}^2\left[\frac{(k_a-k')L}{2}\right]$, which when perfectly phase-matched equals 1 because $(k_a - k') = 0$. However, due to dispersion in the H_2,

the system will not be perfectly phase-matched. Therefore, the dependence of $\mathcal{P}_f$ on $\sin\left[\frac{(k_a-k')L}{2}\right]$ can be viewed as a decrease in the transmitted power due to poor phase-matching.

Dividing equation M.15 by equation M.16 gives the relative power transmitted by the cavity as a function of x. It is

$$\begin{aligned} \mathcal{P}_{rel} &= \frac{\mathcal{P}_f}{\mathcal{P}_{f\,max}} \\ &= \frac{(1+R^2-2R)}{(1+R^2-2R\cos[2k_a x])}. \end{aligned} \tag{M.17}$$

This is the same function as found in Appendix L (equation L.9). Therefore, the variation in relative power from max to min will be the same in both cases. In terms of anti-Stokes generation, this seems to indicate that, even though there is no external input field, the cavity resonances will have the same shape and properties as resonances associated with an input field (like the pump and Stokes).

This issue has not been resolved through this analysis. It is fertile ground for further development.

APPENDIX N

CALIBRATION OF PICTURES

In both Experiments 1 and 2, the pump, Stokes, and anti-Stokes beams traveled different distances from the cavity to the camera. Thus, the pictures were not all on the same scale. This appendix documents how the pictures were rescaled for comparison purposes.

For Experiment 1

Figure N.1 shows the route that the Stokes beam takes from the cavity to the camera. (For the Stokes to reach its power meter, the mirror leading to the camera is flipped out of the beam path.) The pump and anti-Stokes can be seen by the camera by flipping a mirror (shown as dotted lines in the beam paths). As can be seen in the figure, all three beams travel different distances from the cavity to the camera, with the Stokes traveling the farthest and the anti-Stokes traveling the shortest distance. The distance from the center of the Raman cavity to the body of the camera for the

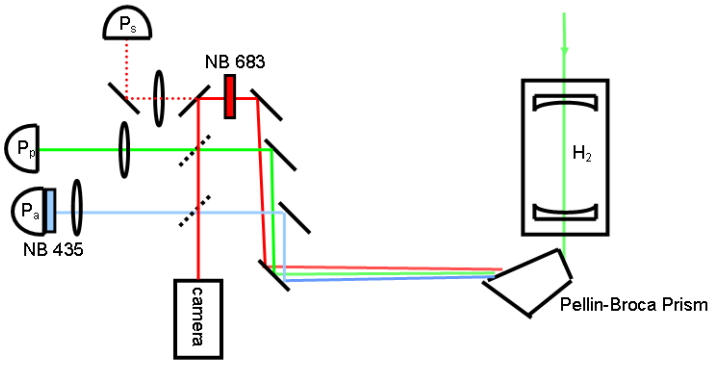

Figure N.1: Detailed layout of Experiment 1 showing all the optics between the cavity and the camera. As drawn, the Stokes is being seen by the camera. By flipping a mirror (dashed lines), the pump or anti-Stokes could be seen by the camera.

Stokes, pump, and anti-Stokes is 162 cm, 145 cm, and 116 cm, respectively.

Measurement of the Magnification

On the front of the camera is a fixed focal length lens whose distance from the CCD array of the camera can be varied. This lens was necessary because the CCD array of the camera was not strong enough to measure the intensity distribution of the non-focused beams. Thus, in addition to having to correct for the different distances traveled, the effects of this lens need to be determined.

The easiest way to determine the magnification of this lens was to place a known object in front of it until the image displayed was in focus. The best object found for this purpose was a drill index because it has labeled holes of known diameter. The labels can be used to determine the placement of the index in front of the camera (i.e. the position of the index was adjusted until they were in focus). The holes serve as objects of known size for the purpose of determining the magnification.

Figure N.2 shows a picture of the drill index taken with *Beamview* beam analysis software. The software is designed to take intensity profiles. The index was

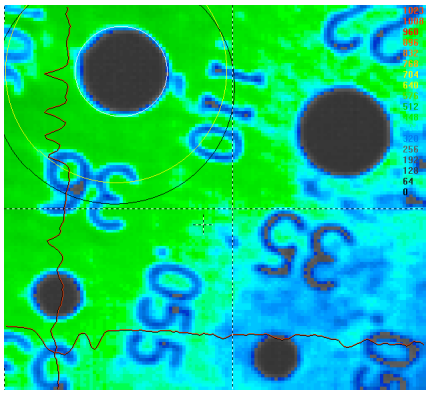

Figure N.2: Picture of a drill index used to determine the magnification of the lens on the front of the camera.

illuminated with white light and had a dark object behind it. Therefore, the holes in the index appear dark and the surface of the index is in shades of blue and green (if viewed in color). Moving clockwise from top-left, the diameter of the four holes

shown is 0.106 inches, 0.110 inches, 0.055 inches, and 0.059 inches. In centimeters, these are 0.26924 cm, 0.2794 cm, 0.1397 cm and 0.14986 cm, respectively.

Given the pixel size of the camera, Beamview can make measurements. The pixel size of the camera used in this dissertation (Pulnix TM745) is 13 μm. Hard to see, at the diameter of the top-left hole is a circle (white). (The yellow and black circles are other apertures that have to be displayed by the program when the white circle is shown.) The white circle has an adjustable radius and position. To measure the diameter of each of the holes, the location and the radius of the white circle was adjusted to each hole. The diameters measured by this method are, from the top-left clockwise, 0.03755 cm, 0.03885 cm, 0.0194 cm, and 0.02201 cm.

The magnification of the system is the ratio of the measured diameter to the actual diameter, from geometric optics [81]. The average magnification as determined by the four holes in the drill index is 0.14.

The index was placed a distance of 20 cm from the body of the camera. The lens attaches to the body of the camera and, therefore, is included in the 20 cm.

Theoretical Beam Diameters

Using Gaussian optics [46], the theoretical values of the three spot sizes can be determined at a distance of 20 cm from the front of the camera body. At this plane, the Stokes, pump, and anti-Stokes have propagated through distances of 142 cm, 125cm, and 96 cm, respectively, from the center of the Raman cavity.

The important equations from Gaussian optics are, from [46] page 83,

$$w_o = \left(\frac{\lambda z_o}{\pi}\right)^{\frac{1}{2}} \tag{N.1}$$

$$w(z) = w_o\left[1+\left(\frac{z}{z_o}\right)^2\right]^{\frac{1}{2}} \tag{N.2}$$

$$R_c(z) = z\left[1+\left(\frac{z_o}{z}\right)^2\right], \tag{N.3}$$

where w_o is the ($1/e$ radius in field) beam waist, $w(z)$ is the spot size (again, $1/e$ radius in field) at a distance z from the waist, z_o is the Rayleigh range, and $R_c(z)$ is the wavefront radius of curvature at z. The Rayleigh range, z_o, is calculated using equation N.3 by setting $z = L/2$ and R_c to the cavity mirror's radius of curvature. Given that the radius of curvature of the mirrors is 50 cm and the cavity length is 7.62 cm, the Rayleigh range of all three beams is 13.3 cm.

Using equation N.1, the beam waists can now be calculated given that the pump, Stokes and anti-Stokes wavelengths are 532 nm, 683 nm, and 435 nm, respectively. In cm, they are:

$$w_{op} = 0.015 \tag{N.4}$$

$$w_{os} = 0.017 \tag{N.5}$$

$$w_{oa} = 0.014. \tag{N.6}$$

(Note, the lensing effects of the Raman mirror substrates are ignored in this analysis. That effect was investigated and determined to be negligible.)

Using equation N.2, the beam characteristics can now be "propagated" forward the proper distance for each field. The spot sizes for each field at a distance of 20 cm

from the body of the camera are, in cm:

$$w_p = 0.142 \tag{N.7}$$

$$w_s = 0.182 \tag{N.8}$$

$$w_a = 0.099. \tag{N.9}$$

Using the magnification of 0.14 determined above, these spot sizes, as measured by the camera would be, in cm,

$$2w_p = 0.040 \tag{N.10}$$

$$2w_s = 0.051 \tag{N.11}$$

$$2w_a = 0.028. \tag{N.12}$$

Comparison of Beam Diameters

Each camera pixel is 13 μm square. Horizontally, *Beamview* subdivides each camera pixel into 5 image pixels. By counting pixels, it is possible to determine the sizes of the objects within each picture. A *Matlab* routine was written by Erik Carlsten that would count the image pixels between two vertical bars. (This code is not included in this dissertation.) Given this, the expected spot sizes at the camera's focal plane, equations N.10 – N.12 are, in pixels,

$$2w_p = 152 \tag{N.13}$$

$$2w_s = 196 \tag{N.14}$$

$$2w_a = 106. \tag{N.15}$$

Figure N.3 shows the pump, Stokes, and anti-Stokes profiles that are associated with the data shown in Figure 5.6. On each picture, there are two solid vertical bars surrounding the mode profile. The spacing between these bars is given at the top of

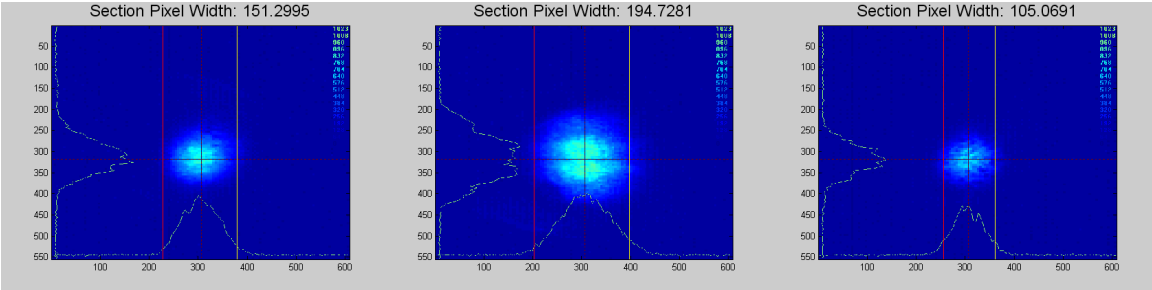

(a) Pump. (b) Stokes. (c) Anti-Stokes.

Figure N.3: Mode profiles. The vertical lines represent the theoretical beam diameters.

each picture and corresponds (as closely as possible) to the theoretical widths (full widths at $1/e^2$ intensity) given in equations N.13 – N.15. The theoretical value of the waists corresponds very well to the images.

Rescaling the Figures

Since the pump traveled the middle distance of the three, the Stokes and anti-Stokes pictures are going to be rescaled so that it is as if they traveled the same distance from the middle of the cavity to 20 cm in front of the camera as the pump. Since the Stokes traveled further, its picture will be scaled down. The anti-Stokes picture will be scaled up to account for it not traveling as far as the pump.

These scale factors are determined from the distances traveled. The scale factors are:

$$S_s = \frac{125}{142} = 0.88 \tag{N.16}$$

$$S_a = \frac{125}{96} = 1.30 \tag{N.17}$$

The rescaled profiles from Figure N.3 are shown in Figure N.4. The grey arrow on the three profiles is 2.3 mrad long. This is the calculated angular width (full width at $1/e^2$ intensity) of the pump mode at 125 cm from the middle of the cavity. Careful

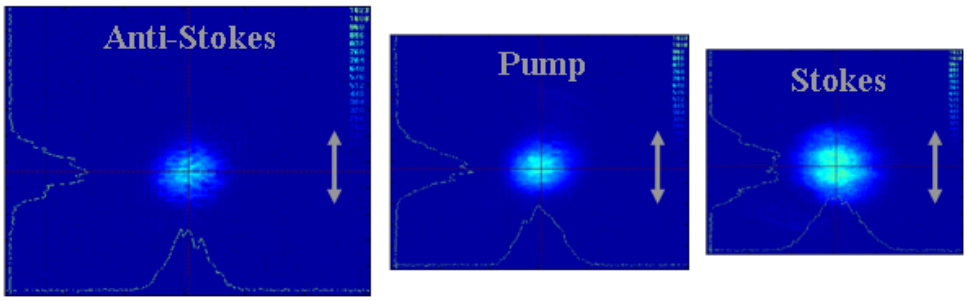

Figure N.4: Rescaled mode profiles. The grey arrow is 2.3 mrad long.

inspection will show that the anti-Stokes mode profile is slightly narrower than 2.3 mrad and the Stokes is slightly wider, as should be expected based upon their relative wavelengths. At 125 cm, the calculated angular widths of the anti-Stokes and Stokes modes are 1.9 mrad and 2.6 mrad.

A Cautionary Note

This analysis was done at the very end of the time period in which the Experiment 1 data was taken. Due to a lack of foresight regarding the use of the pictures while taking data, it is possible that either the camera was moved or the location of the lens relative to the CCD array within the camera was changed. If either change was made, then this analysis in invalidated to some degree.

However, it is felt that if either change was made, it would have been small. The camera's position on the optics table was very near to one edge and there were other optics that needed to be placed between the front of the camera lens and the anti-Stokes flip mirror. Therefore, there is not a great deal of room for the camera to move either closer to or further from the cavity. A best guess was that the maximum that the camera could have been moved is between 2 and 3 inches.

The lens was adjusted to give the best view of the beam profile. This corresponded to the lens being adjusted all the way to one edge of its allowed travel. Moving away

from this position caused the beams to be more focused onto the CCD array and, thus, fewer pixels were covered by the spatial profile, making the details harder to discern.

This is not an issue for Experiment 2 because, by then, it was realized that it would be necessary to be able to place the pictures on the same scale.

For Experiment 2

Figure N.5 shows the route that the Stokes beam takes from the cavity to the camera. Even though the backward Stokes power is measured, the picture is taken of the forward Stokes mode profile. The pump mode profile picture can be taken by changing the NB filter at 683 nm in front of the camera for a NB filter at 532 nm. The anti-Stokes can be seen by the camera by flipping up two mirrors which are shown as dotted lines in the beam path and replacing the NB filter at 632 nm with one at 435 nm. As can be seen in the figure, the pump and Stoked will travel the same distance from the cavity to the front of the camera. The anti-Stokes travels farther. The distance from the center of the Raman cavity to the body of the camera

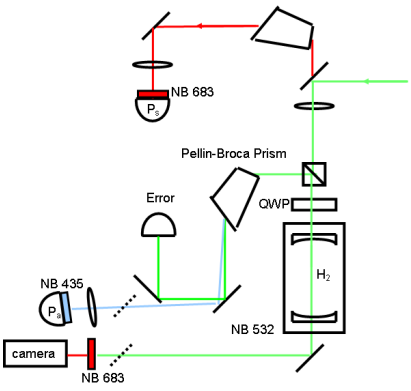

Figure N.5: Detailed layout of Experiment 2 showing all the optics between the cavity and the power meters.

for the pump and Stokes is 103.5 cm and for the anti-Stokes, it is 130.5 cm.

Measurement of the Magnification

The magnification for this experiment was determined by the same method as Experiment 1. Because of the different experimental layout, the lens was adjusted to a different position relative to the camera's CCD array. Thus, the drill index was placed a distance of 23.5 cm from the camera body. The magnification was determined to be 0.13.

Theoretical Beam Diameters

The theoretical beam diameters can be calculated following the same procedure as outlined on page 340. For this experiment, at a distance of 23.5 cm in front of the camera, the spot sizes, in cm, are

$$w_p = 0.091 \tag{N.18}$$

$$w_s = 0.103 \tag{N.19}$$

$$w_a = 0.110. \tag{N.20}$$

Using the magnification of 0.13 determined above, these spot sizes, as measured by the camera would be, in cm,

$$2w_p = 0.024 \tag{N.21}$$

$$2w_s = 0.027 \tag{N.22}$$

$$2w_a = 0.029. \tag{N.23}$$

Comparison of Beam Diameters

As explained on page 342, the theoretical spot sizes as seen by the camera are, in pixels,

$$2w_p = 92 \quad \text{(N.24)}$$

$$2w_s = 104 \quad \text{(N.25)}$$

$$2w_a = 112. \quad \text{(N.26)}$$

Figure N.6 shows the pump, Stokes, and anti-Stokes profiles that are associated with the data shown in Figure 5.18 on page 153. On each picture, there are two solid

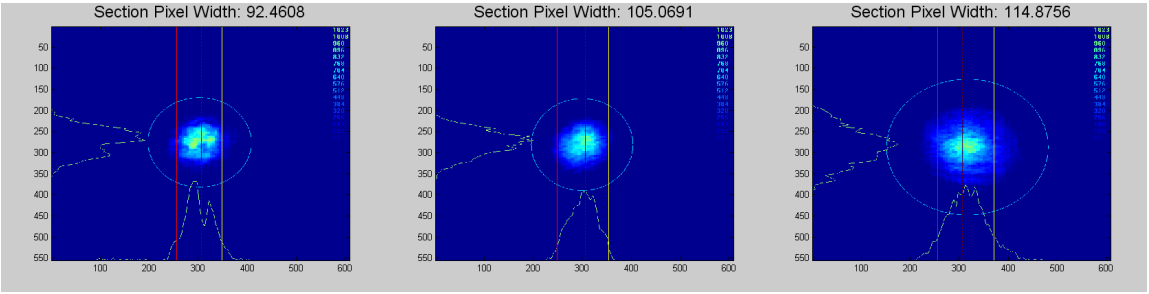

(a) Pump. (b) Stokes. (c) Anti-Stokes.

Figure N.6: Mode profiles. The vertical lines represent the theoretical beam diameters.

vertical bars surrounding the mode profile. The spacing between these bars is given at the top of each picture and corresponds (as closely as possible) to the theoretical widths (full widths at $1/e^2$ intensity) given in equations N.24 – N.26. The theoretical values of the widths correspond very well to the images. (The circle surrounding the profile is an aperture from *Beamview* and is insignificant.)

The structure within the pump mode profile is due to interference fringes from a NB filter.

Rescaling the Figures

Since the pump and Stokes travel the same distance from the center of the cavity to the camera, they are already on the same scale. Therefore, the anti-Stokes will be rescaled to match the other two. Since it travels farther, it needs to be made smaller.

This scale factor is determined from the distances traveled. The scale factors is:

$$S_a = \frac{80}{107} = 0.75 \tag{N.27}$$

The rescaled profiles from Figure N.6 are shown in Figure N.7. The grey arrow on

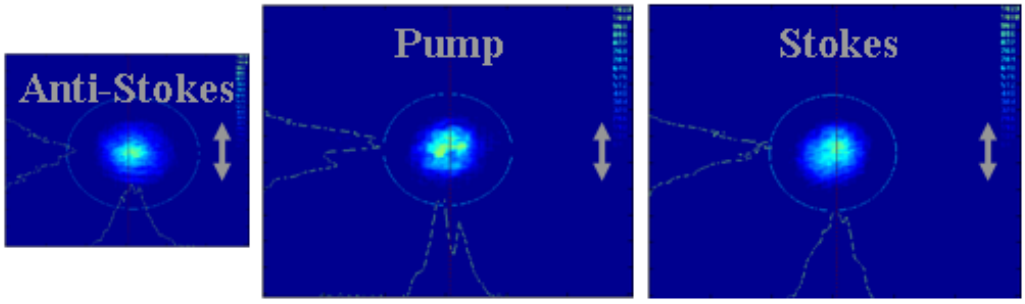

Figure N.7: Rescaled mode profiles. The grey arrow is 2.3 mrad long.

the three profiles is 2.3 mrad long, corresponding to the angular width (full width at $1/e^2$ intensity) of the pump profile.

APPENDIX O

CALIBRATION OF DATA

This appendix goes through the steps needed to calibrate the data taken as a part of this dissertation work. First, the losses of the pump, Stokes, and anti-Stokes beams due to optical elements between the cavity and the power meter are characterized. Secondly, the steps needed to convert the input pump monitor power to coupled input pump power are described.

Losses Due to Optical Elements

The losses for the two experiments are not the same because the experimental set-ups in the two cases are not the same. Therefore, they will be looked at separately.

For Experiment 1 ($R_a = 0.25$)

Figure O.1 shows a schematic of the experimental set-up for the first experiment. For this experiment, the forward pump, Stokes, and anti-Stokes powers were

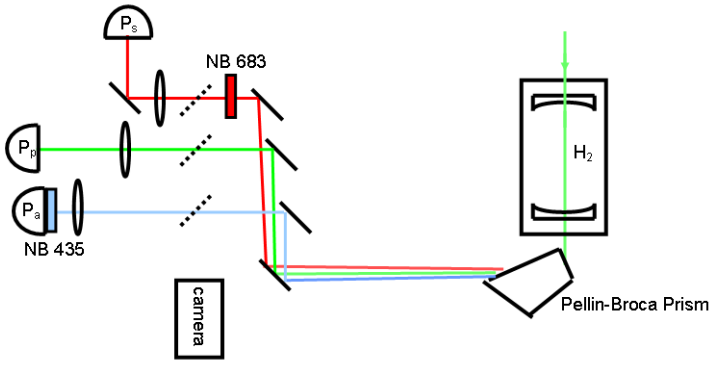

Figure O.1: Detailed layout of Experiment 1 showing all the optics between the cavity and the power meters.

measured. Therefore, Figure O.1 only shows the experimental set-up from the Raman cavity to the power meters. The dashed lines show the position of the flip mirrors that direct the beams to the camera. Both the Stokes and anti-Stokes beams pass

through narrow band (NB) filters at their respective wavelengths. The anti-Stokes NB filter is actually mounted to the front of the power meter. All the mirrors are silver.

The losses of each optical element at the pump and Stokes wavelengths were measured using NB filters and a power meter. When measuring the loss of the NB filter, a second NB filter was placed in the beam before the first (the one under investigation). Then, power measurements were taken with the first NB in and out of the beam. Because the anti-Stokes was so much weaker than the pump and Stokes, it was impossible to measure these optics' losses at the anti-Stokes wavelength. The anti-Stokes losses are either extrapolated from the pump and Stokes losses or obtained from manufacturer's data.

To quantify the loss, the ratio of the power measured before the optic to the power measured after is used. Define this ratio as

$$\eta_q \equiv \frac{\mathcal{P}_{before}}{\mathcal{P}_{after}}. \tag{O.1}$$

The ratio is written in terms of the subscript, q, because it could be different at each wavelength. Since η_q is greater than 1, it is called a correction factor. Table O.1 summarizes the results of these measurements.

Optic	η_p	η_s	η_a
Pellin-Broca Prism	1.06	1.075	1.07
Silver Mirror	1.17	1.15	1.05
Lens	1.07	1.08	1.09
NB Filter @ 683	—	2.435	—
NB filter @ 435	—	—	2.12
Window	1.08	1.08	1.08
Raman Mirror Back Surface	1.04	1.04	1.04
Total Correction Factor	1.7	4.9	3.1

Table O.1: Table characterizing the correction factors of each optic at the pump, Stokes, and anti-Stokes wavelengths.

The last two entries account for the losses of the cavity window (two surfaces) and the back, non-reflective, surface of the Raman mirror. They are assumed to be 4% reflections.

The last row in Table O.1 indicates the total correction factor at that wavelength due to the optics between the cavity and power meter. For example, the pump experiences losses due to the Raman mirror back surface, the cavity window, the Pellin-Broca, two silver mirrors, and a lens. To find the total loss, the losses of each element are multiplied together. Thus, in the case of the pump, the total correction factor is:

$$\begin{aligned} \text{Total Correction Factor} &= (1.04)(1.08)(1.06)(1.17)^2(1.07) \\ &= 1.7 \end{aligned} \tag{O.2}$$

For Experiment 2 ($R_a = 0.5$)

As explained in Chapter 5 on page 148, the experimental set-up had to be modified from Experiment 1 to Experiment 2. In this experiment, the forward pump and the backward Stokes and anti-Stokes were measured. The turning mirror before the cavity is dichroic – it transmits the Stokes and reflects the pump. The Pellin-Broca prism after the dichroic mirror separates the Stokes from the little bit of anti-Stokes that is transmitted by both the PBS and the dichroic mirror.

Because of the different set-up, the loss coefficients at all three wavelengths need to be adjusted. Figure O.2 shows the pertinent details of the set-up for Experiment 2. The dashed lines are flip mirrors that were used to divert the anti-Stokes beam from the power meter to the camera. The pump and Stokes were directed to the camera by removing the lens, NB filter, and power meter used to measure the forward pump power. For each wavelength, a NB filter was placed in front of the camera.

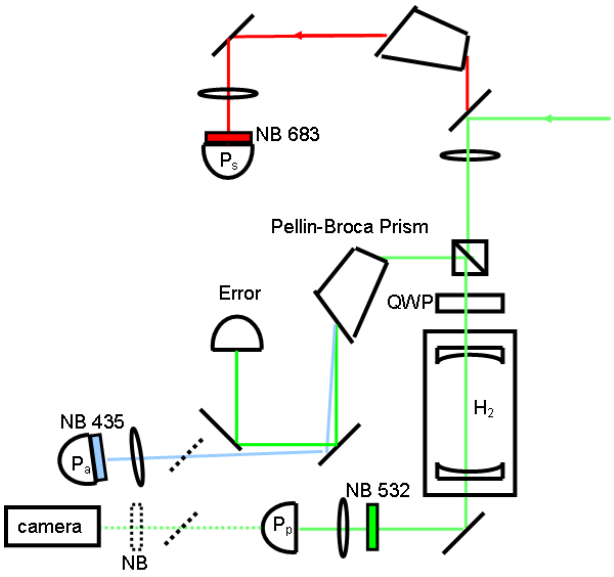

Figure O.2: Detailed layout of Experiment 2 showing the optics between the cavity and the power meters.

As for the first experiment, the losses of all the elements between the cavity and the power meters were measured. These results are shown in Table on the following page, along with the total correction factor at each wavelength. Since different optics were used in places, some of the values in Table O.2 differ from those in Table O.1.

These correction factors ignore any polarization losses for the Stokes and anti-Stokes at the PBS and for the Stokes at the dichroic mirror. Both the Stokes that was reflected by the PBS and the anti-Stokes that was transmitted were measured and found to be small compared to the Stokes that was transmitted and the anti-Stokes that was reflected.

The correction factor of the dichroic mirror was measured using a white light source filtered to 683 nm with a NB filter. The dichroic mirror was placed in the beam at a 45^o angle. The transmitted light was focused onto a detector and measured. The mirror was removed from the beam and the light was again focused onto the detector and measured. The ratio of these two measurements gives the correction factor. As

Optic	η_p	η_s	η_a
Pellin-Broca Prism	—	1.075	1.07
Dichroic Mirror	—	1.52	—
Silver Mirror	1.04	1.04	1.05
Lens	1.07	1.08	1.09
PBS	—	1.08	1.08
QWP	—	1.08	1.08
NB Filter @ 683	—	2.435	—
NB filter @ 435	—	—	2.12
NB filter @ 532	3	—	—
Window	1.08	1.08	1.08
Raman Mirror Back Surface	1.04	1.04	1.04
Total Loss	3.8	6.3	3.4

Table O.2: Table characterizing the correction factors of each optic at the pump, Stokes, and anti-Stokes wavelengths.

a second check, since the reflectivity of the Raman cavity mirrors was known at the pump and Stokes wavelengths, the theoretical value of the backward Stokes was known. The correction factor brought the measured Stokes power into agreement with the theoretical value.

Calibrating the Input Pump

The input pump is not measured directly when the pump, Stokes, and anti-Stokes data is taken. Instead, a monitor is used, as described in Chapter 5 on page 126. The method of converting the input pump monitor power to coupled input pump power is most easily explained with an example. Thus, below, the steps are shown that take the raw data to the form shown in Figure 5.6.

The Raw Data

Figure O.3 shows the data as originally recorded. The input pump is varied by

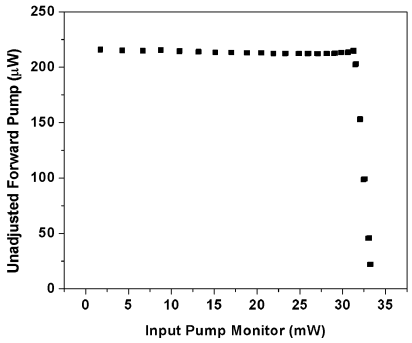

(a) Pump power.

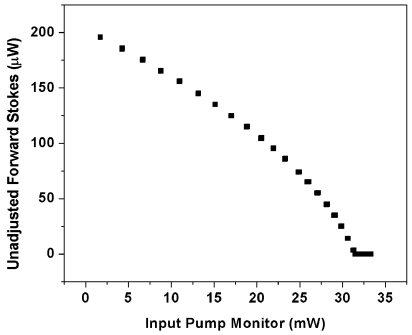

(b) Stokes power.

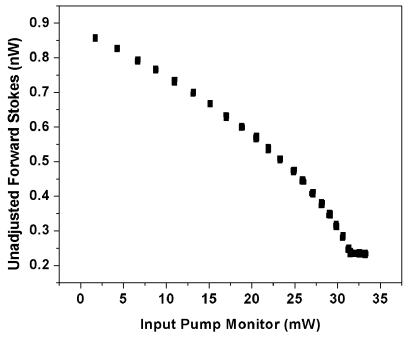

(c) Anti-Stokes power.

Figure O.3: The raw pump, Stokes, and anti-Stokes powers as functions of the input pump monitor power.

adjusting a half-wave plate (HWP) in front of a polarizing beam splitter (PBS). (Figure 5.3 on page 124 might be helpful.) The light transmitted through the PBS is incident upon the Raman cavity. The input light reflected by the PBS is used to monitor the input pump power. As the input pump power is increased, the input pump monitor decreases. The data was taken starting with the input power at its maximum value and ending with its minimum value. Thus, the input pump monitor varies from its minimum value to its maximum value.

The Calibration Data

After the actual data set was taken, the forward pump power meter was moved to in front of the Raman cavity to measure the input pump directly. The HWP was again varied and the input pump monitor power and the input pump power were both measured. This measurement results in a linear relationship between the input pump monitor power and the input pump power to which a line can be fit. The calibration curve for this data set is shown in Figure O.4, along with the linear fit to the data (solid line). The linear fit is used to convert the input pump monitor power to input pump power.

This is the hardest step in this process to perform. It requires the input pump to be steady. If the input pump power changes between the measurement of the data and the measurement of the calibration curve, then this step is not valid. Luckily, it is fairly obvious when this step fails because when the transmitted pump is plotted against the input pump, it does not pass through the point (0,0).

Figure O.5 shows the forward pump, Stokes, and anti-Stokes powers as functions of the input pump power. The correction factors for the pump, Stokes, and anti-Stokes (from Table O.1) have now been included as well. In addition, the background level on the anti-Stokes has been subtracted out.

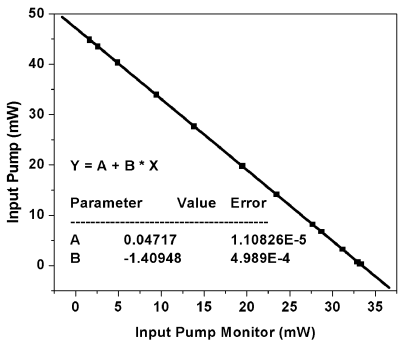

Figure O.4: The input pump as a function of the input pump monitor. The squares are the data and the line is a linear fit. The slope and y-intercept of the linear fit are shown on the plot.

Converting Input Pump Power to Coupled Input Pump Power

As shown by Meng in reference [38] (reference 7 therein), the amount of light coupled into the Raman cavity can be found by looking at the below-threshold slope of the forward pump power as a function of the input power. Below threshold, the forward power as a function of the input power, on resonance, is given by equation L.7, which is restated her

$$\mathcal{P}_{f\,max} = \frac{\mathcal{P}_{in}T^2}{1+R^2-2R}. \tag{O.3}$$

In equation O.3, $\mathcal{P}_{in}$ can be viewed as the actual input power coupled into a given cavity mode. As such, it is a fraction of the actual input power at the front of the cavity. (Possible loss sources that decrease the input power are light reflected due to mode-mismatch with the pump mode in use, reflections from the input window, etc...). Let the ratio of the power coupled into a given mode to the input power measured in front of the cavity be given by

$$\frac{\mathcal{P}_{in}}{\mathcal{P}_{in\,m}} = B, \tag{O.4}$$

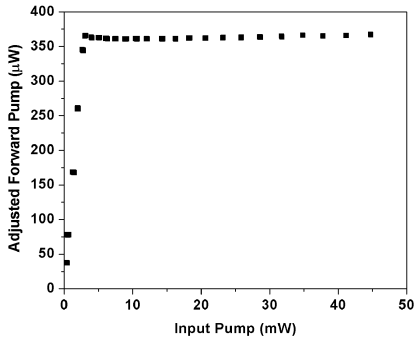

(a) Pump power.

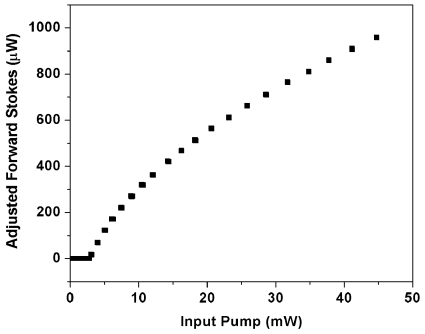

(b) Stokes power.

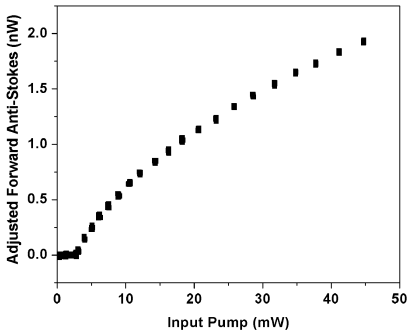

(c) Anti-Stokes power.

Figure O.5: The adjusted pump, Stokes, and anti-Stokes powers as a function of the input pump power.

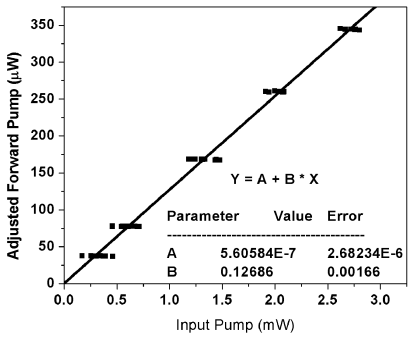

Figure O.6: The below-threshold forward pump power as a function of input power. The data is shown as squares. The line is a linear fit to the data, the parameters of which are shown on the figure.

where $\mathcal{P}_{in\,m}$ is the measured input power. Plugging equation O.4 into equation O.3 gives

$$\mathcal{P}_{f\,max} = \frac{B\mathcal{P}_{in\,m}T^2}{1+R^2-2R}. \tag{O.5}$$

Below threshold, $\mathcal{P}_{f\,max}$ varies linearly with $\mathcal{P}_{in\,m}$, the slope of which is

$$\frac{\Delta\mathcal{P}_{f\,max}}{\Delta\mathcal{P}_{in\,m}} = \frac{BT^2}{1+R^2-2R}. \tag{O.6}$$

Given the mirror's reflectivity, R, and transmittivity, T, at the pump wavelength, then the parameter, B, can be determined. R was measured by the ringdown technique [82]. The transmittivity was measured directly.

Figure O.6 plots only the below-threshold forward pump power as a function of the measured input power, from Figure O.5a. A linear fit (solid line) was made to the data. The y-intercept is not precisely zero, but is small enough that it can be ignored. Using the values of the pump reflectivity and transmittivity from Table 5.1 and the slope as determined by the linear fit, the parameter, B, is

$$B = 0.45 \tag{O.7}$$

The x-axis of Figure O.5 can now be converted from input pump power to coupled input pump power by multiplying the input power by B. The resulting plots are shown in Figure O.7, which are the same as those shown in Figure 5.6.

The same basic process can be used when the cavity mirrors are not matched, as in experiment 2, but equation O.5 must be modified to account for the different reflectivities and transmittivities of the mirrors.

If either the reflectivity or the transmittivity of the mirrors is not known, a second equation can be found based on the amount of light reflected by the cavity when on resonance as a function of the measured input power.

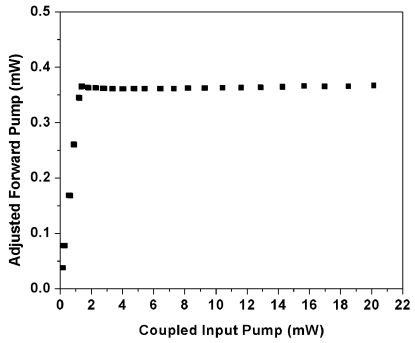

(a) Pump power.

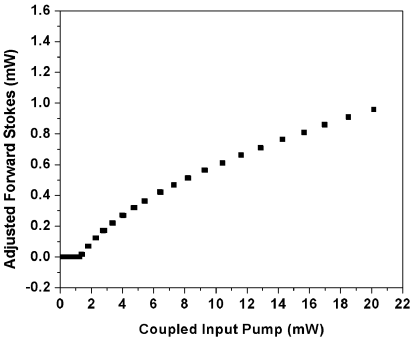

(b) Stokes power.

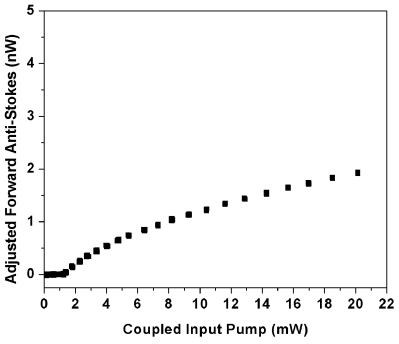

(c) Anti-Stokes power.

Figure O.7: The adjusted pump, Stokes, and anti-Stokes powers as functions of the coupled input pump power.

APPENDIX P

ADDITIONAL EXPERIMENT 1 DATA

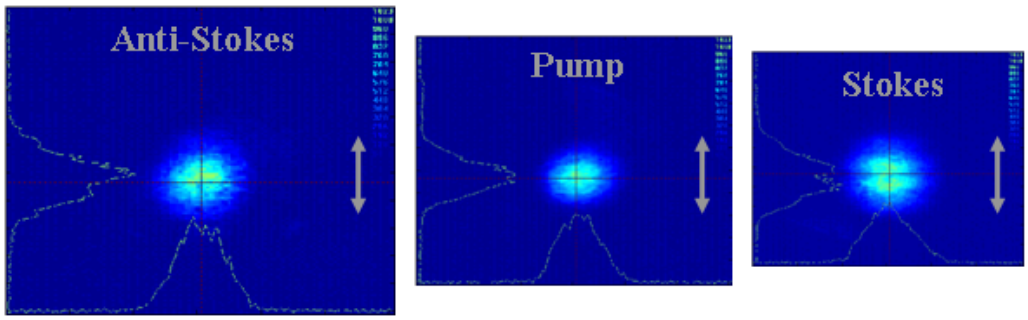

Figure P.1: Spatial profiles of the pump, Stokes, and anti-Stokes at 45.11 psi (3.07 atm). The profiles have been rescaled to account for the different path lengths from the cavity to the camera, as outlined in Appendix N. The grey arrow is 2.3-mrad long.

This appendix presents additional Experiment 1 data. Portions of the data sets in this appendix are used in either Chapter 5 or 6 and their inclusion here is to allow any interested party to see the complete data sets. The theoretical fits were made using the parameters in Table 5.1. The data is organized from lowest pressure to highest.

Since, for the most part, this data is presented elsewhere in the dissertation, the discussion of the data here is fairly terse. It is meant to be just enough to give the reader some indication of what was discussed in the main body of the dissertation without repeating it.

Data at 45.11psi (3.07 atm)

This data set is for pump, Stokes, and anti-Stokes on TEM_{00} modes. It is used in Chapter 5 for comparisons between Experiment 1 and Experiment 2 data (on page 152). It is also used in Chapter 6 for comparisons between mode combinations (Figure 6.29). Figure P.1 shows the mode profiles.

Figure P.2 shows the forward powers as functions of the coupled input pump power. Theory and data for the pump and Stokes are in good agreement. The anti-Stokes data falls within the maximum and minimum values of the Airy function. The threshold for this data set is 2.5 mW. The two theoretical lines on Figure P.2c show the amount of anti-Stokes produced at the maximum and the minimum of the Airy function for the anti-Stokes in this experiment.

Data at 45.14 psi (3.07 atm)

This data set is used in Chapter 6 for comparisons between mode combinations (Figure 6.29). As shown in Figure P.3, the pump is TEM_{00} and the Stokes and anti-Stokes are HG TEM_{10}. Agreement between data and theory in Figure P.4 is excellent, especially considering that both the Stokes and anti-Stokes are HOM. The threshold is 5.6 mW.

Data at 46.6 psi (3.17 atm)

This data set is used in two places in Chapter 6. The first place is an example of the anti-Stokes profile observed when the pump was TEM_{00} and the Stokes was HG TEM_{40}. As shown in Figure 6.26, the anti-Stokes mode is not well-defined and, as discussed in that chapter, is most likely a superposition of modes. This data set is also used for comparisons between mode combinations (Figure 6.29). In Chapter 6, only the anti-Stokes power as a function on input power (Figure 6.26) is shown. Figure P.5 shows the pump, Stokes and anti-Stokes powers as functions of input power. Agreement between data and theory is not perfect. The measured threshold is $\sim$1.2 times the theoretical threshold. In Figure P.5c, the solid line assumes theoretically

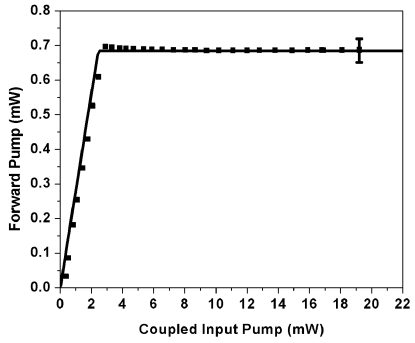

(a) Pump power.

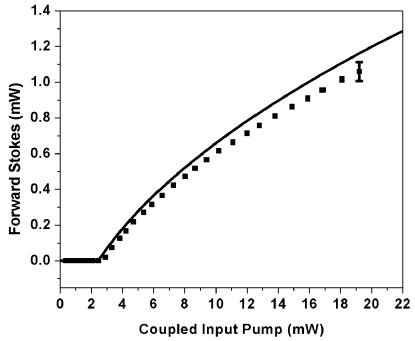

(b) Stokes power.

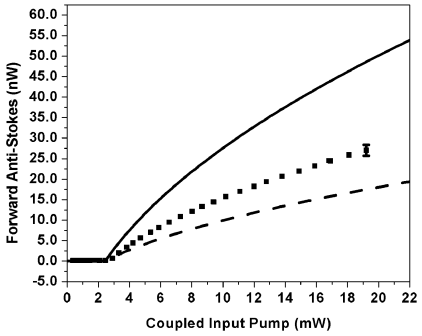

(c) Anti-Stokes power.

Figure P.2: Output powers as functions of coupled input pump power at 45.11 psi (3.07 atm) on gain line-center. Data is shown as squares and theory as lines.

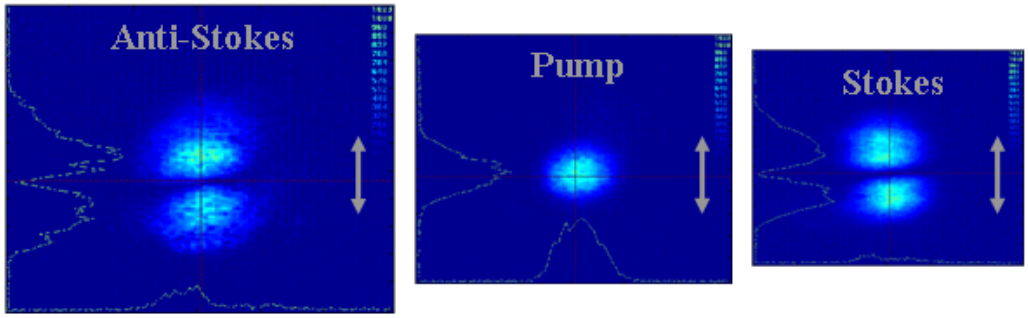

Figure P.3: Spatial profiles of the pump, Stokes, and anti-Stokes at 45.14 psi (3.07 atm). The profiles have been rescaled to account for the different path lengths from the cavity to the camera, as outlined in Appendix N. The grey arrow is 2.3-mrad long.

that the anti-Stokes is HG TEM_{40} while the dashed line assumes the anti-Stokes mode is HG TEM_{20} and the dotted line assumes TEM_{00}. The latter two are almost indistinguishable.

Data at 65.77 psi (4.47 atm)

This data set is used as an example of the mode combination with the pump TEM_{00} and the Stokes HG TEM_{20}. The anti-Stokes mode was not a well-defined mode, as shown in Figure 6.16c. In Chapter 6, only the anti-Stokes power as a function of input power is presented. Figure P.6 shows the pump, Stokes, and anti-Stokes powers as functions of coupled input pump power. Agreement between theory and data is poor. The measured threshold is 1.8 times the theoretical threshold.

Data at 66.56 psi (4.53 atm)

Like the data set at 45.14 psi, this data set is also for the case where the pump is TEM_{00} and the Stokes and anti-Stokes are HG TEM_{10}, as shown in Figure 6.9b. In

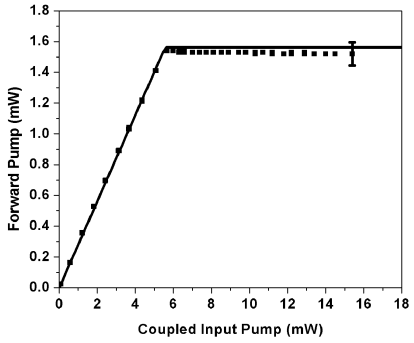

(a) Pump power.

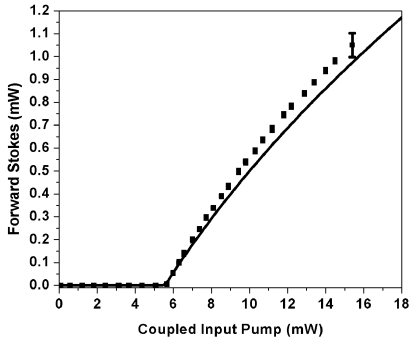

(b) Stokes power.

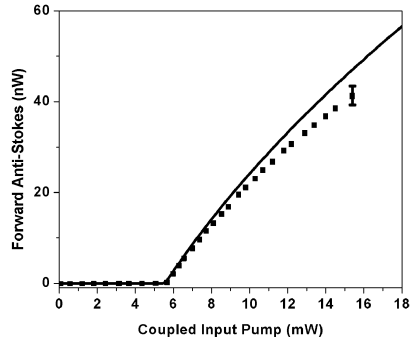

(c) Anti-Stokes power.

Figure P.4: Output powers as functions of coupled input pump power at 45.14 psi (3.07 atm) on gain line-center. Data is shown as squares and theory as lines.

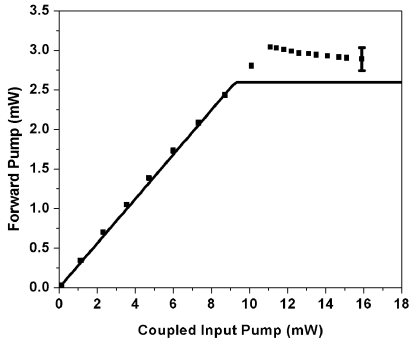

(a) Pump power.

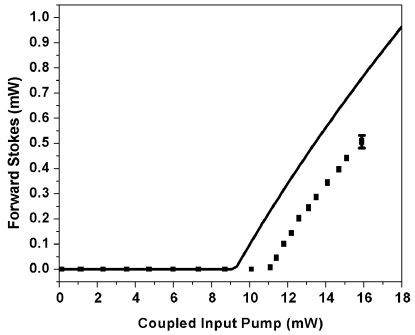

(b) Stokes power.

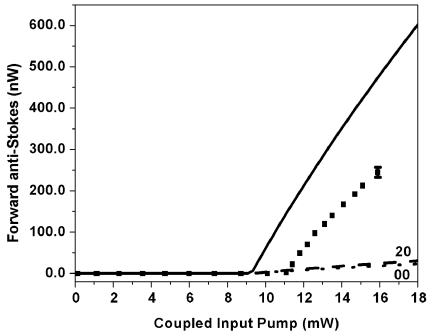

(c) Anti-Stokes power.

Figure P.5: Output powers as functions of coupled input pump power at 46.6 psi (3.17 atm) on gain line-center. Data is shown as squares and theory as lines.

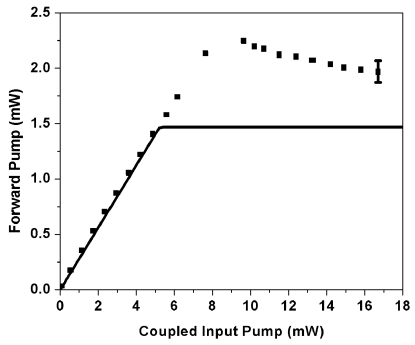

(a) Pump power.

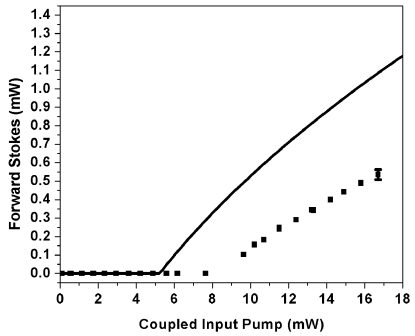

(b) Stokes power.

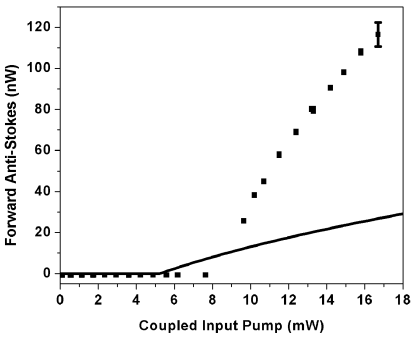

(c) Anti-Stokes power.

Figure P.6: Output powers as functions of coupled input pump power at 65.77 psi (4.47 atm) on gain line-center. Data is shown as squares and theory as lines.

Chapter 6, only the anti-Stokes power is presented as a function of coupled input pump power. Figure P.7 shows all three beams as functions of coupled input pump power. Agreement between data and theory for this data set is quite good for the pump and Stokes. The measured anti-Stokes power is twice as large as the theoretically predicted value.

Data at 90.48 psi (6.2 atm)

This data set has the pump and Stokes TEM_{00}. However, it falls within the range of pressures in Figure 5.14c where the anti-Stokes mode was not TEM_{00}. As discussed in Chapter 6, in this case, the anti-Stokes profile (shown in Figure 6.4 looks like an LG TEM_{10}, But, as discussed in Chapter 6, it is not a pure LG TEM_{10} mode because the distribution of the intensity in the profile is incorrect. A superposition of modes is found that gives the correct intensity distribution.

Figure P.8 shows the pump, Stokes, and anti-Stokes powers as functions of coupled input pump power. The agreement between theory and agreement for the pump and Stokes is excellent. There are two theoretical curves on the anti-Stokes profile. The solid line assumes that the anti-Stokes mode is TEM_{00} and the dashed line assumes LG TEM_{10}. In both cases, the theory is less than the data.

Data at 99.26 psi (6.8 atm)

This data set has the pump and Stokes on TEM_{00} modes, as shown in Figure 6.1, while the anti-Stokes was found to be a superposition of spatial modes.

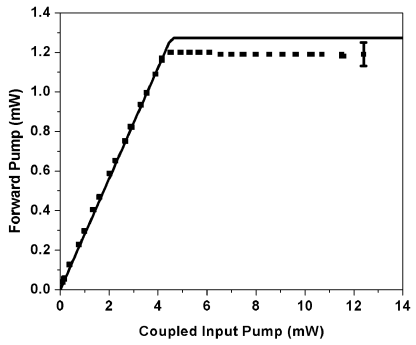

(a) Pump power.

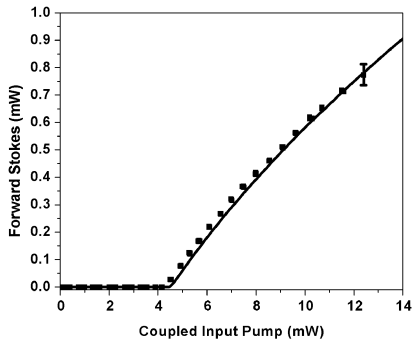

(b) Stokes power.

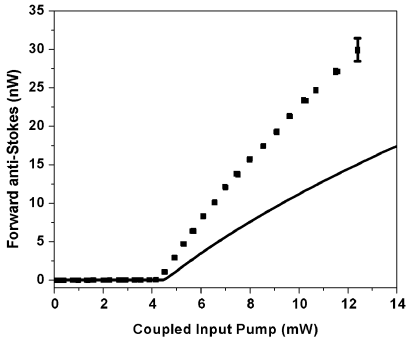

(c) Anti-Stokes power.

Figure P.7: Output powers as functions of coupled input pump power at 66.56 psi (4.53 atm) on gain line-center. Data is shown as squares and theory as lines.

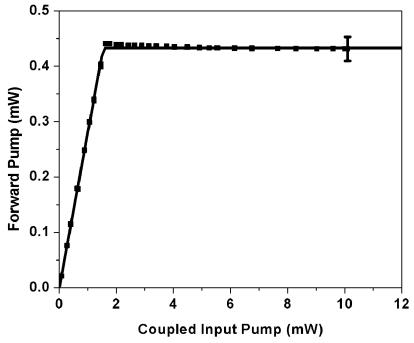

(a) Pump power.

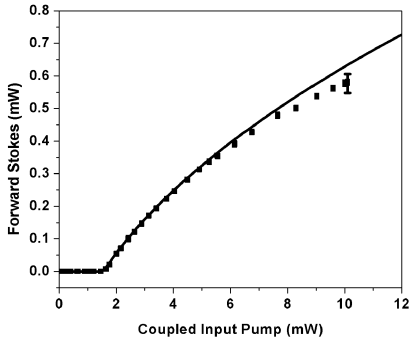

(b) Stokes power.

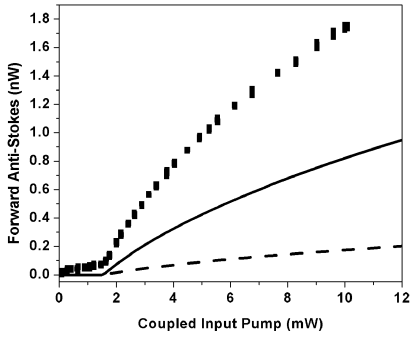

(c) Anti-Stokes power.

Figure P.8: Output powers as functions of coupled input pump power at 90.48 psi (6.2 atm) on gain line-center. Data is shown as squares and theory as lines.

Figure P.9 shows the pump, Stokes, and anti-Stokes powers as functions of coupled input pump power. The theory and data for the pump mode agree quite well (Figure P.9a) .

However, the agreement between theory and data for the Stokes (Figure P.9b) is not as good as seen for other data sets with both the pump and Stokes TEM_{00}. As mentioned in Chapter 5, of all the data sets used to make Figure 5.14b, this set is good example of the sets that do not have near perfect agreement between the Stokes data and theory.

The measured anti-Stokes power in Figure P.9c is so much larger than the theory that they had to be presented on separate vertical axes. The left axis is for the data and the right is for the theory. There are four theoretical curves, each of which assumes a different anti-Stokes mode profile. The solid line assumes that the anti-Stokes mode is a pure TEM_{00}, while the dashed and dotted lines assume pure LG TEM_{10} and LG TEM_{20} modes respectively. The final theoretical line, dot-dash, is an attempt to mimic the superposition of fields that yielded a spatial pattern comparable to the observed pattern.

Data at 154.65 psi (10.52 atm)

The pump, Stokes, and anti-Stokes modes in this data set were all HG TEM_{10}, as shown in Figure 6.27. In Chapter 6, only the anti-Stokes data as a function of coupled input pump power is shown.

Figure P.10 shows the forward pump, Stokes and anti-Stokes powers as functions of coupled input pump power. The agreement between data and theory is not great. However, while there is no indication of this in lab notes, this data set shows characteristics of other sets that are known to have had frequency locking issues during

their acquisition. Specifically, the fact that the pump is not clamped above threshold in Figure P.10a and the deviation of the below threshold slope from the theoretical slope are indicative of frequency locking issues. In P.10b, the above threshold Stokes power does not grow with a square-root dependence of the input. It is thought that if a better data set had been obtained, the agreement between theory and data would be much better. Also, the below threshold growth of the anti-Stokes power in Figure P.10c is due to scattered pump power reaching the anti-Stokes power meter.

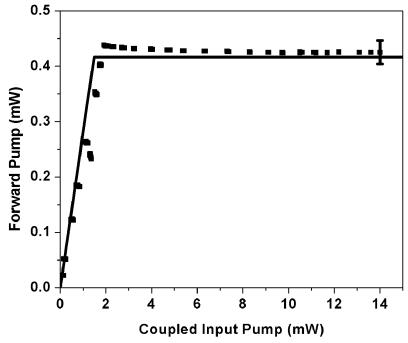

(a) Pump power.

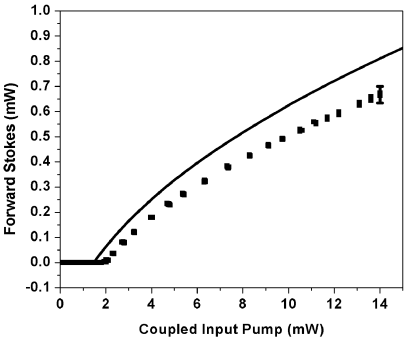

(b) Stokes power.

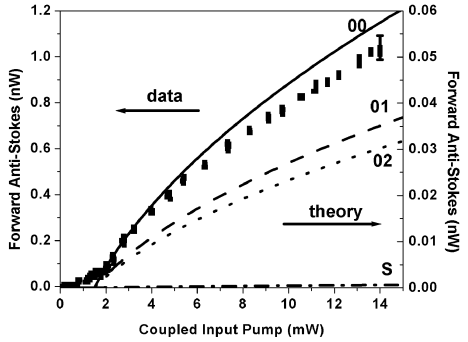

(c) Anti-Stokes power.

Figure P.9: Output powers as functions of coupled input pump power at 99.26 psi (6.8 atm) on gain line-center. Data is shown as squares and theory as lines.

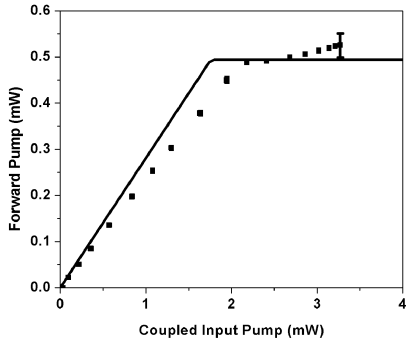

(a) Pump power.

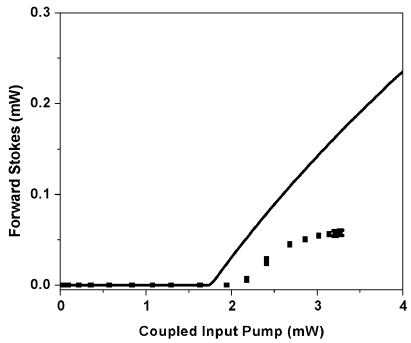

(b) Stokes power.

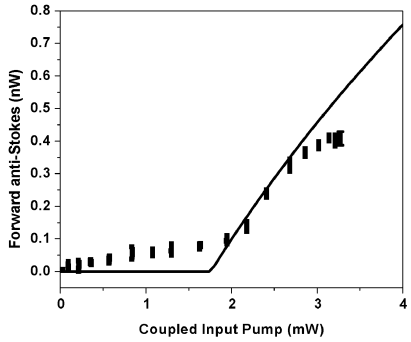

(c) Anti-Stokes power.

Figure P.10: Output powers as functions of coupled input pump power at 154.65 psi (10.52 atm) on gain line-center. Data is shown as squares and theory as lines.

APPENDIX Q

ADDITIONAL EXPERIMENT 2 DATA

This appendix presents additional Experiment 2 data. Portions of the data sets in this appendix are used in either Chapter 5 or 6 and their inclusion here is to allow any interested party to see the complete data sets. The theoretical fits were made using the parameters in Table 5.2. The data is organized from lowest pressure to highest.

Since, for the most part, this data is presented elsewhere in the dissertation, the discussion of the data here is fairly terse. It is meant to be just enough to give the reader some indication of what was discussed in the main body of the dissertation without repeating it.

Data at 45.39 psi (3.08 atm)

As shown in Figure 6.11, the pump for this data set was TEM_{00} while the Stokes and anti-Stokes were identified as HG TEM_{10} and LG TEM_{11} modes, respectively. Figure Q.1 shows the forward pump, Stokes, and anti-Stokes powers as functions of the coupled input pump power. Theory and data are not in good agreement for any of the three beams, which is surprising, since they agreed for the pump and Stokes data from Experiment 1. Unlike other cases where theory and data disagreed, for this data set, the theory is predicting a higher threshold than what was measured. Thus, the cause of the discrepancy might be an error in the calibration of the data.

Data at 45.72 psi (3.11 atm)

As shown in Figure 6.13, the pump for this mode combination was TEM_{00}, while the Stokes and anti-Stokes most closely resemble LG TEM_{10} modes. However, as discussed in Chapter 6, neither the Stokes nor the anti-Stokes are pure LG TEM_{10}

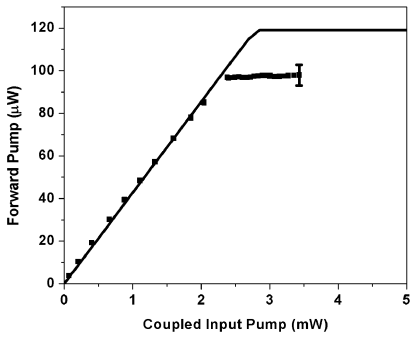

(a) Pump power.

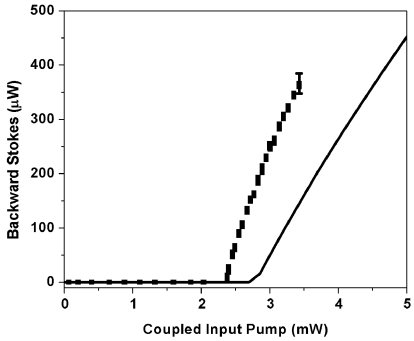

(b) Stokes power.

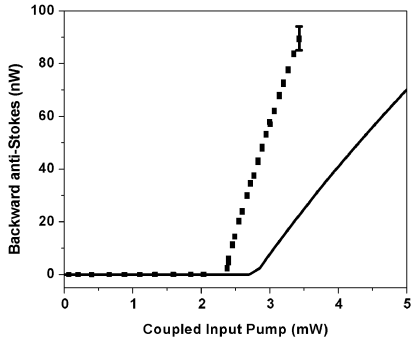

(c) Anti-Stokes power.

Figure Q.1: Output powers as functions of coupled input pump power at 45.39 psi (3.08 atm) on gain line-center. Data is shown as squares and theory as lines.

modes. But, the theory requires that a single pure mode be chosen for both the Stokes and anti-Stokes in order to calculate the overlap integrals. The chosen mode was the LG TEM_{10} for both. Even so, the theoretical and measured thresholds are in very good agreement. However, the theoretical amount of anti-Stokes calculated is a factor of 4 smaller than the data.

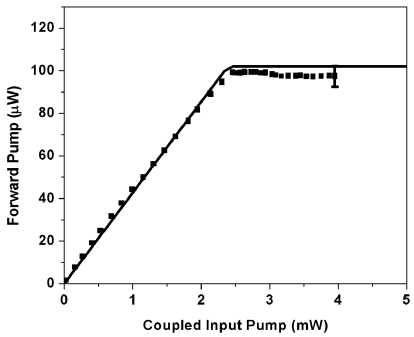

(a) Pump power.

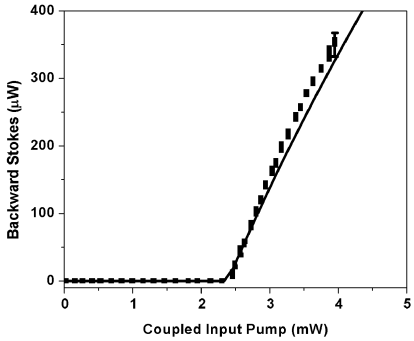

(b) Stokes power.

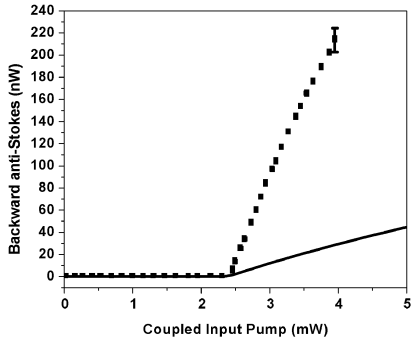

(c) Anti-Stokes power.

Figure Q.2: Output powers as functions of coupled input pump power at 45.72 psi (3.11 atm) on gain line-center. Data is shown as squares and theory as lines.

APPENDIX R

FURTHER THOUGHTS ON PHASE MATCHING

Sometimes the anti-Stokes data in Chapters 5 and 6 is larger than the theory and sometimes it is smaller. When the data was smaller than the theory, it was explained using the Airy function. But, when it was larger the only explanation that was ever offered was that something was improving the phase-matching of the system. In reality, both effects are influencing every data set. And, they can not be separated. The goal of this appendix is to try to clarify the anti-Stokes theory and how it relates to the data.

The Theory

The theory used to fit the data assumes that all three wavelengths are resonant on a single cavity, i.e. there is only one cavity length in the calculation. In reality, for Experiment 1, there are at least two cavity lengths (since it is unclear where the anti-Stokes reflection is coming from), and for Experiment 2, there are three. These different cavity lengths are caused by the coatings on the mirrors. In order to make mirrors that are highly reflective at wavelengths as disparate as the one's in this system, it is necessary to apply separate coating stacks for each wavelength. Each coating stack consists of roughly 40 quarter-wave layers at the wavelength it is designed to reflect. Thus, each cavity length is on the order of tens of microns longer than the previous. (This is why the mirror's are inherently chirped.) However, the exact structure of the mirrors is not known, therefore, any guess at the actual cavity lengths would not be more valid than the assumption that they were all the same.

Because of the assumption that all the cavity lengths are equal, the calculated resonant frequencies do not exactly correspond to the experimental resonant frequencies. Therefore, the calculated wavevectors are not quite the experimental wavevectors, and the calculated value of Δk is not quite accurate. Δk is a very important parameter

when considering the agreement between theory and data and a small difference in it can make a large difference.

This point is best illustrated using the analytical result for V_{FWM} found in Appendix H with the collimated beam approximation. That result is in equation H.19 and is restated here.

$$V_{FWM} = \frac{\pi \varpi_o^2}{4\Delta k} \sin\left[\frac{\Delta k\, L}{2}\right] \tag{R.1}$$

When the system is perfectly phase-matched ($\frac{\Delta k\, L}{2} = 0$ or an even multiple ofπ), $|V_{FWM}|$ is constant at its maximum value of $\frac{\pi \varpi_o^2}{4}$. When $\frac{\Delta k\, L}{2}$ is an odd multiple of π, then V_{FWM} is zero. Near either of these two extremes, small changes in $\frac{\Delta k\, L}{2}$ will not make huge differences in the value of V_{FWM}. However, if $\frac{\Delta k\, L}{2}$ is near $\pi/2$ where the slope of the sine function is the largest, small changes could make a large difference in the value of V_{FWM}.

The question now becomes if the data observed always is smaller than the maximum possible for that mode combination. This may not be 100% conclusive for HOM combinations depending on how well the assumed mode structure actually reflects the observed mode structure. Some of the figures will now be reconsidered on a case-by-case basis.

Figure 5.14c

For the most part, the data in Figure 5.14c falls in between the two theoretical curves shown on the figure. For reference, that figure is again shown in Figure R.1a. There are two theoretical lines. The solid (dashed) one assumes that the anti-Stokes frequency is at the maximum (minimum) of the Airy function and that the input pump power is 11 mW (8 mW). There are five points between roughly 55 psi (3.7

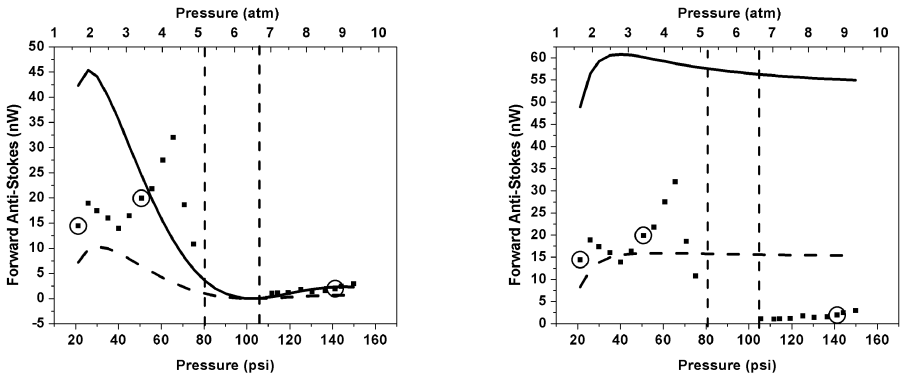

(a) Non-perfect phase-matching. (b) Perfect phase-matching.

Figure R.1: Anti-Stokes power as a function of pressure.

atm) and 75 psi (5.1 atm) which fall above both theoretical curves. It is presumed that something is improving the phase-matching for these five points. Other than these five points, the single-cavity theory seems to predict the data fairly well. The amount of anti-Stokes observed at pressures below the two dashed vertical lines is much larger than that observed above, as predicted by the theory. Also, there was no anti-Stokes observed with the appropriate mode structure between the two dashed vertical lines. The pressures between the two dashed vertical lines include the pressure where, theoretically, there should be no TEM_{00} anti-Stokes observed because V_{FWM} is zero due to phase-matching.

Figure 5.14b is replotted here with the theory modified to assume perfect phase matching ($\Delta k = 0$). (This change does not affect the pump or Stokes plots in Figures 5.14a and b.) In this case, the solid (dashed) line represents the theory which assumes that the system is perfectly phase-matched and that the anti-Stokes optical frequency is at the maximum (minimum) of the Airy function for an input pump power of 11 mW (8 mW). Since V_{FWM} is constant, the shape of the anti-Stokes theory is determined by the behavior of the pump and Stokes as functions of pressure. The five points which before fell above the two curves now fall below the solid curve, therefore, the guess

Pressure (psi)	Correction Factor	Pressure (psi)	Correction Factor
21.18	0.31	95.53	0.015
25.84	0.33	99.26	0.008
29.94	0.31	105.57	0.006
35.16	0.26	114.29	0.008
40.03	0.25	119.38	0.009
45.11	0.28	125.18	0.015
50.75	0.33	130.51	0.014
55.69	0.41	136.67	0.017
60.80	0.49	141.23	0.023
65.66	0.55	144.16	0.026
70.78	0.32	149.91	0.041
75.18	0.19		

Table R.1: Table of the correction factors that make the perfectly phase-matched theory agree with the anti-Stokes data. The correction factor accounts for both the assumed phase-matching being off and the anti-Stokes optical frequency not coinciding with the maximum of the Airy function.

that phase-matching was playing a roll appears to have been a good one. However, the theory no longer predicts why there is a region in pressure where the TEM_{00} mode does not occur nor why the anti-Stokes produced at higher pressures is so much less than that produced at lower pressures.

Table R.1 shows the amount that the theory and data for each of the 27 data points in Figures R.1a and b differ. The "correction factor" is the amount that the perfectly phase-matched theory (assuming that the anti-Stokes frequency is at the maximum of the Airy function) needs to be changed in order to agree with the theory. This correction factor takes into consideration effects related to both phase-matching and the Airy function. As expected from Figure R.1b, at higher pressures the correction factor is a much smaller number than at lower pressures indicating that the theory needed to be reduced much more. It is presumed that if the data had been taken with the anti-Stokes frequency at the maximum of the Airy function, then the variation in the data from one pressure to the next would be less random and the value of $\frac{\Delta k\, L}{2}$

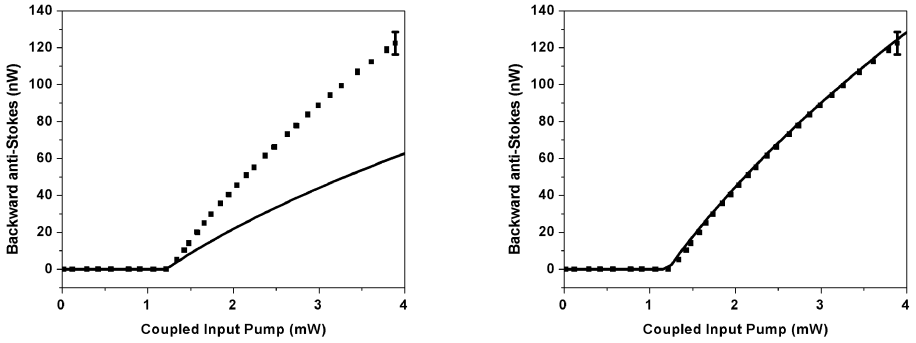

(a) Non-perfect phase-matching. (b) Perfect phase-matching.

Figure R.2: Anti-Stokes power as a function of input pump power at 45.7 psi (3.10 atm). By assuming perfect phase-matching, the anti-Stokes theory agrees with the data.

could be determined.

Figures 5.18c, 6.12, and 6.15

The three figures that are the subject of this section are all from Experiment 2. This experiment is interesting because of the increase in the anti-Stokes reflectivity of one of the mirrors which causes the anti-Stokes Airy function to be narrower and deeper which could lead less dependence on the Airy function. In addition, all three data sets show the measured anti-Stokes larger than the theory.

Figure R.2a repeats Figure 5.18c. Figure R.2b is the same data, but this time, the theory assumes perfect phase-matching. In both cases, it is assumed that the anti-Stokes frequency is at the maximum of the Airy function. By assuming perfect phase-matching, the theory was brought into perfect agreement with the data.

Figure R.3a repeats Figure 6.12c. Figure R.3b is the same data, but this time, the theory assumes perfect phase-matching. In both cases, it is assumed that the anti-Stokes frequency is at the maximum of the Airy function. Since the thresholds

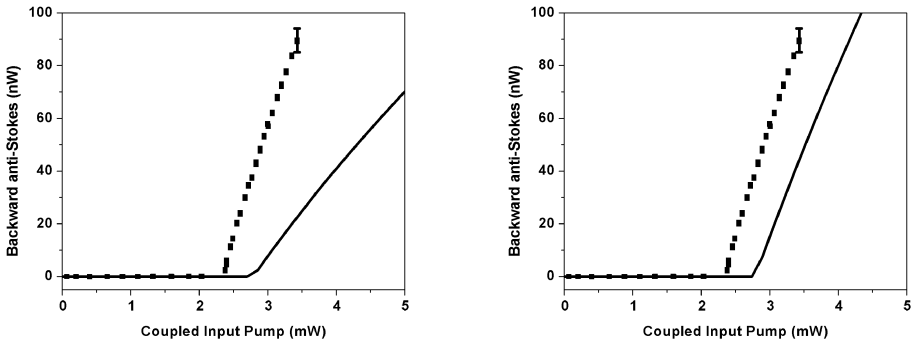

(a) Non-perfect phase-matching. (b) Perfect phase-matching.

Figure R.3: Anti-Stokes power as a function of input pump power at 45.39 psi (3.08 atm). By assuming perfect phase-matching, it appears that the anti-Stokes theory and data would agree if the threshold were correct.

do not agree, the theory and data are not in agreement. However, it appears that if the thresholds were the same, the theory and data would agree perfectly when assuming perfect phase-matching. This is surprising since the mode combination that was assumed when calculating the theory (pump TEM_{00}, Stokes HG TEM_{10}, and anti-Stokes HG TEM_{10}) does not really reflect the observed anti-Stokes profile (as shown in Figure 6.11). Perhaps, if the profile could be better understood, the theory would be higher and the Airy function would come into play.

Figure R.4a repeats Figure 6.15c. Figure R.4b is the same data, but this time, the theory assumes perfect phase-matching. In both cases, it is assumed that the anti-Stokes frequency is at the maximum of the Airy function. The assumption of perfect phase-matching increased the theory, but not by enough to make it at least as large as the data. However, as discussed in the section beginning on page 168, this is a case where the anti-Stokes mode profile assumed for the theory does not properly reflect the observed profile. Before further conclusions can be made about the agreement of the data and theory for this mode combination can be made, the theory needs

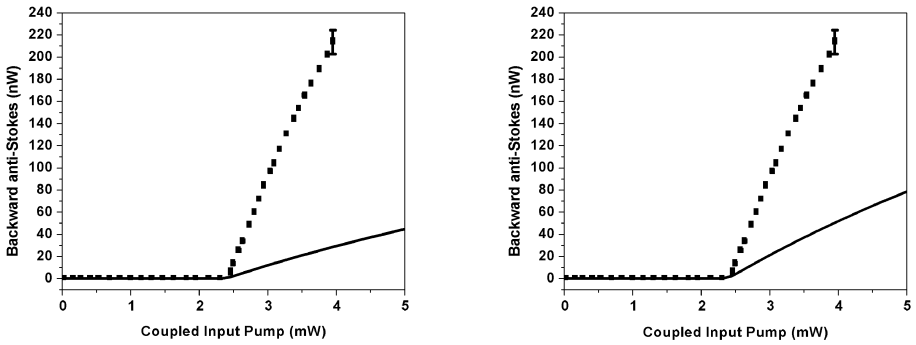

(a) Non-perfect phase-matching. (b) Perfect phase-matching.

Figure R.4: Anti-Stokes power as a function of input pump power at 45.72 psi (3.11 atm). Assuming perfect phase-matching did not bring the theory and data into agreement.

to be improved to properly take into account observed anti-Stokes profiles. This might mean modifying the theory so that more than one anti-Stokes mode can be generated at a time (and possibly augment each other) or mastering the integration of the overlap integrals in elliptic coordinates.

REFERENCES CITED

[1] T. H. Maiman, "Stimulated optical radiation in ruby," Nature **187**, 493–494 (1960).

[2] W. T. Silfvast, *Laser Fundamentals* (Cambridge University Press, 1996).

[3] J. K. Brasseur, "Construction and noise studies of a continuous wave Raman laser," Ph.D. thesis, MONTANA STATE UNIVERSITY, Montana State University, Dept of Physics, EPS 264, Bozeman, MT 59717 (1999).

[4] P. A. Roos, "The diode-pumped continuous wave Raman laser: Classical, quantum, and thermo-optic fundamentals," Ph.D. thesis, MONTANA STATE UNIVERSITY, Montana State University, Dept of Physics, EPS 264, Bozeman, MT 59717 (2002).

[5] L. S. Meng, "Continuous wave raman laser in H2: Semi-classical theory and diode pumping experiments," Ph.D. thesis, MONTANA STATE UNIVERSITY, Montana State University, Dept of Physics, EPS 264, Bozeman, MT 59717 (2002).

[6] Y. Xiong, "Mode-locked raman laser in H2 pumped by a mode-locked external cavity diode laser," Ph.D. thesis, MONTANA STATE UNIVERSITY, Montana State University, Dept of Physics, EPS 264, Bozeman, MT 59717 (2007).

[7] J. K. Brasseur, R. F. Teehan, P. A. Roos, B. Soucy, D. K. Neumann, and J. L. Carlsten, "High-power deuterium Raman laser at 632 nm," Appl. Opt. **43**, 1162–1166 (2004).

[8] G. Herzberg, *Spectra of Diatomic Molecules* (D. Van Norstrand Company, Inc, 1957).

[9] R. W. T. R. W. Minck and C. C. Wang, "Nonlinear optics," Proceedings of IEEE **54**, 1357–1377 (1966).

[10] H. Kavwano, Y. Hirakawa, and T. Imasaka, "Generation of more than 40 rotational Raman lines by picosecond and femtosecond Ti:sapphire laser for Fourier synthesis," Applied Physics B **65**, 1–4 (1997).

[11] D. R. Walker, D. D. Yavus, M. Y. Shverdin, G. Yin, and S. E. Harris, "A quasiperiodic approach to ultrashort pulses," Optics and photonics news pp. 46–51 (2003).

[12] J. K. Brasseur, K. S. Repasky, and J. L. Carlsten, "Continuous-wave Raman laser in H2," Opt. Lett. **23**, 367–369 (1998).

[13] L. S. Meng, P. A. Roos, and J. L. Carlsten, "Longitudinal mode-hopping hysteresis and bistability in a homogeneously broadened, continuous-wave Raman laser," J. Opt. Soc. Am. B **21**, 1318–1327 (2004).

[14] E. E. H. R. W. Minck and W. G. Rado, "Consideration and evaluation of factors influencing the stimulated optical scattering in gases," (1966).

[15] J. K. Brasseur, P. A. Roos, K. S. Repasky, and J. L. Carlsten, "Coherent anti-Stokes emission in a continuous-wave raman laser in H2," J. Opt. Soc. Am. B **17**, 1223–1228 (2000).

[16] R. W. P. Drever, J. L. Hall, F. V. Kowalski, J. Hough, G. M. Ford, A. J. Munley, and H. Ward, "Laser phase and frequency stabilization using an optical resonator," Applied Physics B **31**, 97–105 (1983).

[17] E. D. Black, "An introduction to Pound–Drever–Hall laser frequency stabilization," American Journal of Physics **69**, 79–87 (2001).

[18] Y. R. Shen and N. Bloembergen, "Theory of stimulated Brillouin and Raman scattering," Phys. Rev. **137**, A1787–A1805 (1965).

[19] P. A. Roos, L. S. Meng, S. K. Murphy, and J. L. Carlsten, "Approaching quantum-limited cw anti-Stokes conversion through cavity-enhanced Raman-resonant four-wave mixing," J. Opt. Soc. Am. B **21**, 357–363 (2004).

[20] D. A. Long, *Raman Spectroscopy* (McGraw-Hill, 1977).

[21] G. Venkataraman, *Journey Into Light: Life and Science of C. V. Raman* (Penguin, 1994).

[22] L. D. Kirkpatrick and G. E. Francis, *Physics: A World View, 6th Ed* (Thomson/Brooks/Cole, 2007).

[23] A. Javan, W. R. Bennett, and D. R. Herriott, "Population inversion and continuous optical maser oscillation in a gas discharge containing a He-Ne mixture," Phys. Rev. Lett. **6**, 106–110 (1961).

[24] N. Bloembergen, "The stimulated Raman effect," Amer. J. of Phys. **35**, 989–1023 (1967).

[25] M. Geller, D. P. Bortfeld, W. R. Sooy, and E. J. Woodbury, "Stimulated Raman emission in a normal ruby laser," Proceedings of the IEEE **51**, 1236–1237 (1963).

[26] R. Marx, U. Hubner, I. Abdul-Halim, J. Heppner, Y.-C. Ni, G.-D. Willenberg, and C. O. Weiss, "Far infrared cw Raman lasing and laser gain of NH3," IEEE J. of Quant. Elect. **QE-17**, 1123–1127 (1981).

[27] G. D. Willenberg, U. Hubner, and J. Heppner, "Far infrared cw Raman lasing in NH3," Opt. Comm. **33**, 193–196 (1980).

[28] M. Nakazawa, M. Tokuda, and N. Uchida, "Continuous-wave Raman oscillation for a Nd3+:YAG intracavity fiber laser," J. Opt. Soc. Am. B **1**, 86 (1984).

[29] R. V. Pound, "Electronic frequency stabilization of microwave oscillators," Review of Scientific Instruments **17**, 490–505 (1946).

[30] J. Segre, "High repetition rate operation of ND3+ glass lasers," IEEE J. of Quant. Elect. **QE-4**, 362 (1968).

[31] J. M. Herbelin and J. A. McKay, "Development of laser mirrors of very high reflectivity using the cavity-attenuated phase-shift method," Appl. Opt. **20**, 3341–3344 (1981).

[32] G. Rempe, R. J. Thompson, H. J. Kimble, and R. Lalezari, "Measurement of ultralow losses in an optical interferometer," Opt. Lett. **17**, 363–365 (1992).

[33] K. S. Repasky, J. K. Brasseur, L. Meng, and J. L. Carlsten, "Performance and design of an off-resonant continuous-wave Raman laser," J. Opt. Soc. Am. B **15**, 1667–1673 (1998).

[34] J. K. Brasseur, P. A. Roos, K. S. Repasky, and J. L. Carlsten, "Characterization of a continuous-wave Raman laser in H2," J. Opt. Soc. Am. B **16**, 1305–1312 (1999).

[35] J. K. Brasseur, P. A. Roos, L. S. Meng, and J. L. Carlsten, "Frequency tuning characteristics of a continuous-wave Raman laser in H2," J. Opt. Soc. Am. B **17**, 1229–1232 (2000).

[36] P. A. Roos, J. K. Brasseur, and J. L. Carlsten, "Diode-pumped nonresonant continuous-wave Raman laser in H2 with resonant optical feedback stabilization," Opt. Lett. **24**, 1130–1132 (1999).

[37] P. A. Roos, L. S. Meng, and J. L. Carlsten, "Using an injection-locked diode laser to pump a CW Raman laser," IEEE J. of Quant. Elect. **QE-36**, 1280–1283 (2000).

[38] L. S. Meng, K. S. Repasky, P. A. Roos, and J. L. Carlsten, "Widely tunable continuous-wave Raman laser in diatomic hydrogen pumped by an external-cavity diode laser," Opt. Lett. **25**, 472–474 (2000).

[39] L. S. Meng, P. A. Roos, K. S. Repasky, and J. L. Carlsten, "High-conversion-efficiency, diode-pumped continuous-wave Raman laser," Opt. Lett. **26**, 426–428 (2001).

[40] K. S. Repasky, L. Meng, J. K. Brasseur, J. L. Carlsten, and R. C. Swanson, "High-efficiency, continuous-wave Raman lasers," J. Opt. Soc. Am. B **16**, 717–721 (1999).

[41] P. A. Roos, S. K. Murphy, L. S. Meng, J. L. Carlsten, T. C. Ralph, A. G. White, and J. K. Brasseur, "Quantum theory of the far-off-resonance continuous-wave Raman laser: Heisenberg-Langevin approach," Phys. Rev. A **68**, 013802 (2003).

[42] S. Zaitsu, H. Izaki, and T. Imasaka, "Phase-matched Raman-resonant four-wave mixing in a dispersion-compensated high-finesse optical cavity," Physical Review Letters **100**, 073901 (2008).

[43] D. J. Griffiths, *Introduction to Electrodynamics, 3rd Ed* (Prentice Hall, 1999).

[44] W. K. Bischel and M. J. Dyer, "Temperature dependence of the Raman linewidth and line shift for the Q(1) and Q(0) transitions in normal and para-H2," Phys. Rev. A **33**, 3113–3123 (1986).

[45] R. W. Boyd, *Nonlinear Optics, 1st Ed* (Academic Press, Inc, 1992).

[46] B. E. A. Saleh and M. C. Teich, *Fundamentals of Photonics* (John Wiley and Sons, 1991).

[47] A. E. Siegman, *Lasers* (University Science Books, 1986).

[48] F. L. Kien, J. Q. Liang, M. Katsuragawa, K. Ohtsuki, K. Hakuta, and A. V. Sokolov, "Subfemtosecond pulse generation with molecular coherence control in stimulated Raman scattering," Phys. Rev. A **60**, 1562–1571 (1999).

[49] M. M. Audibert, J. C., and J. Ducuing, "Vibrational relaxation in hydrogen-rare-gases mixtures," Chemical Physics Letters **19**, 26–28 (1973).

[50] M. A. Bandres and J. C. Gutiérrez-Vega, "Ince–Gaussian modes of the paraxial wave equation and stable resonators," J. Opt. Soc. Am. A **21**, 873–880 (2004).

[51] M. A. Bandres and J. Gutiérrez-Vega, "Ince Gaussian beams," Opt. Lett. **29**, 144–146 (2004).

[52] U. T. Schwarz, M. A. Bandres, and J. C. Gutiérrez-Vega, "Observation of Ince–Gaussian modes in stable resonators," Opt. Lett. **29**, 1870–1872 (2004).

[53] A. Yariv, *Quantum Electronics, 3rd Ed* (John Wiley and Sons, 1989).

[54] W. K. Bischel and M. J. Dyer, "Wavelength dependence of the absolute Raman gain coefficient for the Q(1) transition in H2," J. Opt. Soc. Am. B **3**, 677 (1986).

[55] D. E. Gray, ed., *American Institute of Physics Handbook, 2nd Ed* (McGraw Hill, 1963).

[56] G. Tempea, F. Krausz, C. Spielmann, and K. Ferencz, "Dispersion control over 150 Thz with chirped dielectric mirrors," Selected Topics in Quantum Electronics, IEEE Journal of **4**, 193–196 (1998).

[57] F. X. Kärtner, N. Matuschek, T. Schibli, U. Keller, H. A. Haus, C. Heine, R. Morf, V. Scheuer, M. Tilsch, and T. Tschudi, "Design and fabrication of double-chirped mirrors," Opt. Lett. **22**, 831–833 (1997).

[58] N. Matuschek, F. Kartner, and U. Keller, "Theory of double-chirped mirrors," Selected Topics in Quantum Electronics, IEEE Journal of **4**, 197–208 (1998).

[59] R. Szipocs, K. Ferencz, C. Spielmann, and F. Krausz, "Chirped multilayer coatings for broadband dispersion control in femtosecond lasers," Opt. Lett. **19**, 201 (1994).

[60] K. Gabel, P. RuBbuldt, R. Lebert, P. Loosen, R. Poprawe, H. Heyer, and A. Valster, "Diode pumped, chirped mirror dispersion compensated, fs-laser," Opt. Comm. **153**, 275–281 (1998).

[61] R. Paschotta, G. J. Spuhler, D. H. Sutter, N. Matuschek, U. Keller, M. Moser, R. Hovel, V. Scheuer, G. Angelow, and T. Tschudi, "Double-chirped semiconductor mirror for dispersion compensation in femtosecond lasers," Applied Physics Letters **75**, 2166–2168 (1999).

[62] J. A. Armstrong, N. Bloembergen, J. Ducuing, and P. S. Pershan, "Interactions between light waves in a nonlinear dielectric," Phys. Rev. **127**, 1918–1939 (1962).

[63] N. Bloembergen and A. J. Sievers, "Nonlinear optical properties of periodic laminar structures," Applied Physics Letters **17**, 483–486 (1970).

[64] A. Szilagyi, A. Hordvik, and H. Schlossberg, "A quasi-phase-matching technique for efficient optical mixing and frequency doubling," Journal of Applied Physics **47**, 2025–2032 (1976).

[65] M. Fejer, G. Magel, D. Jundt, and R. Byer, "Quasi-phase-matched second harmonic generation: tuning and tolerances," Quantum Electronics, IEEE Journal of **28**, 2631–2654 (1992).

[66] R. C. Miller, "Optical harmonic generation in single crystal BaTiO3," Phys. Rev. **134**, A1313–A1319 (1964).

[67] J. Muzart, F. Bellon, C. A. Arguello, and R. C. C. Leite, "Generation de second harmonique non colineaire et colineaire dans ZnS accord de phase ("phase matching") par la structure lamellaire du cristal," Opt. Comm. **6**, 329–332 (1972).

[68] J. C. F. Dewey and L. O. Hocker, "Enhanced nonlinear optical effects in rotationally twinned crystals," Applied Physics Letters **26**, 442–444 (1975).

[69] L. O. Hocker and J. C. Fobes Dewey, "Enhancement of second-harmonic generation in zinc selenide by crystal defects," Applied Physics Letters **28**, 267–270 (1976).

[70] V. G. Besplaov and N. S. Makarov, "Quasi-phase matching generation of blue coherent radiation at stimulated raman scattering," Opt. Comm. **203**, 413–420 (2002).

[71] G. D. Boyd and C. K. N. Patel, "Enhancement of optical second-harmonic gneration (SHG) by reflection phase matching in zns and gaas," Applied Physics Letters **8**, 313–315 (1966).

[72] H. Komine, J. W. H. Long, J. W. Tully, and E. A. Stappaerts, "Quasi-phase-matched second-harmonic generation by use of a total-internal-reflection phase shift in gallium arsenide and zinc selenide plates," Opt. Lett. **23**, 661–663 (1998).

[73] A. Ashkin, G. D. Boyd, and J. M. Dziedzic, "Resonant optical second harmonic generation and mixing," IEEE J. of Quant. Elect. **QE-2**, 109 (1966).

[74] S. O. Konorov, D. A. Akimov, A. N. Naumov, A. B. Fedotov, R. B. Miles, J. W. Haus, and A. M. Zheltikov, "Bragg rsonance-enhanced coherent anti-Stokes Raman scattering in a planar photonic band-gap waveguide," J. of Raman Spect. **33**, 955–961 (2002).

[75] L. E. Myers, R. C. Eckardt, M. M. Fejer, R. L. Byer, W. R. Bosenberg, and J. W. Pierce, "Quasi-phase-matched optical parametric oscillators in bulk periodically poled LiNbO3," J. Opt. Soc. Am. B **12**, 2102 (1995).

[76] A. Siegman, "Laser beams and resonators: Beyond the 1960s," Selected Topics in Quantum Electronics, IEEE Journal of **6**, 1389–1399 (2000).

[77] A. E. Siegman, "Excess spontaneous emission in non-Hermitian optical systems. i. laser amplifiers," Phys. Rev. A **39**, 1253–1263 (1989).

[78] A. E. Siegman, "Orthogonality properties of optical resonator eigenmodes," Opt. Comm. **33**, 193–196 (1980).

[79] D. Zwillinger, ed., *Standard Mathematical Tables and Formulae, 30th Ed* (CRC Press, 1996).

[80] I. Kimel and L. Elias, "Relations between Hermite and Laguerre Gaussian modes," IEEE J. of Quant. Elect. **29**, 2562–2567 (1993).

[81] E. Hecht, *Optics, 3rd Ed* (Addison-Wesley, 1998).

[82] D. Z. Anderson, J. C. Frisch, and C. S. Masser, "Mirror reflectometer based on optical cavity decay time," Appl. Opt. **23**, 1238 (1984).